Development of Calcium Carbonate-based Nano- and Micro- Structural Materials

Trinity College Dublin
Coláiste na Tríonóide, Baile Átha Cliath
The University of Dublin

A thesis submitted to the School of Chemistry,

Trinity College Dublin,

for the degree of Doctor of Philosophy

By

Fearghal C Donnelly

Under the supervision of Prof. Yurii K. Gun'ko

September 2020

Summary

The main aim of this work was to develop the synthesis of $CaCO_3$ nano- and microparticles by various methods and to explore their potential applications. Specifically, the following techniques were used: precipitation reactions involving Ca^{2+} and CO_3^{2-} containing salts, a completely novel dry ice carbonation method, and finally CO_2 bubbling - the industrially used method of $CaCO_3$ production.

Chapter 1 of this thesis presents a review of the literature with particular relevance to this research, from $CaCO_3$ nano- and micro- materials to chiral and lumninescent nanomaterials, and will more generally give an introduction to $CaCO_3$ chemistry.

Chapter 2 describes all experimental details, including the starting materials used and the experimental procedures followed for each chapter specifically. The instrumental techniques which are used in this work are also discussed in this chapter.

Chapter 3 is focused on the precipitation reactions that were used for the finely controlled synthesis of $CaCO_3$ microspheres and their subsequent chiral functionalisation. For the first time, the synthesis of chiroptically active $CaCO_3$ microspheres was achieved using a variety of *L*- and *D*-amino acids as additives. The selected microspheres were then loaded with two different quantum dot (QDs) species as well as trivalent lanthanides, resulting in chiral luminescent microspheres with luminescence of varying colours. Gold nanoparticles (Au NPs) were also loaded separately to produce chiral plasmonic microspheres. Using similar principles to those involved in microsphere production, novel $CaCO_3$ helices have also been produced using 16-

2-16 gemini tartrates as chiral precursors.

Chapter 4 describes our work towards the production, by three methods, of a biocompatible drug delivery vesicle using the afore-mentioned $CaCO_3$ microspheres which were loaded with *S*-ibuprofen.

Chapter 5 describes, for the first time, our new dry ice carbonation method. Taking advantage of the retrograde solubility of $CaCO_3$, we developed this new method which utilises dry ice as both a source of CO_2 and as a coolant for the system to produce $CaCO_3$ nano- and microparticles with new morphologies. The effect of the solvent used has been studied in-depth showing that in H_2O calcite nanoparticles are formed preferentially, whereas in a 75 % % v/v CH_3OH solution, vaterite microspheres are formed almost exclusively.

Chapter 6 reports the further development of this research, specifically dealing with the production of new luminescent $CaCO_3$ materials. Building on this new approach, we have synthesised luminescent Eu^{3+} and Tb^{3+}-doped $CaCO_3$ materials presenting a novel 'bow tie' morphology. The effect of the dopant concentration on the morphology and properties of the $CaCO_3$ microstructures produced has been studied using x-ray diffraction and photoluminescence spectroscopy.

Chapter 7 describes the final aspect of our research involving $Ca(OH)_2$ and a CO_2 bubbling technique which is the most common industrial method of $CaCO_3$ production. This section of our work was focused on the optimisation of the synthesis of various morphologies for further potential development by McGraths Limestone (Cong) Ltd. for a range of potential applications. Specifically, this has involved studying the effect of the $Ca(OH)_2$ slurry concentration on the morphology of calcite formed. Using these results, we then investigated the effect of the CO_2 flow rate used at two different $Ca(OH)_2$ concentrations before examining the effect of the reaction temperature.

Finally, Chapter 8 contains our conclusions regarding each area of research and describes some of the ongoing research to be carried out in Future work.

Declaration

I declare that this report details entirely my own work. Due reference and acknowledgement of the work of others is given where appropriate.

Signed .....

Fearghal C Donnelly B.A. (Mod.)

Summary

The main aim of this work was to develop the synthesis of $CaCO_3$ nano- and microparticles by three methods: precipitation reactions involving Ca^{2+} and CO_3^{2-} containing salts, a completely novel dry ice carbonation method, and finally CO_2 bubbling - the industrially preferred method of $CaCO_3$ production.

Initially, precipitation reactions, exploring both template and microemulsion-based systems, were used for the finely controlled synthesis of $CaCO_3$ microspheres and their subsequent chiral and luminescent functionalisation with amino acids and two different quantum dot (QDs) species and trivalent lanthanide species, resulting in chiral luminescent microspheres with luminescence of varying colours. Gold nanoparticles (Au NPs) were also loaded separately to produce chiral plasmonic microspheres. Using similar principles to those involved in microsphere production, novel $CaCO_3$ helices have been formed using 16-2-16 gemini tartrates as chiral precursors.

In an attempt to produce a completely biocompatible drug delivery vesicle, $CaCO_3$ microspheres were loaded with *S*-ibuprofen. While the encapsulation has been achieved with various different methods, a controlled-drug release is yet to be carried out, however this will be carried out in future work.

Taking advantage of the retrograde solubility of $CaCO_3$, we have developed a new carbonation method which utilises dry ice as both a source of CO_2 and as a coolant

for the system to produce $CaCO_3$ nano- and microparticles with new morphologies. The effect of the solvent used has been studied in-depth showing that in H_2O calcite nanoparticles are formed preferentially, whereas at and above 75 % % v/v CH_3OH vaterite microspheres are formed almost exclusively.

Building on this new approach, we have synthesised luminescent Eu^{3+} and Tb^{3+}-doped $CaCO_3$ materials presenting a novel 'bow tie' morphology. The effect of dopant concentration has been studied using x-ray diffraction and photoluminescence spectroscopy. This novel approach has the potential to be expanded for the synthesis of other important carbonate nanomaterials (e.g. Li_2CO_3, $SrCO_3$), opening new possibilities in this research area and a variety of relevant industrial applications.

The final part of the work involved CO_2 bubbling which, as mentioned, is the most common industrial method of $CaCO_3$ formation. Our work was focused on the optimisation of the synthesis of various morphologies for further potential development by McGraths Limestone (Cong) Ltd. for a range of potential applications. Specifically, this has involved studying the effect of the $Ca(OH)_2$ slurry concentration on the morphology of calcite formed. Using these results, we then studied the effect of the CO_2 flow rate used at two different $Ca(OH)_2$ concentrations. The reaction temperature was then examined as well as the effect of various additives on the product formed.

Acknowledgements

First and foremost, I must thank Prof. Yurii Gun'ko for his time, dedication, knowledge, and most importantly his support. Through the various highs and lows of a Ph.D., the benefit of having a mentor of his caliber can't be overstated. I will be forever grateful for his taking a chance on me as an undergraduate, and hopefully this work goes some small way to thanking him.

To my parents, Nuala and Fearghal, who are my greatest sources of inspiration, and my brothers, Cathal, Pearse and Emmet, my greatest sources of grief, thank you for everything. I couldn't ask for a group of people I'm prouder to call my family.

To my esteemed colleague Shelley Stafford Sch., your love and support (and ungodly amount of time spent proofreading) have made writing this thesis that much easier. I only hope that I can repay the favour when your time comes, or at least book you a Rome-bound flight and be waiting at Sant' Eustachio Il Caffè.

To the other members of the Gun'ko group, past and present, I would like to extend my sincerest thanks for their support and considerable friendship. They have become a second family to me, and I am lucky to have made some lifelong friends throughout my time with them.

Sincere thanks must go to Dr. Finn Purcell-Milton with whom I formed a successful writing partnership. His seemingly endless knowledge coupled with a natural gift for teaching make for a formidable academic and much of the work on luminescent nanomaterials would not have been possible if not for his considerable expertise. Likewise, Dr. Peter Dunne deserves special thanks, not only for his expertise with XRD and all areas of chemistry, but also for his friendship. I would also like to thank Dr. Olan Cleary, for convincing me to do a Ph.D. and with whom much of the chiral work was carried out; Dr. Brendan Twamley for his help with XRD; Dr. Aran Rafferty who helped with TGA and porosimetry analysis; and Fred Cowzer and Maura Boland for their help with all things BOC.

Contents

List of Figures

Abbreviations

ACC - Amorphous calcium carbonate

BJH - Barrett-Joyner-Halenda analysis

CD - Circular dichroism

CIP - Cahn-Ingold-Prelog rules

CPL - Circularly polarised light

CTB - Charge transfer band

D - Dextrorotatory

DOX - Doxorubicin

DRCD - Diffuse reflectance circular dichroism

DTA - Differential thermal analysis

EDX - Energy-dispersive X-ray spectroscopy

FIB - Focused ion beam

FT-IR - Fourier transform - infrared spectroscopy

FWHM - Full width at half maximum

HPH - High pressure homogenisation

IBU - Ibuprofen

ICP-MS - Inductively coupled plasma - mass spectrometry

L - Levorotatory

MNP - Magnetic nanoparticle

NSAID - Non steroidal anti-inflammatory drug

OCD - Obsessive-Compulsive Disorder

PCC - Precipitated calcium carbonate

PPB - Parts per billion

PPM - Parts per million

PLEm - Photoluminescence emission spectroscopy

PLEx - Photoluminescence excitation spectroscopy

PNC - Pre-nucleation cluster

PVP - Polyvinylpyrrolidone

REE - Rare earth element

RoP - Ratio of peaks

R - Rectus

QD - Quantum dot

S - Sinistro

SDS - Sodium dodecyl sulfate

SEM - Scanning electron microscopy

TEM - Transmission electron microscopy

TGA - Thermogravimetric analysis

W/O - Water-in-oil

W/O/W - Water-in-oil-in-water

XRD - X-ray diffraction

Chapter 1

Introduction

1.1 Nanomaterials

The study of nanomaterials currently represents one of the most vibrant areas of research and spans a variety of fields across the sciences. Some nanomaterials have, for example, found uses as fuel cells,[1] photovoltaic devices,[2] mesoporous frameworks,[3] heterogeneous catalysts,[4] or more generally in the fields of optics[5–7] or biomedicine.[8,9] Nanomaterials are typically defined as those materials whose size measures less than 100 nm in at least one dimension (see Figure 1.1).

The intense interest generated by these materials stems from the fact that on the nanoscale, materials display radically different properties to their bulk counterparts. In short this arises from their large surface area-to-volume ratios which lead to markedly different activities. This is particularly relevant to calcium carbonate: in its bulk form, as the major constituent in limestone, its uses are considerably more limited than its nano- or microscale equivalent, precipitated calcium carbonate (PCC).

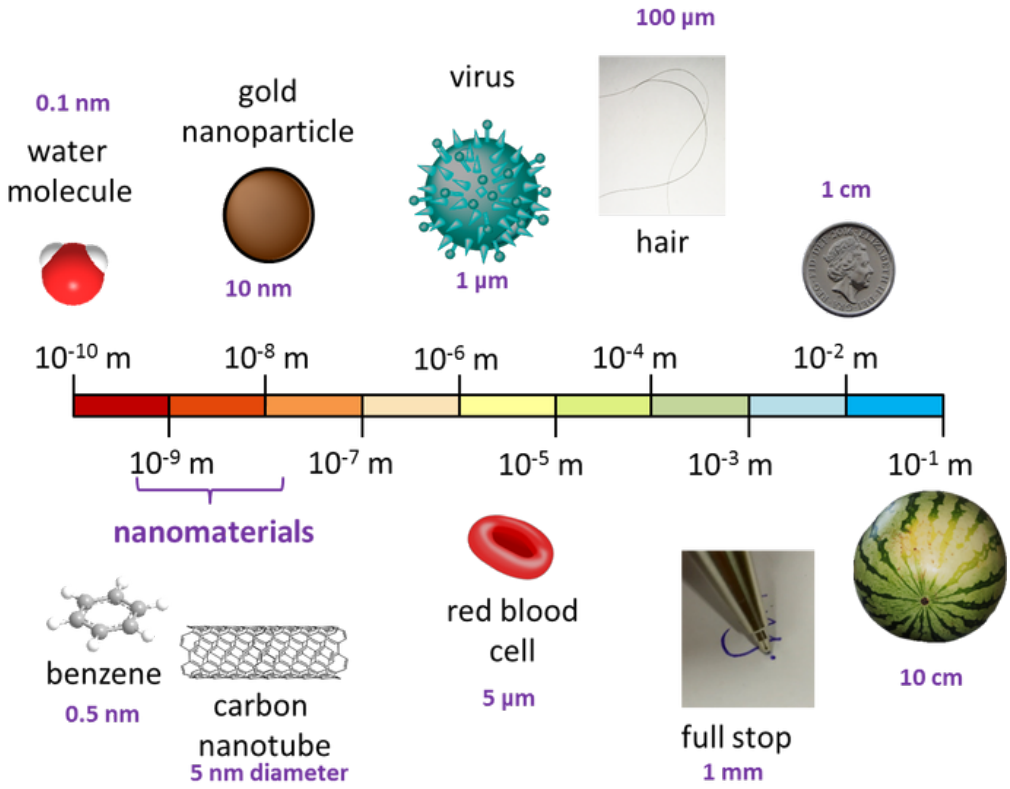

Figure 1.1: A visual representation of the nanoscale in perspective. Adapted from ref[10]

1.2 Calcium Carbonate, $CaCO_3$

A truly abundant material, $CaCO_3$ has always, and continues to, attract considerable attention. In the natural world, it is found in a wide array of systems from limestone, marble, and chalk, to the shells and bones of marine life. Actually, it is in marine life where $CaCO_3$ plays one of its most naturally important roles in biomineralisation. The ability of $CaCO_3$ to absorb atmospheric CO_2 is, in an age where the effects of global warming are increasingly felt, a particularly important area of research[11]. It is also a highly commercially important material, and has become an integral part of a number of significant applications.[12] For example, it has traditionally found uses in the construction industry in the production of lime mortar and cement. Due to its whiteness and high refractive index, it is also used in the manufacturing of high-gloss paper[13] and as a white pigment[14] in the paint

industry. The formation of porous $CaCO_3$ materials has opened the possibility for their use as catalytic supports where their large surface area provides many advantages over other heterogeneous supports.[15]

1.2.1 $CaCO_3$ Formation and Polymorphism

$CaCO_3$ exists in three anhydrous crystal polymorphs namely, calcite, aragonite, and vaterite (Figure 1.2) with two further hydrated forms: monohydrocalcite and a hexahydrate form, ikaite.[12,16] Amorphous calcium carbonate (ACC) is the least stable polymorph of $CaCO_3$.

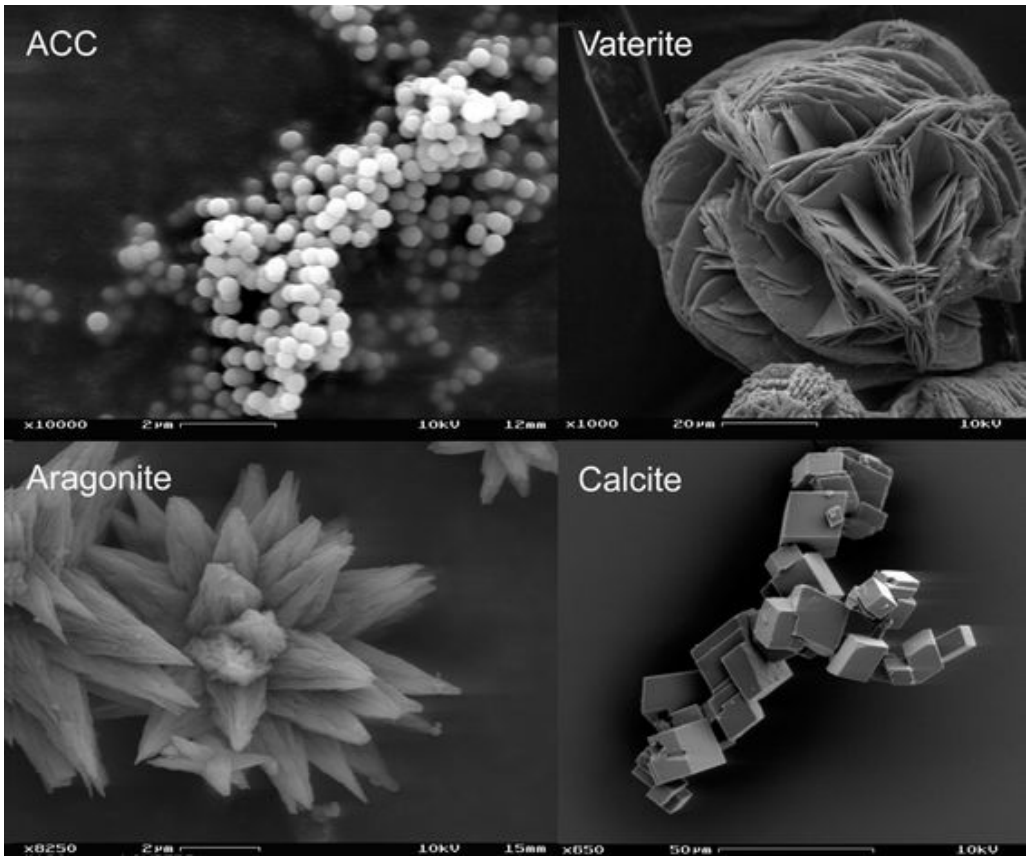

Figure 1.2: The four most common forms of $CaCO_3$ listed in terms of increasing stability: ACC, Vaterite, Aragonite, and Calcite. Adapted from ref[17]

Calcite is the most stable polymorph with a trigonal rhombohedral crystal structure, and typically has a rhombohedral morphology. Its stability arises from the fact both its alternating layers of Ca^{2+} and CO_3^{2-} as well as the fact that the CO_3^{2-} groups are at 60 ° to eachother. Aragonite is a metastable polymorph with the orthorhombic crystal structure which is formed preferentially in syntheses above 50 °C, and typically has a acicular, or needle-like morphology.[18,19] A decrease in stability, when compared with calcite, is rationalised by its staggered CO_3^{2-} layers. The presence of small amounts of other cations, such as Mg^{2+} in solution also promote the formation of the aragonite polymorph.[20,21] Finally, vaterite is the least stable form of anhydrous $CaCO_3$ with a hexagonal crystal system and polycrystalline spherulite morphology.[22] Partial CO_3^{2-} occupancies and distortions have made determining the definitive crystal structure of vaterite difficult. Nevertheless the structures of calcite and aragonite, as well as the predicted structure of vaterite, are illustrated in Figure 1.3.

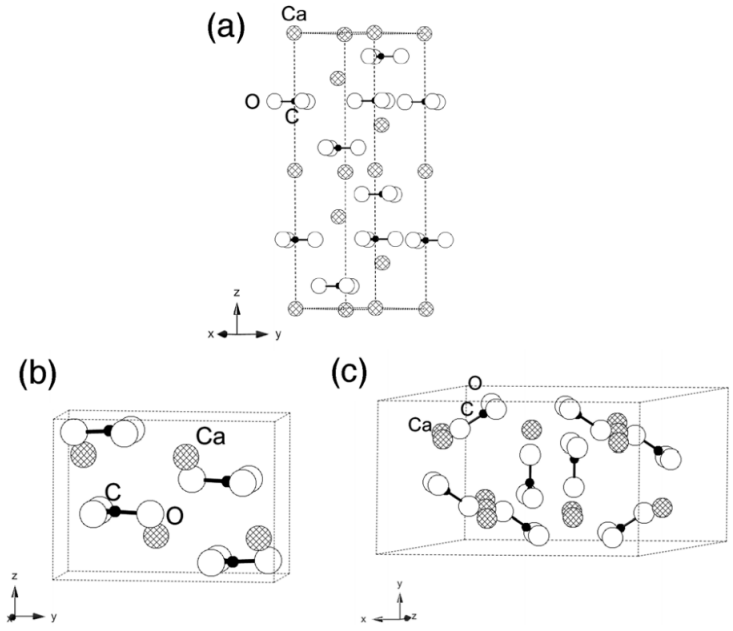

Figure 1.3: The crystal structures of (a) calcite (b) aragonite and (c) vaterite. Adapted from ref[23]

In order to understand $CaCO_3$ formation, the equilibrium between CO_2 and H_2O must first be considered as this is of crucial importance to $CaCO_3$ formation, both in the natural world and a laboratory setting. Initially, the equilibrium between gaseous CO_2 and the dissolved CO_2 in solution can be illustrated in the following manner:[24]

$$CO_{2(g)} \rightleftharpoons CO_{2(aq)} \tag{1.1}$$

With K_H, = 29 atm/(mol/L) at 25 ^oC.[25]

This dissolved CO_2 then reacts with H_2O to form carbonic acid, H_2CO_3, with the hydration equilibrium constant, $K_h = 1.7 \times 10^{-3}$ at 25 ^oC:

$$CO_{2(aq)} + H_2O \rightleftharpoons H_2CO_{3(aq)} \tag{1.2}$$

Initially, carbonic acid dissociates in water to form the bicarbonate ion in the following manner:

$$H_2CO_{3(aq)} \rightleftharpoons HCO_3^- + H^+ \tag{1.3}$$

Where its equilibrium constant, K_{a1} is described by:

$$K_{a1} = \frac{[H^+][HCO_3^-]}{[H_2CO_3]} \tag{1.4}$$

Where $K_{a1} = 4.9 \times 10^{-7}$ at 25 ^oC.

As a diprotic acid however, H_2CO_3 is capable of undergoing a second ionisation to form the carbonate ion:

$$HCO_{3(aq)}^- \rightleftharpoons CO_{3\ (aq)}^{2-} + H^+ \tag{1.5}$$

and its equilibrium constant, K_{a2} is described by:

$$K_{a2} = \frac{[H^+][CO_3^{2-}]}{[HCO_3^-]} \tag{1.6}$$

Where $K_{a2} = 5.6 \times 10^{-11}$ at 25 °C.

Finally, the carbonate anion is then free to react with Ca^{2+} to form $CaCO_3$:

$$Ca^{2+}_{(aq)} + CO_3^{2-}{}_{(aq)} \rightleftharpoons CaCO_{3(s)} \tag{1.7}$$

Generally, the equilibrium between H_2CO_3, HCO_3^-, and CO_3^{2-} can be described by the Bjerrum plot illustrated in Figure 1.4. This plot illustrates the effect pH has on concentrations of different species of a polyprotic acid. The plot shows that at higher pH, CO_3^{2-} is dominant with a crossover point at around a pH of 9-10 where bicarbonate starts to dominate until a pH of approximately 6 is reached, at which point the system favours the formation of H_2CO_3.

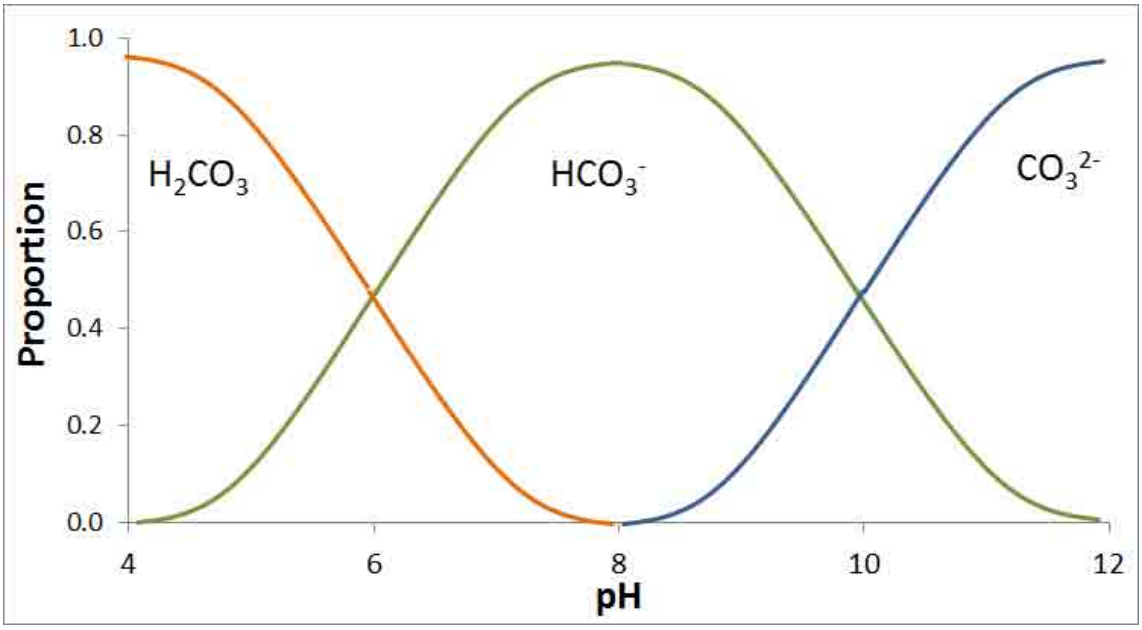

Figure 1.4: The pH dependence of the equilibrium between H_2CO_3 (orange), HCO_3^- (green), and CO_3^{2-} (blue). Adapted from ref[26]

The saturation index, SI, is imperative to understanding the precipitation of $CaCO_3$. $CaCO_3$ is a highly insoluble material, having a solubility in water of 15 mg L^{-1} at 25 °C. Its solubility product, K_{sp}, is described in the following manner:

$$K_{sp} = [Ca^{2+}][CO_3^{2-}] \tag{1.8}$$

Where K_{sp} = 3.5 x10^{-9} at 25 °C.

The ion activity product, IAP, is described by:

$$IAP = (a_{Ca^{2+}})(a_{CO_3^{2-}}) \tag{1.9}$$

Where $a_{Ca^{2+}}$ and $a_{CO_3^{2-}}$ are the activities of Ca^{2+} and CO_3^{2-}, respectively.

Together, these products can be used to show the likelihood of $CaCO_3$ precipitation:

$$SI = \log\frac{IAP}{K_{sp}} \tag{1.10}$$

$CaCO_3$ formation is a highly complex multi-step process. Whilst classic nucleation theory assumes that single ion attachment results in the formation of critical nuclei,[27,28] recent studies have illustrated that the first step in $CaCO_3$ precipitation is in fact the formation of pre-nucleation clusters (PNCs) (Figure 1.5).[29] PNCs can be described as larger neutral aggregates, which are made up of tens of ions, and their existence has been proven by both analytical ultracentrifugation[30] and subsequently cryogenic transmission electron microscopy (Cryo-TEM).[31] Computer simulations[29] have shown that these PNCs form large alternating chains of Ca^{2+} and CO_3^{2-} in a structure which has been termed 'dynamically ordered liquid-like polymers' or DOLLOPs.[32]

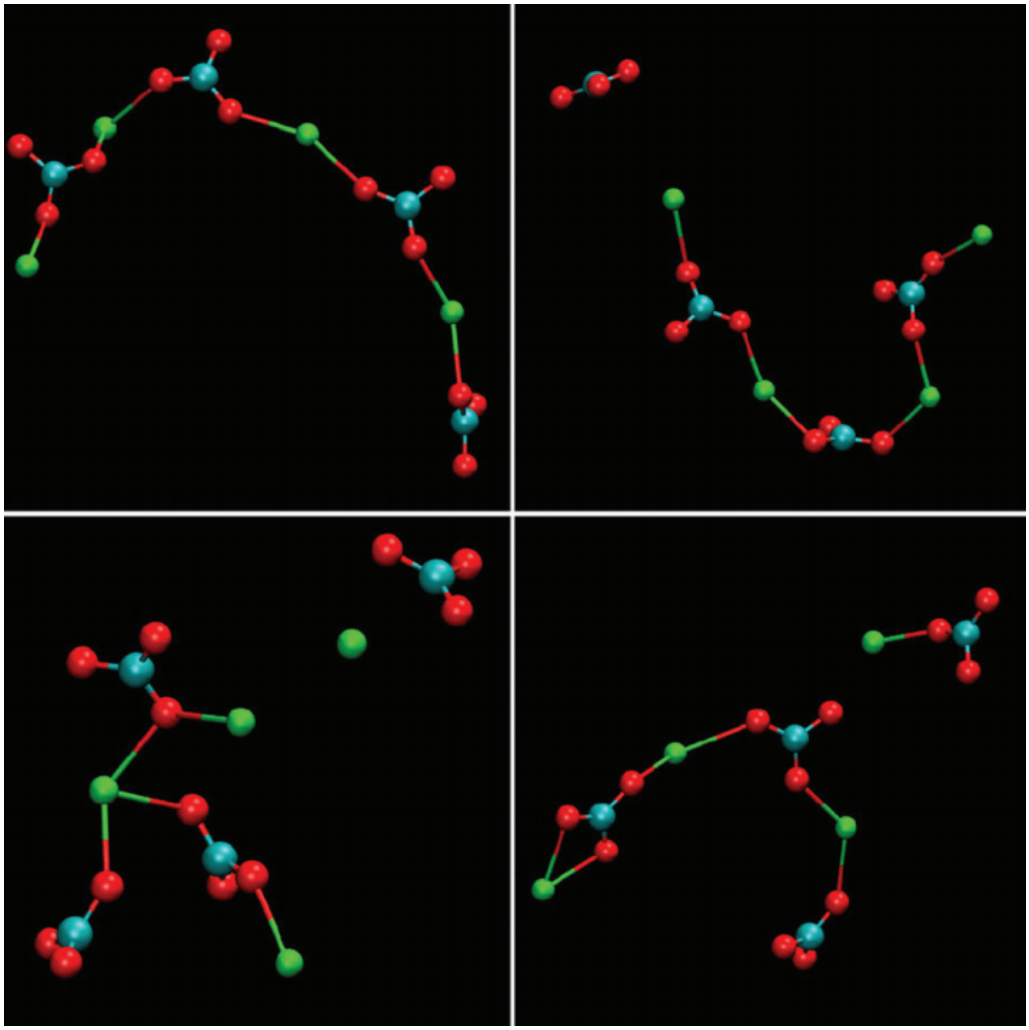

Figure 1.5: Simulations of PNCs obtained with molecular dynamics using the experimental parameters $[Ca^{2+}]$ = 0.4 mM, $[HCO_3]$ = 10 mM, and pH = 10. Adapted from ref[29]

Under typical conditions, Ca^{2+} concentration increases until a critical size is reached, whereby nucleation occurs, followed by a sharp decrease to a constant value in Ca^{2+}. The first stage of nucleation is then the formation of amorphous calcium carbonate (ACC).[33–37] This amorphous phase tends towards either proto-calcite at lower pH values (9-9.25) or proto-vaterite at a higher pH (9.5-10).[38] This arises due to the polyamorphism of ACC[39] i.e. its ability to exist with different structural characteristics, as well as in varying levels of metastability. The lack of thermodynamic

stability of this phase leads to its rapid transformation to vaterite, which in turn transforms to calcite (typically within minutes) at ambient temperatures.[18] In addition, above 50 °C, vaterite will transform to aragonite[19,40] which, over a period of months, again transforms to calcite.

The stability of the metastable phases is inextricably linked to the choice of solvent used for the system. The solvent chosen will affect the solvent-crystal interface's surface energy and can therefore stabilise the otherwise unstable preliminary phases of $CaCO_3$ crystallisation. For example, rather than availing of surfactants or additives to alter the conditions of carbonation, the simple addition of alcohols helps in stabilising the vaterite phase and preventing its subsequent transition to calcite.[41–43] This is achieved by, as mentioned, decreasing the surface energy at the solvent–crystal interface as well as the formation of a three-dimensional hydrogen-bonded network which stabilises the emerging vaterite nuclei.[44]

1.2.2 Synthetic Methods for $CaCO_3$ Production

Although there are various methods of calcium carbonate synthesis, the two most commonly used are precipitation reactions between two salt solutions, and CO_2 bubbling.

In this case, precipitation reactions describe those between soluble calcium and carbonate-containing salts which lead to an insoluble precipitate (in this case $CaCO_3$) and an aqueous secondary product, an example of which is shown below in equations 1.11 and 1.12:

$$\mathrm{CaCl_{2(aq)} + Na_2CO_{3(aq)} \longrightarrow CaCO_{3(s)} + 2\,NaCl_{(aq)}} \tag{1.11}$$

$$\mathrm{Ca(NO_3)_{2(aq)} + (NH_4)_2CO_{3(aq)} \longrightarrow CaCO_{3(s)} + 2\,NH_4NO_{3(aq)}} \tag{1.12}$$

Precipitation reactions are a straightforward and attractive method of synthesis where greater control is required over the product formed. This method can be especially valuable when considering that additives can strongly influence the reaction which allows a bottom up approach to the formation of pre-designed nano- and microstructures.[45,46] This method can prove expensive however, when considering said additives, and is limited in its ability to be expanded to larger scale syntheses.

A modified version of precipitation-based syntheses are microemulsion reactions. These rely on a combination of water and oil soluble materials to affect the parameters of synthesis. The most common type is the water in oil (W/O) microemulsion that involve the use of aliphatic/aromatic hydrocarbon, ionic surfactant, co-surfactant and water. In this method, the surfactant and co-surfactant form a mixed film at the oil-water interface which spontaneously generates reverse micelles (see Figure 1.6). This method enables the introduction of otherwise water insoluble materials, such as various pharmaceutical compounds, into calcium carbonate structures.

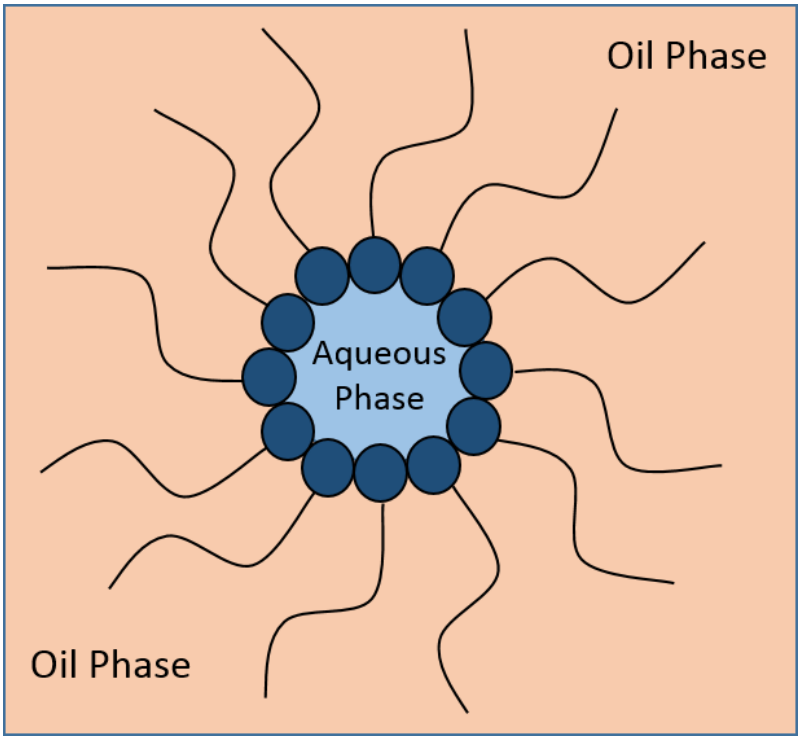

Figure 1.6: The typical structure of a reverse micelle

The industrial partners for this project, McGraths Cong Ltd., use the following CO_2 bubbling method, whereby bulk limestone is calcined at around 800 - 1000 °C to form calcium oxide.

$$CaCO_3 \xrightarrow{\Delta} CaO + CO_{2(g)} \tag{1.13}$$

The oxide formed is then hydrated using an excess of water in an exothermic procedure known as 'lime slaking'.

$$CaO + H_2O \longrightarrow Ca(OH)_2 + \Delta \tag{1.14}$$

CO_2 is again bubbled through the hydroxide solution leading to the formation of PCC.

$$Ca(OH)_2 + CO_{2(g)} \longrightarrow CaCO_3 + H_2O \tag{1.15}$$

This is the preferred method for the industrial preparation of $CaCO_3$ due to its inherent scalability. However, this method is not without its drawbacks. Monodispersity of products typically remains a challenge due to the diffusion-limited nature of the reaction. Along with this, the precise control over the morphology and properties of the products formed can also present a problem.

1.2.3 Biomineralisation

Biomineralisation can be broadly described as the process by which living organisms produce inorganic materials, and $CaCO_3$ represents the most abundant biologically-derived crystalline material found in nature.[47] While this thesis does not explicitly study the biomineralisation of $CaCO_3$, it would be remiss not to mention it. Biomineralisation offers organisms a level of control over the production of inorganic-organic composite materials, the emulation of which is a important goal in materials science. The biominerals formed fulfil a variety of roles from structural supports such as in coral skeletons, for protection in sea urchin spines, or in a mechanical role such as in sea urchin teeth. A particularly interesting role of biologically-induced $CaCO_3$ is as a form of accelerometer known as the otolithic membrane in mammals and fish.[31]

There are three main strategies by which organisms control the production of biominerals, namely through crystal-protein interactions on specific faces[48], growth in a pre-defined and well-controlled space,[49] or finally in a gel-like environment which allows the control of the crystal morphology formed through an alteration of the reaction kinetics as needed.[50] The mechanical properties of biologically produced

$CaCO_3$ are of particular interest where nature has presented many ingenious solutions to some of the problems associated with $CaCO_3$.[51] Calcite is quite brittle along its cleavage {104} plane which is a significant problem to overcome for organisms which rely on it for support. In a novel method of overcoming this problem, sea urchins introduce proteins into the crystals which act as a crack-deviation mechanism. In this manner, they allow dislocations oblique to the {104} plane resulting in conchoidal fractures (an example is illustrated in Figure 1.7), thus preserving the structural integrity of the material.

Figure 1.7: Illustration of a conchoidal fracture (in obsidian). Reproduced from ref[52]

Another such example is found in nacre, or mother of pearl which comprises the inner shell of various mollusks. Nacre is a composite material made up of hexagonal aragonite platelets in a lamellar formation which are interwoven with thin layers of protein fibres and polysaccharides to form a structure (Figure 1.8) which is 3000 times more fracture-resistant than a single crystal of aragonite.[53,54] Nature has shown on innumerable occasions that it can control almost every aspect of $CaCO_3$ formation which, as material scientists, is an attractive target to aim for.

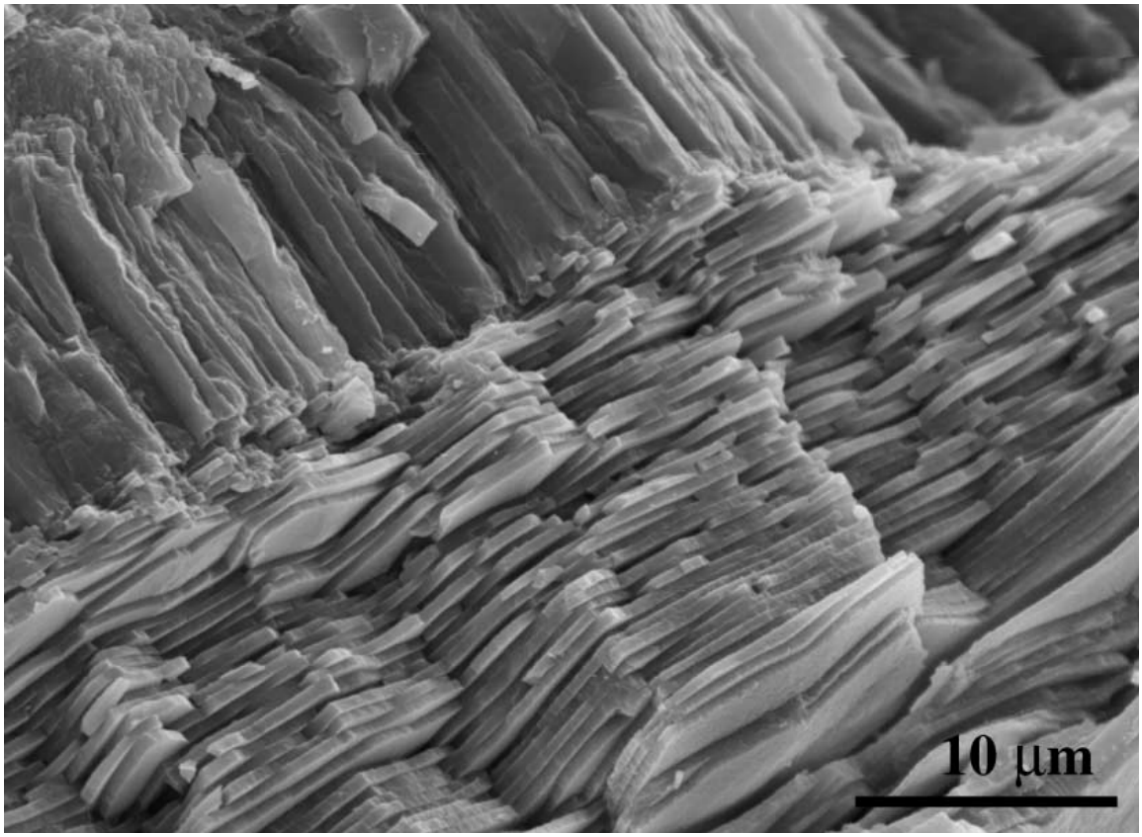

Figure 1.8: SEM image of the structure of nacre, or mother of pearl. Reproduced from ref[55]

1.3 The Role of $CaCO_3$ in Drug Delivery

Nanomaterials have, in recent years, become highly important in the field of biomedicine (See Figure 1.9). From magnetic nanoparticles being used for magnetic hyperthermia,[56–58] Au plasmonic nanoparticles as photodynamic therapy (PDT) agents,[59] to the application of electrospun nanofibers in regenerative medicine,[60] nanomaterials are beginning to play a wide and important role in a huge variety of fields in medicine.

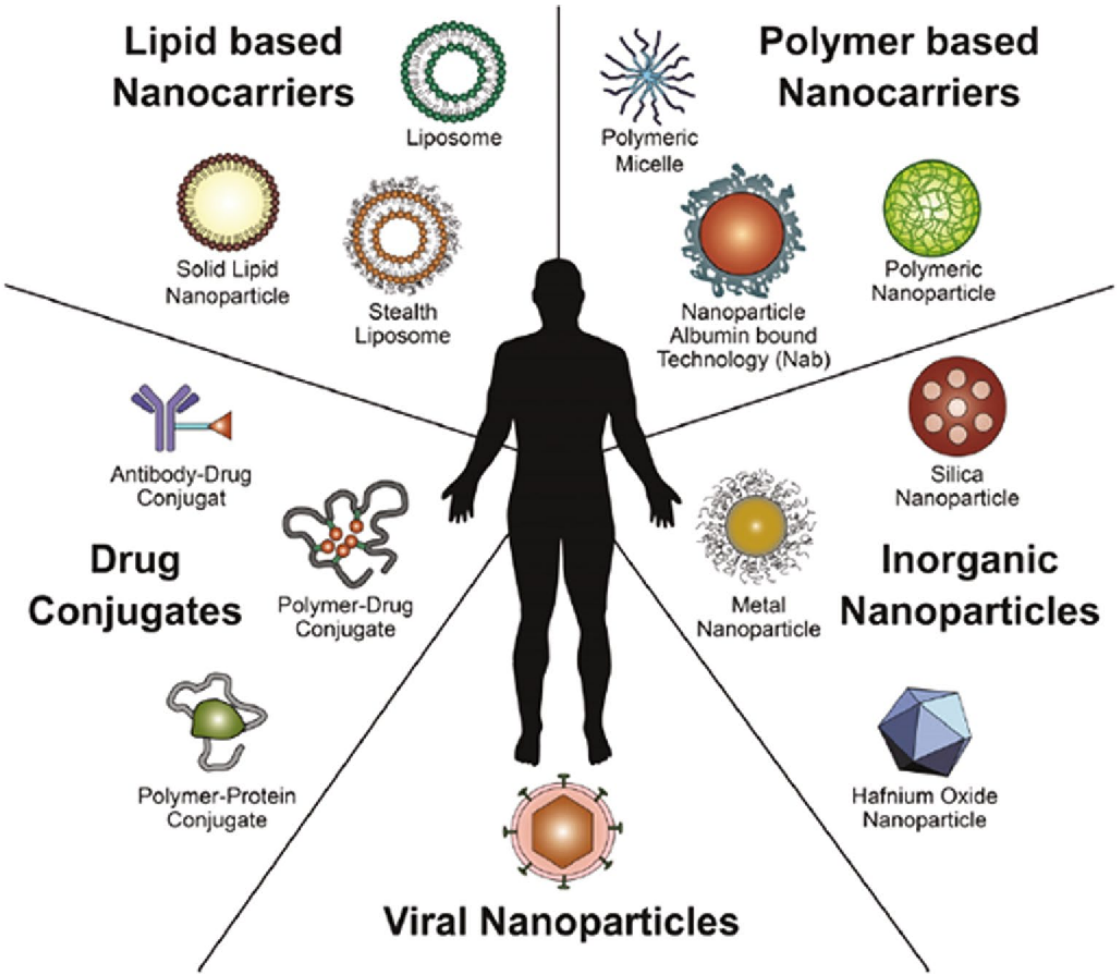

Figure 1.9: An illustration of the various roles played by nanomaterials in biomedicine. Adapted from ref[61]

An important area of biomedicine is the use of inorganic or composite materials as vesicles for drug delivery.[62–67] If effectively utilised, these drug delivery agents should increase therapeutic efficacy whilst reducing the side effects associated with some drugs.[68] In particular, calcium carbonate microparticles are attractive vesicles for drug delivery[69] due to their mechanism of degradation either through phagocytosis by macrophages or through bodily dissolution by lysosomal enzymes.[70] The pH sensitivity of $CaCO_3$ has enabled its use as an anti-cancer drug delivery system whereby there is minimal drug release in healthy tissue but full release when in contact with the acidic medium of a tumour. These dissolution-based calcium carbonate delivery systems also produce Ca^{2+} ions which can actively participate in metabolism and bone regeneration without any accompanying tissue calcification, before excretion through the kidneys and liver, whilst CO_3^{2-} is released into the extracellular matrix prior to excretion.[70]

There are a variety of methods by which to produce $CaCO_3$ drug delivery vesicles. A variety of microemulsions are frequently used which generally rely on the use of micelles to encapsulate the required drug within the $CaCO_3$ matrix. These methods are highly effective as the loading can be carried out *in situ* in contrast to forming the vesicles and loading the drug after the fact. Oil-in-water (O/W) microemulsions, for example, have recently been used to encapsulate the anticancer drug doxorubicin (DOX) through a high pressure homogenisation (HPH) system and showed high selectivity with minimal associated toxicity in healthy tissue.[71] One drawback in the use of O/W emulsions is the need for an external system such as the HPH mentioned, or a flame synthesis method.[72]

W/O reverse microemulsions[73–75] and W/O/W double emulsions,[76,77] however, are relatively straightforward in their production and utilise the inner region of the as-formed micelles as 'nano-reactors'. W/O microemulsions use an initial aqueous

phase (typically containing Ca^{2+}) in an organic phase forming the microemulsion. A second aqueous phase containing CO_3^{2-} is added to this whereby the Ca^{2+} and CO_3^{2-} containing nano-reactors are allowed to precipitate through Brownian motion i.e. once their micelles come into contact they rupture precipitating $CaCO_3$ microspheres. (W/O/W) double emulsions similarly form an initial (W/O) phase which is then added to a larger aqueous phase containing CO_3^{2-} forming the (W/O/W) double emulsion.

Solvent evaporation, by contrast, utilises an *ex-situ* method of loading by forming $CaCO_3$ microspheres initially and soaking them in a solvent in which the intended drug is soluble.[78,79] This process can take between hours and days, after which the suspension is separated by evaporation at reduced pressure to yield microspheres loaded with a variety of otherwise poorly water soluble drugs. A possible limitation to this method is the disparity between the proportion of the drug actually loaded within the microsphere and that which is coating it, as by definition these will have different release profiles.

Nevertheless it is clearly evident that one of the most exciting applications of $CaCO_3$ is in biomedicine, and specifically within the area of drug delivery where its favourable biocompatibility, straightforward and highly cost-efficient method of production, and lack of toxic byproducts make it an obvious choice for potential drug excipients.

1.4 Chiral Nanomaterials

Another high interest area of materials science is in the field of chiral nanomaterials. First termed 'dissymmetry' by Louis Pasteur after his ground-breaking separation of the two enantiomers of sodium ammonium tartrate,[80] chirality describes a material which exists in two non-superimposable mirror-image forms known as enantiomers. The term 'chirality' was first publicly used by Lord Kelvin in his Baltimore lecture series in 1904 (Figure 1.10).

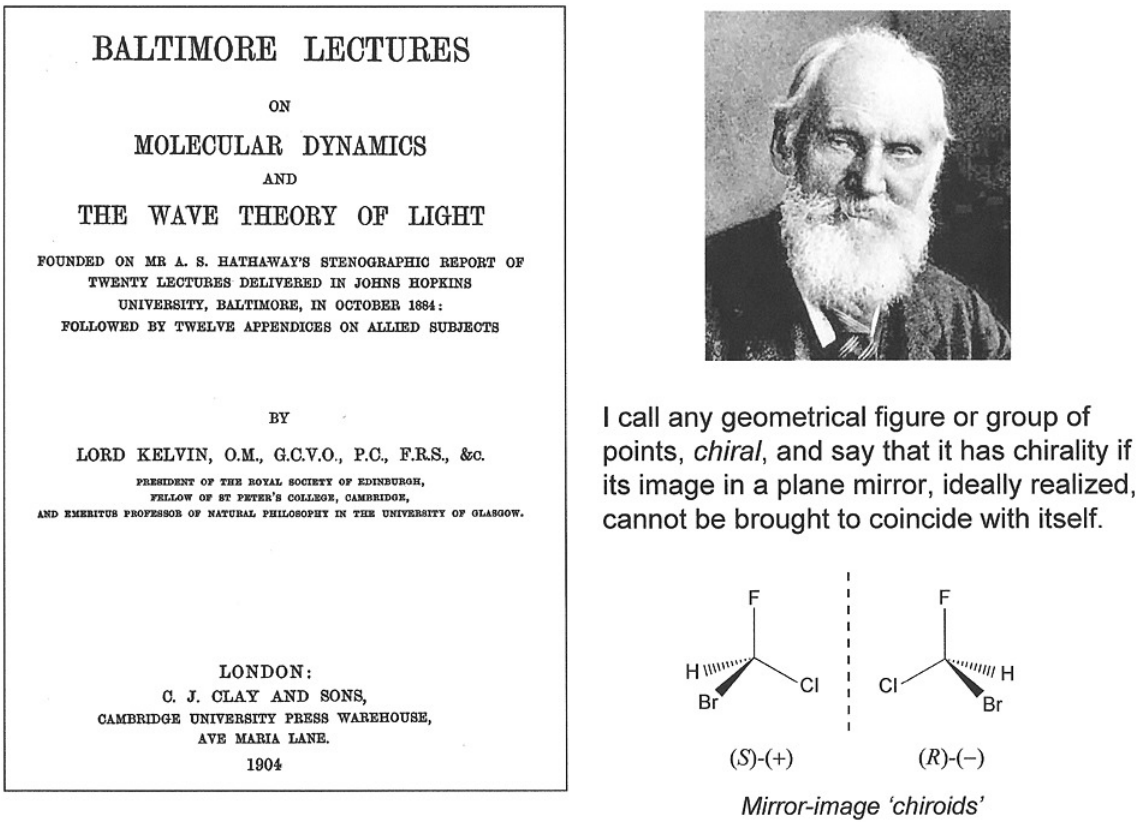

Figure 1.10: Lord Kelvin's Baltimore lecture series where the definition of chirality provided appears on page 619[81]

Enantiomers possess many of the same physical properties but differ in their interaction with both circularly polarised light (CPL) and other chiral molecules. These chiral molecules exhibit circular birefringence which is the possession of two refractive indices which are dependent on both the direction of propagation and the

polarisation of light. It is also important to note that CD only occurs at wavelengths of light that can be absorbed by a chiral molecule.

The handedness of enantiomers can be assigned both in terms of their absolute configuration or their interaction with circularly polarised light (CPL). For absolute configuration, the notation *S* and *R*, or *sinistro* and *rectus* are used to define left- and right handed enantiomers, respectively and are governed by the Cahn-Ingold-Prelog (CIP) rules. In terms of their interaction with CPL, enantiomers are notated *L* or 'levorotatory' for left-handed or counter-clockwise rotation of light and *D* or 'dextrorotatory' if that rotation is right-handed or clockwise.

There are many different forms of chirality including axial, helical, and planar chirality which have a considerable effect on their use in a variety of fields such as drug delivery and catalysis where each enantiomer provides a further layer of selective recognition. Importantly for biomedical use of chiral nanomaterials, most biologically active molecules are chiral e.g. amino acids (See Figure 1.11) and sugars naturally occur in their *sinistro* and *rectus* forms, respectively and therefore in drug delivery, chirality provides the possibility of enantioselective recognition for selective drug release.[82] In the field of catalysis they represent a promising catalysts for asymmetric synthesis,[83] which is both a time and cost-efficient approach of the synthesis of enantiomerically pure materials.

While the above definitions of chirality work well for biological or organic molecules, they fall short when applied to chiral nanomaterials. In these materials, chirality is observed on the atomic, nano, micro and macroscales and each must be considered in their own right. Specifically three forms of chiral nanomaterials can be considered: intrinsically chiral nanoparticles, ligand-induced chirality, and finally hierarchical or macrostructural chirality.

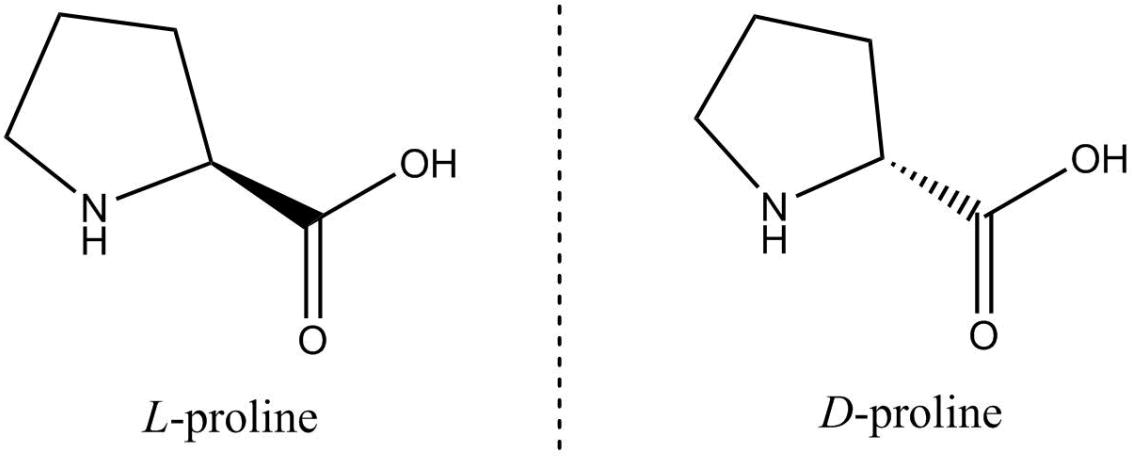

Figure 1.11: Proline, like all other amino acids, is an example of a chiral molecule

Intrinsic chirality in nanomaterials can arise either from an asymmetry in the inorganic core as shown, for example, for Au nanoparticles[84] or nanoclusters[85] or from distortions in the particle surface e.g. through screw dislocations.[86] Another example from Ben-Moshe *et al.* used tellurium nanocrystals with a chiral shape in the production of chiral gold and silver telluride nanomaterials with a high degree of optical activity.[87]

Ligand-induced chirality has been well-studied in recent years, particularly in the field of chiral quantum dots,[88] magnetic nanoparticles,[89] and plasmonic nanoparticles.[90] Ligand-induced chirality arises through the chiral moiety adsorbing on, or chemically bonding to, the surface of the nanoparticle. The mechanism of chiral induction is thought to originate from either an overlapping of the electronic states[91] or through a Coulombic interaction between the inorganic nanomaterial and organic chiral ligand.[92]

Finally, hierarchical or macrostructural chirality describes a nanomaterial which self-assembles to form a chiral superstructure e.g. a helix.[93] In a similar fashion to how amino acids arrange into polypeptides which form the chiral secondary structure of

proteins, chiral nanoparticles can aggregate to form larger chiral macrostructures.[94] Indeed, this is a fitting analogy when considering that as circular dichroism spectroscopy is used in materials science for the analysis of chiral structures, it is also commonly used in biology for the elucidation of the secondary structure of proteins. It is also worth noting that the building blocks of a chiral material do not in fact have to be chiral themselves e.g. achiral CuO sub units have been illustrated to self-assemble into chiral 'nanoflowers'.[95] As can be seen from these examples, chirality is an important phenomenon in both research and the natural world, and is therefore a powerful tool at the disposal of material scientists.

1.5 Luminescent Nanomaterials

The final class of materials to be discussed here are luminescent inorganic nanomaterials. This field is ever-evolving and comprises a huge number of materials from quantum dots, upconversion nanomaterials, carbon dots, and rare earth element doped inorganic materials. While the techniques used in this thesis present the possibility of using all of the aforementioned materials, for the sake of brevity, the use of quantum dots and rare earth dopants for the production of luminescent inorganic nanomaterials will be considered.

As mentioned previously, perhaps the central defining characteristic of nanomaterials research lies in the fact that on the nanoscale, materials possess unique properties which are not present in their bulk forms. Nowhere is this more evident than in quantum dots (QDs). As these zero dimensional nanomaterials decrease in size to the order of 10 nm their size falls below the exciton Bohr radius, leading to the quantisation of their energy levels, known in semiconductor QDs as 'quantum confinement'. In QDs, the crystal size and the energy gap between the highest valence band and

lowest conduction band are inversely proportional (as illustrated by Figure 1.12). As a result of this effect, the colour emitted by QDs can be tuned by altering their size.[96]

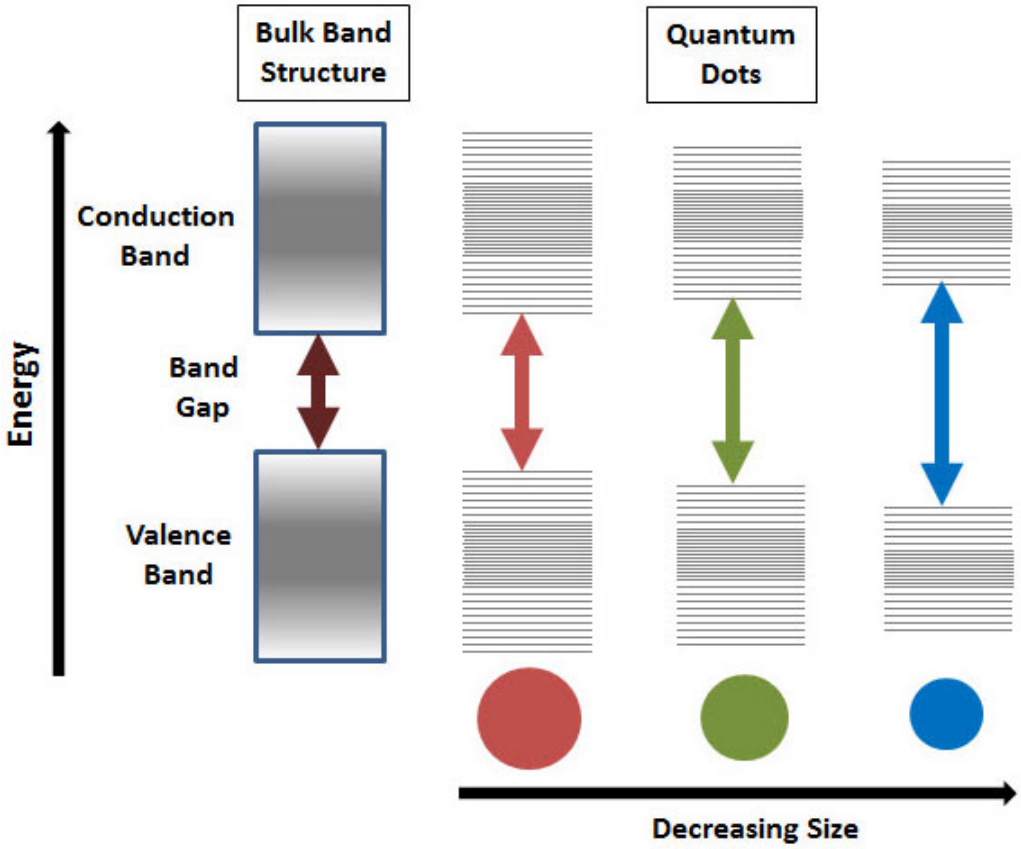

Figure 1.12: Quantum confinement effect: the decrease in crystal size leads to an increase in the semiconductor band gap. Adapted from ref[97]

Core shell QDs, which are used in this work, involve the coating of a semiconductor with a shell of a second wide band gap semiconductor which allows further tuning of their optical properties.[98] A further layer of interest to these materials is in their chiral modification, first reported by Moloney *et al.*[99] which has added yet another layer of interest to these materials.[100–102] As such, these materials have a huge variety of applications e.g. in optics[103] and biology.[104]

The doping of inorganic materials with rare earth elements (REEs), and in particular phosphorescent REEs has in recent years become an area of considerable interest. Inorganic materials provide a perfect support to exploit the favourable luminescence of REEs (Figure 1.13), namely, their narrow emission bands and large Stokes shifts. To this end, rare earth doping has been carried out in a variety of materials from Al_2O_3[105] and TiO_2[106] to YF_3.[107] Recently, the doping of $CaCO_3$ with Eu^{3+}[108] and Tb^{3+}[109] has been described, however there is still much scope for advancement of this research area.

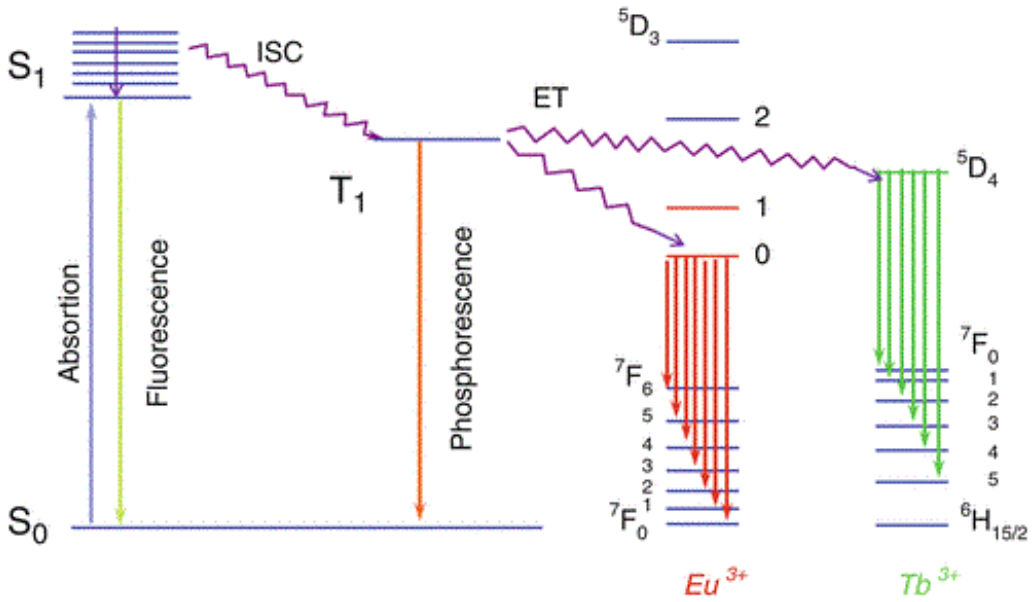

Figure 1.13: A simple schematic of the photophysics of lanthanide complexes.

1.6 Aims of the Project

The overall goal of the project is to prepare various new $CaCO_3$-based nano- and micro- structures by a variety of synthetic techniques including CO_2 bubbling, chemical precipitation, and a novel dry ice carbonation approach. The produced $CaCO_3$ materials are planned to be fully characterised by various techniques including, but not limited to, SEM, XRD, FT-IR, TGA, Raman, and, where appropriate, TEM. An in-depth study of the factors that influence industrial precipitated calcium carbonate (PCC) formation is intended to be studied using a CO_2 bubbling method. Chemical precipitation will be used in an attempt to synthesise a variety of chiral $CaCO_3$ products, namely microspheres and helices. Finally, a new method of $CaCO_3$ formation using a dry ice carbonation method is to be developed. This has the potential to capitalise on the retrograde solubility of $CaCO_3$, limiting the use of high temperature syntheses of novel $CaCO_3$ materials.

The scientific and technical objectives of this work include:

1. Synthesis of $CaCO_3$ microspheres using polyvinylpyrrolidone and sodium dodecyl sulfate.

2. Incorporation of various chiral ligands into $CaCO_3$ hollow microspheres via a precipitation reaction, in order to produce new chiroptically active nanomaterials.

3. The application of the above precipitation techniques in the synthesis of novel $CaCO_3$ helices.

4. Development of a new $CaCO_3$ microsphere-based drug delivery systems by various synthetic techniques.

5. Development of a novel $CaCO_3$ synthesis using dry ice carbonation.

6. Investigation into the effect of various CH_3OH : H_2O ratios on the new dry ice carbonation.

7. Synthesis of novel lanthanide-doped $CaCO_3$ using dry ice synthesis and an investigation into the effects of lanthanide concentration on the product obtained.

8. Synthesis and characterisation of rhombohedral and scalenohedral $CaCO_3$ using a CO_2 bubbling method for potential utilisation at the industrial scale.

9. Investigation of various parameters of the above synthesis and their subsequent optimisation.

It is expect that this work will contribute to the further development of $CaCO_3$-based materials as well as their biomedical and optical applications, among others.

References

(1) E. Sakaue, *18th IEEE International Conference on Micro Electro Mechanical Systems, 2005. MEMS 2005.*, 2005, 600–605.

(2) S. Fan, *Nature Nanotechnology*, 2014, **9**, 92–93.

(3) Y.-F. Wu, Y.-T. Nien, Y.-J. Wang and I.-G. Chen, *Journal of the American Ceramic Society*, 2012, **95**, 1360–1366.

(4) S. Shylesh, V. Schünemann and W. R. Thiel, *Angewandte Chemie International Edition*, 2010, **49**, 3428–3459.

(5) A. S. Baimuratov, T. P. Pereziabova, M. Y. Leonov, W. Zhu, A. V. Baranov, A. V. Fedorov, Y. K. Gun'ko and I. D. Rukhlenko, *ACS Nano*, 2018, **12**, 6203–6209.

(6) A. K. Visheratina, A. O. Orlova, F Purcell-Milton, V. A. Kuznetsova, A. A. Visheratin, E. V. Kundelev, V. G. Maslov, A. V. Baranov, A. V. Fedorov and Y. K. Gun'ko, *J. Mater. Chem. C*, 2018, **6**, 1759–1766.

(7) O. Cleary, F. Purcell-Milton, A. Vandekerckhove and Y. K. Gun'ko, *Advanced Optical Materials*, 2017, **5**, 1601000.

(8) L Zhang, F. X. Gu, J. M. Chan, A. Z. Wang, R. S. Langer and O. C. Farokhzad, *Clinical Pharmacology & Therapeutics*, 2008, **83**, 761–769.

(9) S. Marchesan and M. Prato, *ACS Medicinal Chemistry Letters*, 2013, **4**, 147–149.

(10) Chembam.com, *Nanomaterials and Nanotechnology*, [Online; accessed July 7th, 2017], 2017.

(11) S. C. Doney, V. J. Fabry, R. A. Feely and J. A. Kleypas, *Annual Review of Marine Science*, 2009, **1**, 169–192.

(12) Y. Boyjoo, V. K. Pareek and J. Liu, *J. Mater. Chem. A*, 2014, **2**, 14270–14288.

(13) S Wang, P Ihalainen, J Järnström and J Peltonen, *Journal of Dispersion Science and Technology*, 2009, **30**, 961–968.

(14) F. Karakaş, B. Vaziri Hassas and M. S. Çelik, *Progress in Organic Coatings*, 2015, **83**, 64–70.

(15) K. C. Mondal, L. M. Cele, M. J. Witcomb and N. J. Coville, *Catalysis Communications*, 2008, **9**, 494–498.

(16) M. Ni and B. D. Ratner, *Surface and interface analysis : SIA*, 2008, **40**, 1356–1361.

(17) A. Niedermayr, A. Immenhauser, *Trace element incorporation and isotopic fractionation in calcium carbonate phases (calcite, aragonite, vaterite, monohydrocalcite, ikaite and ACC)*, [Online; accessed July 12th, 2017], 2017.

(18) T. Ogino, T. Suzuki and K. Sawada, *Geochimica et Cosmochimica Acta*, 1987, **51**, 2757–2767.

(19) J. Jiang, S.-F. Chen, L. Liu, H.-B. Yao, Y.-H. Qiu, M.-R. Gao and S.-H. Yu, *Chem. Commun.*, 2009, 5853–5855.

(20) L. C. Nielsen, J. J. D. Yoreo and D. J. DePaolo, *Geochimica et Cosmochimica Acta*, 2013, **115**, 100–114.

(21) K. J. Davis, P. M. Dove and J. J. De Yoreo, *Science*, 2000, **290**, 1134–1137.

(22) U Wehrmeister, A. L. Soldati, D. E. Jacob, T Häger and W Hofmeister, *Journal of Raman Spectroscopy*, 2010, **41**, 193–201.

(23) B. Xu and K. M. Poduska, *Physical Chemistry Chemical Physics*, 2014, **16**, 17634–17639.

(24) S. L. Goss, K. A. Lemons, J. E. Kerstetter and R. H. Bogner, *Journal of Pharmacy and Pharmacology*, 2007, **59**, 1485–1492.

(25) R. Sander, *Atmospheric Chemistry and Physics*, 2015, **15**, 4399–4981.

(26) M. Kelly, *Relationship between pH and the proportion of inorganic carbon as free carbon dioxide (or carbonic acid, H_2CO_3 – orange line), bicarbonate (HCO_3^- – green line) and carbonate (CO_3^{2-} – blue line).* [Online; accessed October 24th, 2019], 2019.

(27) R. Becker and W. Döring, *Annalen der Physik*, 1935, **416**, 719–752.

(28) S Karthika, T. K. Radhakrishnan and P Kalaichelvi, *Crystal Growth & Design*, 2016, **16**, 6663–6681.

(29) D. Gebauer, M. Kellermeier, J. D. Gale, L. Bergström and H. Cölfen, *Chemical Society Reviews*, 2014, **43**, 2348–2371.

(30) D. Gebauer, A. Völkel and H. Cölfen, *Science*, 2008, **322**, 1819–1822.

(31) E. M. Pouget, P. H. H. Bomans, J. A. C. M. Goos, P. M. Frederik, G De With and N. A. J. M. Sommerdijk, *Science*, 2009, **323**, 1455–1458.

(32) R. Demichelis, P. Raiteri, J. D. Gale, D. Quigley and D. Gebauer, *Nature Communications*, 2011, **2**, 590.

(33) C. W. Turner and D. W. Smith, *Industrial & Engineering Chemistry Research*, 1998, **37**, 439–448.

(34) S.-Y. Yang, H.-H. Chang, C.-J. Lin, S.-J. Huang and J. C. C. Chan, *Chem. Commun.*, 2016, **52**, 11527–11530.

(35) S. Sun, D. Gebauer and H. Colfen, *Chem. Commun.*, 2016, **52**, 7036–7038.

(36) J. Ihli, A. N. Kulak and F. C. Meldrum, *Chem. Commun.*, 2013, **49**, 3134–3136.

(37) S.-F. Chen, H. Colfen, M. Antonietti and S.-H. Yu, *Chem. Commun.*, 2013, **49**, 9564–9566.

(38) D. Gebauer, P. N. Gunawidjaja, J. Y. P. Ko, Z. Bacsik, B. Aziz, L. Liu, Y. Hu, L. Bergström, C.-W. Tai, T.-K. Sham, M. Edén and N. Hedin, *Angewandte Chemie International Edition*, 2010, **49**, 8889–8891.

(39) J. H. E. Cartwright, A. G. Checa, J. D. Gale, D. Gebauer and C. I. Sainz-Díaz, *Angewandte Chemie International Edition*, 2012, **51**, 11960–11970.

(40) W. Sun, S. Jayaraman, W. Chen, K. A. Persson and G. Ceder, *Proceedings of the National Academy of Sciences*, 2015, **112**, 3199–3204.

(41) Q. Li, Y. Ding, F. Li, B. Xie and Y. Qian, *Journal of Crystal Growth*, 2002, **236**, 357–362.

(42) F Manoli and E Dalas, *Journal of Crystal Growth*, 2000, **218**, 359–364.

(43) L. Zhang, L.-H. Yue, F. Wang and Q. Wang, *The Journal of Physical Chemistry B*, 2008, **112**, 10668–10674.

(44) D. B. Trushina, T. V. Bukreeva and M. N. Antipina, *Crystal Growth & Design*, 2016, **16**, 1311–1319.

(45) Y. Pan, X. Zhao, Y. Guo, X. Lv, S. Ren, M. Yuan and Z. Wang, *Materials Letters*, 2007, **61**, 2810–2813.

(46) M. M. M. G. P. G. Mantilaka, H. M. T. G. A. Pitawala, R. M. G. Rajapakse, D. G. G. P. Karunaratne and K. G. Upul Wijayantha, *Journal of Crystal Growth*, 2014, **392**, 52–59.

(47) F. Nudelman and N. A. J. M. Sommerdijk, *Angewandte Chemie International Edition*, 2012, **51**, 6582–6596.

(48) L Addadi and S Weiner, *Proceedings of the National Academy of Sciences*, 1985, **82**, 4110–4114.

(49) L. Addadi and S. Weiner, *Angewandte Chemie International Edition in English*, 1992, **31**, 153–169.

(50) L. Addadi and S. Weiner, *Angewandte Chemie International Edition in English*, 1992, **31**, 153–169.

(51) J. D. Currey, *Journal of Experimental Biology*, 1999, **202**, 3285.

(52) Cosmictome.com, *Conchoidal-Fracture-Obsidia*, [Online; accessed October 22nd, 2019], 2019.

(53) J. D. Currey and P. M. Sheppard, *Proceedings of the Royal Society of London. Series B. Biological Sciences*, 1977, **196**, 443–463.

(54) A. P. Jackson, J. F. V. Vincent and R. M. Turner, 1988, **234**, 415–440.

(55) S Blank, M Arnoldi, S Khoshnavaz, L Treccani, M Kuntz, K Mann, G Grathwohl and M Fritz, *Journal of Microscopy*, 2003, **212**, 280–291.

(56) R. V. Stigliano, F Shubitidze, K Kekalo, I Baker, A. J. Giustini and P. J. Hoopes, *Proc SPIE Int Soc Opt Eng*, 2013, **8584**, 85840e.

(57) D. Chang, M. Lim, J. A. C. M. Goos, R. Qiao, Y. Y. Ng, F. M. Mansfeld, M. Jackson, T. P. Davis and M. Kavallaris, *Frontiers in Pharmacology*, 2018, **9**, 831.

(58) S. Stafford, C. Garnier and Y. Gun'ko, *Nanomaterials*, 2018, **8**, 1044.

(59) X. Yang, M. Yang, B. Pang, M. Vara and Y. Xia, *Chemical Reviews*, 2015, **115**, 10410–10488.

(60) W. Liu, S. Thomopoulos and Y. Xia, *Advanced Healthcare Materials*, 2012, **1**, 10–25.

(61) S. Tran, P.-J. DeGiovanni, B. P. Piel and P. Rai, Clinical and Translational Medicine, 2017.

(62) R. Singh and J. W. Lillard, *Experimental and molecular pathology*, 2009, **86**, 215–223.

(63) J. Yu, J. C. Yu, L. Zhang, X. Wang and L. Wu, *Chem Commun (Camb)*, 2004, 2414–2415.

(64) M. Lundin Johnson, D. Noreland, P. Gane, J. Schoelkopf, C. Ridgway and A. Millqvist Fureby, *Food & Function*, 2017, **8**, 1627–1640.

(65) A. B. Jindal, *International Journal of Pharmaceutics*, 2017, **532**, 450–465.

(66) S. Bamrungsap, Z. Zhao, T. Chen, L. Wang, C. Li, T. Fu and W. Tan, *Nanomedicine*, 2012, **7**, 1253–1271.

(67) Z. Dong, L. Feng, Y. Hao, M. Chen, M. Gao, Y. Chao, H. Zhao, W. Zhu, J. Liu, C. Liang, Q. Zhang and Z. Liu, *Journal of the American Chemical Society*, 2018, **140**, 2165–2178.

(68) S. Maleki Dizaj, M. Barzegar-Jalali, M. H. Zarrintan, K. Adibkia and F. Lotfipour, *Expert Opinion on Drug Delivery*, 2015, **12**, 1649–1660.

(69) V. L. Kudryavtseva, L. Zhao, S. I. Tverdokhlebov and G. B. Sukhorukov, *Colloids and Surfaces B: Biointerfaces*, 2017, **157**, 481–489.

(70) M. Ming-Guo and S. Run-Cang, in *Advances in Biomimetics*, ed. M. Cavrak, Open Access, 2011, ch. 2, pp. 18–19.

(71) A Shafiu Kamba, M Ismail, T. A. Tengku Ibrahim and Z. A. Zakaria, *Biomed Res Int*, 2013, **2013**, 587451.

(72) M. Huber, W. J. Stark, S. Loher, M. Maciejewski, F. Krumeich and A. Baiker, *Chem. Commun.*, 2005, 648–650.

(73) R. G. Alany, T Rades, J Nicoll, I. G. Tucker and N. M. Davies, *Journal of Controlled Release*, 2006, **111**, 145–152.

(74) F. T. M. C. Vicentini, T. R. M. Simi, J. O. D. Ciampo, N. O. Wolga, D. L. Pitol, M. M. Iyomasa, M. V. L. B. Bentley and M. J. V. Fonseca, *European Journal of Pharmaceutics and Biopharmaceutics*, 2008, **69**, 948–957.

(75) H. Y. Karasulu, B. Karabulut, E. Göker, T. Güneri and F. Gabor, *Drug Delivery*, 2007, **14**, 225–233.

(76) F. T. Meng, G. H. Ma, W. Qiu and Z. G. Su, *Journal of Controlled Release*, 2003, **91**, 407–416.

(77) X. Qi, L. Wang and J. Zhu, *Journal of Pharmaceutical Sciences*, 2011, **100**, 2203–2211.

(78) M. Farzan, R. Roth, G. Québatte, J. Schoelkopf, J. Huwyler and M. Puchkov, *Pharmaceutics*, 2019, **11**, 32.

(79) D. Preisig, D. Haid, F. J. O. Varum, R. Bravo, R. Alles, J. Huwyler and M. Puchkov, *European Journal of Pharmaceutics and Biopharmaceutics*, 2014, **87**, 548–558.

(80) J. Gal, *Chirality*, 2011, **23**, 1–16.

(81) L. D. Barron, *Chirality*, 2012, **24**, 879–893.

(82) Z. Guo, Y. Du, X. Liu, S.-C. Ng, Y. Chen and Y. Yang, *Nanotechnology*, 2010, **21**, 165103.

(83) E. Cho and T. H. Kim, *Tetrahedron Letters*, 2014, **55**, 6470–6473.

(84) C. Gautier and T. Bürgi, *Journal of the American Chemical Society*, 2006, **128**, 11079–11087.

(85) P. D. Jadzinsky, G. Calero, C. J. Ackerson, D. A. Bushnell and R. D. Kornberg, *Science*, 2007, **318**, 430–433.

(86) M. V. Mukhina, V. G. Maslov, A. V. Baranov, A. V. Fedorov, A. O. Orlova, F. Purcell-Milton, J. Govan and Y. K. Gun'ko, *Nano Letters*, 2015, **15**, 2844–2851.

(87) A. Ben-Moshe, S. G. Wolf, M. B. Sadan, L. Houben, Z. Fan, A. O. Govorov and G. Markovich, 2014, **5**, 4302.

(88) M. P. Moloney, J. Govan, A. Loudon, M. Mukhina and Y. K. Gun'Ko, 2015, **10**, 558–573.

(89) Y. A. Gromova, V. G. Maslov, M. A. Baranov, R. Serrano-García, V. A. Kuznetsova, F. Purcell-Milton, Y. K. Gun'ko, A. V. Baranov and A. V. Fedorov, *The Journal of Physical Chemistry C*, 2018, **122**, 11491–11497.

(90) X.-K. Wan, S.-F. Yuan, Z.-W. Lin and Q.-M. Wang, *Angewandte Chemie International Edition*, 2014, **53**, 2923–2926.

(91) U. Tohgha, K. K. Deol, A. G. Porter, S. G. Bartko, J. K. Choi, B. M. Leonard, K. Varga, J. Kubelka, G. Muller and M. Balaz, *ACS Nano*, 2013, **7**, 11094–11102.

(92) A. O. Govorov, Y. K. Gun'ko, J. M. Slocik, V. A. Gérard, Z. Fan and R. R. Naik, *J. Mater. Chem.*, 2011, **21**, 16806–16818.

(93) A. Nemati, S. Shadpour, L. Querciagrossa, L. Li, T. Mori, M. Gao, C. Zannoni and T. Hegmann, *Nature Communications*, 2018, **9**, DOI: 10.1038/s41467-018-06400-0.

(94) G. Cheng, D. Xu, Z. Lu and K. Liu, *ACS Nano*, 2019, **13**, 1479–1489.

(95) Y. Qian, Y. Duan and S. Che, *Advanced Optical Materials*, 2017, **5**, 1601013.

(96) S Sarkar, D Banerjee, U. K. Ghorai, N. S. Das and K. K. Chattopadhyay, *Journal of Luminescence*, 2016, **178**, 314–323.

(97) S. Aldrich, *Splitting of energy levels in quantum dots due to the quantum confinement effect, semiconductor band gap increases with decrease in size of the nanocrystal*, [Online; accessed October 26th, 2019], 2019.

(98) S. D. Elliott, M. P. Moloney and Y. K. Gun'ko, *Nano Letters*, 2008, **8**, 2452–2457.

(99) M. P. Moloney, Y. K. Gun'ko and J. M. Kelly, *Chem. Commun.*, 2007, 3900–3902.

(100) Z. Zhu, J. Guo, W. Liu, Z. Li, B. Han, W. Zhang and Z. Tang, *Angewandte Chemie International Edition*, 2013, **52**, 13571–13575.

(101) N. Suzuki, Y. Wang, P. Elvati, Z.-B. Qu, K. Kim, S. Jiang, E. Baumeister, J. Lee, B. Yeom, J. H. Bahng, J. Lee, A. Violi and N. A. Kotov, *ACS Nano*, 2016, **10**, 1744–1755.

(102) C. Han and H. Li, *Small*, 2008, **4**, 1344–1350.

(103) F. Purcell-Milton and Y. K. Gun'ko, *J. Mater. Chem.*, 2012, **22**, 16687–16697.

(104) K. E. Sapsford, T. Pons, I. L. Medintz and H. Mattoussi, *Sensors (Basel, Switzerland)*, 2006, **6**, 925–953.

(105) Y. Onishi, T. Nakamura and S. Adachi, *Japanese Journal of Applied Physics*, 2016, **55**, 112401.

(106) H. Li, Y. Sheng, H. Zhang, J. Xue, K. Zheng, Q. Huo and H. Zou, *Powder Technology*, 2011, **212**, 372–377.

(107) G. Wang, W. Qin, J. Zhang, J. Zhang, Y. Wang, C. Cao, L. Wang, G. Wei, P. Zhu and R. Kim, *Journal of Fluorine Chemistry*, 2008, **129**, 621–624.

(108) Y. Sun, H. Zou, B. Zhang, X. Zhou, Q. Huo and Y. Sheng, *Journal of Materials Chemistry C*, 2015, **3**, 5316–5321.

(109) Q. Cheng, Y. Dong, M. Kang and P. Zhang, *Journal of Luminescence*, 2014, **156**, 91–96.

Chapter 2

Materials and Experimental Methods

2.1 Starting Materials

Calcium oxide was provided by McGraths Cong Ltd. CO_2 liquid and vapour withdrawal cylinders were obtained from BOC Gases Ireland. Other starting materials were supplied by Sigma-Aldrich, Alpha Aesar and STREM chemicals. All solvents used were supplied by Trinity College Dublin Hazardous Materials facility. All starting materials were used without further purification. Quantum dots and plasmonic nanoparticles were synthesised in-house by Dr. Finn Purcell-Milton and Shelley Stafford, respectively.

2.2 Experimental Procedures for Chapter 3

2.2.1 Template-Directed Synthesis of $CaCO_3$ Microspheres

This synthesis was performed according to the modified published procedure of Zhao *et al.*[1] PVP (0.5 g; 90 mmol) and SDS (0.5 g; 34.7 mmol) were added to a solution of Na_2CO_3 (50 ml; 100 mmol) before being stirred for 30 mins. Subsequently, an aqueous solution of $CaCl_2$ (50 ml; 100 mmol) and SDS (0.721 g; 50 mmol) was added to the Na_2CO_3 solution. The reaction mixture was then stirred for 60 mins, before centrifugation at 9000 rpm, washing with Millipore water and ethanol and drying at 80 ^oC for 24 h (0.39 g; 78%).

2.2.2 Chiroptically Active $CaCO_3$ Microspheres

This synthesis was performed according to the above procedure with some modifications. In order to achieve chiral modification of the $CaCO_3$ microspheres, the above method was carried out while *L*- and *D*- Proline (115 mg; 1 mmol), or S- and R-BINOL (286 mg; 1 mmol) added to the Na_2CO_3 solution.

2.2.3 Synthesis of Chiral Luminescent $CaCO_3$ Microspheres

Again, this synthesis was performed according to the above procedure with some modifications. In the synthesis of multi-modal microspheres, the nanomaterial to be encapsulated was, in all cases, included in the initial mixing step along with the Na_2CO_3, SDS, PVP and amino acid. Specifically, for QDs and Au NPs a 0.1 ml aliquot was added, whilst $Eu(NO_3)_3.6H_2O$ (0.223 g; 10 mmol) was added for the lanthanide doped microspheres.

2.2.4 Synthesis of 16-2-16 Gemini Surfactant

1-bromohexadecane (4.9 ml; 16 mmol) and N,N,N',N'-tetramethylethylenediamine (3 ml; 20 mmol) were added to acetonitrile (50 ml) and heated to 40 °C for 72 h. The product, hexadecyl dimethyl [1-(2-dimethylamino)ethyl]ammonium bromide (5.45 g), was obtained through rotary evaporation and a subsequent recrystallisation from ethanol. This product was confirmed by ^{1}H NMR. A portion of the product (3 g) was added to a mixture of ethyl acetate (70 ml) and 1-bromohexadecane (8.7 ml) and refluxed at 100 °C for 48 h. After this time the product was again separated by solvent evaporation and 4 recrystallisations from a 50:50 mixture of chloroform and acetone resulting in a white solid (0.473 g; 93%).

^{1}H NMR (400 MHz, $CDCl_3$): 3.71 (s, 4H), 3.59 (t, 4H, J=8.2), 3.23 (s, 12H), 1.83 (s, 4H), 1.41 (s, 4H), 1.28 (s, 48H), 0.90 (t, 6H, J=6.5)

2.2.5 Synthesis of 16-2-16 Gemini *D*-Tartrate

A mixture of *D*-tartaric acid (103 mg; 0.69 mmol) and Ag_2CO_3 (95 mg; 0.5 eq) was stirred in 10 ml Millipore water for 1 h before the addition of the as-synthesised 16-2-16 gemini surfactant (500 mg; 0.88 mmol) and stirring for 5 minutes. After a solvent evaporation, CH_3OH was used to dissolve the resulting powder before filtration through celite to give a colourless solution. The product was subsequently separated by solvent evaporation and dissolved in a mixture of 9:1 chloroform and CH_3OH before precipitation through the addition of ethyl acetate. Finally, the product was filtered and then dried resulting in a yellowish powder (473 mg, 96%) The formation of the 16-2-16 gemini *D*-tartrate was confirmed using mass spectrometry: HRMS (m/z) (ES+): Calculated for $C_{42}H_{87}N_2O_{11}$ m/z = 714.6486 Found for $[M+H]^+$ $C_{42}H_{87}N_2O_{11}$ m/z = 714.6486

The process was carried out in the same manner using *L*-tartaric acid to afford the 16-2-16 gemini *L*-tartrate

2.2.6 Synthesis of $CaCO_3$ Helices

The as-synthesised 16-2-16 gemini *L*/*D*-tartrate (10 mg) was added to a solution of Na_2CO_3 (2.5 ml; 0.1 M) and heated to 55 °C before stirring for 1 h. After this point $CaCl_2$ (2.5 ml; 0.1 M) was added and the reaction mixture was again allowed to stir for 1h. The product was separated by centrifugation at 5000 rpm and washed with water, a 50:50 mixture of water and ethanol, and finally ethanol before drying at 80 °C for 24 h resulting in yields between 60 and 80%.

2.3 Experimental Procedures for Chapter 4

2.3.1 Template-Directed synthesis of $CaCO_3$ Microspheres for Drug Delivery

This synthesis was performed according to the same procedure as detailed in section 2.2.1, along with the addition of *S*-IBU (0.25g; 28 mmol) to the solution of Na_2CO_3.

2.3.2 Reverse (W/O) Microemulsion Synthesis of $CaCO_3$ Microspheres

S-IBU (0.02 g; 3.9 mmol), SDS (0.5 g; 34.7 mmol), and PVP (0.5 g; 90 mmol) in hexane (50 ml) were added to $CaCl_2$ (25 ml; 100 mmol). This solution was stirred for 30 mins to ensure homogeneity among the micelles. Na_2CO_3 (25 ml; 100 mmol) was added before stirring for 1 h. Particles were separated by centrifugation before washing with Millipore water and ethanol and drying at 80 ^oC for 24 h (0.15 g; 76%).

2.3.3 Double (W/O/W) Microemulsion Synthesis of $CaCO_3$ Microspheres

S-IBU (0.02 g; 3.9 mmol), SDS (0.5 g; 34.7 mmol) and PVP (0.5 g; 90 mmol) were added to a $CaCl_2$ solution (25 ml; 100 mmol) and stirred for 30 mins. This solution was added to an RBF containing 50 ml of hexane before stirring for a further 30 mins. This solution was then added Na_2CO_3 (80 ml; 100 mmol) and allowed to stir

for 1 h. The product was washed with Millipore water and ethanol before separation by centrifugation and drying at 80 °C for 24 h (0.12 g; 62%).

2.4 Experimental Procedures for Chapter 5

2.4.1 Calcite Rhombohedra Synthesis

A 250 g dry ice pellet was sequentially added to a solution of calcium oxide (1.25 g; 89 mmol) in water (25 ml) over a timescale of 1 h, while the temperature was kept between 0 and 10 °C. Following this, the product was filtered, washed with Millipore water and ethanol, and dried at 80 °C for 24 h producing $CaCO_3$ (1.85 g; 83%).

2.4.2 Vaterite Microsphere Synthesis

In vaterite synthesis, a 250 g dry ice pellet was sequentially added to calcium oxide (1.25 g; 89 mmol) in a 25 ml 75 %v/v CH_3OH solution for 1 h, while the temperature was kept within the range -20 to -50 °C. Following this, the product was filtered, washed with Millipore water and ethanol, and dried at 80 °C for 24 h producing $CaCO_3$ (2.08 g; 93%).

2.4.3 Methanol:Water Ratios

Specifically, four different ratios of methanol:water were used in the production of calcite nanoparticles and vaterite microspheres, as detailed in Table 2.1 below.

Total volume (ml)	**CH_3OH (v/v)**	**vol. of CH_3OH (ml)**	**vol. of H_2O (ml)**
25	0	0	25
25	25	6.25	18.75
25	50	12.5	12.5
25	75	18.75	6.25

Table 2.1: Table illustrating the various ratios of methanol:water used in dry ice carbonation

2.5 Experimental Procedures for Chapter 6

2.5.1 Synthesis of Lanthanide Doped $CaCO_3$ Micro 'Bow Ties'

CaO (0.7 g; 12.5 mmol) along with varying quantities of $Eu(NO_3)_3$, $Tb(NO_3)_3$ or $Ce(NO_3)_3$ (Tables 2.2, 2.3 and 2.4, respectively) were added to 25 ml of H_2O and allowed to stir for 15 min to ensure complete conversion to $Ca(OH)_2$. Subsequently, portions of a dry ice pellet (500 g) were added sequentially. The pH was then measured to determine reaction completion (pH 7). The product was separated by centrifugation at 3000 rpm and washed with water and ethanol before drying at 80 ^oC for 24 h resulting in yields in excess of 75%.

molar weight %	**Moles**	**Mass (g)**
0.5	0.0025	0.0278
1.68	0.0084	0.0935
2.5	0.0124	0.1392
3.4	0.017	0.1892
5.0	0.248	0.2782
6.7	0.3347	0.3780

Table 2.2: Europium doping levels

molar weight %	**Moles**	**Mass (g)**
0.5	0.0025	0.0271
1.68	0.0084	0.0911
2.5	0.0124	0.1357

Table 2.3: Terbium doping levels

molar weight %	**Moles**	**Mass (g)**
0.5	0.0025	0.0271
1.68	0.0084	0.091
2.5	0.0124	0.1355
3.4	0.017	0.1842
5.0	0.248	0.2708

Table 2.4: Cerium doping levels

2.6 Experimental Procedures for Chapter 7

2.6.1 Production of $CaCO_3$ Using CO_2 Gas

A range of CaO concentrations between 0.05 - 5 mol L^{-1} were added to a predetermined amount of Millipore water (50 ml) in a 200 ml graduated cylinder and allowed to stir for 30 mins to ensure complete conversion to $Ca(OH)_2$. After this period, gaseous CO_2 was introduced using either fritted glass or a deflected point needle. The length of carbonation was 30 mins, again ensuring reaction completion. The product was then separated via centrifugation at 9000 rpm before washing with Millipore water, ethanol, and a mixture thereof. It was then dried for 24 h at 80 °C resulting in yields in excess of 70%.

2.6.2 Effect of Initial $Ca(OH)_2$ Concentration

The effect of the initial $Ca(OH)_2$ slurry concentration was studied using the parameters detailed in Table 7.1, Chapter 7. The stirring and carbonation times detailed in Table 7.1 are also applicable for the remaining sections in this chapter.

2.6.3 Effect of CO_2 Flow Rate

The effect of the CO_2 flow rate was studied using the parameters detailed in Table 7.2, Chapter 7.

2.6.4 Effect of Reaction Temperature

The effect of the reaction temperature was studied using the parameters detailed in Table 7.3, Chapter 7.

2.7 Instrumentation

2.7.1 X-ray Diffraction (XRD)

X-ray diffraction relies on the scattering of x-ray radiation by electrons. This scattering is dependent on how many surrounding electrons are present. As a result, a periodic array of atoms diffract light in such a way as to construct a pattern which can be measured. Consequently, materials which do not exhibit long range ordering are considered X-ray amorphous.

When studying XRD patterns, Miller indices are used which describe planes of atoms using (hkl) coordinates. The d_{hkl} vector which extends from the origin to the hkl plane is used in tandem with Bragg's Law to estimate diffraction peaks:

$$\lambda = 2\, d_{hkl} \sin\theta$$

The wavelength, λ, is usually fixed. The angle θ which causes constructive interference from x-rays will produce diffraction peaks.

Powder x-ray diffraction is a specific case which utilises Bragg-Brentano Geometry (Figure 2.1) to calculate a powder diffraction pattern. The sample is typically rotated to increase the number of crystallites observed, and therefore obtain a more reliable pattern.

The Scherrer equation is used to calculate the crystallite size through its relationship to the width of a specific peak:

$$\tau = \frac{K\lambda}{\beta \mathrm{Cos}\theta}$$

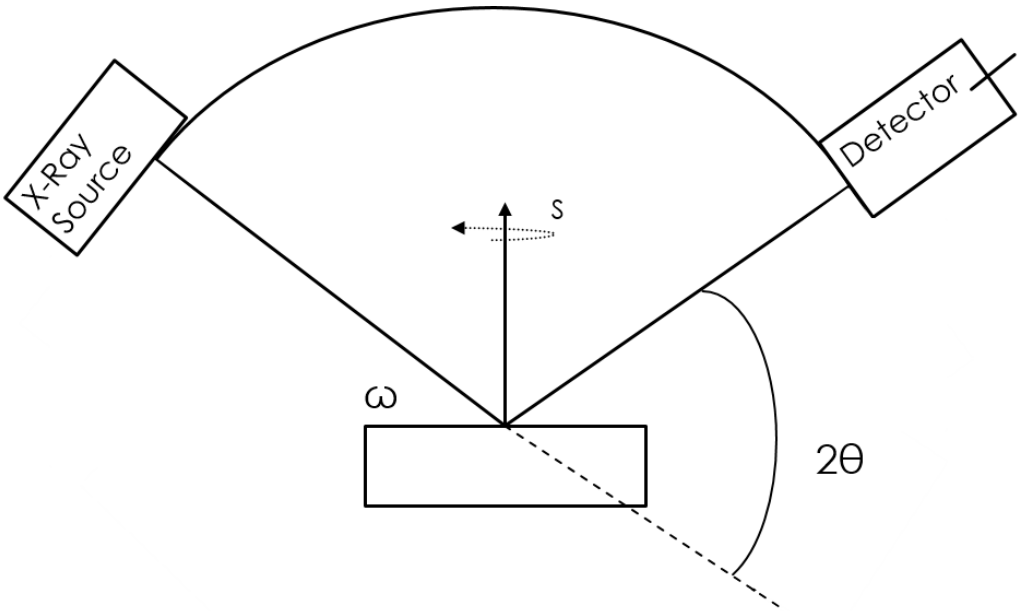

Figure 2.1: An illustration of Bragg-Brentano geometry used for powder diffraction where ω is the incident angle, 2θ is the diffraction angle and S is the plane rotation angle

Where τ is the mean ordered crystallite size, K is the shape factor which is typically taken to be 0.9, but is dependent on the crystallite shape, β is the peak width, and θ is the Bragg angle.

Typically either the full width at half maximum (FWHM) or integral breadth (which measures the total area under a curve) can be used however, integral breadth requires much more precision regarding the tails of the peaks.

In this work, x-ray powder diffraction was carried out on a zero background Si sample holder using a Bruker: D2 Phaser 2nd Gen benchtop diffractometer using Cu Kα radiation (λ = 1.5418 Å) across a 2θ range of 15 to 55 ^{o} with a step–size of 0.01 ^{o} at 1s/step using a zero–background Si sample holder. Unit cell parameters and crystallite size were determined by Rietveld refinement of the obtained patterns performed using GSAS implemented in EXPGUI.[2,3] The starting point for refinements was (R -3c; a = 4.99; c = 17.0615).[4]

2.7.2 Circular Dichroism (CD) Spectroscopy

Circular dichroism describes the difference in absorption of left- and right-handed circularly polarised light (CPL) by optically active molecules:

$$\Delta A(\lambda) = A(\lambda)_{LCPL} - A(\lambda)_{RCPL}$$

where λ describes the wavelength, A is the absorbance and LCPL and RCPL are left and right handed circularly polarised light, respectively.

When horizontal and vertical polarised light are in phase they form 45 ^{o} polarised light however, when a quarter-wave plate is used, the two are one quarter wave out of phase, which leads to the formation of circularly polarised light (CPL). CPL forms a left- or right-handed helix which is in turn differentially absorbed by chiral molecules. As evidenced by the equation above, circular dichroism is dependent on absorbance and can only be measured in conjunction with absorption bands. Cotton effects, which will be observed later, are described as the change of optical rotation in the region of an absorption band where the CD signal reaches a maximum before decreasing, reaching zero, and then continuing in the other direction and can be either positive or negative.

For this work, circular dichroism was carried out using a Jasco J-815 CD spectrometer. Liquid samples were typically run in a high performance quartz cuvette with a path length of 10 mm. The solvent of choice was ethanol or, in some instances, Millipore water. Solid state measurements were performed using a diffuse reflectance DRCD-575 integrating sphere with an internal background of $BaSO_4$.

2.7.3 Scanning Electron Microscopy (SEM)

A scanning electron microscope (Figure 2.2) utilises a focused beam of electrons to interact with, and provide information about, the surface of a material. The electron beam is formed at the cathode (typically a tungsten filament) through thermionic emission i.e. when thermal energy overcomes the work function of the material to produce electrons. The electron beam is then focused via magnetic lenses and, upon interaction with the material, causes the emission of various signals which can be detected.

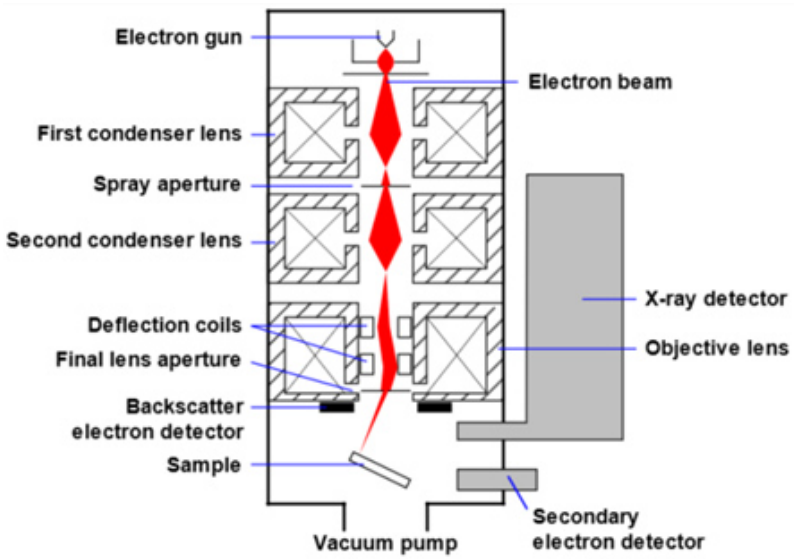

Figure 2.2: Simple schematic of a scanning electron microscope. Reproduced from ref[5]

Secondary electrons are produced via inelastic scattering between the electron beam and sample and provide morphological and topographical information about the material. Backscattered electrons, however, are produced via elastic scattering between the beam and the deeper sample and provide phase and atomic information. Upon the interaction between the beam and the sample, characteristic X-rays are released when an inner-shell electron is removed by the electron beam and is in turn returned to a relaxed state when an outer-shell electron fills this vacancy and emits an x-ray photon concurrently. These characteristic x-rays can provide elemental information

and are used in energy dispersive x-ray (EDX) analysis.

In this work, SEM images were obtained using a Zeiss Ultra Plus Scanning Electron Microscope using the secondary electron detector at a voltage of between 3 and 5 kV. Samples were dropped from the solid state onto carbon tabs on SEM stubs.

2.7.4 Transmission Electron Microscopy (TEM)

Transmission electron microscopy (TEM) (Figure 2.3) differs from SEM in that the electron beam is transmitted through the sample rather than scanning its surface. The electron source can either be a thermionic (e.g. W or LaB_6) or field emission gun (Schottky-type or cold field emission). Similar to SEM, magnetic lenses are used to focus the electron beam which is then transmitted through the sample and projected onto a fluorescent screen to form the image.

Owing to the higher acceleration voltage of TEM (60 - 300 kV), a much higher resolution is possible and as such TEM is typically used to provide crystallographic information. A particularly useful feature of TEM is the ability to combine features of TEM and SEM in the form of scanning transmission electron microscopy (STEM) which differs from conventional TEM (cTEM) by focusing the beam to scan the sample area rather than transmitting through it.

In this work, TEM images were obtained by Dr. Finn Purcell-Milton on an FEI Titan – Transmission Electron Microscope operating at 300 kV.

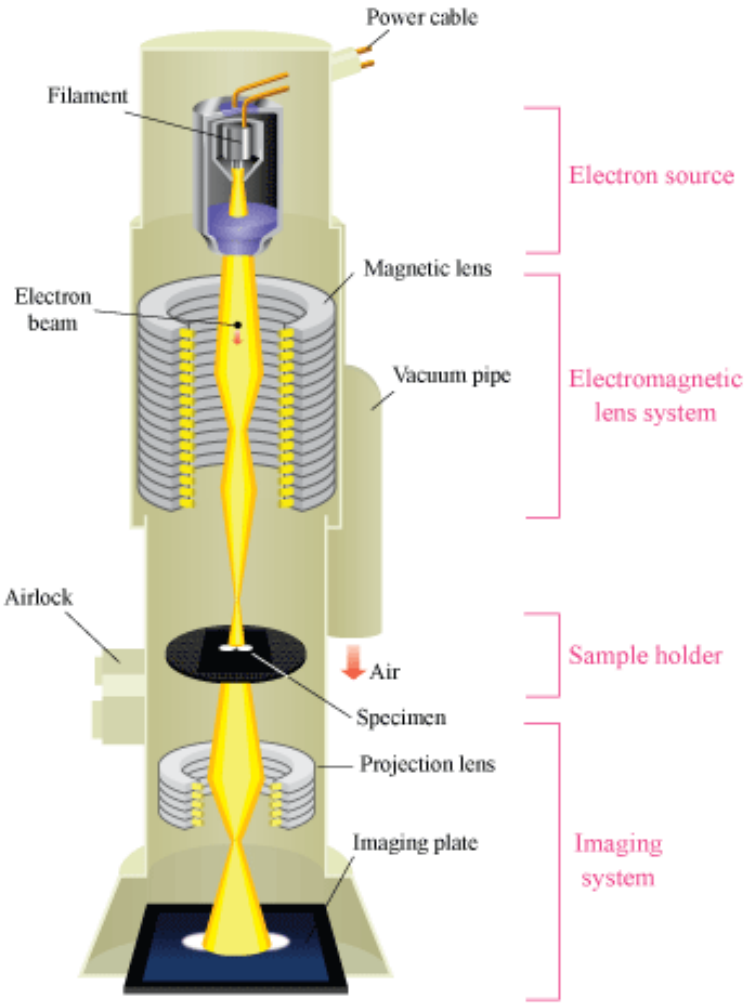

Figure 2.3: Simple schematic of a transmission electron microscope. Reproduced from ref[6]

2.7.5 Inductively Coupled Plasma - Mass Spectrometry

Inductively coupled plasma - mass spectrometry (Figure 2.4 is a technique used for the detection of ions on a scale of parts per billion (ppb) or μg L^{-1}. It can also be used to determine the isotopic composition of samples. Briefly, a sample which has previously been digested (typically in HNO_3 or HCl) is introduced through a peristaltic pump towards a nebuliser. Once in aerosol form, the sample is injected to an argon plasma. This plasma is formed via the partial ionisation of argon through pulsing an alternating electric current around the Argon so that

$$Ar \rightarrow Ar^{+} + e^{-}$$

and is typically in the range of 6000 - 8000 K.

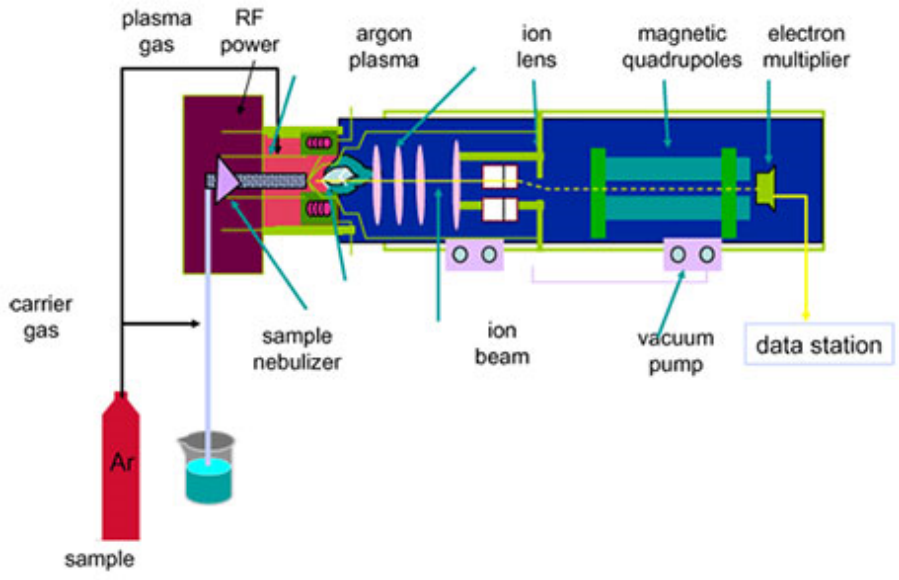

Figure 2.4: Simple schematic of an ICP-MS. Reproduced from ref[7]

Mass spectrometry is then carried out whereby skimmer and sampler cones allow only a small fraction of the ions through towards the electrostatic lenses where they are focused into the quadrupole which separates ions based on mass. Finally, an electron multiplier is used to generate a measurable signal.

ICP-MS was carried out by Aleksandra Rulikowska, ESHI, TU Dublin.

2.7.6 Photoluminescence (PL) Spectroscopy

Luminescence describes the phenomenon whereby a material absorbs a photon/ charged particle and subsequently undergoes photo-emission. Upon light absorption, an electron is promoted from the ground electronic state to an excited electronic state (whereby the electron's spin is conserved). Emission from this state is termed fluorescence and occurs on a timescale of 10^{-5} - 10^{-8}s. Also possible is intersystem crossing whereby there is a transition from the ground vibrational level of an excited state to a higher vibrational level of a lower energy level with different multiplicity (singlet-triplet, for example). Emission from this state to a ground state of different spin represents phosphorescence and occurs on a much longer timescale of 10^{-4} - 10^{4}s. These processes are detailed in a Jablonski diagram (Figure 2.5).

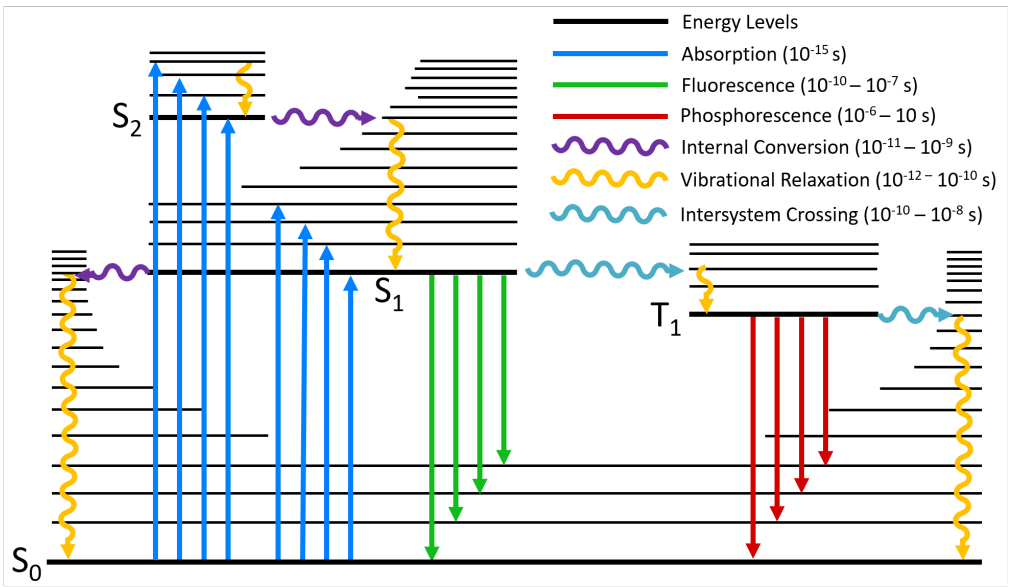

Figure 2.5: Schematic of a typical Jablonski diagram illustrating radiative and non-radiative transitions. Figure reproduced from ref[8]

Photoluminescence measurements are typically divided into excitation and emission spectra. The emission spectrum is obtained by setting the excitation spectrum to a fixed wavelength (typically the area of maximum absorbance) while the emission monochromator is scanned a range of wavelengths. Excitation spectra, by contrast, sets the emission monochromator to a fixed wavelength and scans the excitation monochromator through different wavelengths. The emission spectra is measured at a higher wavelength than excitation due to the fact that an emitted photon is lower in energy than the initial excited photon - known as the Stokes shift (Figure 2.6).

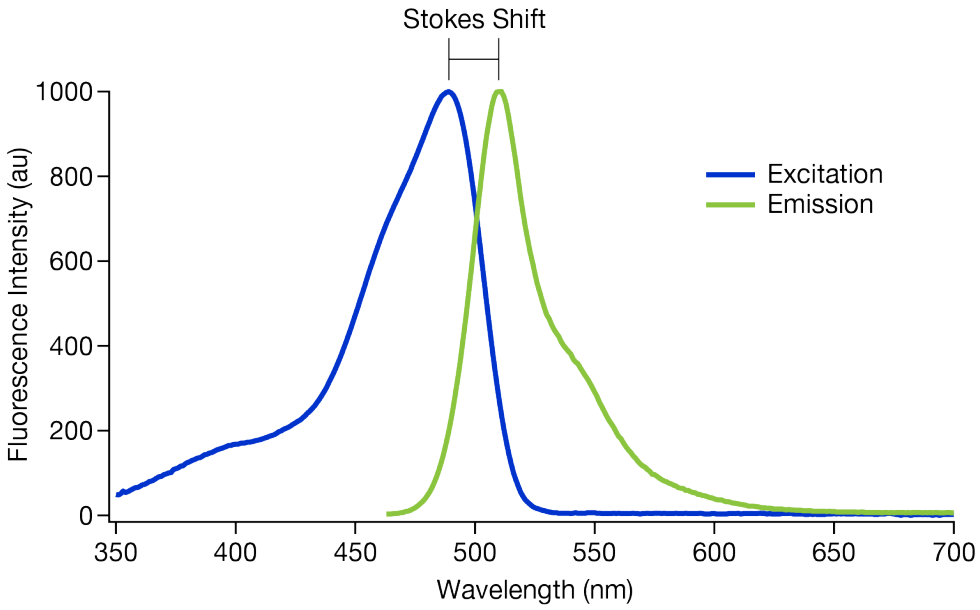

Figure 2.6: Fluorescence spectrum illustrating the concept of Stokes shift whereby the emission wavelength is higher than that of the initial absorption. Reproduced from ref[9]

In this work, phosphorescence data was collected using a Horiba FluorMax-4 in phosphorimetry mode. Steady state measurements were made using a 0.1 ms delay, sample window of 25 ms and a flash count of 200 and an increment of 1 nm, using a solid-state powder. Excitation spectra were measured using excitation and emission slits of 2 nm and 2 nm while emission spectra were measured using excitation and emission slits of 3 nm and 3 nm. Phosphorescence lifetime decay was determined

using the decay by window mode, a flash delay of 0.05 ms, flash count of 200 and excitation/emission slits of 3 nm and 3 nm.

2.7.7 Fourier Transform-Infrared Spectroscopy (FT-IR)

Infrared spectroscopy measures the interaction of materials with infrared light. It functions on the principle that specific frequencies of infrared light are absorbed by molecules which invokes a change in the dipole moment. Without this change in the dipole moment, molecules are said to be IR-inactive. It is important to remember that the energy of the absorbed photon matches the difference in energy between the initial and final states. In terms of vibrational modes, linear molecules have 3N-5 degrees of freedom whereas non-linear possess 3N-6.

Fourier transform-infrared spectroscopy (FT-IR) is a modified version of IR spectroscopy which utilises an interferometer, as opposed to a monochromator. An interferometer splits light into two beams where one passes to a stationary mirror, while the other passes to a movable mirror. This introduces a time delay which allows the measurement of the temporal coherence of the two signals.

In this work, FT-IR was carried out using a Bruker: Tensor II FT-IR spectrometer with diamond UATR.

2.7.8 Raman Spectroscopy

Raman spectroscopy measures the inelastic scattering of light by molecules - known as Raman scattering. In measuring the Raman spectrum of a material, said material is irradiated, typically by a laser, the resulting radiation of which is then collected by a lens before passing to a monochromator. Importantly, a notch filter is used to block elastic scattered light (Rayleigh scattering). A transition is considered Raman active if there is a change in polarisability (as opposed to IR-activity which stems from a change in the dipole moment).

As mentioned, Raman scattering is inelastic scattering of light. This means that the incident photon is different in energy to the emitted photon. Rayleigh scattering, by contrast, describes elastic scattering whereby the incident and emitted photons are of the same energy. Raman scattering where the emitted photon is lower in energy is termed the Stokes shift while an emitted photon of higher energy is an anti-Stokes shift.

Raman can act as a complementary technique to IR spectroscopy as described by the rule of mutual exclusion of centrosymmetric molecules which illustrates that a transition which is strongly Raman active will be weakly IR active and vice versa.

Raman spectra were obtained for this work via a Renishaw inVia Raman Microscope using a 785 nm Renishaw HP NIR Laser by Dr. Olan Cleary.

2.7.9 Differential Thermal Analysis - Thermogravimetric Analysis (DTA-TGA)

In differential thermal analysis (DTA) the sample, along with an inert reference material (e.g. alumina), undergo identical thermal treatments while the heat flow (mW) is measured. This is then plotted against temperature and is used to illustrate events which can be exothermic in nature e.g. combustion or crystallisation, or endothermic e.g. thermal decomposition or the glass transition temperature.

It is often used in tandem with thermogravimetric analysis (TGA) which measures the change in sample mass as a function of increasing temperature. TGA can illustrate absorption/desorption, phase transitions as well as other phenomena. In this way DTA and TGA can be coupled with each other to provide a more in-depth analytical technique.

Differential thermal analysis-Thermogravimetric analysis was carried out by Dr. Aran Rafferty on a Stanton Redcroft STA 1500 using a platinum crucible.

References

(1) L. Zhao and J. Wang, *Colloids and Surfaces A: Physicochemical and Engineering Aspects*, 2012, **393**, 139–143.

(2) A. V. D. Larson R.B., *GSAS - General Structure Analysis System*, Los Alamos National Laboratory, New Mexico, 2004.

(3) B. Toby, *Journal of Applied Crystallography*, 2001, **34**, 210–213.

(4) D. L. Graf, *American Mineralogist*, 1961, **46**, 1283–1316.

(5) nanoScience Instruments, *Schematic of a Scanning Electron Microscope*, [Online; accessed July 29th, 2019], 2019.

(6) H. Physics, *The schematic outline of a TEM*, [Online; accessed August 20th, 2019], 2019.

(7) M. KGaA, *Schematic of an ICP-MS*, [Online; accessed August 8th, 2019], 2019.

(8) E. Instruments, *A typical Jablonski diagram showing the possible radiative and non-radiative transitions*, [Online; accessed August 20th, 2019], 2019.

(9) Scientifica, *A graph showing the Stokes shift of GFP*, [Online; accessed August 20th, 2019], 2019.

Chapter 3

Chiral $CaCO_3$-Based Materials

3.1 Introduction

The development of multi-modal nano- and micro-structures has become an increasingly popular area of research in recent years.[1,2] In particular, the combination of two or more interesting or desirable properties within a single structure opens up a variety of opportunities from biomedicine,[3] sensing, and asymmetric catalysis, to a variety of optical applications.

In this work, multi-modal chiral luminescent $CaCO_3$ microspheres are presented for the first time. Whilst $CaCO_3$ microspheres have previously been reported as robust encapsulation agents,[4] this is the first example of chiral luminescent and chiral plasmonic $CaCO_3$ microspheres with a porous morphology. The chirality of these materials derives from their functionalisation with amino acids, while their luminescent properties are provided through loading with either CuInZnS/ZnS QDs or CdSe@ZnS/ZnS QDs, or trivalent lanthanide, particularly Eu^{3+}, doping. In this manner, chiral microspheres with orange, green, and red luminescence have been synthesised. In addition, it is demonstrated that for each loaded nanoparticle the modality of the initial NPs are preserved or even enhanced due to the incorporation.

In a similar manner, chiral plasmonic microspheres have also been synthesised using gold nanoparticles (Au NPs).

This method relies on the use of sodium dodecyl sulfate (SDS) and polyvinylpyrrolidone (PVP) to form complex micelles (Figure 3.1). The micelles form through sodium bridging between the headgroups of SDS and the electronegative centres of PVP.[5] In this manner, Na_2CO_3 was included in the initial micellar solution in order to interact at the outer surface of the micelles. As such, precipitation occurs rapidly upon the addition of $CaCl_2$ resulting in the formation of monodispersed microspheres.

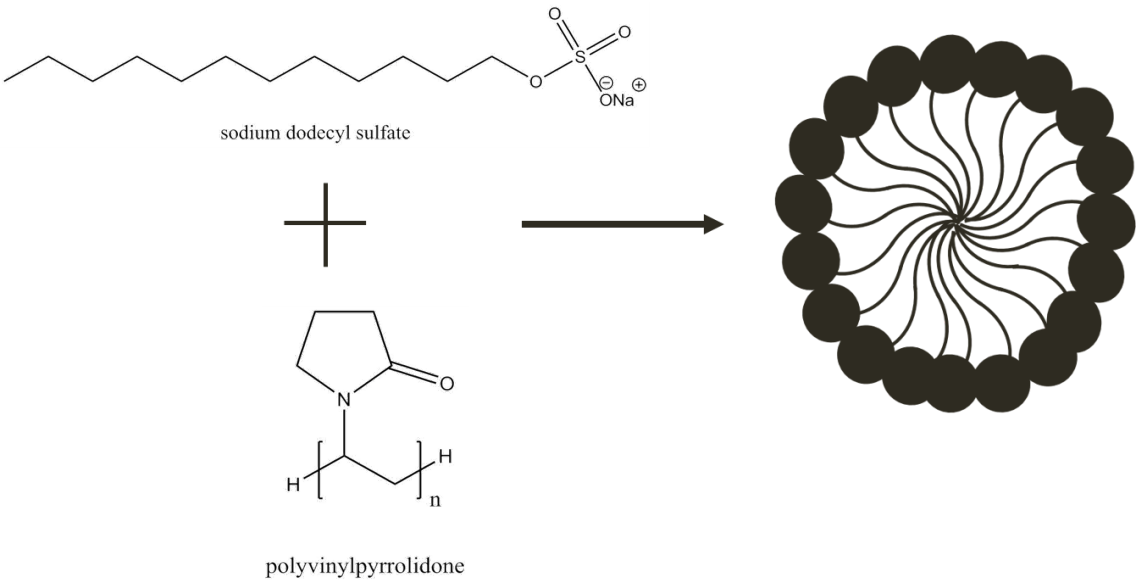

Figure 3.1: A schematic of the complex micelle formation from the interaction of SDS and PVP

3.2 Aims

The main aim of this area of work was the development of new chiral $CaCO_3$ based materials. Specifically, the synthesis of chiroptically active $CaCO_3$ microspheres using a template-directed synthesis which is based on a modified published procedure will be carried out.[6] The chiroptically active microspheres are planned to be used for the encapsulation of various luminescent and plasmonic materials, giving a further layer of interest to these materials. The materials are then to be characterised using circular dichroism (CD) and photoluminescence (PL) spectroscopy as well as XRD, SEM, and TEM. The synthesis of novel chiral $CaCO_3$ helices using 16-2-16 gemini surfactants is then planned which are to be characterised using CD spectroscopy, SEM, EDX and XRD.

3.3 Results and Discussion

3.3.1 Chiroptically Active $CaCO_3$ Microspheres

Chiroptically active calcium carbonate microspheres were synthesised according to a modified procedure, as discussed above.

Using this template-directed method, chiral ligands, *L/D*-proline and *S/R*-BINOL, were selected for introduction into the $CaCO_3$ microspheres. Proline (illustrated previously, Figure 1.11) and BINOL, which exhibits axial chirality, (see Figure 3.2) were chosen as chiral ligands due to the presence of hydroxyl groups.

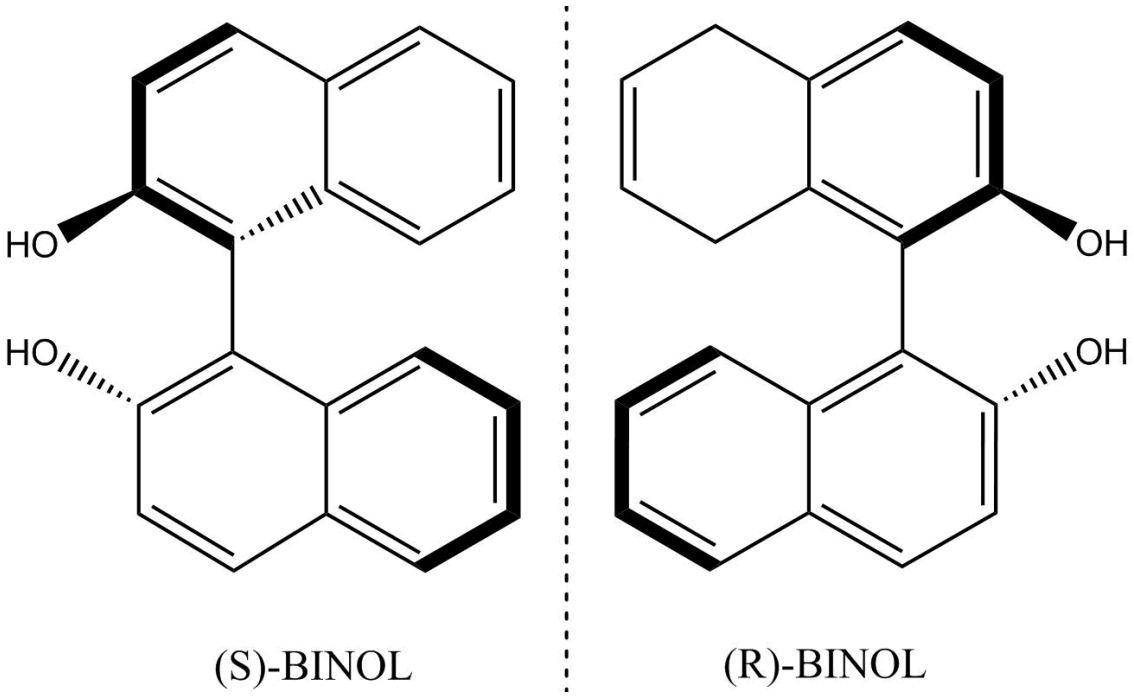

Figure 3.2: The *S*- (left) and *R*- (right) enantiomers of BINOL (1,1'-Bi-2-naphthol)

Calcium, as a hard acid, exhibits a high degree of oxophilicity and this high affinity for oxygen maximises the chances of incorporating these ligands into the microspheres. The SEM image of $CaCO_3$ microspheres which were successfully functionalised with *L*-proline is shown below (Figure 3.3).

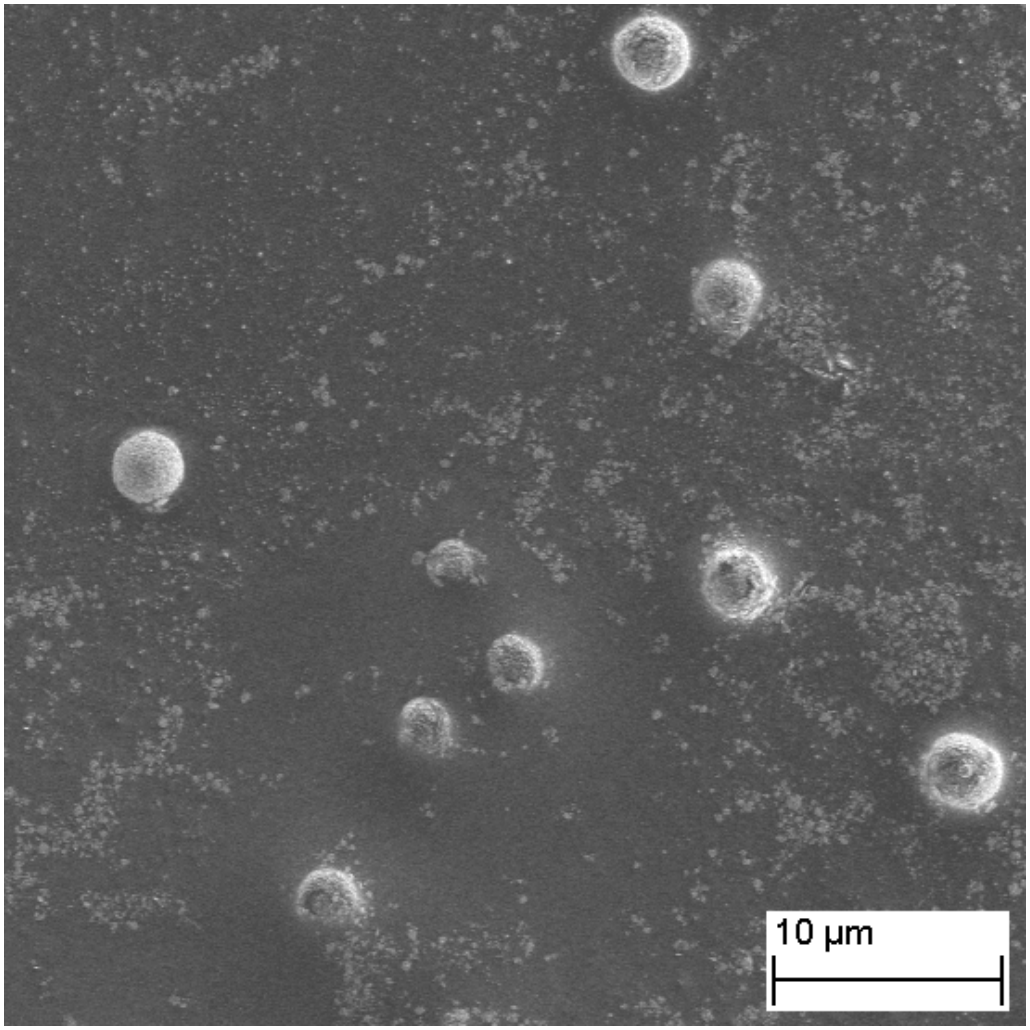

Figure 3.3: *L*-proline-functionalised $CaCO_3$ Microspheres

In order to determine whether the incorporation of the chiral ligands was successful, circular dichroism (CD) spectroscopy was used. The CD spectroscopy measurements (Figures 3.4 and 3.5) gave some very interesting results. Both spectra exhibit a chiral signal, but it is the difference between the spectra that is particularly important. Initially, it can be clearly observed that the *L/D*-proline-functionalised microspheres show a weak but optically active signal with a definitive mirror-image. The *S/R*-BINOL-functionalised microspheres, however, exhibit a substantially stronger and more complex CD signal where Cotton effects (a change in sign of the CD signal, as previously mentioned[7]) can be observed at 230 nm. Initially, this difference in signal was thought to be due to a stronger binding of BINOL, which is a biden-

tate ligand, however upon further analysis it was determined that this signal was observed due to an unsuccessful functionalisation i.e. the signal observed is simply that of the free *S/R*-BINOL ligand (See Figure 3.6). By contrast, the spectrum of the *L/D*-proline-functionalised microspheres shows no Cotton effects. A potential rationalisation of this phenomenon is that the amino acid is bonded to $CaCO_3$ in such a way that its conformational freedom is highly restricted. In this scenario, the amino acid is incapable of rotating in such a way as to produce Cotton effects i.e. the 'switching' of the chiral signal at the point of maximum absorbance. This observation, which is here termed 'chiral scattering' or 'chiral complexation' is not only highly interesting, but also has the potential to be useful in that it should be possible to evaluate whether functionalisation has been successful or not simply by looking at the CD spectrum for the absence or presence of Cotton effects, respectively.

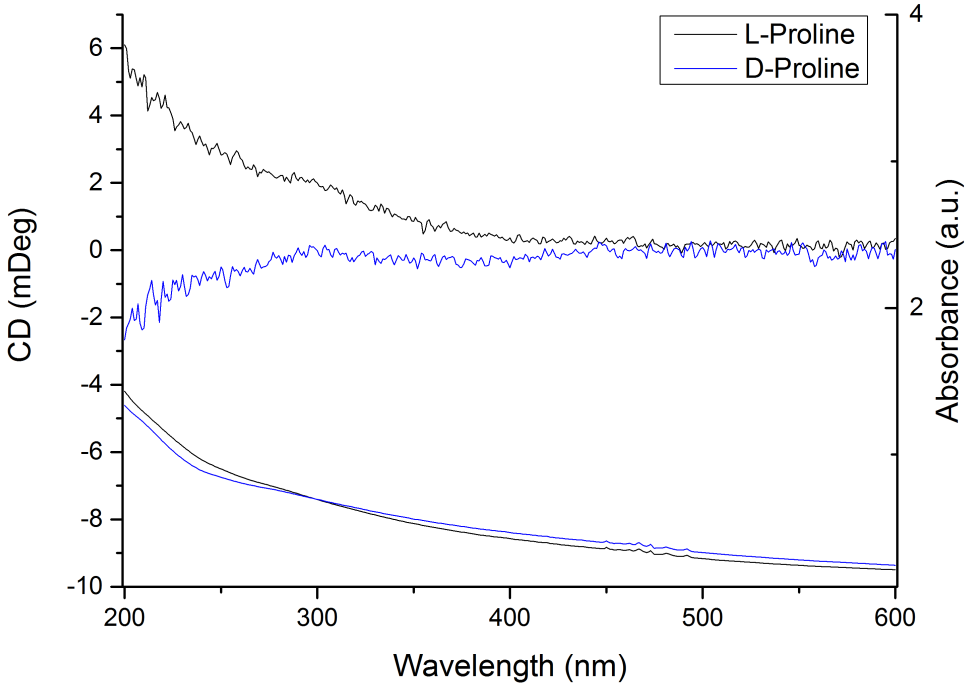

Figure 3.4: CD spectrum of *L/D*-proline-functionalised $CaCO_3$ microspheres

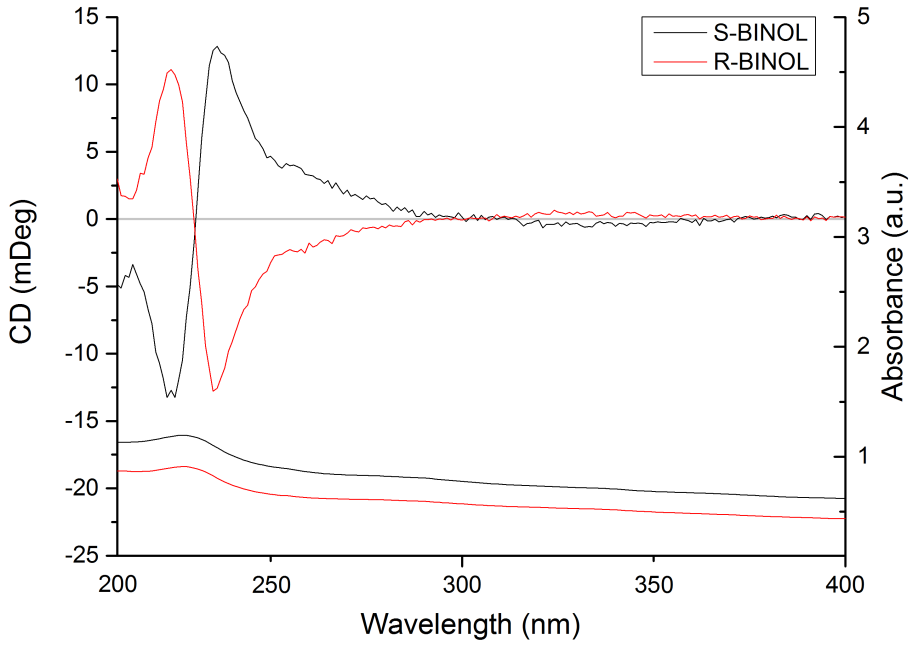

Figure 3.5: CD spectrum of *S*/*R*-BINOL-functionalised $CaCO_3$ microspheres

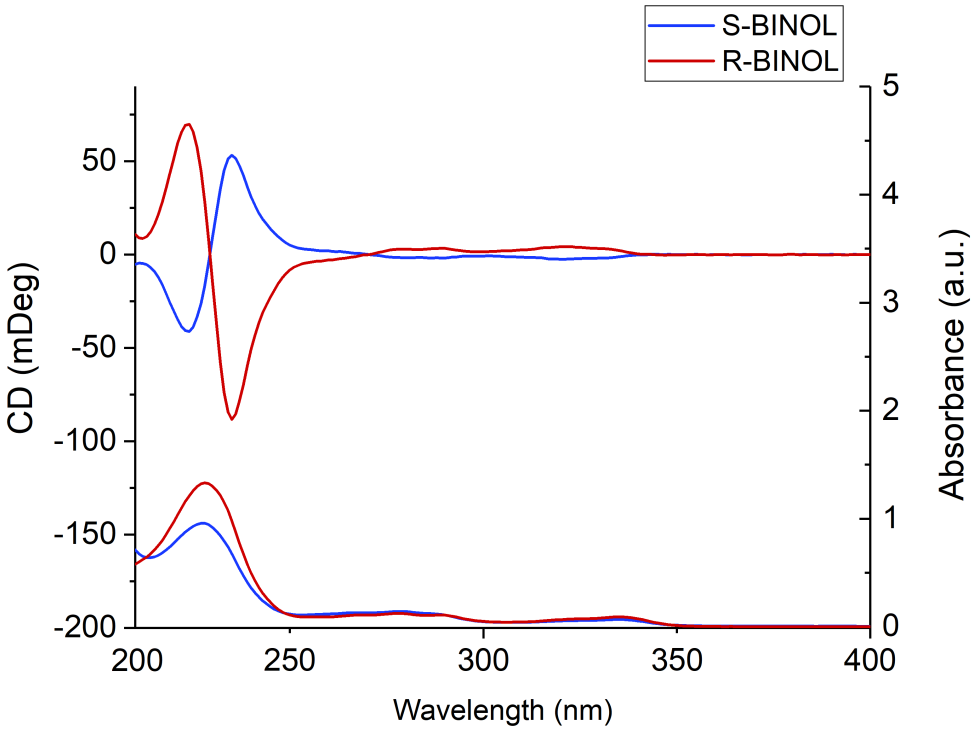

Figure 3.6: CD spectrum of free *S*/*R*-BINOL

This work also serves as proof of concept for microemulsion-based drug delivery systems, where valuable compounds can potentially be introduced to a completely biocompatible system for release *in vivo* with minimal side effects.

3.3.2 Characterisation of Chiral Luminescent $CaCO_3$ Microspheres

TEM images of the nanomaterials used for encapsulation is shown in Figure 3.7. Two types of quantum dots were chosen for incorporation, namely CuInZn/ZnS and CdSe@ZnS/ZnS QDs, whilst Au NPs were used for chiral plasmonic microsphere synthesis. These QDs and Au NPs were chosen specifically for their monodispersity and favourable optical and electronic properties.

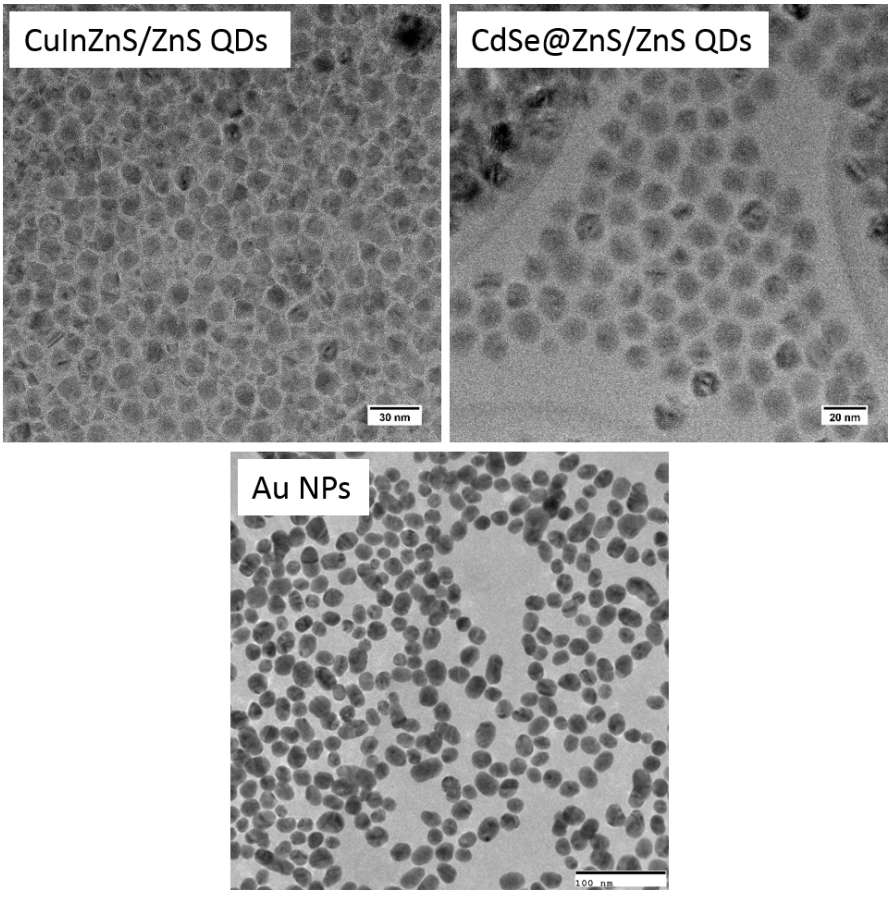

Figure 3.7: TEM images of the encapsulated materials, namely CuInZn/ZnS QDs, CdSe@ZnS/ZnS QDs and Au NPs

Quantum dot (QD) loaded and rare earth elements (REE) doped microspheres have been produced *in situ* using the previously described micelle-directed approach (Figure 3.1). SEM images of the as-produced chiral luminescent $CaCO_3$ materials (Figure 3.8) show the formation of microspheres with a well-defined structure and obvious porosity as well as high monodispersity.

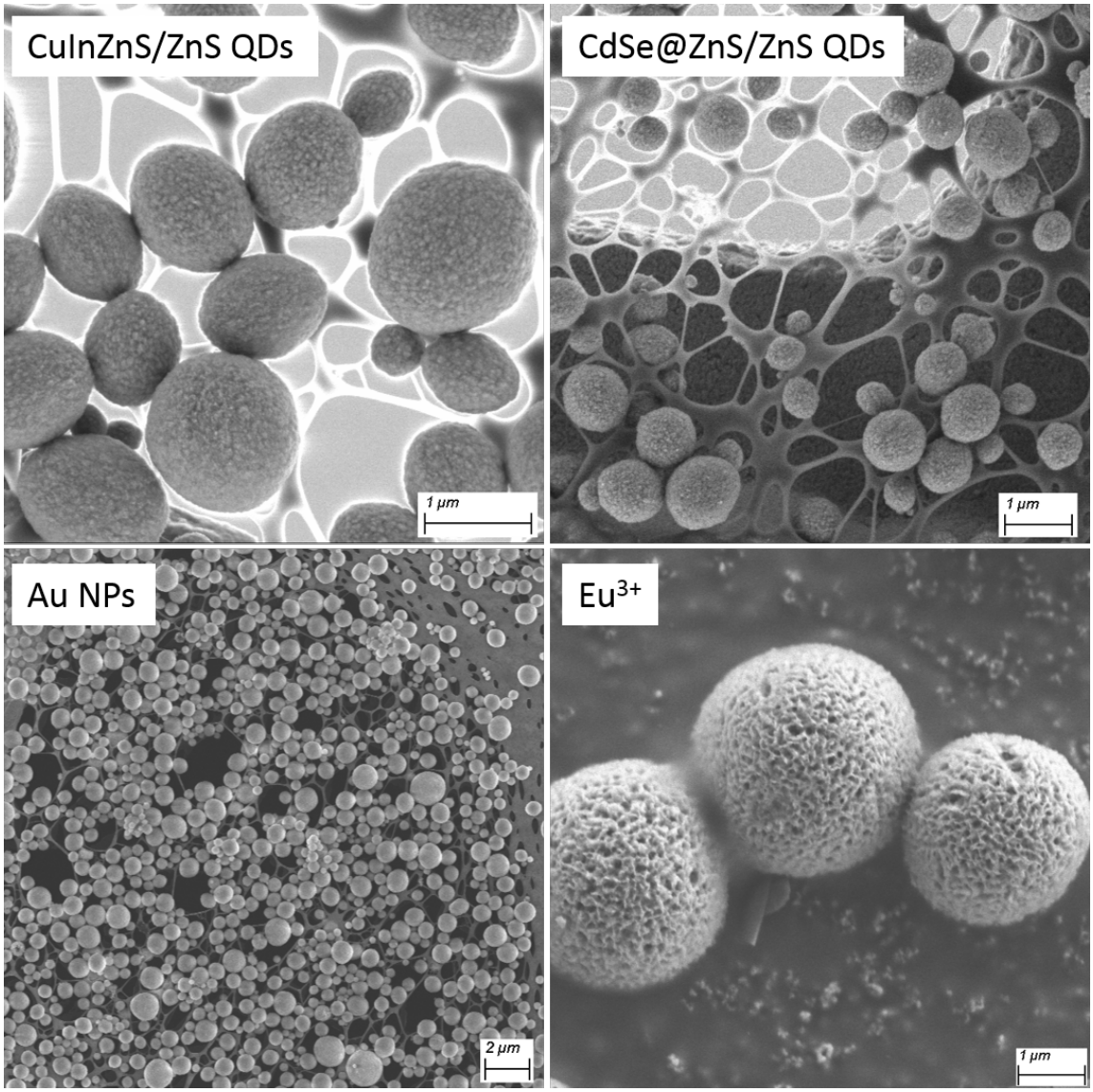

Figure 3.8: SEM images of the as-synthesised microspheres showing a well-defined structure as well as a porous morphology

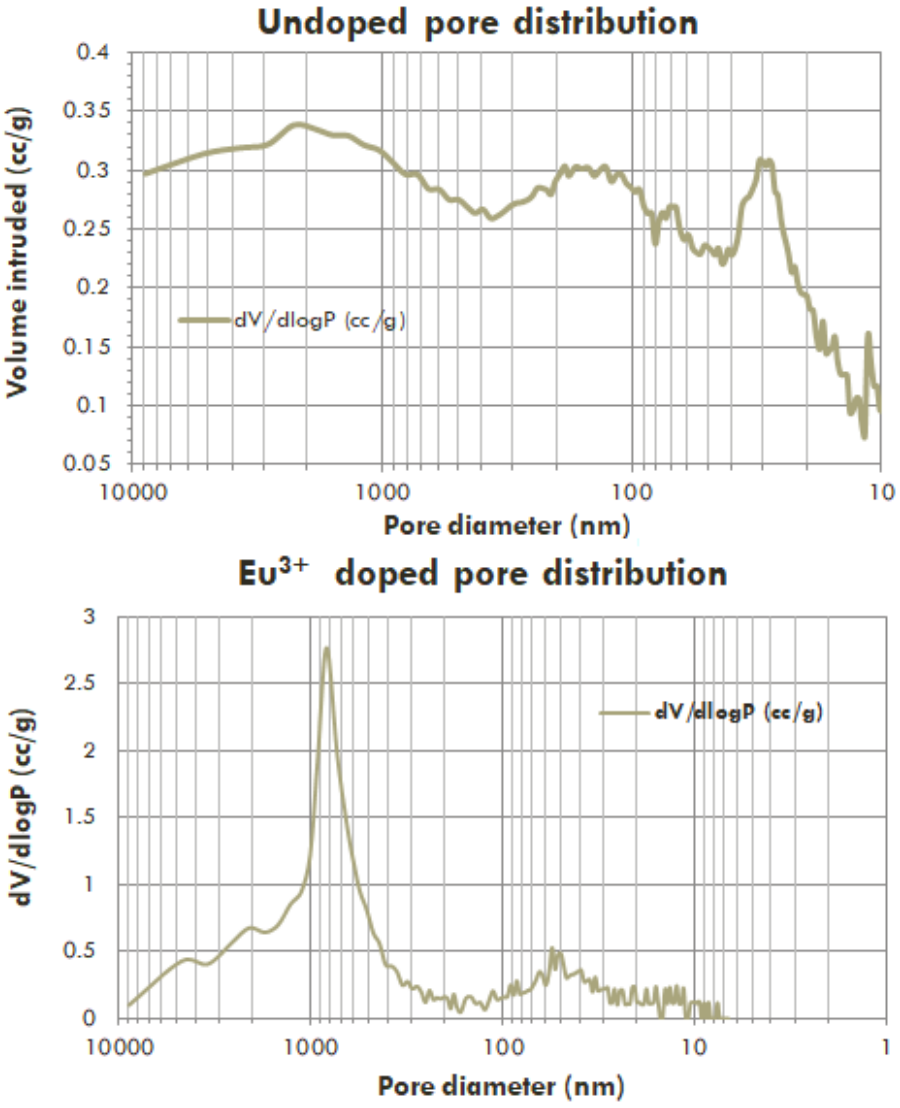

Figure 3.9: Mercury porosimetry measurements of doped and undoped $CaCO_3$ microspheres

The microspheres formed show no obvious differences to each other, with the exception of those doped with europium which show a marked increase in porosity from with the onset of doping (see Figure 3.9). In the undoped microspheres there are two main pore sizes of 30 and 11 nm. In the doped samples, the average pore diameter is c. 70 nm. In both plots, the large peaks at higher diameters correspond to voids between the microspheres and can therefore be discounted This difference is somewhat to be expected since Eu^{3+} possesses a high partition coefficient for

calcite and is therefore most likely doped into the calcite lattice itself. As well as the obvious charge disparity between Ca^{2+} and Eu^{3+}, there is also an important size disparity between the ionic radii of Ca^{2+} and Eu^{3+}, which are 114 and 108.7 pm, respectively. This size and charge disparity is likely to induce defects in the calcite lattice where two Eu^{3+} ions are likely to replace three Ca^{2+} ions. These defects are, therefore, highly likely to increase the porosity of these materials. Importantly however, this does not significantly impact the luminescence properties of the Eu doped $CaCO_3$ microspheres. Also, XRD (Figure 3.10) showed that the microspheres were made up of predominantly calcite with a small amount of vaterite.

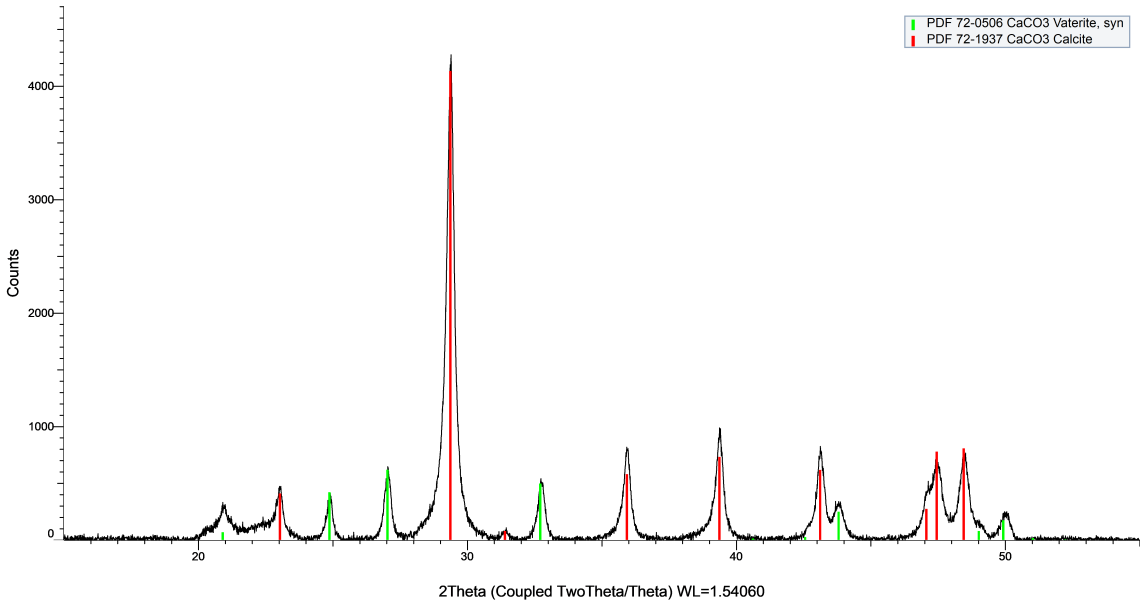

Figure 3.10: XRD pattern of $CaCO_3$ microspheres loaded with CuInZn/ZnS QDs

Focused ion beam (FIB) analysis (Figure 3.11) showed that the microspheres formed are in fact not hollow, while still being porous throughout. It is expected to lose some of this porosity during the gallium milling step of FIB which causes an effect known as 'curtaining' whereby the mill pattern leads to the formation of large periodic strips down the microspheres.[8]

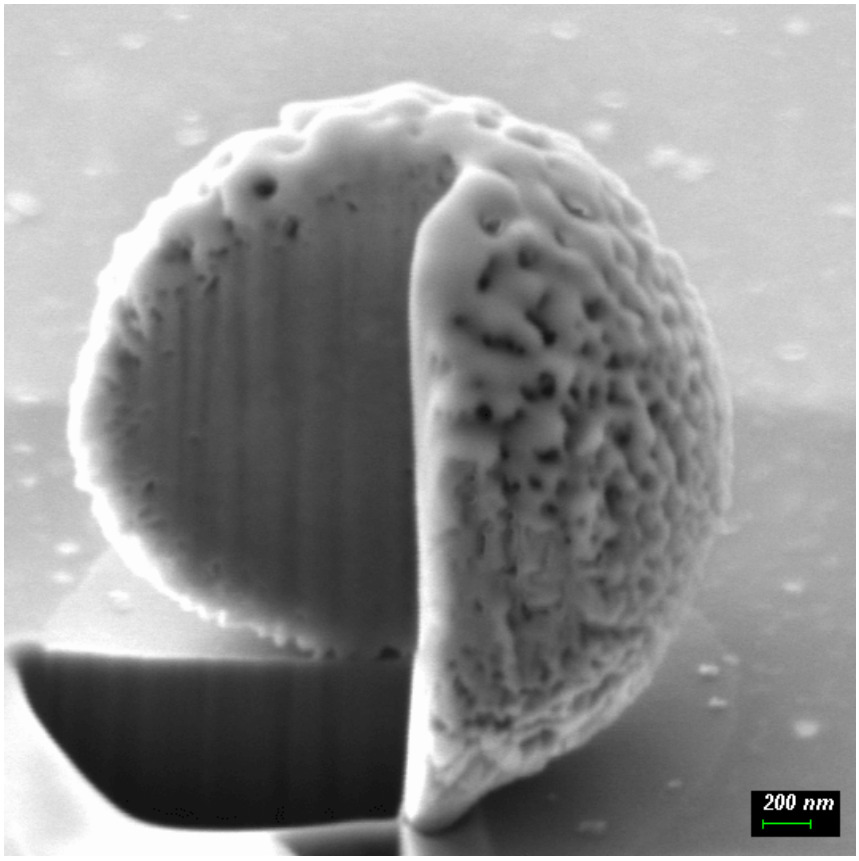

Figure 3.11: SEM image of $CaCO_3$ microspheres milled using focused ion beam (FIB)

Diffuse reflectance circular dichroism (DRCD) spectroscopy was carried out on all materials, as illustrated in Figure 3.12. A solid-state analytical technique was chosen owing to the poor solubility of $CaCO_3$ which limits the effectiveness of analysis in solution. In DRCD, an integrating sphere coated with $BaSO_4$ is used to allow the precise solid-state analysis of chiral compounds. The CD data of the four samples illustrates the chiral nature of each. Interestingly, the CD signal differs significantly from the CD spectrum of L-cysteine (Figure 3.13), proving that the signal is not due to free cysteine.

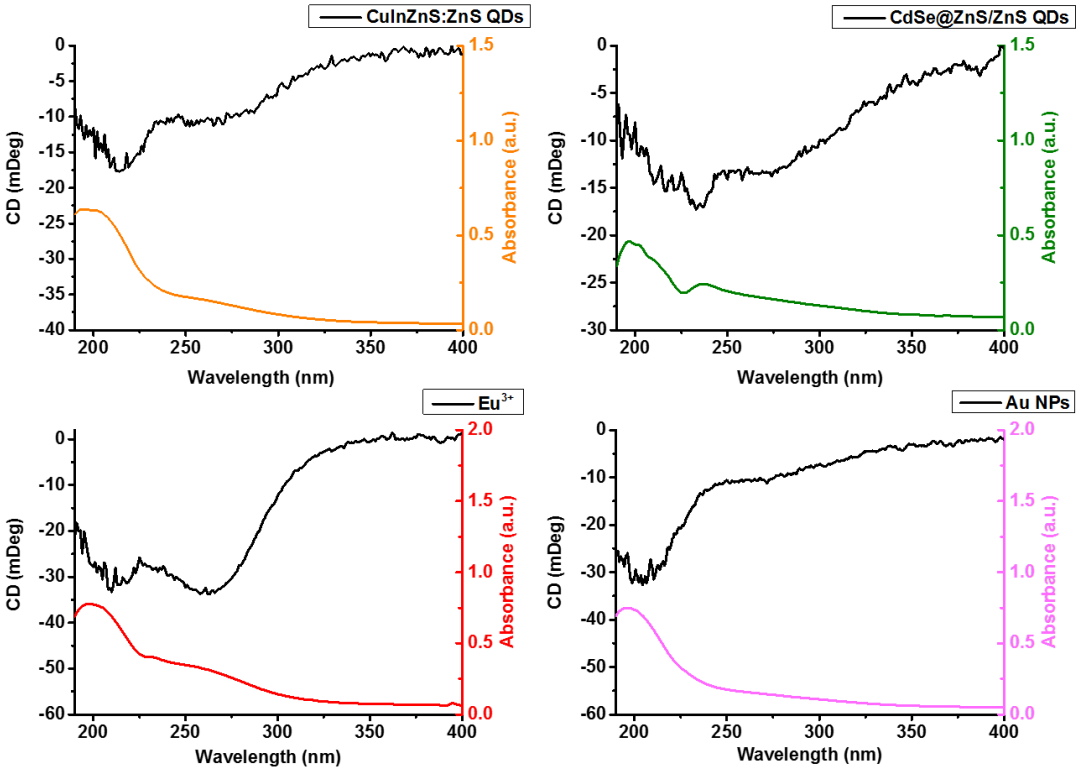

Figure 3.12: Absorbance (coloured lines) and diffuse reflectance circular dichroism (DRCD) (black line) spectra of the $CaCO_3$ microspheres.

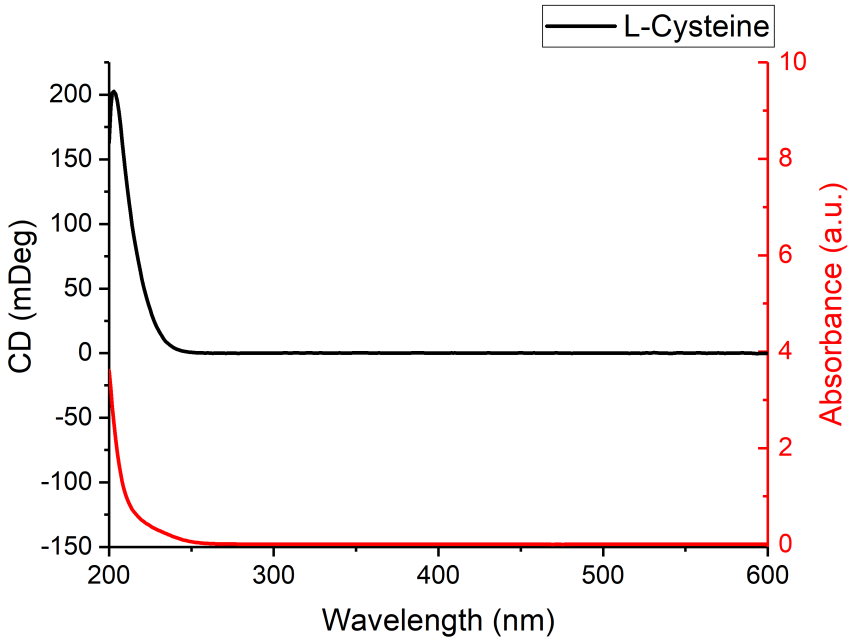

Figure 3.13: CD spectrum of L-Cysteine in water

Following this work, characterisation of the luminescent properties of the Eu doped and the CuInZnS/ZnS QD and CdSe@ZnS/ZnS QD loaded microspheres was carried out in the solid state, with the results shown in Figures 3.14 and 3.15.

The excitation photoluminescence spectra (PLEx) and the emission photoluminescence spectra (PLEm) of Eu^{3+} doped $CaCO_3$ microspheres are shown in Figure 3.14 with the characteristic peaks observed.[9] PLEm was measured from 560 nm to 720 nm using an excitation of 393 nm corresponding to $^7F_0$–$^5L_6$ and using an excitation wavelength of 270 nm corresponding to the absorption energy of the O^{2-} / Eu^{3+} charge transfer band (CTB).[10] PLEx was measured from 230 nm to 500 nm using the 614 nm emission peak. The excitation spectra contain a group of sharp lines in the longer wavelength region, which can be ascribed to the f–f transitions within the $4f^6$ configuration of Eu^{3+} ions (further detailed assignment of these transitions can be found in Chapter 6, Section 6.3.4).

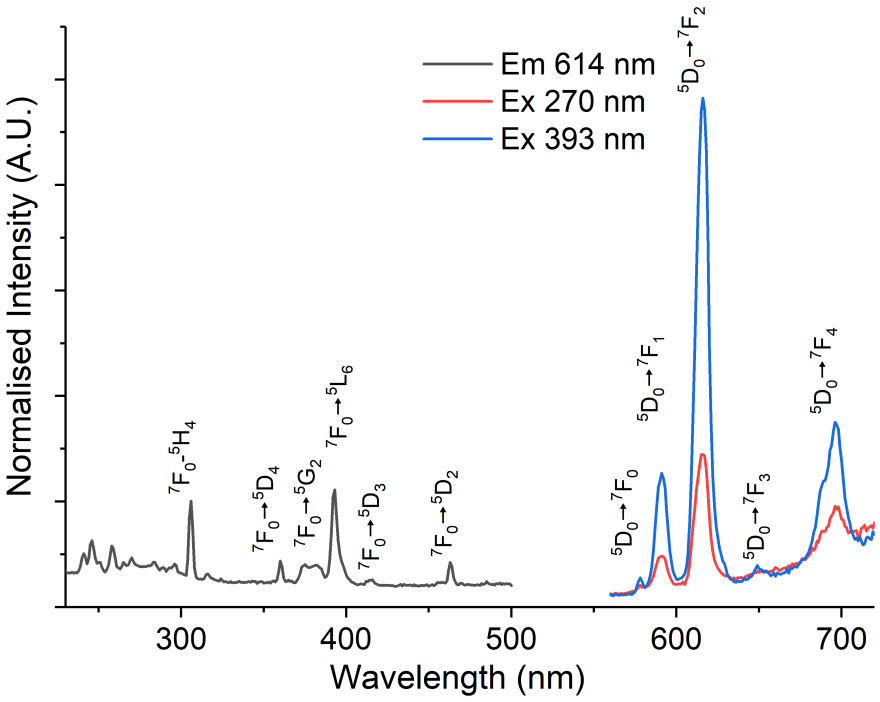

Figure 3.14: Emission and excitation photoluminescence spectra of Eu^{3+} doped $CaCO_3$ microspheres. Emission was measured using excitation at 270 nm and 393 nm, while excitation spectra was measured using the peak at 614 nm which corresponds to the $^5D_0$–$^7F_2$ transition

Photoluminescent spectra of the QD loaded samples is shown in Figure 3.15, compared to the original QD PL in solution. The CuInZnS/ZnS QD loaded $CaCO_3$ demonstrated a broad emission profile with a full width at half maximum (FWHM) of 131 nm, peaking at 608 nm which is indicative of this type of QD. The CdSe@ZnS /ZnS QDs loaded $CaCO_3$ showed a much sharper emission peak with a FWHM of 21.8 nm centred on 525 nm, which again is well documented.[11]

When comparing the QD loaded microspheres' PL to the PL of the original solutions, the absence of any significant red shifting of the peak position is noticeable upon incorporation inside the $CaCO_3$ lattice for either sample, with the CuInZnS/ZnS in fact showing a minor blue shift. The absence of red shifting indicates that both QDs are incorporated singly throughout the microsphere structure and have avoided aggregation which leads to strong red shifting in the PL emission peak.

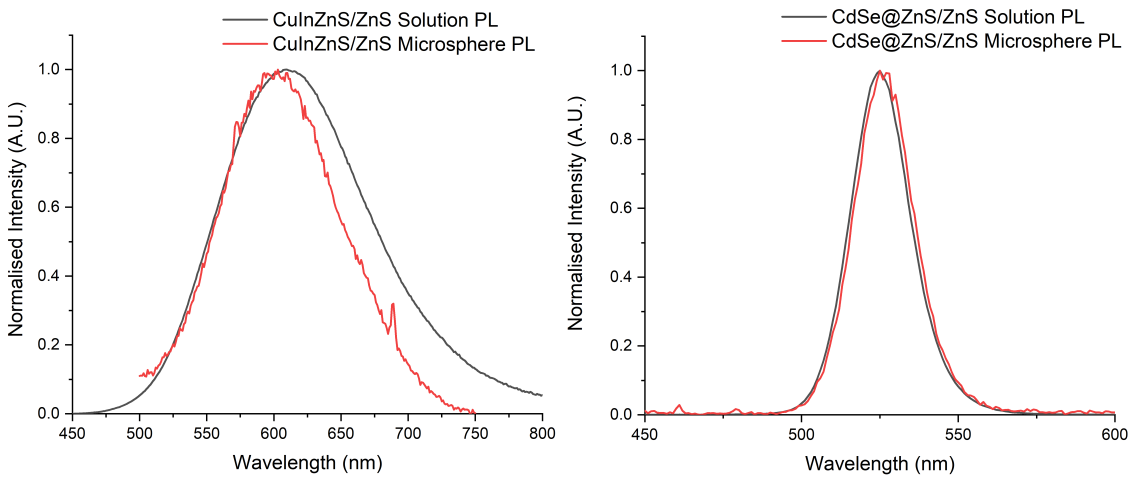

Figure 3.15: Photoluminescent emission spectra of (Left) CuInZnS/ZnS and (Right) CdSe@ZnS/ZnS in solution and loaded into $CaCO_3$ microspheres

To further characterise the effects of microsphere loading upon the PL emission, the fluorescence lifetime was measured for each sample and compared to the original QD prior to incorporation. These data were fit using a triexponential decay with results presented in Table 3.16. Each exponential used corresponds to a photophysical process, and while Eu^{3+} is fitted using a biexponential corresponding to both possible positions within the lattice, quantum dots require the use of a triexponential decay. This addresses the fact that these are not individual atoms being considered but rather a distinct material. As such it is more pertinent to fit using a triexpoential which can then be used to determine the average lifetime.

In both cases the QDs displayed a minor decrease in PL lifetime, with CdSe@ZnS/ZnS QDs showing a decrease from an average time of 10.4 $x10^{-7}$ s in solution to 8.4 $x10^{-9}$ s in the $CaCO_3$, while CuInZnS/ZnS QDs showed a more significant decrease from 4.34 $x10^{-7}$ to 2.95 $x10^{-7}$ s. This, therefore, indicates increased de-excitation, which can be explained via a change in how effectively the excited state of the QD is isolated from the external environment upon incorporation inside the lattice.

Average	Sample	T1	Amplitude (A1)	T2	Amplitude (A2)	T3	Amplitude (A3)	sum of amplitude	CHISQ
4.34E-07	CuInZnS/ZnS in solution	1.63E-07	0.2287	3.35E-07	0.5854	1.08E-06	0.1859	1	1.10828
2.95E-07	CuInZnS/ZnS in $CaCO_3$	7.15E-08	1.42E-01	3.35E-07	0.8502	8.32E-09	0.0074	1	1.056418
1.04E-08	CdSe@ZnS/ZnS in solution	3.69E-09	8.51E-02	9.78E-09	0.8067	2.03E-08	0.1082	1	1.024932
8.39E-09	CdSe@ZnS/ZnS in $CaCO_3$	7.15E-08	0.00E+00	3.35E-07	0.0002	8.32E-09	0.9998	1	1.175195

Figure 3.16: Fluorescence lifetimes of QD loaded microspheres fited using a triexponential decay

3.3.3 Synthesis and Characterisation of $CaCO_3$ Helices

Building on the synthesis of chiroptically active $CaCO_3$ microspheres, the preparation of a novel $CaCO_3$ material which would be intrinsically chiral was attempted. To clarify, while the microspheres synthesised had an induced chiral signal from the amino acids, they were not structurally chiral. By contrast a helix, or ribbon-like structure composed of $CaCO_3$ would fulfil the requirements for being intrinsically chiral, in this case possessing helical chirality.

In order to prepare $CaCO_3$ helices, the same idea behind the microsphere synthesis was applied once again, whereby a micelle self-assembles around which $CaCO_3$ can form. To this end, bis-quaternary ammonium gemini surfactants with the formula C_2H_4-1,2-$((CH_3)2N^+C_{16}H_{33})_2$ - known as 16-2-16 gemini surfactants (Figure 3.17) were chosen as the template. These amphiphilic molecules self-assemble to form cationic helical micelles in nature, and allow the transcription of the helical morphology to inorganic nanostructures (Figure 3.18) e.g. silica nanohelices.[12–16]

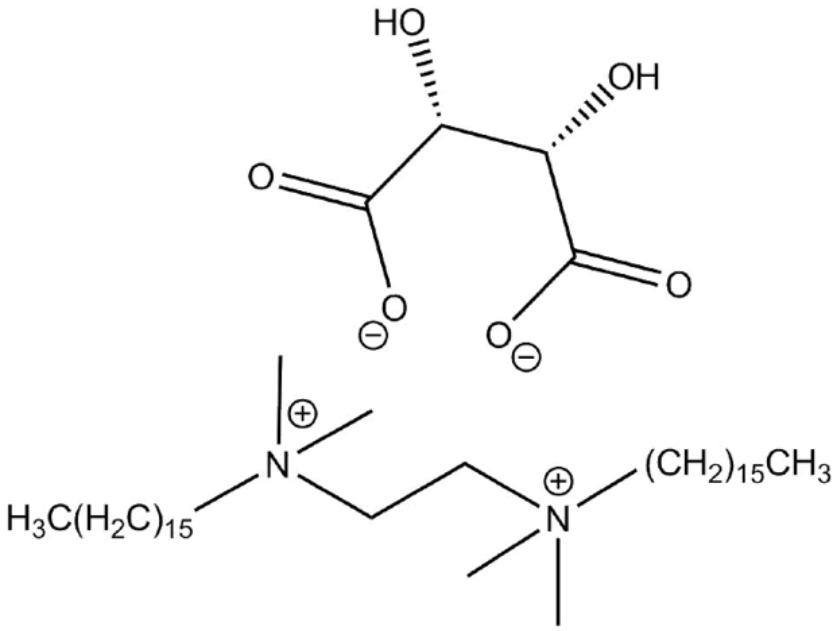

Figure 3.17: 16-2-16 Gemini Tartrate: A chiral template for the production of $CaCO_3$ helices

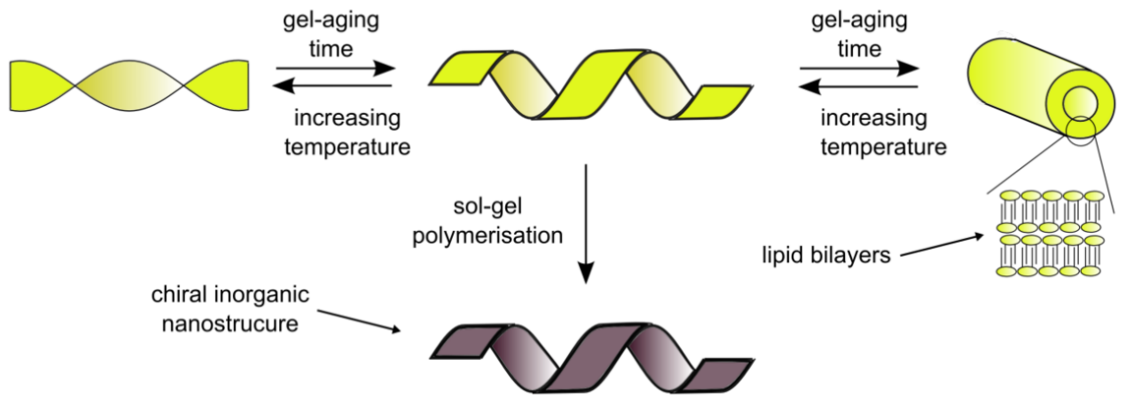

Figure 3.18: Schematic illustrating the chiral transcription of 16-2-16 gemini surfactants

The 16-2-16 gemini tartrate was prepared via a previously reported procedure[14] (as illustrated in Figure 3.19) and their formation was confirmed using mass spectrometry. Using the newly formed 16-2-16 tartrates, a chiral transcription with $CaCO_3$ was carried out in the following manner: the *L*- and *D*-tartrates were heated to 55 °C, which is above their Kraft temperature. To this micellar solution, Na_2CO_3 was added and allowed to stir for one hour. To this, $CaCl_2$ was added and the suspension was again allowed to stir for another hour. The product was separated by centrifugation and washed and dried in the manner described previously.

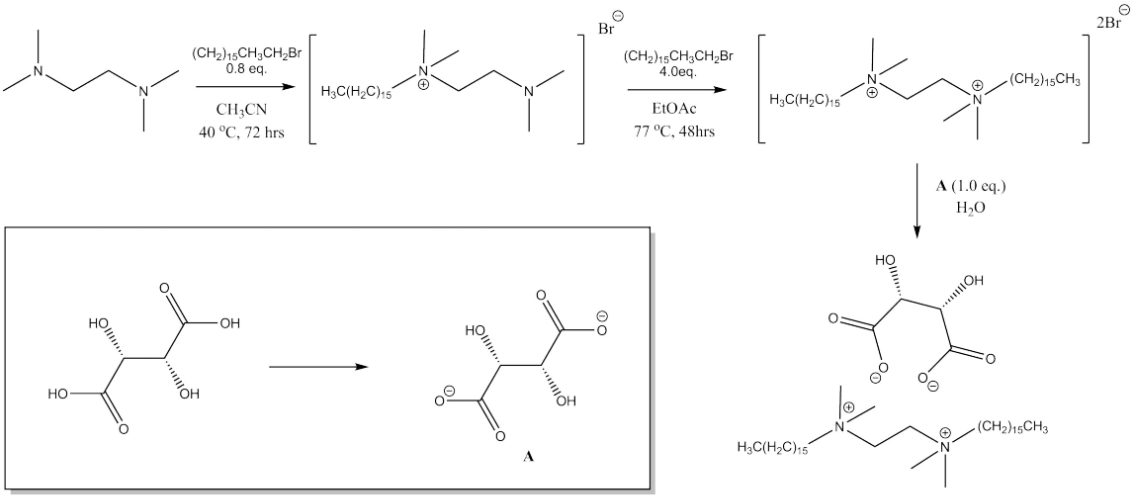

Figure 3.19: Synthesis of 16-2-16 gemini tartrate

Initial SEM images were quite promising and showed the formation of some large helical microstructures (Figure 3.20a). EDX analysis of the helical structures showed the characteristic peaks of Ca, C and O (Figure 3.20b), and therefore a refinement of the synthetic procedure was carried out.

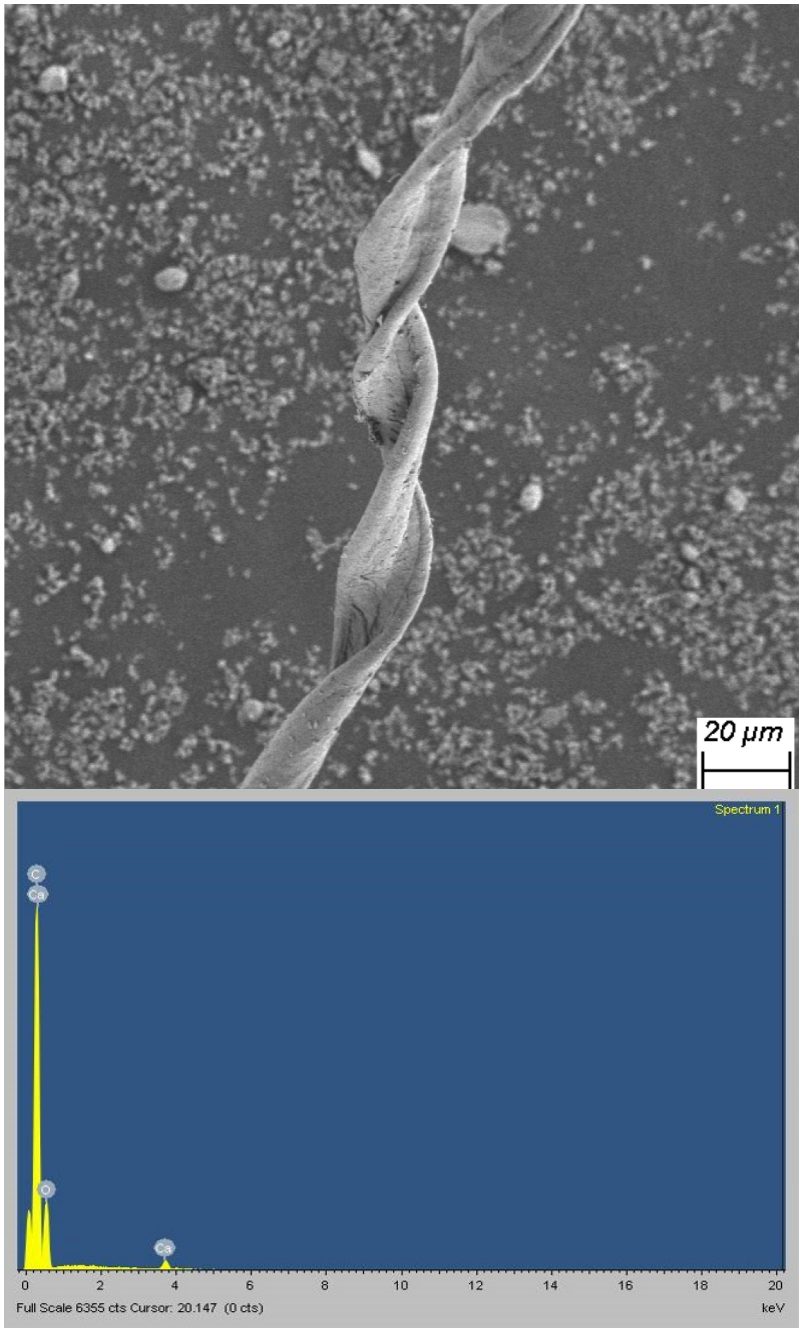

Figure 3.20: (A) SEM images of *L*-tartrate based $CaCO_3$ helices formed via early syntheses and (B) EDX spectrum of $CaCO_3$ helices

Further modification of the synthesis, specifically increasing their aging time post $CaCl_2$ addition from 1 h to 5 h resulted in the production of novel *L*- and *D*- $CaCO_3$ helices. The helices formed are illustrated in Figure 3.21 and show a clearly observable left- and right-handed helical chirality.

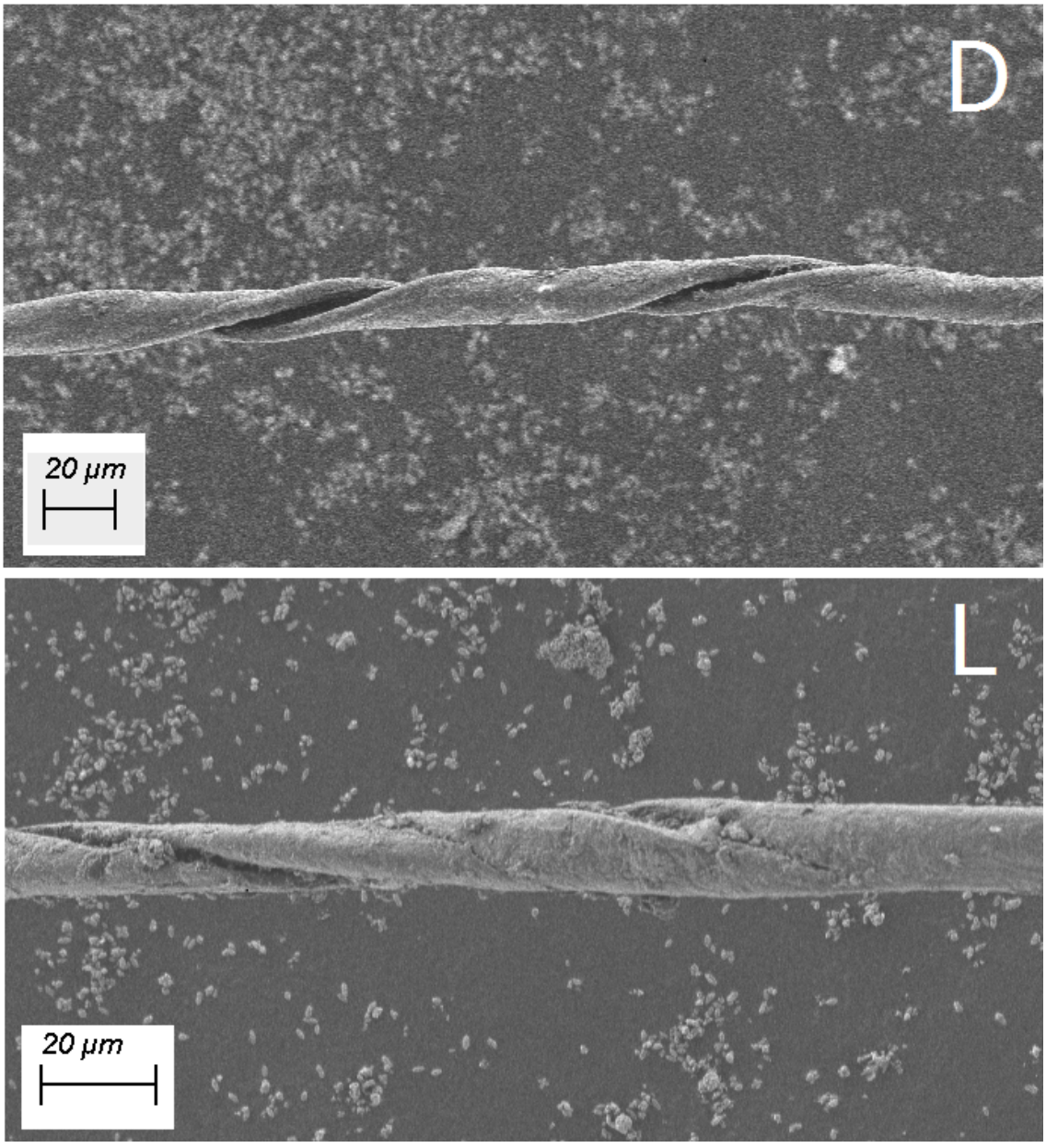

Figure 3.21: SEM images of *D*- and *L*- $CaCO_3$ helices

CD spectroscopy was carried out on these chiral macrostructures. The CD spectra obtained (Figure 3.22) shows a strong chiral signal (approximately 30 mDeg) for both enantiomers which extend well into the higher wavelengths (above 800 nm). The obtained spectrum is markedly different from that of the 16-2-16 starting material (see Figure 3.23), which is evidence of the formation of a new $CaCO_3$ structure. The extension of the CD signal is itself evidence of the formation of the a chiral macrostructure. The extension of a chiral signal to higher wavelengths (c. 700-800 nm) as observed in the CD spectrum of a helix is typically in contrast with that observed at low wavelengths for molecular chirality. When studying chiral molecules, there is little to no CD activity at the higher wavelengths coupled with a large signal, and most often Cotton effects, at lower wavelengths where the molecules themselves absorb.

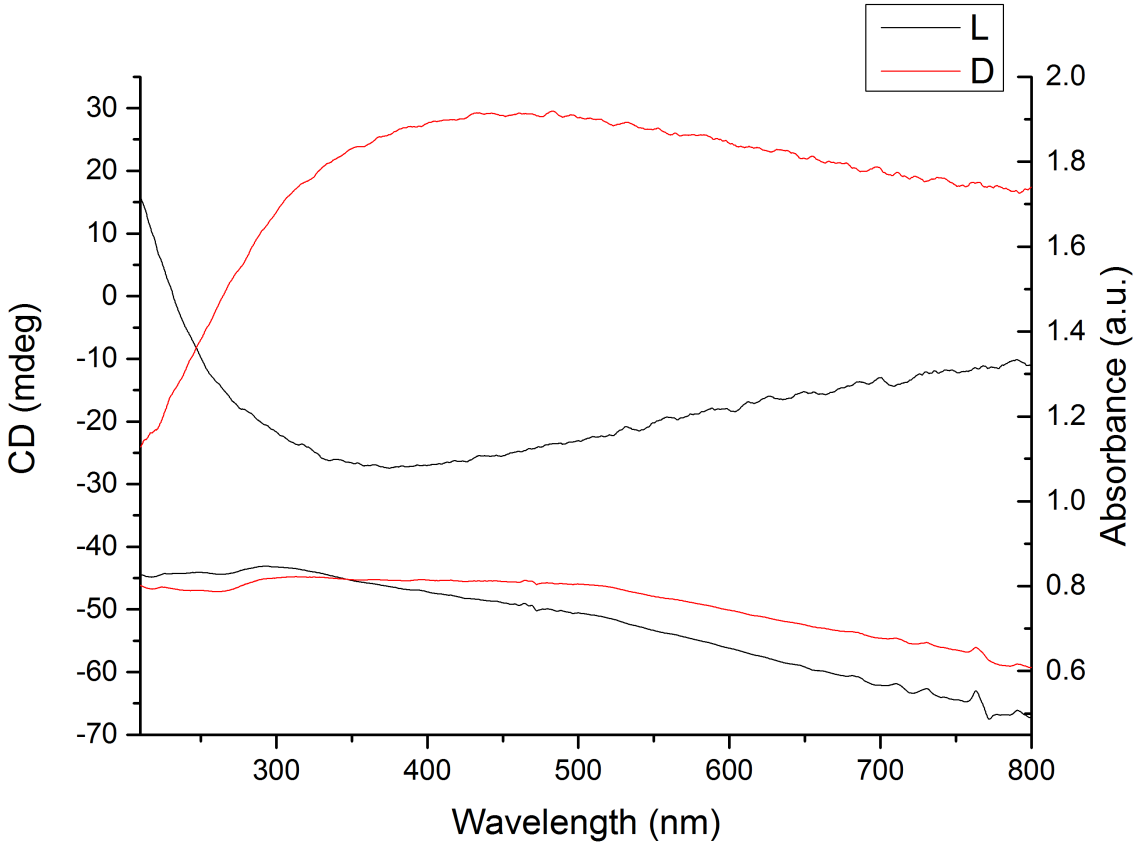

Figure 3.22: CD spectrum of *L*- and *D*- $CaCO_3$ helices

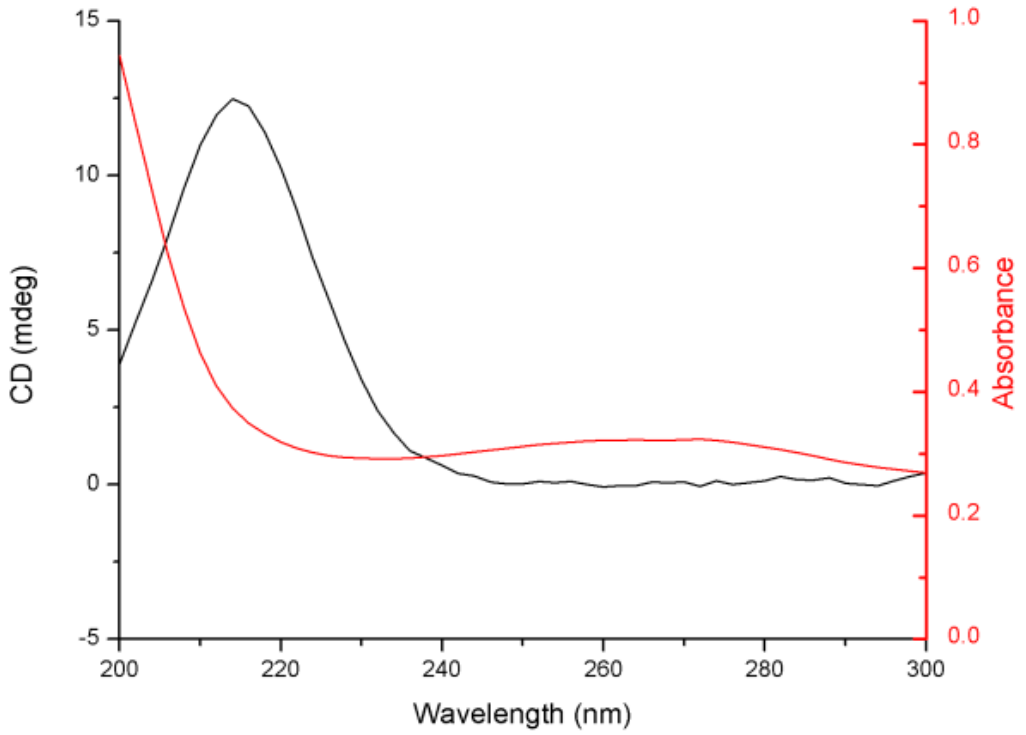

Figure 3.23: CD spectrum of 16-2-16 gemini *D*-tartrate

Finally, the helical $CaCO_3$ materials where characterised by XRD and, as with the $CaCO_3$ microspheres were confirmed to be calcite with no evidence of any other crystalline phases (Figure 3.24).

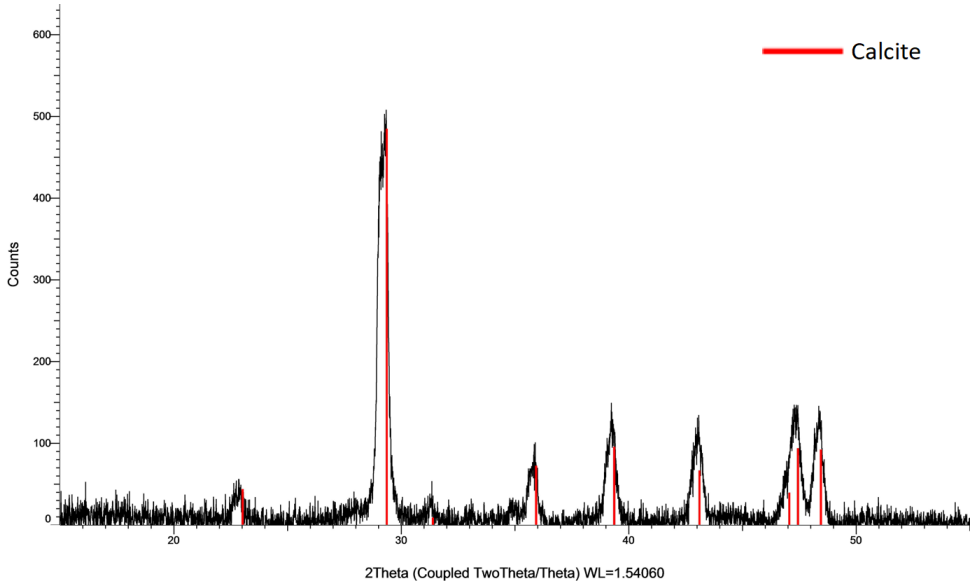

Figure 3.24: XRD pattern of *D*- $CaCO_3$ helices

3.4 Conclusions

In summary, several novel chiral $CaCO_3$ based nano- and micro-structural materials have been synthesised. Initially, achiral $CaCO_3$ microspheres were synthesised using a modified published procedure. Their subsequent functionalisation with amino acids imparted a chiral signal to these structures for the first time. The chiral signal itself presents a significant research interest, as its extension to the higher wavelengths seems to point to a type of 'chiral scattering' or 'chiral complexation' whereby the amino acid is bonded to $CaCO_3$ in a manner which restricts its conformational freedom, thus preventing the onset of any Cotton effects in the spectrum. Using this observation, the occurrence of chiral encapsulation can be determined using CD spectroscopy.

These microspheres have subsequently been used to encapsulate various luminescent and plasmonic materials. The encapsulation of CdSe@ZnS/ZnS and CuInZnS@ZnS QDs imparted a green and red fluorescence respectively whilst Eu^{3+} was used to provide red phosphorescence. Plasmonic Au NPs were also encapsulated to provide a chiral plasmonic material which may have multiple potential optical applications.

Using template-directed synthetic techniques, $CaCO_3$ helices have been produced for the first time using 16-2-16 gemini-tartrates. This is notable as these materials are truly chiral (as opposed to being 'chiroptically active') and exhibit helical microscale chirality.

Future work in this area will involve the expansion of the multi-modal microspheres to include other chiral ligands and luminescent nanomaterials, as well as perhaps magnetic nanoparticles (MNPs) which could provide the possibility of adding imaging (e.g. MRI) or magnetic hyperthermia to the microspheres' potential applications.

Lanthanide doping of the $CaCO_3$ with a view to investigating the possibility of circularly polarised luminescence (CPL) is currently ongoing.

References

(1) D.-H. Kim, W. Li, J. Chen, Z. Zhang, R. M. Green, S. Huang and A. C. Larson, 2016, **6**, 29653.

(2) R. John, F. T. Nguyen, K. J. Kolbeck, E. J. Chaney, M. Marjanovic, K. S. Suslick and S. A. Boppart, *Molecular Imaging and Biology*, 2012, **14**, 17–24.

(3) G. B. Sukhorukov, D. V. Volodkin, A. M. Günther, A. I. Petrov, D. B. Shenoy and H. Möhwald, *J. Mater. Chem.*, 2004, **14**, 2073–2081.

(4) D. V. Volodkin, N. I. Larionova and G. B. Sukhorukov, *Biomacromolecules*, 2004, **5**, 1962–1972.

(5) Y. Wu, M. Chen, Y. Fang and W. Wang, *RSC Advances*, 2017, **7**, 9338–9346.

(6) L. Zhao and J. Wang, *Colloids and Surfaces A: Physicochemical and Engineering Aspects*, 2012, **393**, 139–143.

(7) F. Zsila, Z. Bikádi and M. Simonyi, *Tetrahedron: Asymmetry*, 2003, **14**, 2433–2444.

(8) T. H. Loeber, B. Laegel, S. Wolff, S. Schuff, F. Balle, T. Beck, D. Eifler, J. H. Fitschen and G. Steidl, *Journal of Vacuum Science & Technology B*, 2017, **35**, 06GK01.

(9) F. Donnelly, F. Purcell-Milton, P. Dunne, A. Rulikowska, V. Alguacil and Y. Gun'ko, *Materials Today Communications*, 2019, **20**, DOI: `10.1016/j.mtcomm.2019.100590`.

(10) V Blanco-Gutierrez, A Demourgues, V Jubera and M Gaudon, *J. Mater. Chem. C*, 2014, **2**, 9969–9977.

(11) L. J. Brennan, F. Purcell-Milton, B. McKenna, T. M. Watson, Y. K. Gun'ko and R. C. Evans, *J. Mater. Chem. A*, 2018, **6**, 2671–2680.

(12) M. F. M. and K. J. S., *Angewandte Chemie International Edition*, 2000, **39**, 1906–1920.

(13) R. Oda, I. Huc and S. J. Candau, *Angewandte Chemie International Edition*, 1998, **37**, 2689–2691.

(14) T. Delclos, C. Aime, E. Pouget, A. Brizard, I. Huc, M.-H. Delville and R. Oda, 2008, **8**, 1929–1935.

(15) Y. Okazaki, N. Ryu, T. Buffeteau, S. Pathan, S. Nagaoka, E. Pouget, S. Nlate, H. Ihara and R. Oda, *Chem. Commun.*, 2018, **54**, 10244–10247.

(16) N. Ryu, Y. Okazaki, K. Hirai, M. Takafuji, S. Nagaoka, E. Pouget, H. Ihara and R. Oda, *Chemical Communications*, 2016, **52**, 5800–5803.

Chapter 4

Synthesis of $CaCO_3$ Microspheres for Potential Applications in Drug Delivery

4.1 Introduction

Calcium carbonate has a range of various existing and potential biomedical applications. For example, its excellent biocompatibility allows its current uses in antacid tablets, as calcium supplements, in bone regeneration and as drug delivery systems.[1–5] The use of various micro- and nanomaterials in targeted drug delivery systems has proven effective in previous studies.[6–8] These targeted systems increase the therapeutic window by delivering more of the drug to the target site, thus reducing the minimum effective dose and any latent side effects related to its toxicity.[9] It is important to consider that therapeutic agents in high dosages can lead to oxidative stress which has been linked with illnesses such as Obsessive-Compulsive Disorder (OCD), depression[10] and Alzheimer's disease.[11]

As of yet, however, the use of diffusion-based $CaCO_3$ drug delivery systems is relatively unexplored. While anti-cancer drugs such as cis-platin or carboplatin can be released using a pH-dependent approach, nonsteroidal anti-inflammatory drugs (NSAIDs) like Ibuprofen (see Figure 4.1) require a porous support system to allow their release, and are therefore typically used in combination with nanocomposite matrices.[12]

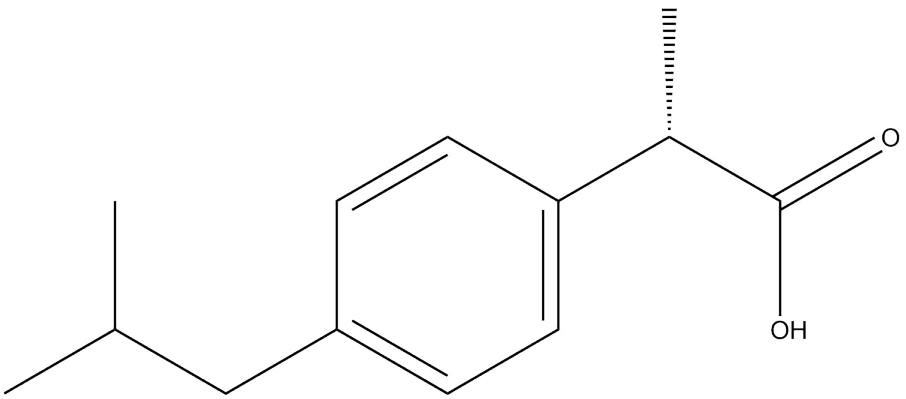

Figure 4.1: *S*-Ibuprofen: A commonly used NSAID

An NSAID such as ibuprofen is considered suitable for this work for various reasons. A short biological half life of two hours facilitates its study for sustained drug release while its size makes it readily available for inclusion in, and release from, the pores of mesoporous calcium carbonate.[13] The *S*-enantiomer of ibuprofen is shown in Figure 4.1 as this is the biologically active form. The *R*-enantiomer also readily undergoes 'metabolic inversion' to its *R*- counterpart.[14]

4.2 Aims

The main aim of this area of work is to develop the synthesis of NSAID-loaded $CaCO_3$ microspheres using various approaches. Specifically, the microspheres are to be synthesised by the aforementioned template-based synthesis and subsequently two microemulsion methods: a reverse (water-in-oil (W/O)) and a double (water-in-oil-in-water (W/O/W)) microemulsion. The microspheres formed will be examined by electron microscopy to determine morphology and monodispersity, x-ray diffraction for polymorphic discrimination and finally FT-IR spectroscopy and DTA-TGA to determine the presence of the NSAID.

4.3 Results and Discussion

4.3.1 Template-Directed Synthesis of $CaCO_3$ Microspheres for Drug Delivery

As detailed previously, the modified template-based approach has been highly successful for the preparation of encapsulating agents. To this end, the loading of monodispersed $CaCO_3$ microspheres with ibuprofen has been attempted. In order to achieve this, *S*-IBU was added, along with SDS and PVP, to the Na_2CO_3 solution. There are two possibilities here: firstly, Na_2CO_3 is a base and could therefore increase the solubility of *S*-IBU (which is itself a weak acid) to a point of relative stability within the solution. The second possibility is that, due to its poor solubility in water, *S*-IBU could potentially be adsorbed in the organic inner region of the micelles. Finally, the $CaCO_3$ microspheres with encapsulated *S*-IBU are then prepared by the direct precipitation reaction involving the addition of the $CaCl_2$ and Na_2CO_3 solutions.

The SEM image of the microspheres formed via this method is shown in Figure 4.2. From this image it can be observed that the microspheres possess a polycrystalline and porous morphology. The SEM image also clearly shows the formation of two different populations of microspheres with the size distribution histogram (Figure 4.3) used to determine that they have a mean diameter of 4.09 $\pm$ 0.51 μm and 1.94 $\pm$ 0.42 μm, respectively. This is of course not ideal for drug delivery as the different sizes of microspheres will likely lead to two different loading levels, and therefore release profiles, of *S*-IBU.

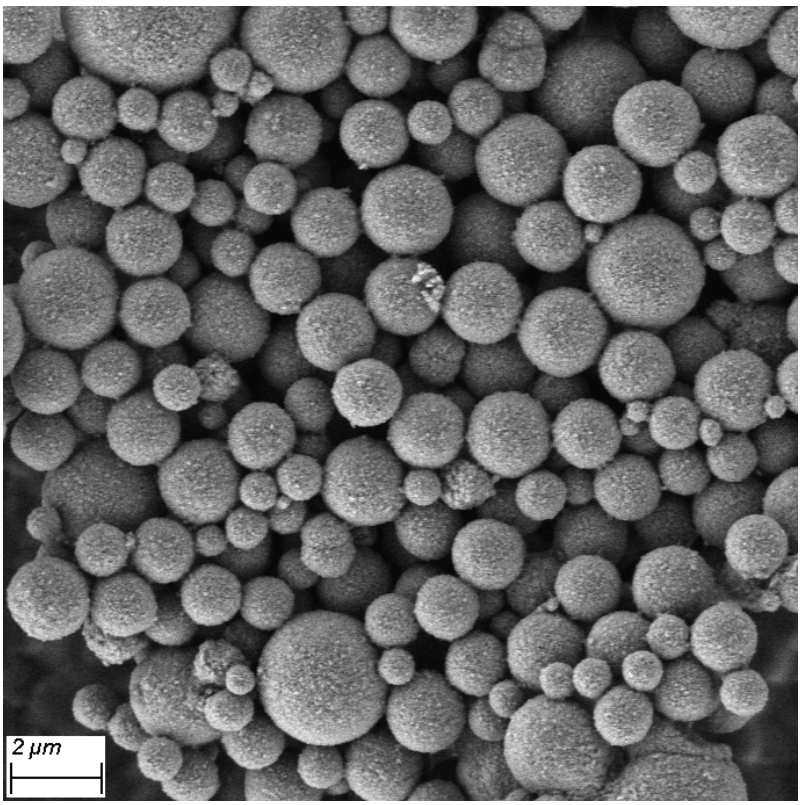

Figure 4.2: SEM image of $CaCO_3$ microspheres formed via a template-directed synthesis

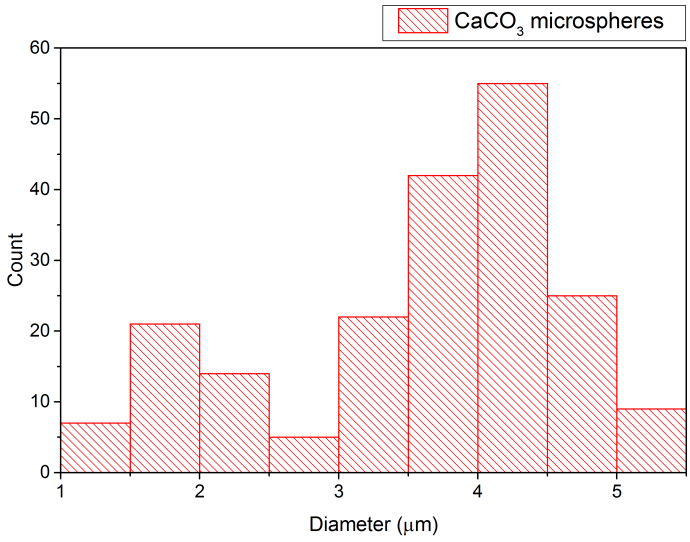

Figure 4.3: Size distribution histogram of the microspheres formed via the template-directed synthesis showing two populations of microspheres with mean diameters of 4.09 ± 0.51 μm ($N = 153$) and 1.94 ± 0.42 μm ($N = 47$), respectively

X-ray diffraction analysis was carried out on the microspheres and presented the characteristic pattern of calcite (Figure 4.4), illustrating that the microspheres formed are composed of predominantly calcite with some small vateritic peaks and are also highly crystalline.

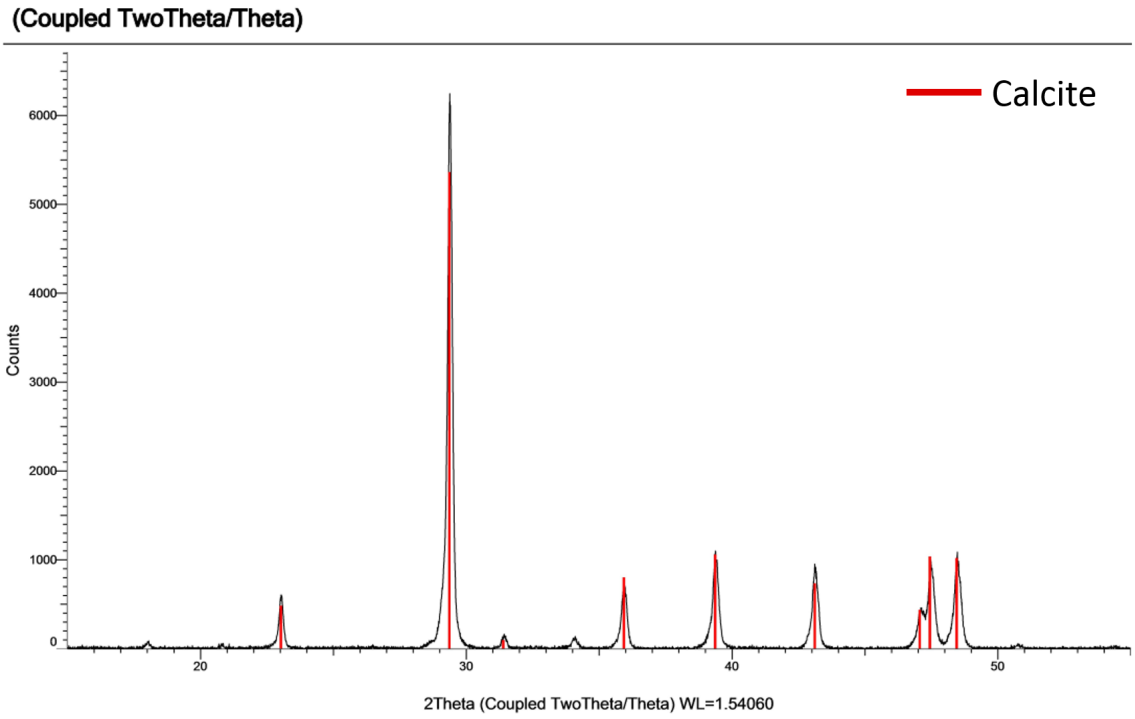

Figure 4.4: XRD pattern of *S*-IBU loaded $CaCO_3$ microspheres prepared via a template-directed synthesis. The characteristic pattern of calcite is illustrated as red lines

FT-IR was used to determine the presence of *S*-IBU in the microspheres and is shown in Figure 4.5. The characteristic spectra of the bare microspheres and pure ibuprofen are presented above and below the loaded microspheres, respectively. The peak at 1700 cm^{-1} is assigned to the carboxylic group of *S*-IBU. The fact that this is not present in the loaded microspheres would imply that *S*-IBU binds to the calcium ion through this group which, again, is to be expected due to the oxophilicity of calcium. While this is an encouraging result, there is quite some room for refinement

of the loading procedure and indeed microsphere synthesis. For this reason, it was decided that a microemulsion method could provide an additional layer of control over the loading procedure.

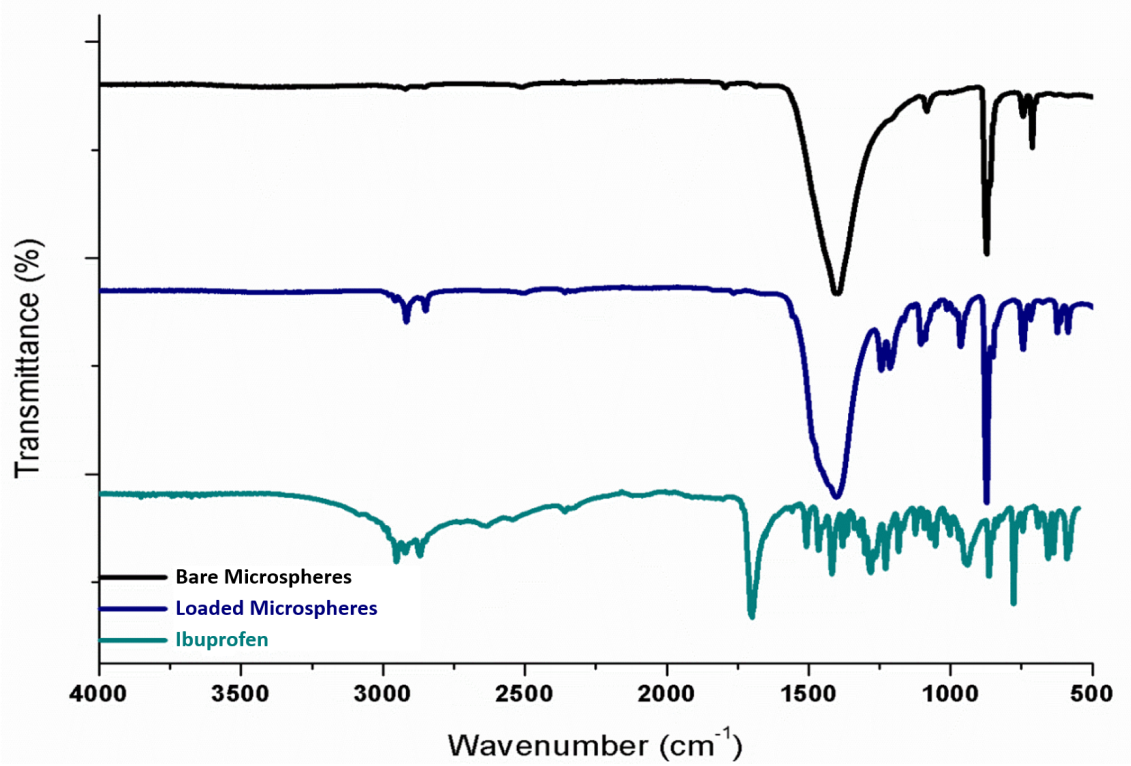

Figure 4.5: FT-IR spectra of bare $CaCO_3$ microspheres, *S*-IBU loaded microspheres formed via template-directed synthesis, and free *S*-IBU

4.3.2 Reverse (W/O) Microemulsion Synthesis of $CaCO_3$ Microspheres

A reverse (W/O) microemulsion involves the utilisation of water droplets in an organic medium as 'nanoreactors' as illustrated in in Figure 4.6. The initial aqueous phase in this work contained both the Ca^{2+} and *S*-IBU relying on the oxophilicity of calcium. Once the W/O microemulsion is formed, an aqueous solution including

the CO_3^{2-} was added. In this manner, the two aqueous phases are mixed in the organic medium until they come into contact with each other wherein precipitation occurs immediately leading to the encapsulation of the drug within the microsphere.

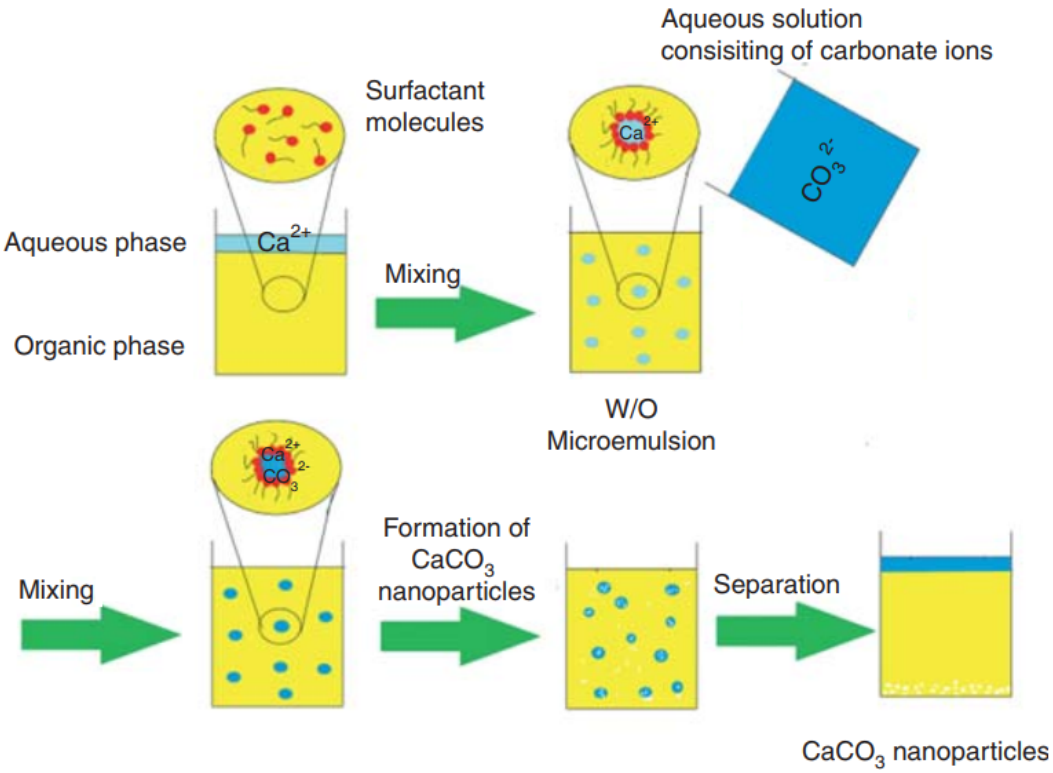

Figure 4.6: A schematic representation illustrating the synthesis of $CaCO_3$ by a reverse (W/O) microemulsion. Adapted from ref[2]

SEM images (Figures 4.7a and 4.7b) have shown the successful formation of the microspheres while the size distribution analysis (Figure 4.8) provides an average diameter of 1.15 ± 0.23 μm. This represents a high degree of monodispersity and a marked improvement upon the microsphere production via the template-driven synthesis. Powder X-ray diffraction analysis showed that the microspheres are highly crystalline and consist of predominantly calcite with some minor traces of vaterite as shown below (Figure 4.9).

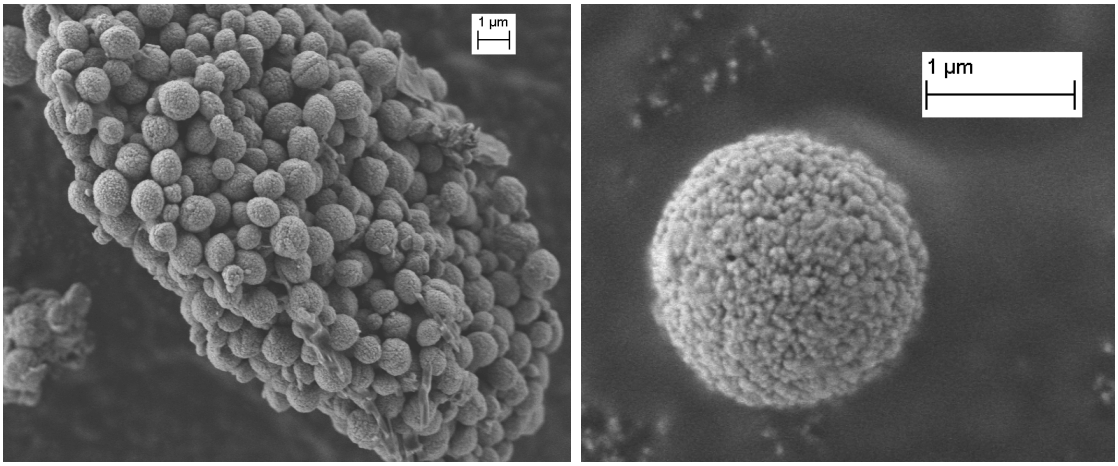

Figure 4.7: SEM images of *S*-IBU loaded microspheres produced via a reverse (W/O) microemulsion method

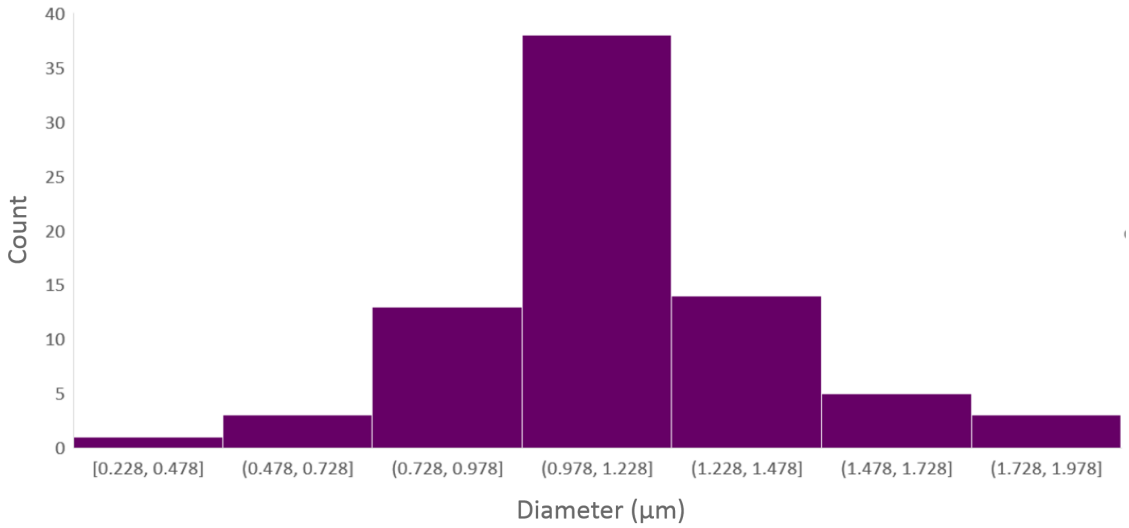

Figure 4.8: A histogram illustrating the size distribution of *S*-IBU loaded $CaCO_3$ microspheres formed via a reverse (W/O) microemulsion, ($N = 80$)

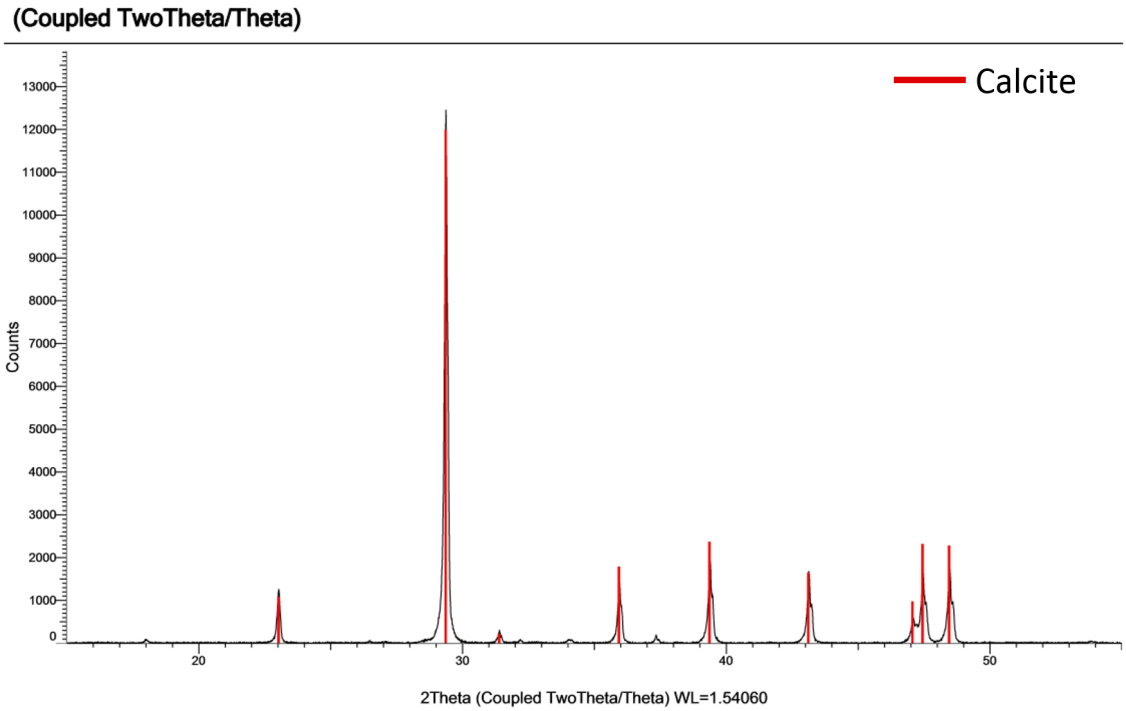

Figure 4.9: XRD pattern of *S*-IBU loaded $CaCO_3$ microspheres prepared via a reverse (W/O) microemulsion method. The characteristic pattern of calcite is illustrated as red lines

As with the previous encapsulation method, the successful loading with *S*-IBU was proven with FT-IR spectroscopy (Figure 4.10). The FT-IR spectrum obtained was used to show the associated organic functional groups of *S*-IBU within the microspheres. Once again, the lack of a sharp peak at 1700 cm^{-1} indicates the *S*-IBU is bound to calcium via the carbonyl group.

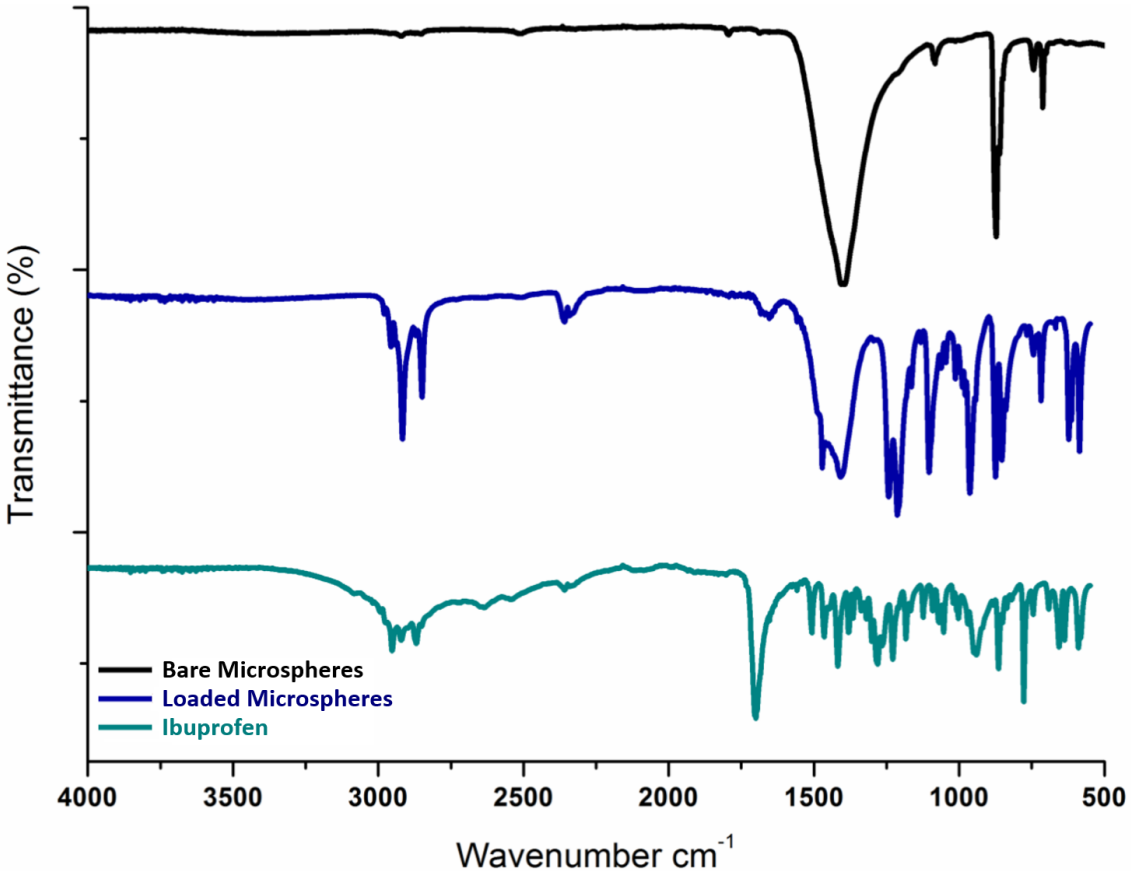

Figure 4.10: FT-IR spectra of bare $CaCO_3$ microspheres, *S*-IBU loaded $CaCO_3$ microspheres formed via a reverse (W/O) microemulsion, and free *S*-IBU

DTA-TGA was used in an attempt to quantify drug loading on the microspheres (in terms of weight %). TGA was used to show overall weight loss as well as phenomena such as absorption or desorption, while DTA will show endothermic, or exothermic processes e.g. combustion or crystallisation. Figure 4.11 presents the thermal decomposition curves of the drug-delivery vesicles under an inert N_2 atmosphere.

The TGA curve shows three main regions of weight loss: between 100 and 200 °C, 220 to 700 °C and 780 to 825 °C. The first region is due to a loss of adsorbed water, the second represents the decomposition of *S*-IBU, while the third is the calcination of $CaCO_3$ to CaO. The DTA analysis shows the removal of adsorbed water represented by an exothermic peak at 150 °C, followed by the combustion of *S*-IBU with

two exothermic peaks at c. 200-400 °C and 520 °C. The large endotherm at 820 °C again represents the calcination of $CaCO_3$ to CaO. The TGA analysis shows that 80 % of the overall weight remains above 700 °C, which implies that the *S*-IBU loading was approximately 20 wt%.

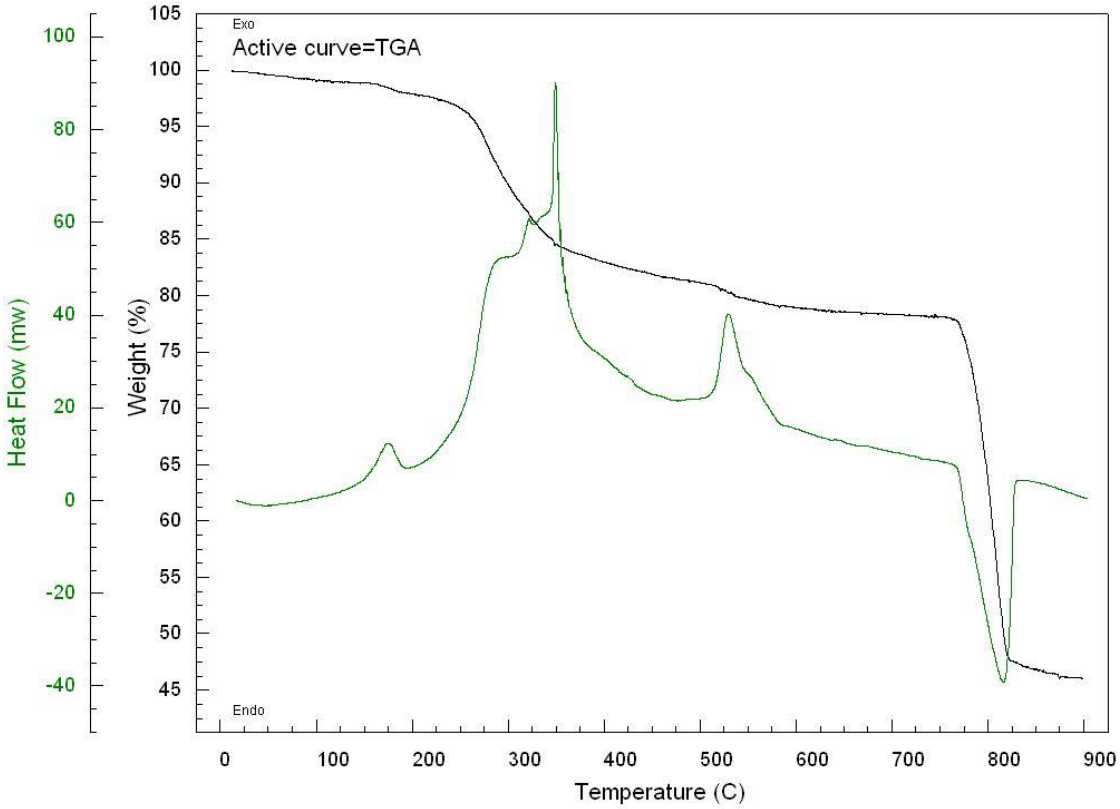

Figure 4.11: DTA-TGA Analysis of *S*-IBU loaded $CaCO_3$ microspheres. DTA is illustrated as a green line while the black line represents the TGA curve

Having achieved the production of monodispersed microspheres through two different methods, it was decided that a double or water-in-oil-in-water (W/O/W) microemulsion could be used in order to produce some interesting microspheres. This extra layer which is unique to these types of microemulsions could offer a further layer of control over the product formed, as well as possibly having an effect on the morphology formed.

4.3.3 Double (W/O/W) Microemulsion Synthesis of $CaCO_3$ Microspheres

Finally, a double (W/O/W) microemulsion was prepared according to the scheme in Figure 4.12. Briefly, as previously detailed, an aqueous phase containing the Ca^{2+} along with *S*-IBU was added dropwise to an organic phase and allowed to stir. This W/O microemulsion was subsequently added to an external aqueous phase containing the CO_3^{2-}.

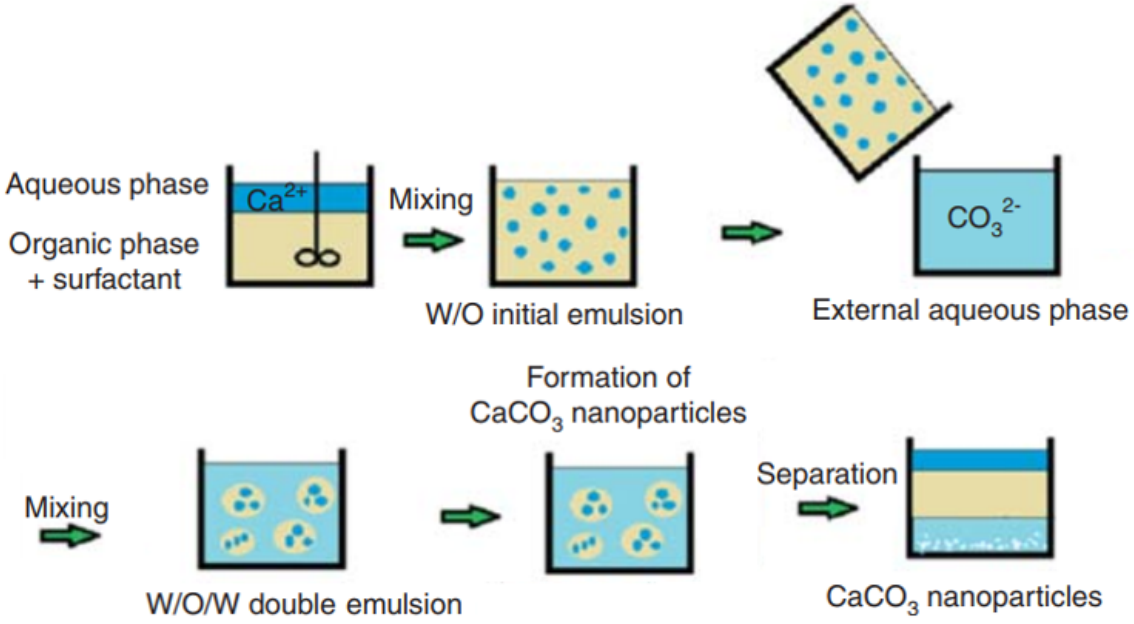

Figure 4.12: A simple scheme illustrating the synthesis of $CaCO_3$ via a double (W/O/W) microemulsion. Adapted from ref[2]

The microspheres formed are presented in the SEM images in Figures 4.13a and 4.13b. The microspheres have a novel morphology with rhombohedral particles crystallising on the surface of the microsphere. This unusual morphology likely occurs as a result of the double (W/O/W) microemulsion where the inner organic layer allows the formation of hollow microspheres whereas the crystallisation on the surface is allowed to complete in a straightforward manner i.e. the Ca^{2+} and CO_3^{2-} forming rhombohedral calcite (as detailed in the XRD pattern, Figure 4.14).

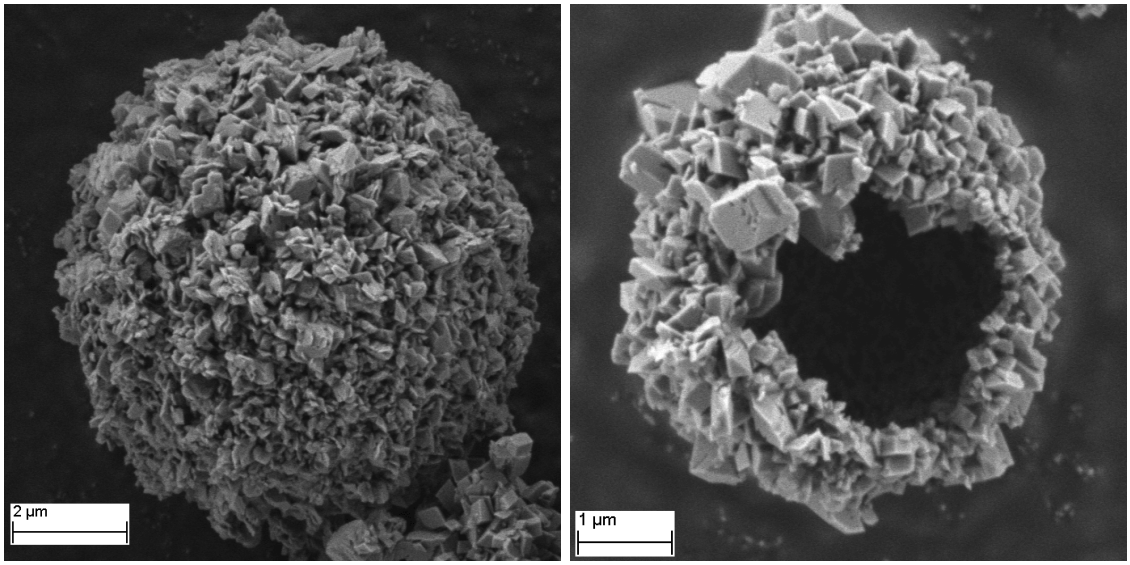

Figure 4.13: SEM images of *S*-IBU loaded microspheres produced via a double (W/O/W) microemulsion method

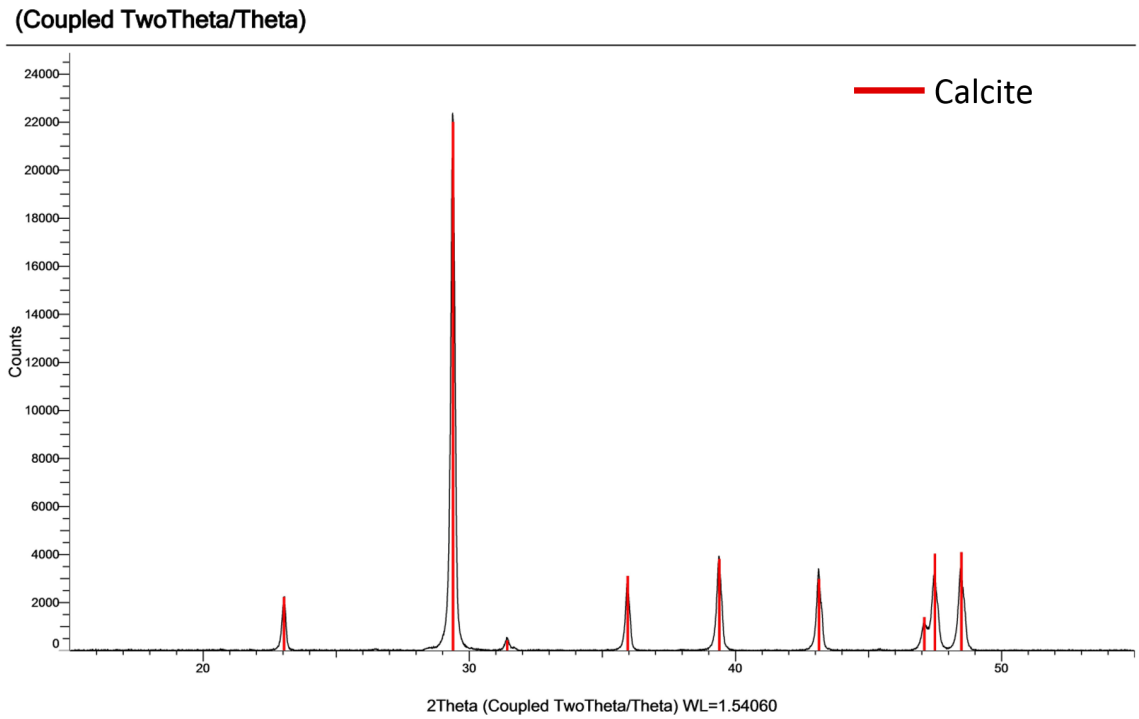

Figure 4.14: XRD pattern of *S*-IBU loaded $CaCO_3$ microspheres prepared via a double (W/O/W) microemulsion method. The characteristic pattern of calcite is illustrated as red lines

The histogram in Figure 4.15 illustrates that the microspheres formed posses a mean diameter of 3.4 ± 0.7 μm showing a good level of monodispersity. FT-IR was again employed to determine the presence of *S*-IBU, as shown in Figure 4.16, and showed the same spectrum of *S*-IBU as the previous two synthetic methods.

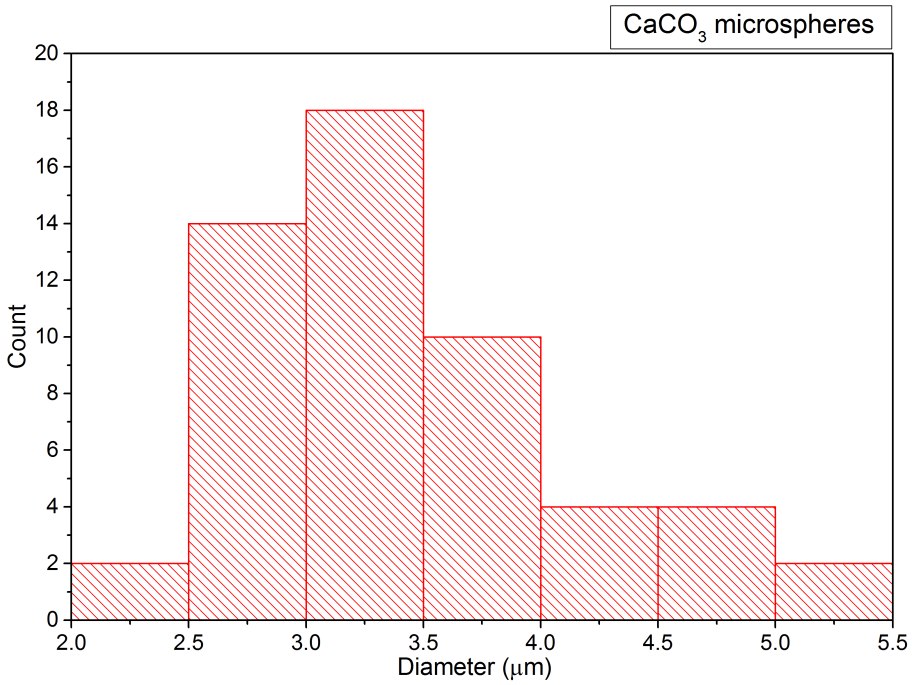

Figure 4.15: A histogram illustrating the size distribution of *S*-IBU loaded $CaCO_3$ microspheres formed via a double (W/O/W) microemulsion, ($N = 80$)

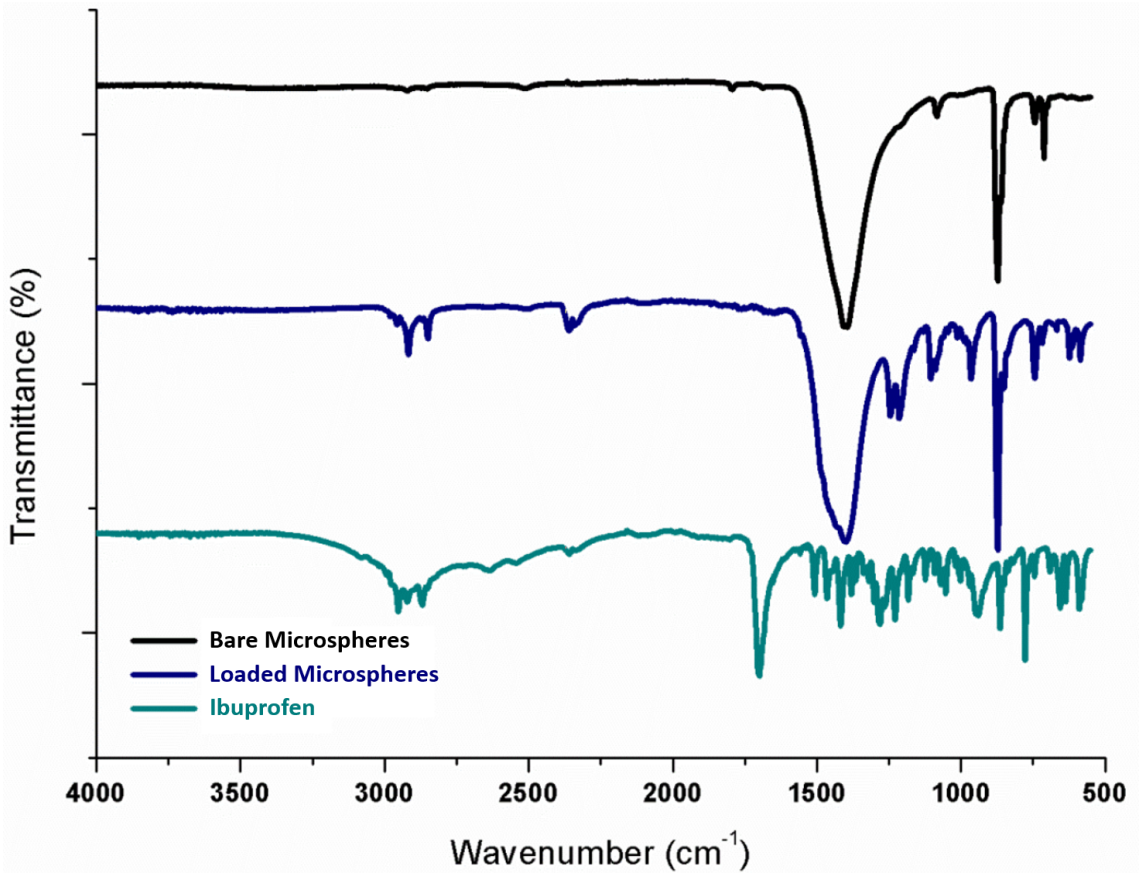

Figure 4.16: FT-IR spectra of bare $CaCO_3$ microspheres, *S*-IBU loaded microspheres formed via a double (W/O/W) microemulsion, and free *S*-IBU

4.4 Conclusions

In conclusion, the synthesis of *S*-IBU-loaded $CaCO_3$ microspheres has been successfully achieved by three methods, namely a template-directed synthesis, reverse (W/O) microemulsion and finally a double (W/O/W) microemulsion, which have shown levels of *S*-IBU loading of up to 20 %. The materials formed have been analysed fully and in all cases show the formation of calcite microspheres, of high purity and with varying degrees of monodispersity. In terms of potential for use as drug delivery vesicles, the microspheres produced via the reverse (W/O) microemulsion are likely the most promising candidates owing to their monodispersity, porous structure and high loading percentage of ibuprofen. The microspheres formed via the W/O/W microemulsion were, in a morphological sense, the most interesting product forming a new type of hollow microsphere with a surface comprised of rhombohedral calcite particles.

The next step in this work is to carry out a controlled drug release study in an appropriate medium and while some preliminary experiments have, in fact, been carried out, it has proven difficult to properly measure and control the drug release. A number of factors must be taken into account when considering a diffusion controlled drug delivery system. Controlling the pore size of the synthesised microspheres seems essential in attaining an effective release profile and this work is currently ongoing.

References

(1) E. A. Genina, Y. I. Svenskaya, I. Y. Yanina, L. E. Dolotov, N. A. Navolokin, A. N. Bashkatov, G. S. Terentyuk, A. B. Bucharskaya, G. N. Maslyakova, D. A. Gorin, V. V. Tuchin and G. B. Sukhorukov, *Biomed. Opt. Express*, 2016, **7**, 2082–2087.

(2) S. Maleki Dizaj, M. Barzegar-Jalali, M. H. Zarrintan, K. Adibkia and F. Lotfipour, *Expert Opinion on Drug Delivery*, 2015, **12**, 1649–1660.

(3) A. Som, R. Raliya, L. Tian, W. Akers, J. E. Ippolito, S. Singamaneni, P. Biswas and S. Achilefu, *Nanoscale*, 2016, **8**, 12639–12647.

(4) H.-D. Yu, Z.-Y. Zhang, K. Y. Win, J. Chan, S. H. Teoh and M.-Y. Han, *Chem. Commun.*, 2010, **46**, 6578–6580.

(5) D. Preisig, D. Haid, F. J. O. Varum, R. Bravo, R. Alles, J. Huwyler and M. Puchkov, *European Journal of Pharmaceutics and Biopharmaceutics*, 2014, **87**, 548–558.

(6) R. Singh and J. W. Lillard, *Experimental and molecular pathology*, 2009, **86**, 215–223.

(7) Z. Dong, L. Feng, Y. Hao, M. Chen, M. Gao, Y. Chao, H. Zhao, W. Zhu, J. Liu, C. Liang, Q. Zhang and Z. Liu, *Journal of the American Chemical Society*, 2018, **140**, 2165–2178.

(8) Y. Svenskaya, B. Parakhonskiy, A. Haase, V. Atkin, E. Lukyanets, D. Gorin and R. Antolini, *Biophysical Chemistry*, 2013, **182**, 11–15.

(9) J. Sudimack and R. J. Lee, *Advanced Drug Delivery Reviews*, 2000, **41**, 147–162.

(10) S. Kar and I. Choudhury, *International Journal of Nutrition, Pharmacology, Neurological Diseases*, 2016, **6**, 139–145.

(11) W.-J. Huang, X. Zhang and W.-W. Chen, *Biomedical Reports*, 2016, **4**, 519–522.

(12) Y. Zhao, L.-N. Lin, Y. Lu, S.-F. Chen, L. Dong and S.-H. Yu, *Advanced Materials*, 2010, **22**, 5255–5259.

(13) C. Wang, C. He, Z. Tong, X. Liu, B. Ren and F. Zeng, *International Journal of Pharmaceutics*, 2006, **308**, 160–167.

(14) T. S. Tracy and S. D. Hall, *Drug Metabolism and Disposition*, 1992, **20**, 322–327.

Chapter 5

Synthesis of $CaCO_3$ Nano- and Micro- Particles by Dry Ice Carbonation

5.1 Introduction

As mentioned previously, calcium carbonate exhibits the unusual property of retrograde, or inverse, solubility.[1] While the solubility of most materials increases with increasing temperature, $CaCO_3$ however, shows a decrease. This provides a significant barrier to the use of high temperature syntheses to produce novel $CaCO_3$ materials. $CaCO_3$ formation is an exothermic process and as such Le Chatelier's principle states that heating the system will shift the equilibrium towards the reactants. As such, the application of a low temperature synthesis provides the significant benefit of shifting the equilibrium towards the products.

As with $CaCO_3$, the solubility of CO_2 also decreases with increasing temperature[2] and therefore dry ice is used, not only as a source of CO_2, but also as a coolant for the system. The combination of increasing the solubility of both $CaCO_3$ and CO_2

will favour nucleation over growth, so that the calcium carbonate formed should exhibit high monodispersity and will likely be considerably smaller than that typically obtained from ambient or high temperature syntheses.

5.2 Aims

This chapter will detail the efforts made to develop, for the first time, a dry ice carbonation method for the synthesis of calcium carbonate nano- and micro-particles. There are no previous reports of dry ice synthesis of metal carbonates despite the favourability and promise of this approach, as discussed above. As such, it is intended to use this novel method to prepare new metal carbonate-based nanomaterials for the first time.

Specifically, the main aim of this work is to synthesise calcite and vaterite structures using dry ice carbonation. A study will then be carried out on the effect of various alcohol:water ratios on the product formed. The products formed are to be studied using electron microscopy, x-ray diffraction, and Raman spectroscopy.

5.3 Results and Discussion

5.3.1 Dry Ice Carbonation

This new synthetic approach, illustrated in Figure 5.1, involves the sequential addition of an excess of dry ice to a solution of CaO in water which is allowed to react over 60 minutes, as per experimental procedures (Chapter 2.3). In addition, the crystal phase formed can be preferentially controlled through the choice of solvent system. In order to produce calcite nanoparticles, water was the required solvent, whereas in the production of vaterite microspheres, a 75% v/v CH_3OH solution was used.

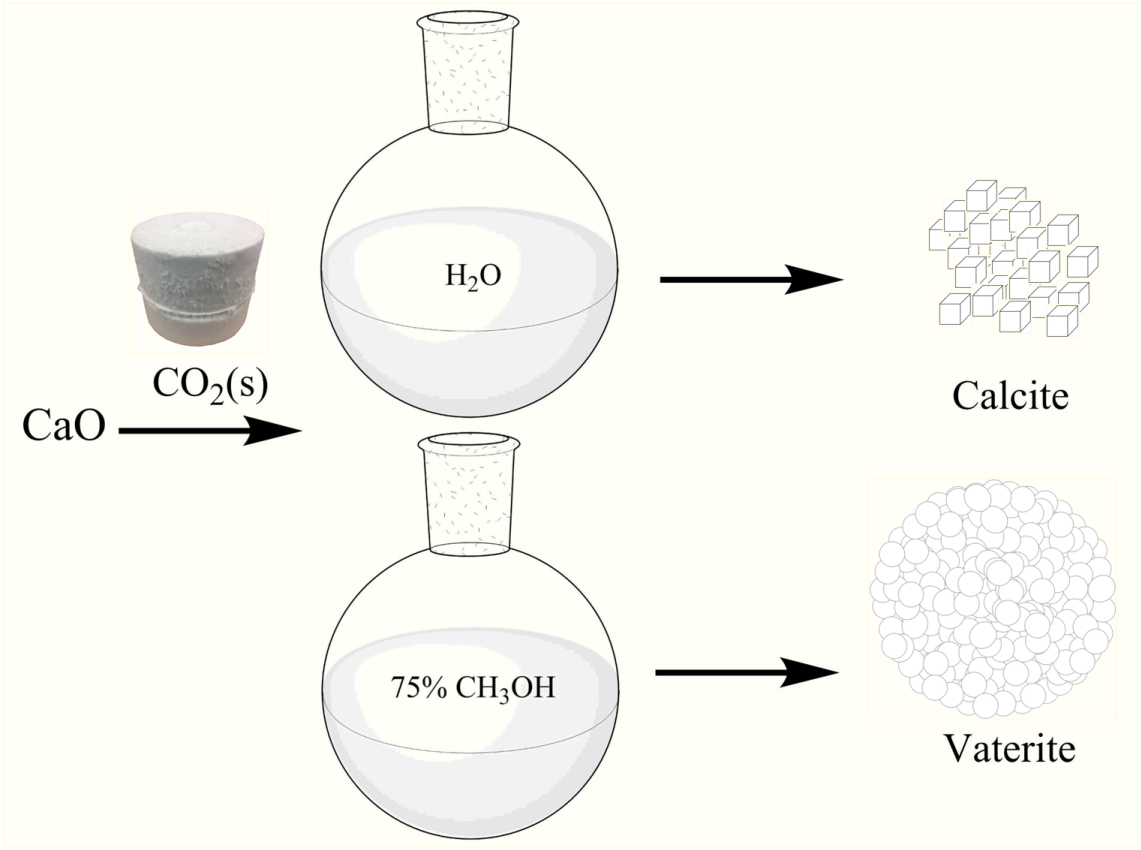

Figure 5.1: Schematic showing the process of dry ice carbonation. Specifically, the production of calcite nanoparticles or vaterite microspheres is controlled by the choice of solvent with water or 75% CH_3OH used, respectively

5.3.2 Synthesis of Calcite Nanoparticles

Calcite nanoparticles were synthesised using dry ice carbonation in Millipore water. The obtained diffraction pattern (Figure 5.2) is in good agreement with the characteristic patterns of calcite.[3] The pattern itself indicates phase purity and high crystallinity. The average crystallite size was determined to be 35 nm using the Scherrer equation and the FWHM of the peaks.

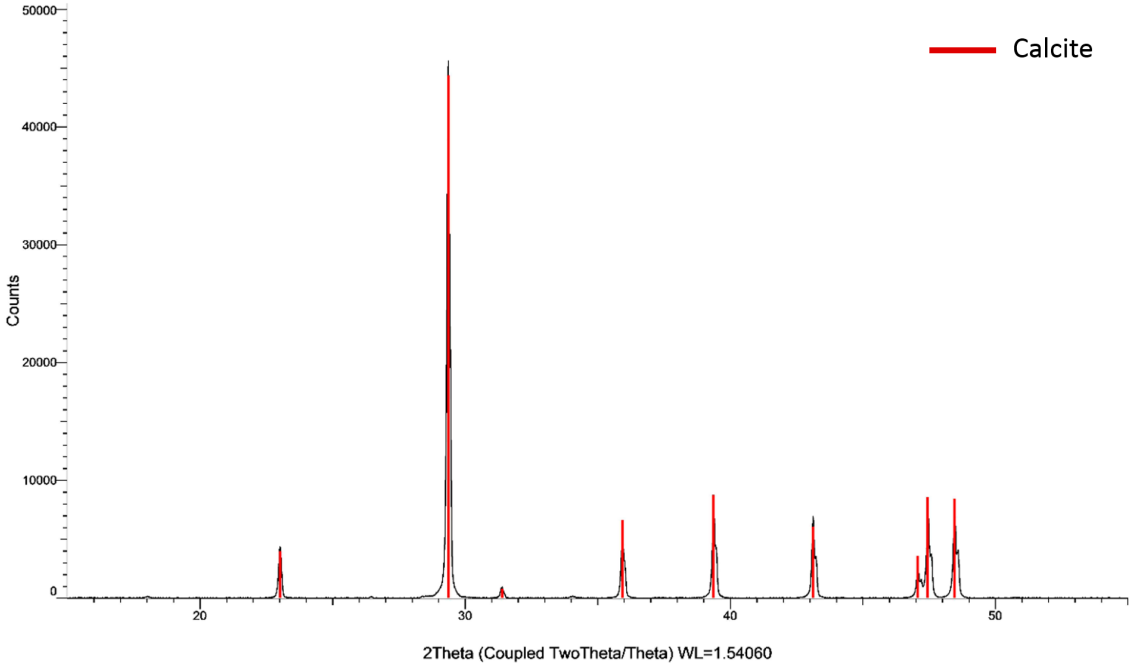

Figure 5.2: XRD pattern of dry ice carbonation carried out in pure Millipore water. The characteristic pattern of calcite is illustrated as red lines (R-3c, a=4.9844 Å, c=17.0376 Å)

Raman spectroscopy studies showed the characteristic peaks of calcite (Figure 5.3).[4] The singlet peak at 1085 cm^{-1} for calcite corresponds to the A_g internal mode that derives from the ν_1 symmetric stretching mode of the carbonate ion. The ν_4 in-plane bending mode of carbonate can be found at 712 cm^{-1}. Finally, the peaks below 300 cm^{-1} correspond to the translational and rotational lattice modes of calcite.

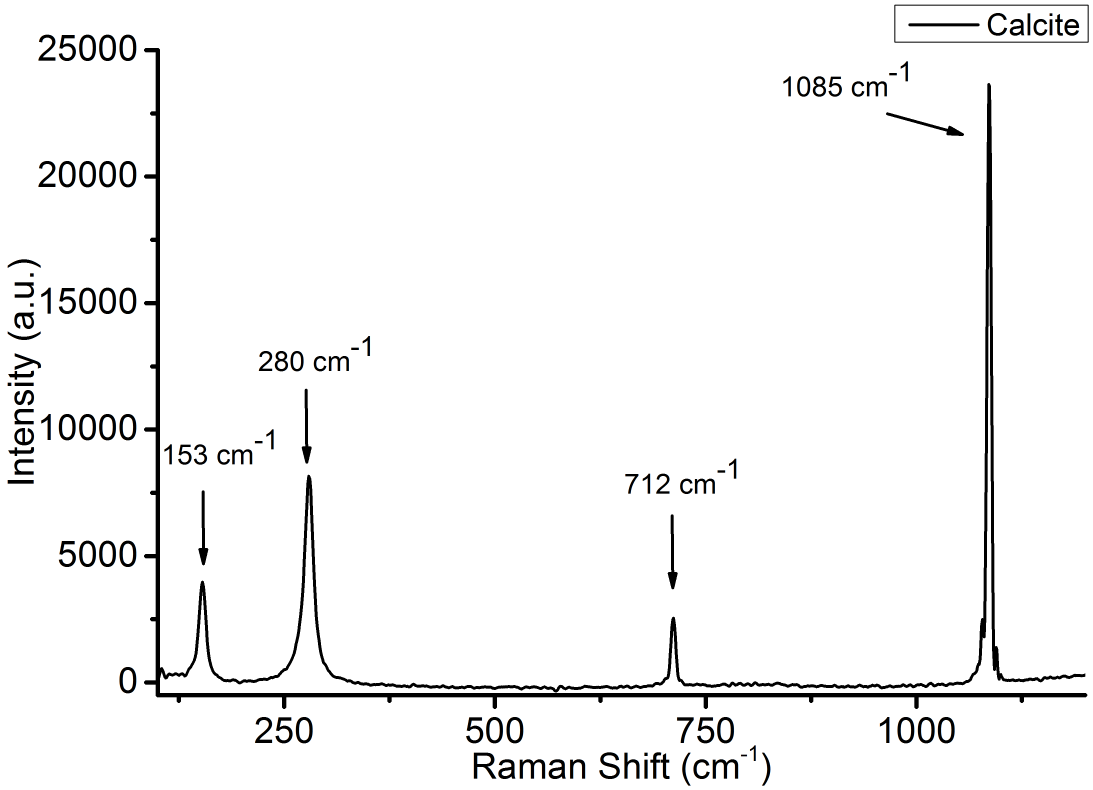

Figure 5.3: Raman spectrum of calcite

The particles formed are smaller than is typically achievable via standard carbonation. SEM (Figures 5.5 (A) and (B)) and TEM (Figure 5.5 (C) and (D)) images of the calcite samples show that the nanoparticles formed exhibit a faceted rhombohedral morphology. The mean diameter of these structures was determined to be 54.2 ± 11.2 nm (see Figure 5.4) which is in good agreement with the average crystallite size obtained from the XRD patterns (Figure 5.2 (A)), as well as showing a high degree of control in the distribution of particle size produced. HR-TEM imaging was also carried out (Figure 5.5 (E)), revealing lattice fringes, indicating that the nanoparticles possess a high degree of crystallinity. A select sample was subjected to dark field TEM imaging, as shown in Figure 5.5 (F). This clearly highlights the crystalline rhombohedral morphology of the calcite nanoparticles.

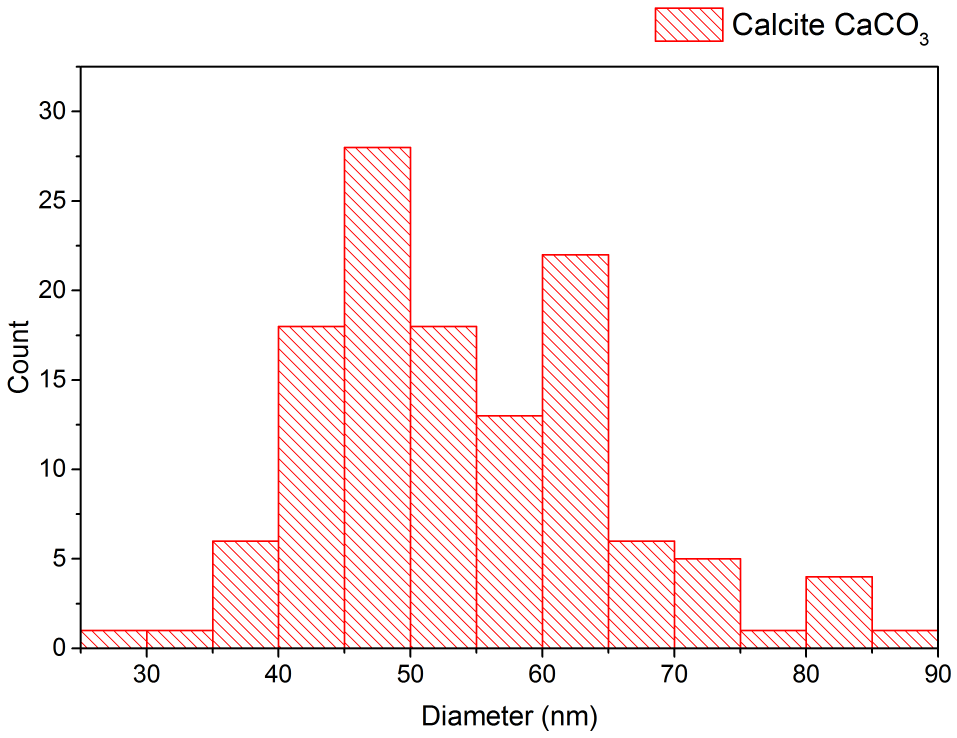

Figure 5.4: Size distribution of calcite nanoparticles obtained from measurement of TEM images, giving an average of diameter of 54.3 ± 11.2 nm (*N=125*)

The small size distribution of the calcite particles can be explained by the combination of retrograde solubility[5] and the low temperature synthesis provided by dry ice. The low temperature and subsequent high solubility of $CaCO_3$ tend towards a nucleation of the calcite seeds rather than a growth phase and therefore smaller and more monodispersed rhombohedral nanoparticles are formed.

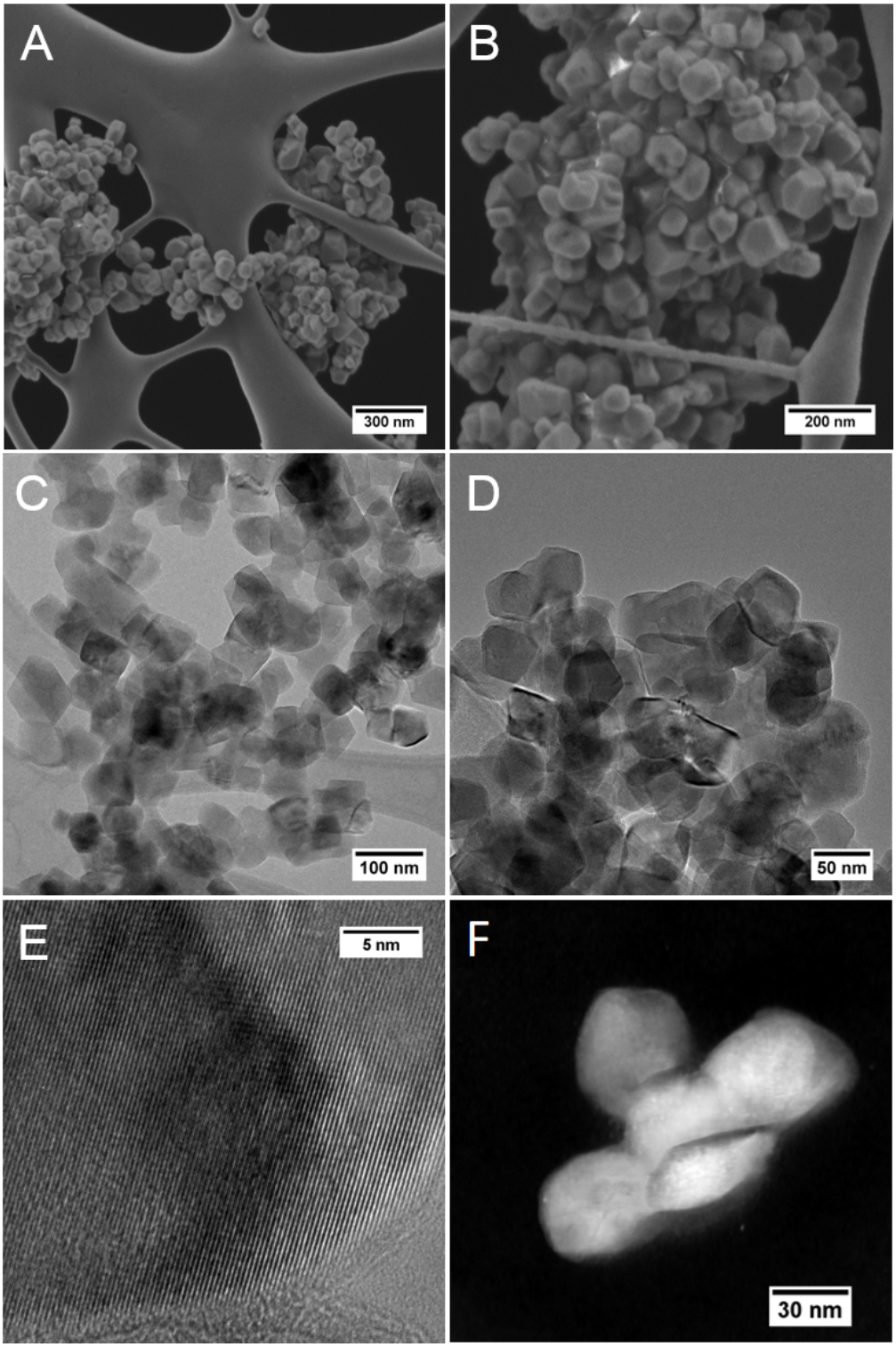

Figure 5.5: Electron microscopy images of calcite nanoparticles: (A) and (B) SEM images illustrating a facetted rhombohedral morphology, (C) and (D) TEM images of calcite, (E) calcite nanoparticles observed with HR-TEM and (F) dark field STEM

5.3.3 Synthesis of Vaterite Microspheres

Vaterite microspheres were synthesised via dry ice carbonation in a 75% CH_3OH solution. It has previously been shown that vaterite, which is typically a metastable polymorph, can be stabilised by certain additives including alcohols.[6] It has been proposed that this is due to a directly proportional increase in the solution supersaturation rate which preferences the kinetic product, vaterite, over the thermodynamically favoured calcite.[6–8]

As with calcite, XRD was used to determine the polymorph formed (Figure 5.6). The obtained diffraction pattern is, once again, in good agreement with the characteristic patterns of vaterite[9] and shows that vaterite predominates with minor peaks corresponding to calcite visible at 2θ of 29 ^{o} and 39 ^{o}. The average crystallite sizes for vaterite was calculated to be 19 nm using the Scherrer equation and the FWHM of the peaks. This is smaller than that of calcite and is explained by the fact that vaterite is, in fact, a polycrystalline microsphere, made up of many smaller crystallites.

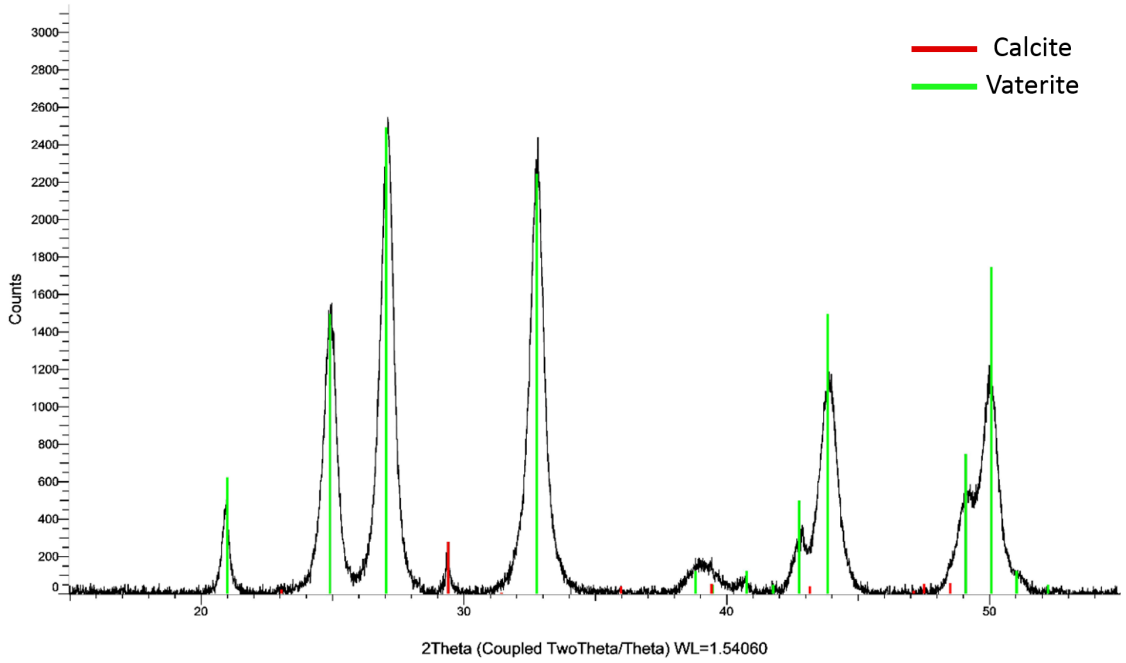

Figure 5.6: XRD pattern of dry ice carbonation carried out in a 75% v/v CH_3OH solution. The characteristic pattern of vaterite is illustrated as green lines (P 63/mmc, a=4.1300 Å c=8.4900 Å)

The Raman spectrum (Figure 5.7) again showed the characteristic peaks of vaterite.[4] The peaks at 1080 and 1090 cm^{-1} correspond to the A_g internal mode which, as previously detailed, derives from the ν_1 symmetric stretching mode of the carbonate ion. The ν_4 in-plane bending mode of the carbonate can be found at 739–749 cm^{-1}. Finally, as before, the peaks below 300 cm^{-1} correspond to the translational and rotational lattice modes of vaterite.

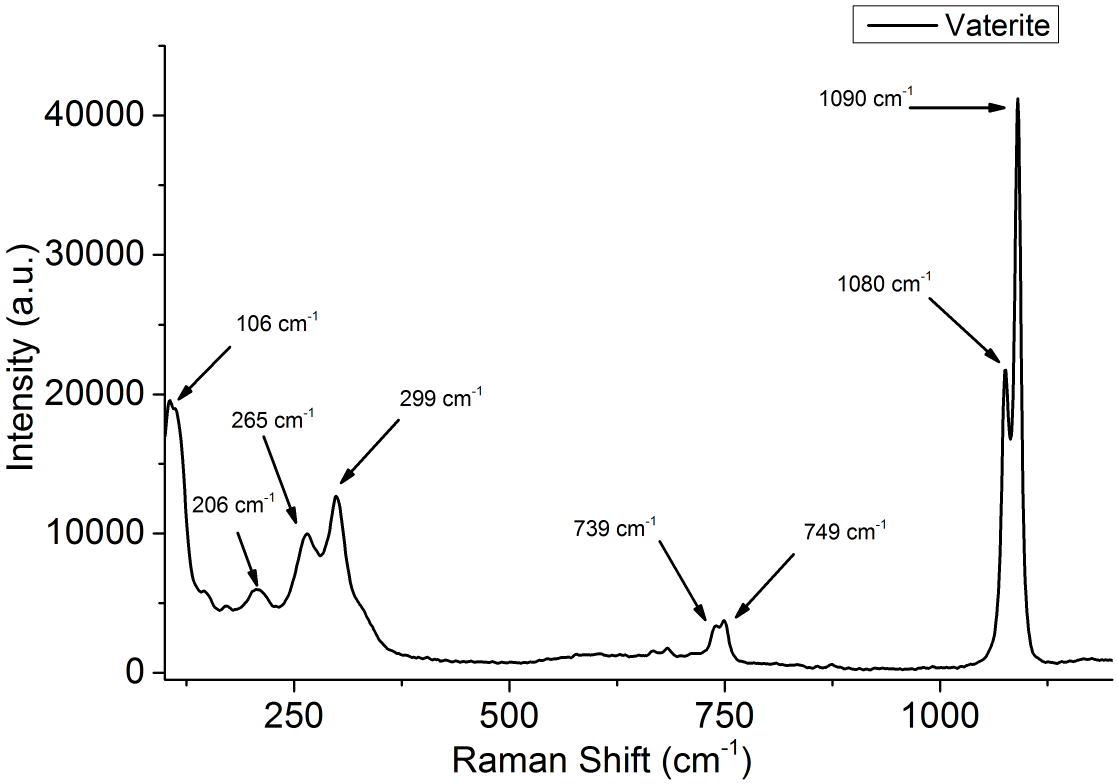

Figure 5.7: Raman spectrum of vaterite

SEM (Figure 5.8 (A) and (B)) and TEM (Figure 5.8 (C) and (D)) images of the vaterite particles revealed an oblong shape, measuring 628 ± 122 nm in length and 480 ± 100 nm in width (see Figure 5.9). These particles exhibit a narrow size distribution, but show a large difference in size relative to the calcite particles, and the calculated crystallite size by XRD, with dimensions differing by more than an order of magnitude. However, as mentioned, the vaterite microspheres are comprised of smaller (around 20 nm in diameter), fused nanocrystals, as can be clearly seen in the TEM image in Figure 5.8 (D). Thus, vaterite consists of aggregates of small nanosized crystallites. Such particles are likely to possess very high surface areas, and similar microsphere-like structures are very interesting and have found many applications as catalytic supports and carriers in drug-delivery.[10] Meanwhile, the preparation of vaterite microspheres specifically, in an innately inexpensive and easily scalable method, with a good level of monodispersity provides further development of these structures as potential drug delivery systems.[11–15]

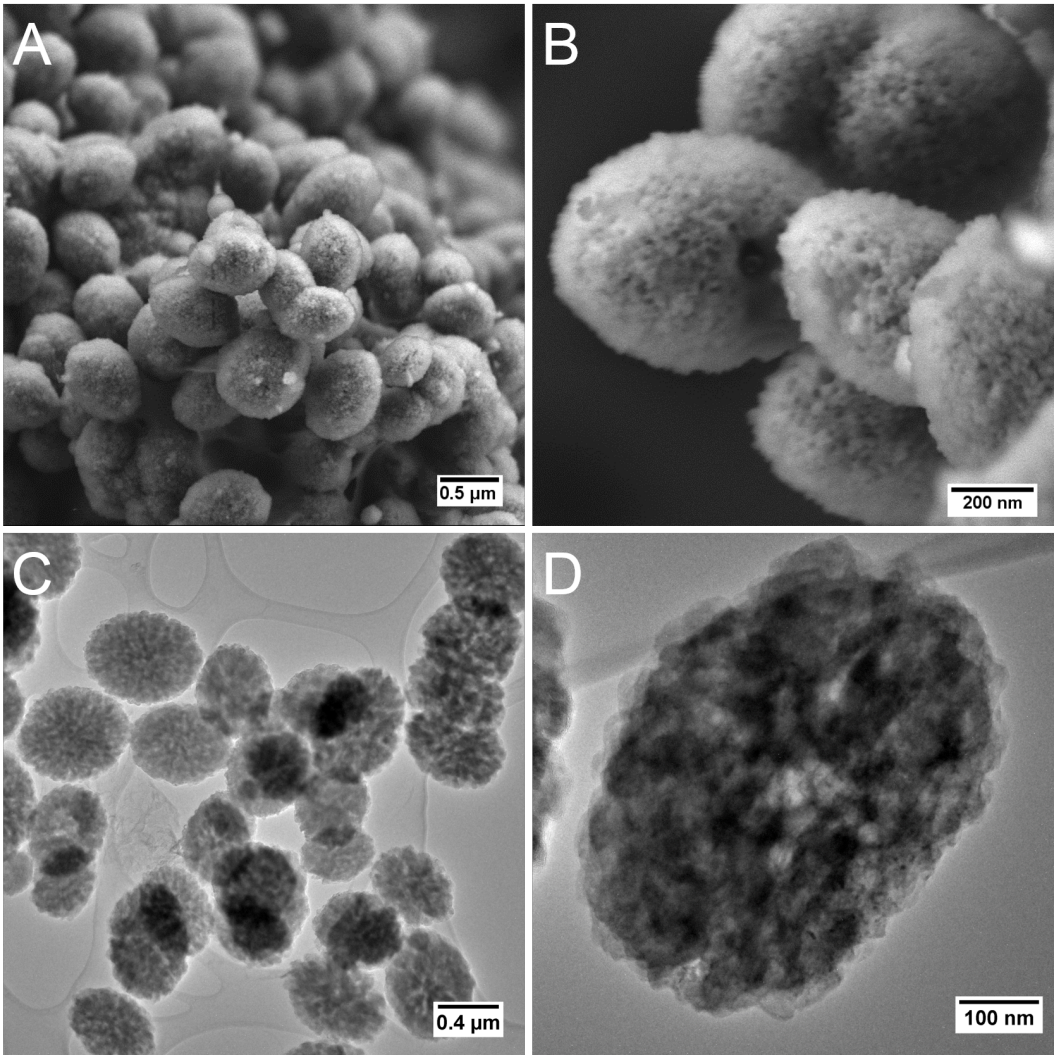

Figure 5.8: (A) and (B) SEM images of vaterite microspheres with an oblong morphology, (C) and (D) TEM images of vaterite illustrating polycrystallinity

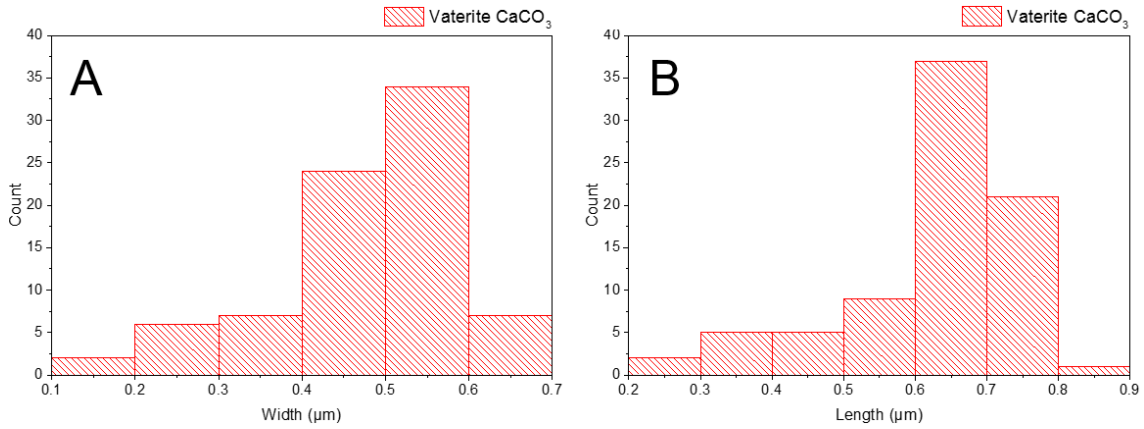

Figure 5.9: Size distribution of vaterite microspheres giving an average width (A) of 480 ± 108 nm (*N=80*) and length (B) of 627 ± 121 nm (*N=80*)

5.3.4 Effect of Varying Water-Alcohol Ratios

As mentioned previously, alcohols have been shown to stabilise the metastable vaterite phase.[16] In this way, a more in-depth analysis of the effect of varying the water-alcohol ratio was carried out for a variety of CH_3OH-H_2O solutions using dry ice carbonation. In pure water, phase pure calcite is formed (Figure 5.2). This is to be expected as there is no route by which the vaterite can be stabilised in this system. This observation is again confirmed when a 25% v/v CH_3OH solution was used (Figure 5.10). However, a small amount of vaterite begins to appear as the CH_3OH proportion of the solution was increased to 50% v/v (Figure 5.11). The most significant result was observed upon dry ice carbonation in a 75% v/v CH_3OH solution (as previously mentioned), which represents an almost complete stabilisation of the vaterite polymorph, which was evidenced by the obtained XRD pattern as shown earlier (Figure 5.6).

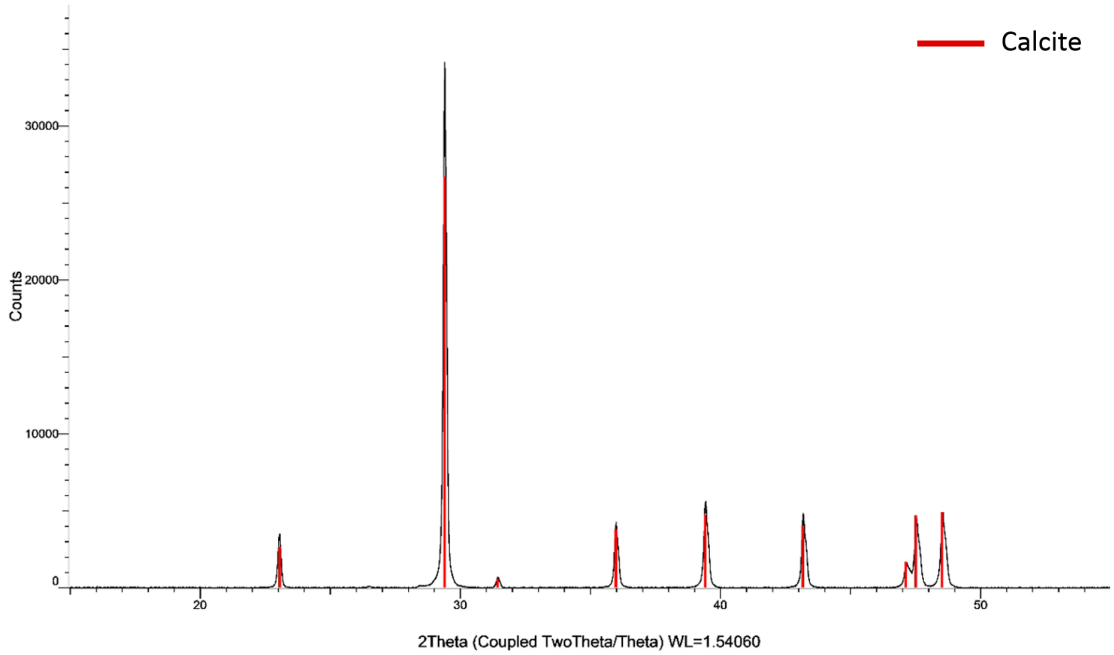

Figure 5.10: XRD pattern of dry ice carbonation carried out in 25% v/v CH_3OH solution

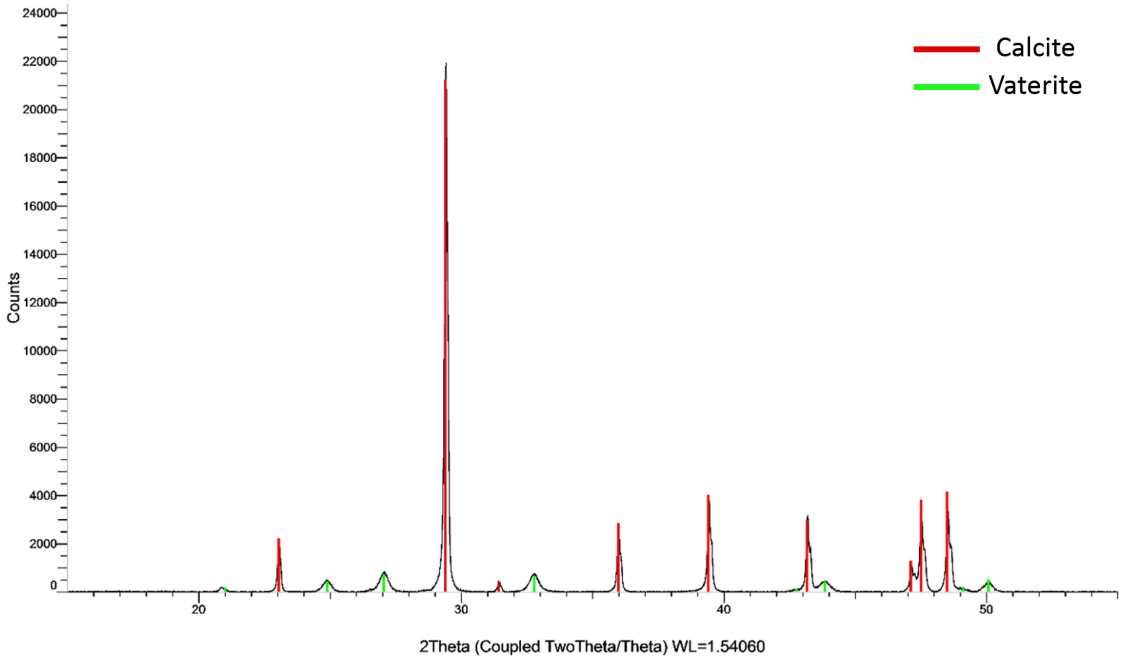

Figure 5.11: XRD pattern of dry ice carbonation carried out in a 50 % v/v CH_3OH solution

Finally, a study of pH versus time has been carried out for the various CH_3OH : H_2O ratios (Figure 5.12). These results have shown that the increase in the CH_3OH percentage of the solution leads to a faster rate of carbonation, which is in line with the higher solubility of CO_2 in CH_3OH. Once the solution reached 50 % v/v CH_3OH, the carbonation also led to the formation of a visible amorphous calcium carbonate (ACC) phase, which then transformed to vaterite or calcite (this was observed particularly at 10 and 20 minutes in 75% v/v CH_3OH (Figure 5.12)). It is worth noting that the additional alcohol content enabled a more rapid addition of dry ice due to a further depressed freezing point and this therefore reduced the time taken for complete carbonation.

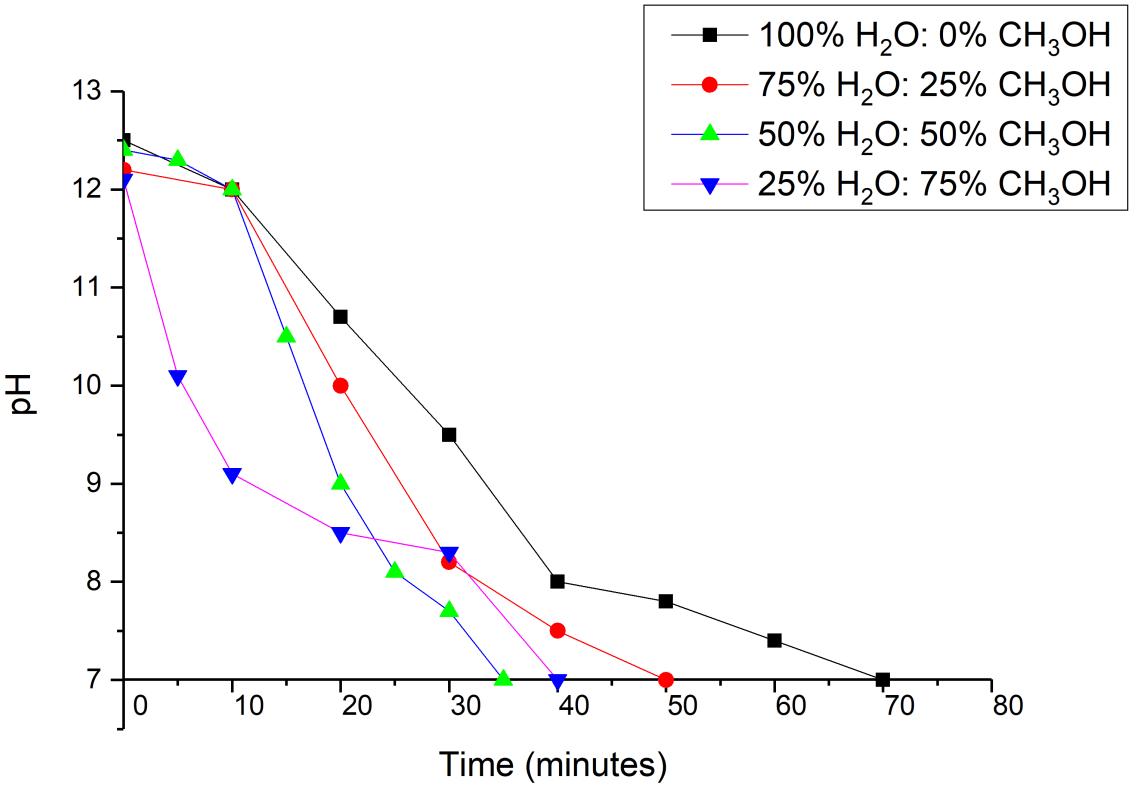

Figure 5.12: Graph of pH versus time (mins) for various H_2O: CH_3OH ratios

5.4 Conclusions

In conclusion, a novel method for the synthesis of $CaCO_3$ nanostructures using dry ice carbonation has been developed. This technique enabled the production of calcium carbonate materials with high phase purity and particle size control, using appropriate solvent systems. Potentially this new carbonation approach can also be used in the large scale synthesis of other important carbonate nanomaterials (e.g. Li_2CO_3, $SrCO_3$), opening new possibilities in this research area and a variety of relevant industrial applications. This dry ice approach provides an opportunity to perform the carbonation process at low temperatures, favouring the nucleation phase over growth and enabling the production of small metal carbonate nanoparticles of high monodispersity, which is not feasible in ambient or high temperature syntheses. The use of low temperatures can also potentially enable the synthesis of unstable carbonate polymorphs such as vaterite and other metal carbonate polymorphs with unusual morphologies. Finally, this approach is economical and intrinsically scalable and therefore potentially applicable at the industrial scale.

References

(1) A. F. Wallace, L. O. Hedges, A. Fernandez-Martinez, P. Raiteri, J. D. Gale, G. A. Waychunas, S. Whitelam, J. F. Banfield and J. J. De Yoreo, *Science*, 2013, **341**, 885.

(2) R Wiebe and V. L. Gaddy, *Journal of the American Chemical Society*, 1940, **62**, 815–817.

(3) J. M. Gregg, D. L. Bish, S. E. Kaczmarek and H. G. Machel, *Sedimentology*, 2015, **62**, 1749–1769.

(4) C. G. Kontoyannis and N. V. Vagenas, *Analyst*, 2000, **125**, 251–255.

(5) W. Sun, S. Jayaraman, W. Chen, K. A. Persson and G. Ceder, *Proceedings of the National Academy of Sciences*, 2015, **112**, 3199–3204.

(6) F Manoli and E Dalas, *Journal of Crystal Growth*, 2000, **218**, 359–364.

(7) D. C. Green, J. Ihli, Y.-Y. Kim, S. Y. Chong, P. A. Lee, C. J. Empson and F. C. Meldrum, *Crystal Growth & Design*, 2016, **16**, 5174–5183.

(8) L. Zhang, L.-H. Yue, F. Wang and Q. Wang, *The Journal of Physical Chemistry B*, 2008, **112**, 10668–10674.

(9) J. Wang and U. Becker, *American Mineralogist*, 2009, **94**, 380.

(10) E. Mathiowitz, J. S. Jacob, Y. S. Jong, G. P. Carino, D. E. Chickering, P. Chaturvedi, C. A. Santos, K. Vijayaraghavan, S. Montgomery, M. Bassett and C. Morrell, *Nature*, 1997, **386**, 410–414.

(11) A. Som, R. Raliya, L. Tian, W. Akers, J. E. Ippolito, S. Singamaneni, P. Biswas and S. Achilefu, *Nanoscale*, 2016, **8**, 12639–12647.

(12) S. J. Parkin, R. Vogel, M. Persson, M. Funk, V. L. Y. Loke, T. A. Nieminen, N. R. Heckenberg and H. Rubinsztein-Dunlop, *Optics Express*, 2009, **17**, 21944–21955.

(13) Z. Zhang, B. Yang, H. Tang, X. Chen and B. Wang, *Journal of Materials Science*, 2015, **50**, 5540–5548.

(14) J. Yu, J. C. Yu, L. Zhang, X. Wang and L. Wu, *Chem Commun (Camb)*, 2004, 2414–2415.

(15) T. Tomioka, M. Fuji, M. Takahashi, C. Takai and M. Utsuno, *Crystal Growth & Design*, 2012, **12**, 771–776.

(16) D. Konopacka-Łyskawa, *Crystals*, 2019, **9**, 223.

Chapter 6

Lanthanide-doped Luminescent $CaCO_3$ Micro 'Bow Tie' Structures

6.1 Introduction

An interesting prospective use of calcium carbonate, and calcite in particular lies in its capacity to adsorb and incorporate other ions. This has potential implications for the remediation and sequestration of hazardous metals and radionuclides from both natural and anthropogenic sources. The capacity of calcite to act as a radionuclide trap has previously been examined using trivalent lanthanide ions as non-radioactive analogues.[1] These studies have shown that the lanthanide ions have a high partition coefficient with calcite, with various lanthanide ions readily incorporated into the calcite lattice, though the precise mechanism of incorporation remains the subject of some debate.[2]

The use of lanthanide dopants in $CaCO_3$ also opens up unique opportunities to produce new biocompatible, luminescent materials, which may offer many advan-

tages over other sources of luminescence such as quantum dots[3] or organic dyes.[4] These advantages include high stability and biocompatibility, coupled with narrow emission bands and large Stokes shifts. A narrow emission band improves energy efficiency while a large Stokes shift is particularly important in bioimaging where excitation can be carried out in the in the near-IR region which reduces autofluorescence (the light emitted by mitochondria and lysosomes) and increases image contrast.

6.2 Aims

The main aim of this part of our research is to develop the synthesis of novel $CaCO_3$ materials utilising our previously detailed dry ice carbonation method, in combination with lanthanide doping. Specifically, the goal of this chapter is to produce novel Eu^{3+} and Tb^{3+} doped $CaCO_3$ microstructures which could present red and green phosphorescence, respectively. A study will then be carried out on the effect of dopant concentration on both the morphology and photoluminescence properties of the as-synthesised materials using both x-ray diffraction and photoluminescence (PL) spectroscopy. The materials are to be fully characterised using a variety of instrumental techniques including SEM, XRD, EDX, ICP-MS, and PL.

6.3 Results and Discussion

6.3.1 Preparation of Lanthanide-Doped $CaCO_3$ Microspheres

The synthesis of the lanthanide-doped calcium carbonate (Figure 6.1) was performed by dissolving CaO in Millipore water with appropriate amounts of the lanthanide nitrate salt ($Eu(NO_3)_3$, $Tb(NO_3)_3$ or $Ce(NO_3)_3$), followed by the sequential addition of dry ice (solid CO_2) until a pH of 7 was reached. The solid products were isolated by centrifugation and washed with water and ethanol prior to drying in an oven at 80 °C for 24 h. Samples were characterised by X-ray powder diffraction (XRD), scanning electron microscopy (SEM), energy dispersive X-ray analysis (EDX), steady state photoluminescence spectroscopy, time-dependent photoluminescent decay spectroscopy and inductively coupled plasma mass spectrometry (ICP-MS).

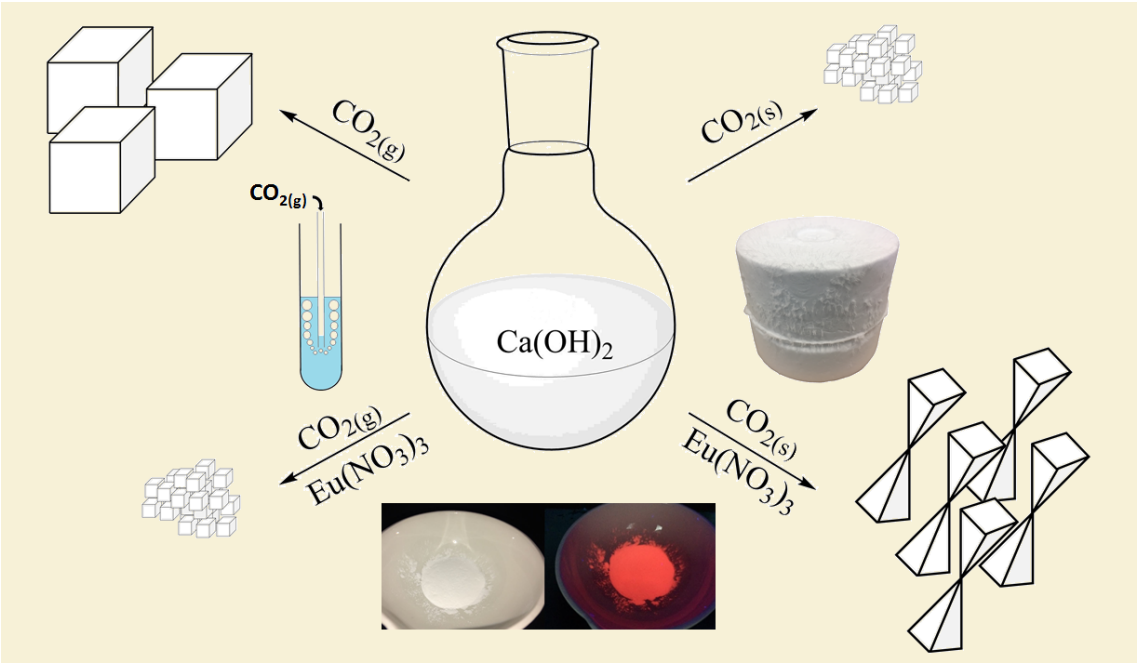

Figure 6.1: Synthetic scheme illustrating the effect of both the method of CO_2 introduction as well as the presence of lanthanide dopants

6.3.2 Investigation of Lanthanide-Doped $CaCO_3$ Microspheres by Electron Microscopy and Porosimetry

Scanning electron microscopy (SEM) images showed the formation of unique twinned structures of $CaCO_3$ (see Figure 6.2). The twinned structures appear to have a central nucleation point, which grows through acicular-like structures to form an anisotropic material, the morphology of which we have termed 'bow tie'. The structures formed have an average length of 11.1 ± 2.7 μm when measured end to end (see histogram, Figure 6.3 (A)).

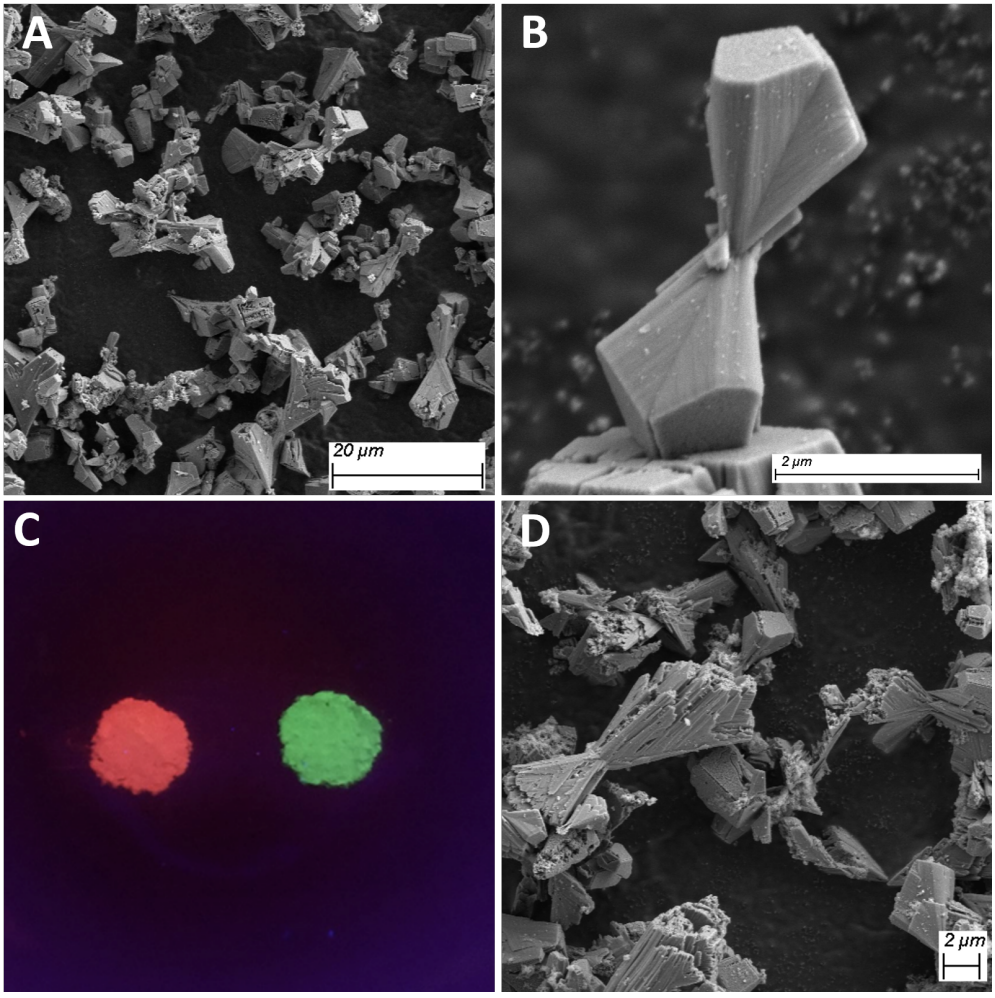

Figure 6.2: SEM images of (A) and (B) 3.4 mol % Eu^{3+} doped $CaCO_3$ 'bow ties' (C) Eu^{3+} (left) and Tb^{3+} (right) doped $CaCO_3$ under UV light and (D) 2.5 mol % Tb^{3+} doped $CaCO_3$ bow ties

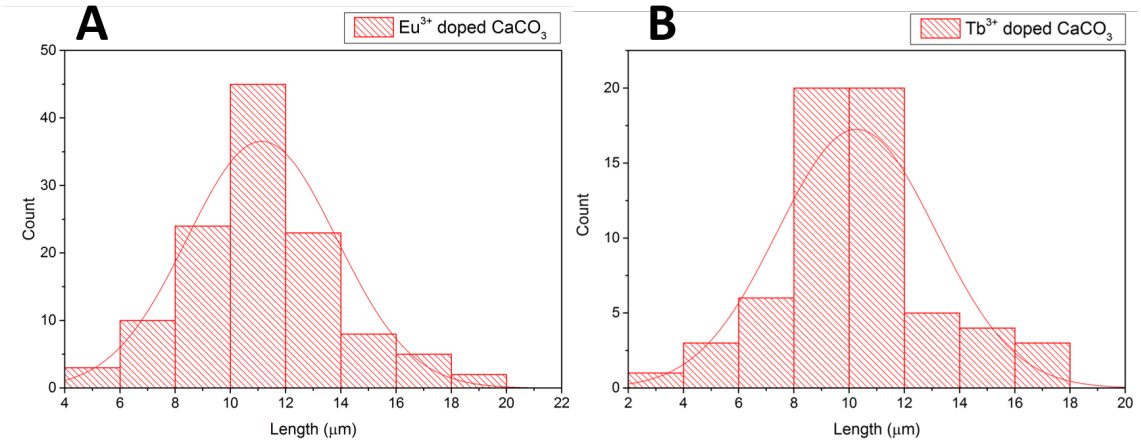

Figure 6.3: Histograms representing the size distributions of (A) Eu^{3+} and (B) Tb^{3+} doped $CaCO_3$ where $N = 120$ and 62, respectively

The 'bow ties' formed not only exhibit twinning, but also a readily visible porous morphology at their ends (see Figure 6.4). The desorption plot obtained from Barrett-Joyner-Halenda (BJH) pore size and absorption analysis (Figure 6.5) gives a mean pore diameter of approximately 12 nm. This, in conjunction with a pore volume of 0.03 cc/g and a surface area of 7.63 m^2/g implies that the 'bow ties' are only partially porous - a side effect of their likely acicular growth mechanism. This porosity adds a further layer of interest to these materials which potentially enables their use for encapsulation. Interestingly, we have found that without the addition of Eu^{3+} or Tb^{3+}, no 'bow tie' structures were present, instead forming small calcite nanoparticles which is typical of dry ice carbonation.[5]

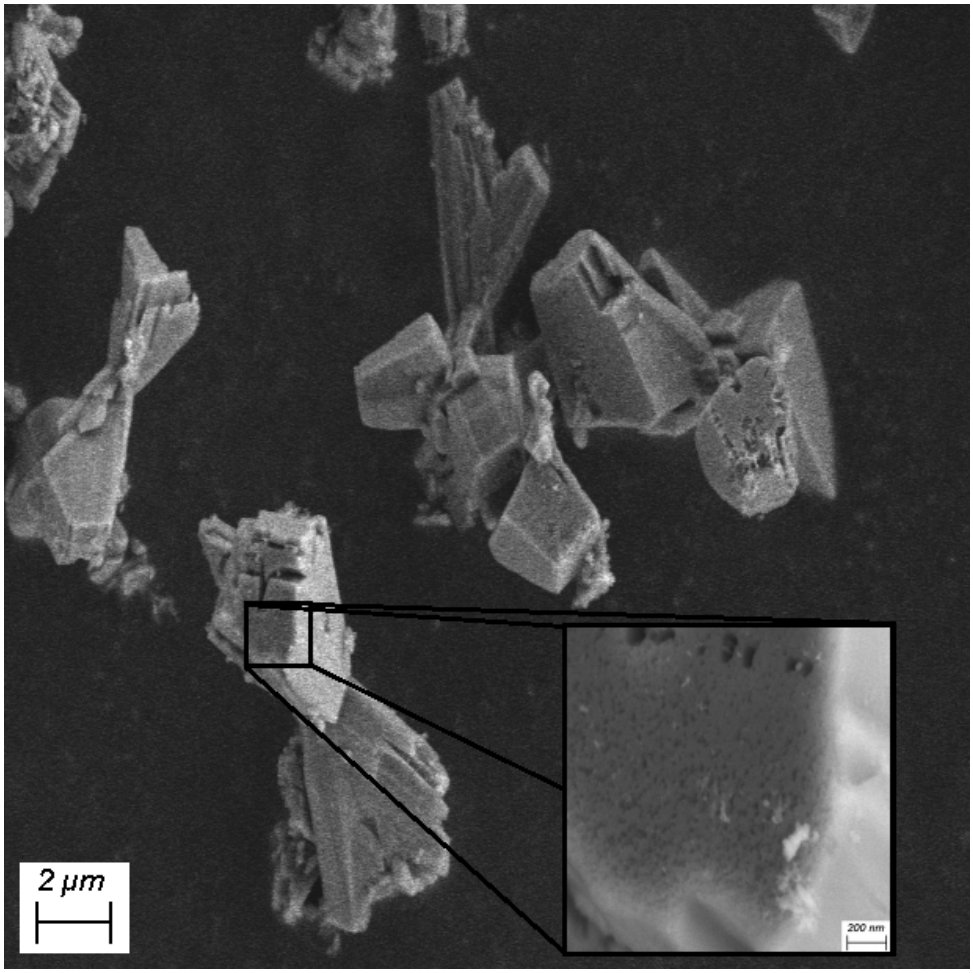

Figure 6.4: SEM image of 1.68 mol % Eu^{3+} doped $CaCO_3$ illustrating porous morphology

It was revealed that the 'bow tie' morphology only appears at concentrations of Eu^{3+} of 1.68 mol % and above (see Figure 6.6). This implies that there must be a sufficient concentration of the lanthanide dopant to induce anisotropy and therefore invoke the twinning mechanism in the calcite structures. In addition, the gross 'bow tie' morphology is retained on further increasing the Eu^{3+} concentrations.

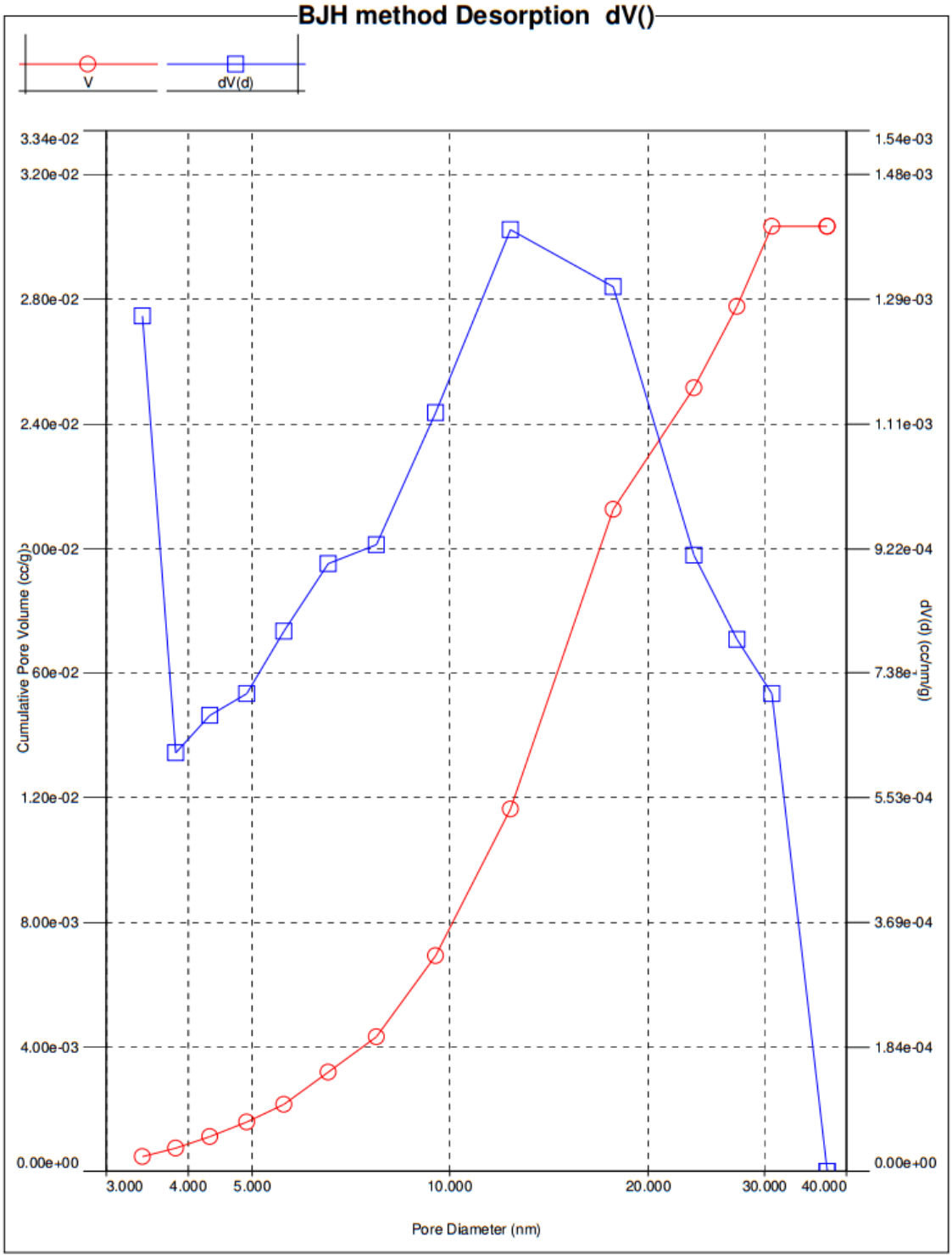

Figure 6.5: BJH analysis of pore size and volume showing a dominant pore diameter of c. 12 nm

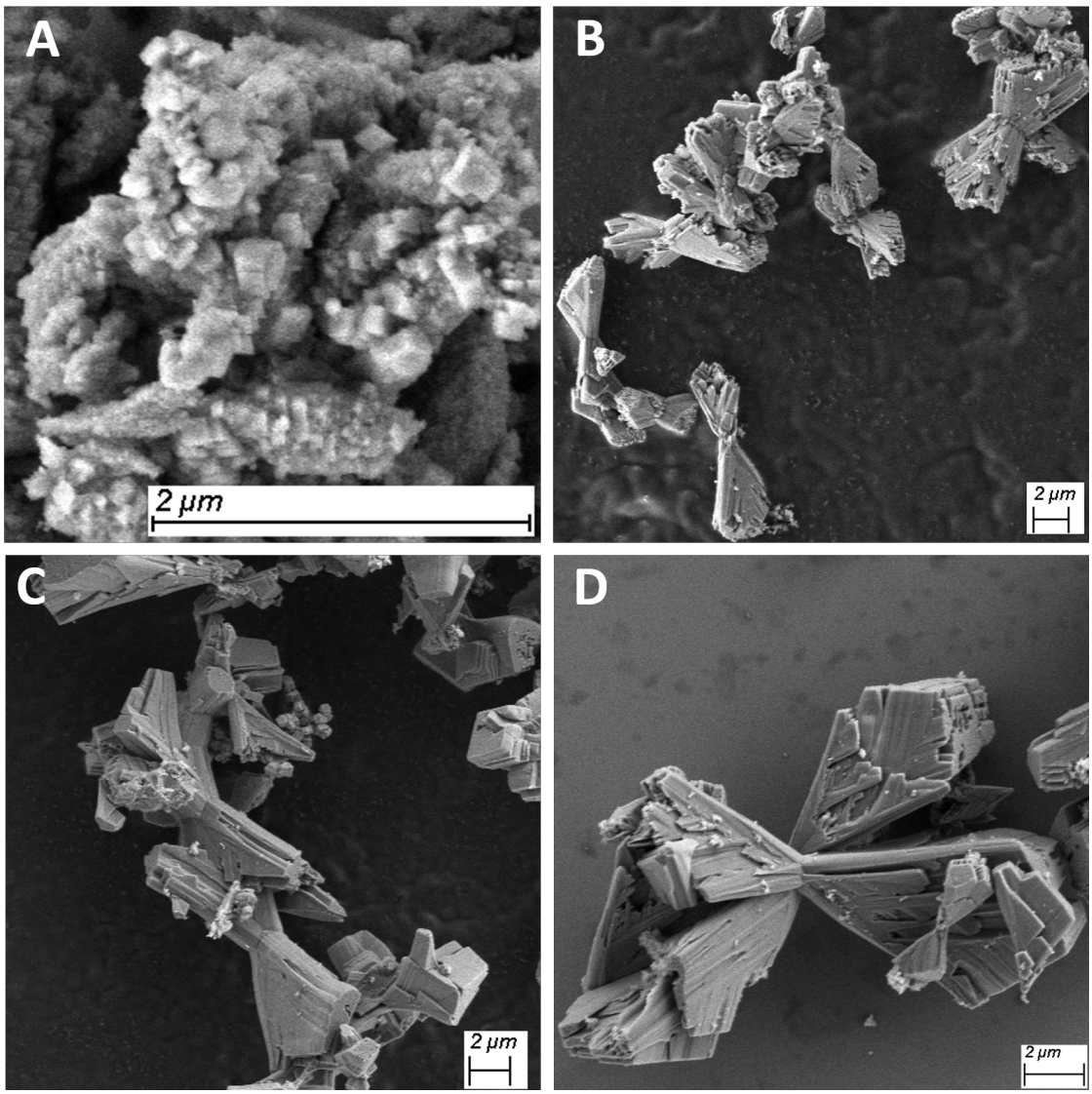

Figure 6.6: $CaCO_3$ obtained at (A) 0.5 (B) 1.68 (C) 2.5 and (D) 3.4 mol %. Eu^{3+}

The same behaviour was found to occur from Tb^{3+} doping, with three concentrations examined in detail, giving the onset of twinning with concentrations above 1.68 mol % and 'bow tie' structures showing an average size of 10.3 ± 2.9 μm (Figure 6.3 (B)), with SEM images shown in Figure 6.7.

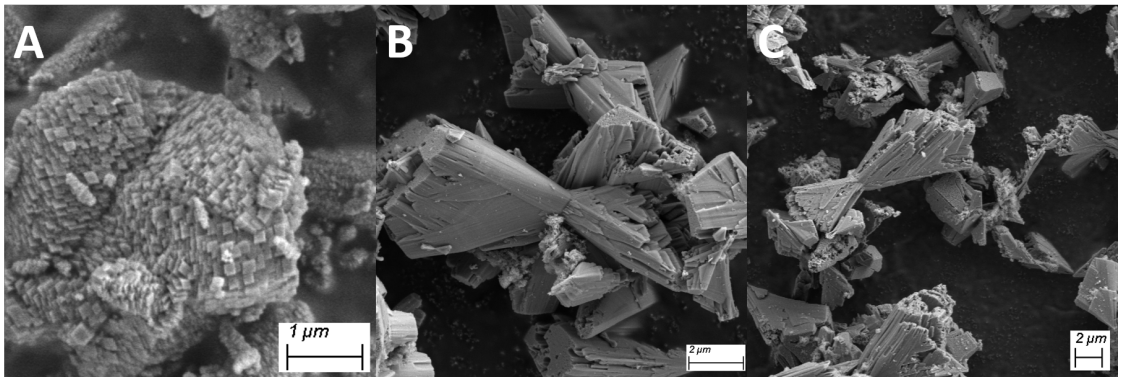

Figure 6.7: Terbium doping levels of (A) 0.5 (B) 1.68 and (C) 2.5 mol %

A series of experiments using conventional gaseous CO_2 bubbling and chemical precipitation methods were also carried out with the same materials and concentration range, however none of these experiments resulted in any similar 'bow tie' microstructures (see Figure 6.8).

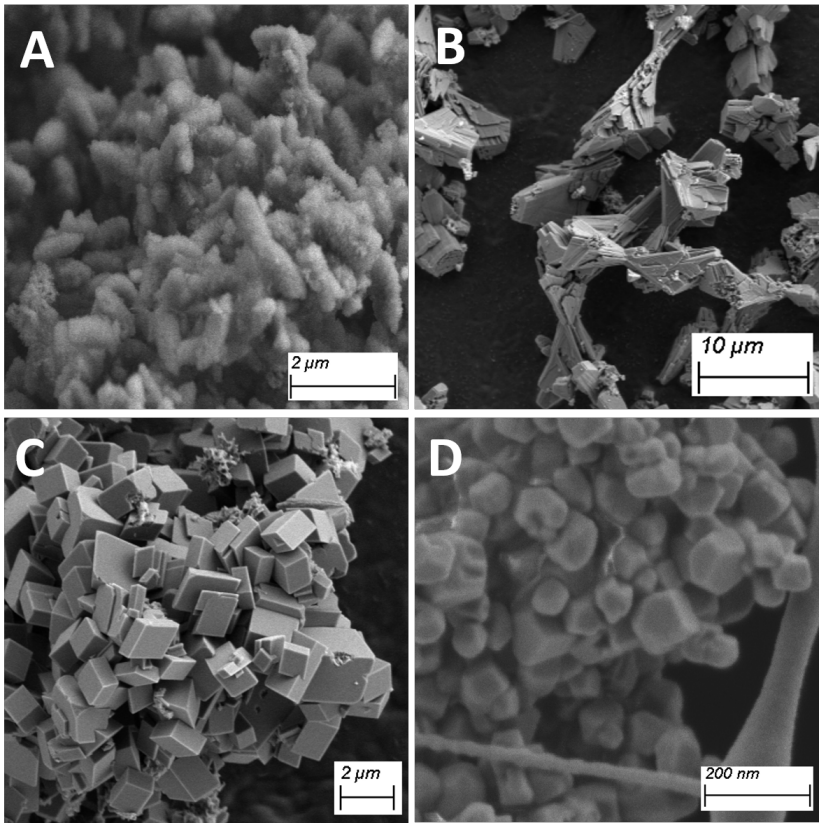

Figure 6.8: SEM images of $CaCO_3$ produced with 3.4 mol % Eu^{3+} via (A) CO_2 bubbling and (B) dry ice carbonation. $CaCO_3$ produced with (C) 3.4 mol % Ce^{3+} and (D) without lanthanide present

This is the first known report of calcite 'bow ties' with no similar structures being reported for $CaCO_3$. The fact that these structures were only encountered using the dry ice method in the presence of lanthanide ions (Figure 6.8 (B)) suggests that the lanthanides must play a significant role (dry ice carbonation without the presence of lanthanides results in the formation of rhombohedral nanoparticles (Figure 6.8 (D)). There exists both a size and charge disparity between the divalent calcium and trivalent lanthanide cations, with Ca^{2+} having an ionic radius of 114 pm, while Eu^{3+} and Tb^{3+} have radii of 108.7 and 106.3 pm, respectively.[6] The influence of the size disparity was investigated by substituting $Ce(NO_3)_3$ (which has an ionic radius similar to Ca^{2+} at 115 pm) for $Eu(NO_3)_3$ and carrying out otherwise identical reactions at Ce^{3+} levels of 0.5 to 5 mol % (see experimental methods, Table 2.4). All Ce^{3+} doped samples were also identified by XRD as phase pure calcite; however the 'bow tie' morphologies were not observed, with large rhombohedral microparticles obtained in their place (see Figure 6.8 (C)) suggesting that the ionic radius of the Ce^{3+} dopant was not sufficiently different to that of Ca^{2+} to invoke twinning.

Additional syntheses were performed using $EuCl_3$ to explore the effect of the nitrate counter ions, as these have previously been identified as having a significant influence on lanthanide uptake into calcite. It was found that the products obtained from dry ice carbonation with $EuCl_3$ also yielded the twinned 'bow tie' structures (see Figure 6.9).

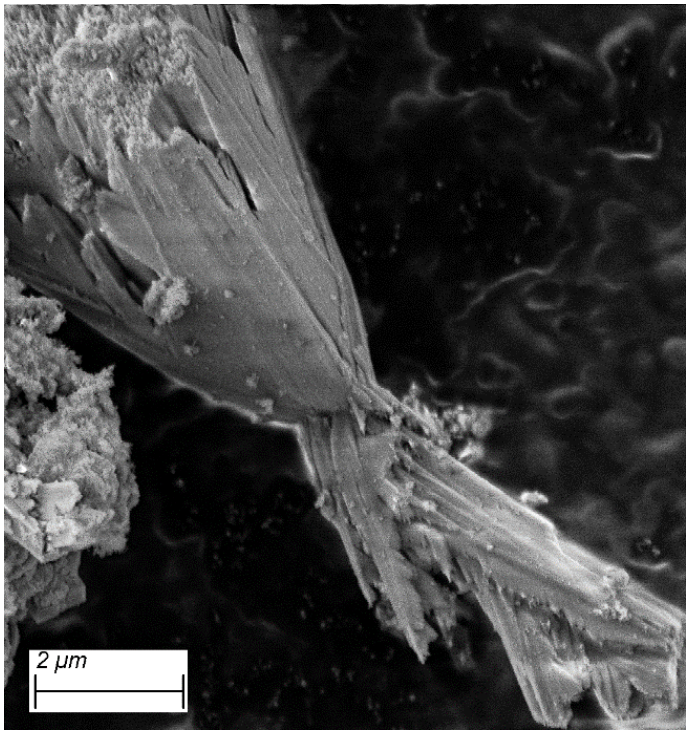

Figure 6.9: SEM images of 1.68 mol % Eu^{3+} doped $CaCO_3$ using $EuCl_3$

It can thus be inferred that it is the lanthanide ions which are responsible for the observed morphology, with the charge disparity likely causing the increased particle size, relative to the undoped samples, while the difference in ionic radii between Eu^{3+} or Tb^{3+} and Ca^{2+} induces the formation of the unusual 'bow tie' structures.

While these 'bow ties' are unique for $CaCO_3$, similar morphologies have previously been observed in the crystallisation of $BaSO_4$ at the air-water interface in the presence of organic surfactant monolayers. These studies have attributed the unusual $BaSO_4$ 'bow tie' morphologies obtained to the adsorption of the surfactant species to specific facets, which could be further influenced by varying the dielectric constant of the interface.[7,8] This suggests that at higher lanthanide concentrations a surface-bound lanthanide carbonate species is involved in directing the growth of the 'bow ties'.

In addition to the clear impact of the dopant ions, the use of the dry ice carbonation method[5] is also found to be a key requirement in forming these new structures. By performing the carbonation step using the conventional CO_2 bubbling method, only rhombohedral nanoparticles were obtained, even in the presence of 3.4 mol % Eu^{3+} (Figure 6.8 (A)). The fact that the 'bow tie' morphology is only obtained from the dry ice carbonation method is attributed to the cooling effect of the dry ice. Due to the retrograde solubility of $CaCO_3$[9] and CO_2,[10] cooling the system increases the solubility of both, thus allowing more significant growth to occur with the influence of the lanthanide ions leading to the 'bow tie' morphology. EDX analysis showed that the lanthanides are evenly distributed throughout the structures, as shown in Figure 6.10.

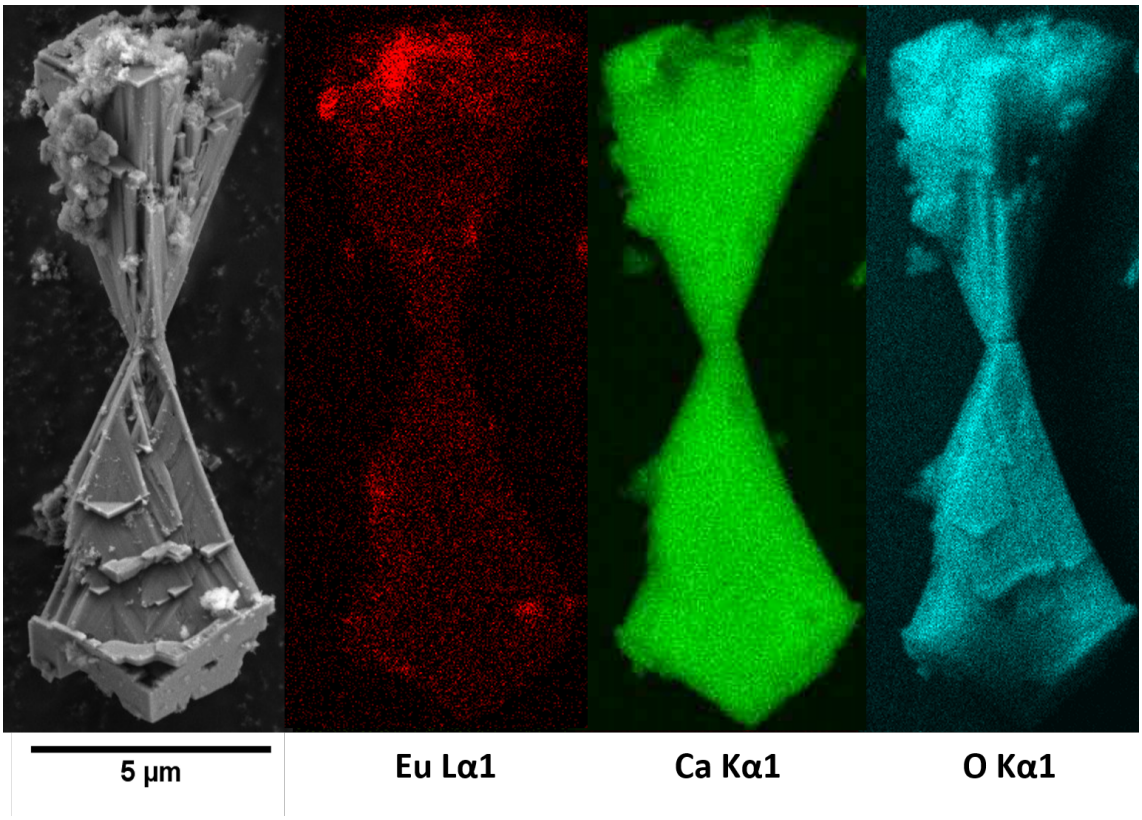

Figure 6.10: EDX analysis of the 'bow tie' structures showing their elemental composition with Eu (Red), Ca (green) and O (blue)

6.3.3 X-Ray Powder Diffraction Analysis

The XRD patterns (Figure 6.11 (A) and (B)) of all samples confirm that only calcite is obtained, with no evidence of any other crystalline phase, regardless of dopant or dopant concentration. There is also some peak splitting as dopant concentration increases resulting in the formation of doublet peaks at $2\theta = 47°$.

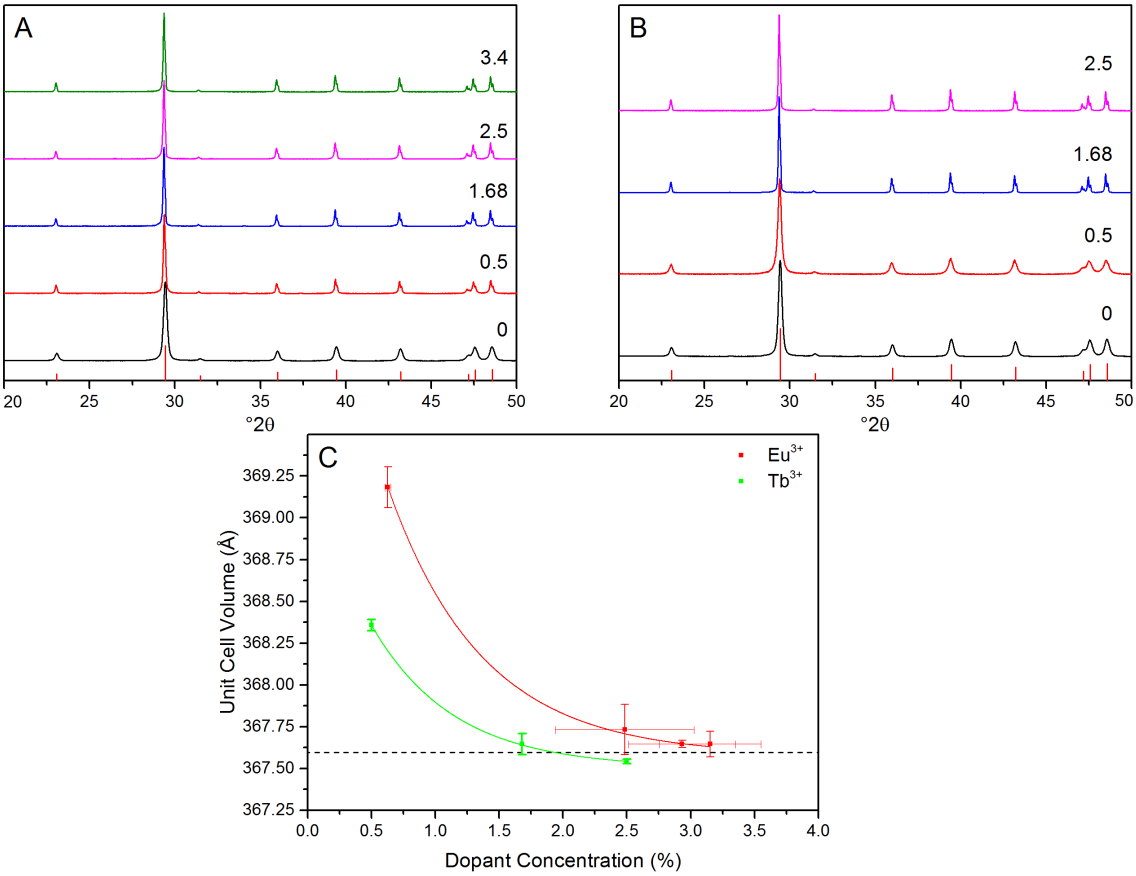

Figure 6.11: (A and B) XRD patterns of the various doping levels of $CaCO_3$ doped with Eu^{3+} and Tb^{3+}, respectively (the characteristic pattern of calcite is illustrated as red lines) (C) cell volume ($Å^3$) vs dopant concentration (%) as determined by Rietveld refinement and ICP-MS, respectively

While no other phases are observed, Rietveld refinement shows some significant changes in unit cell parameters (see Figure 6.12 and Table 6.1). Upon the inclusion of 0.5 mol % Eu^{3+} in the synthesis, the unit cell volume increases from 367.66 $Å^3$

for the undoped calcite, to 369.30 Å^3 for that prepared by this procedure. As the dopant level is further increased to 1.68 mol % and above, the cell volume returns to its initial value (Figure 6.11 (C)). This may indicate that at lower dopant levels the Eu^{3+} is incorporated into the calcite lattice, while at higher concentrations a surface doping mechanism may predominate.

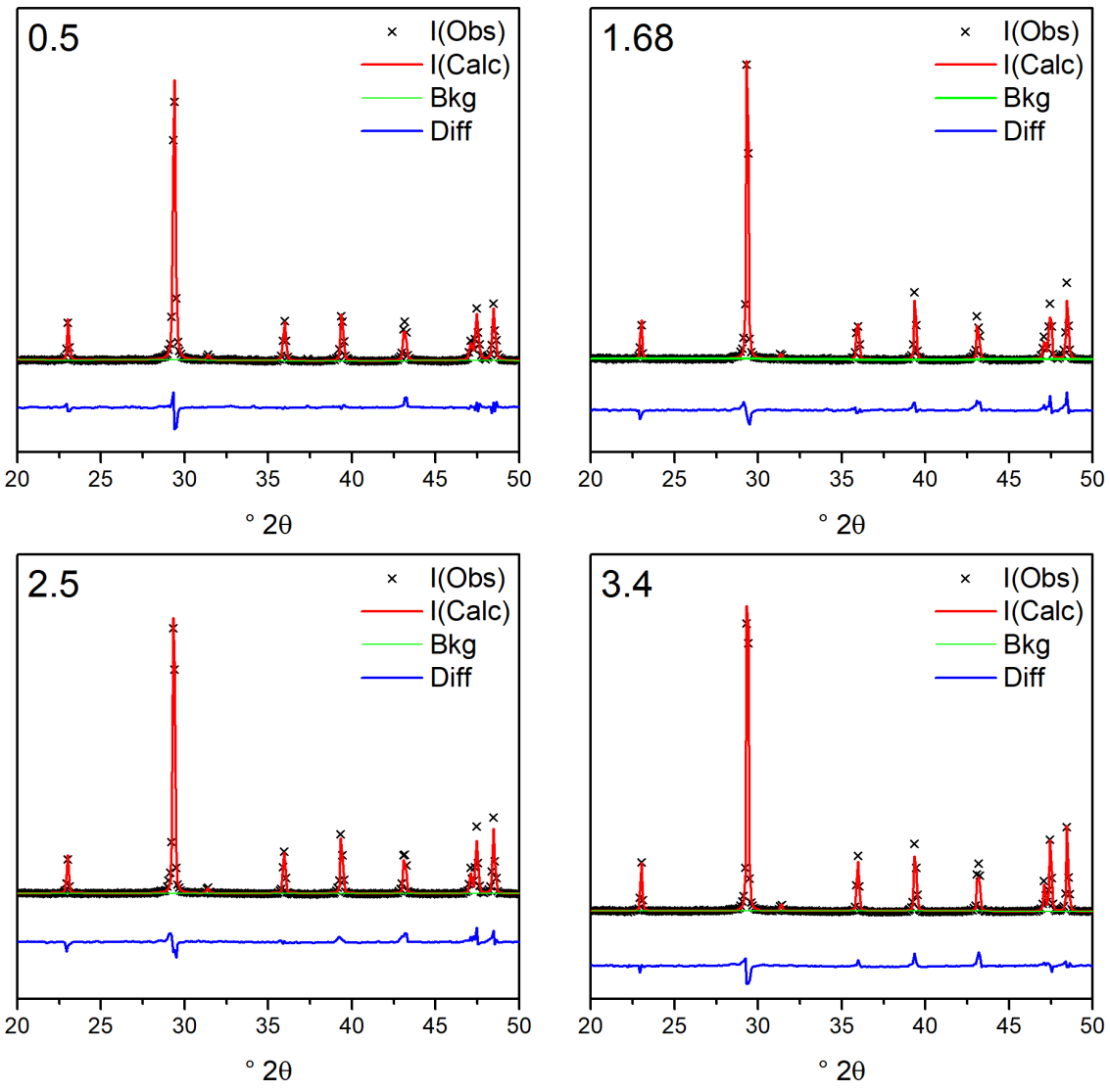

Figure 6.12: Rietveld refinements of calcite doped with Eu^{3+} at the indicated levels (mol %)

Dopant	Concentration (mol %)	a (Å)	c (Å)	Unit cell volume (Å^3)	Crystallite size (nm)
N/A	0	4.989(3)	17.054(7)	367.6559	99.3
Eu	0.5	4.998(8)	17.066(2)	369.3021	118.9
	1.68	4.987(9)	17.074(8)	367.8788	163.5
	2.5	4.987(5)	17.070(1)	367.7282	169.6
	3.4	4.987(0)	17.070(3)	367.6569	194.7
Tb	0.5	4.993(1)	17.062(2)	368.382	47.6
	1.68	4.987(2)	17.070(2)	367.673	199.4
	2.5	4.986(4)	17.072(6)	367.608	203.6

Table 6.1: Refined cell parameters of undoped and doped samples

6.3.4 Photoluminescence Analysis

The excitation photoluminescence spectra (PLEx) and the emission photoluminescence spectra (PLEm) of Eu^{3+} doped $CaCO_3$ showed the characteristic spectrum of Eu^{3+} as illustrated by Figure 6.13. PLEm was measured from 560 nm to 720 nm using an excitation wavelength of 393 nm corresponding to the $^7F_0$–$^5L_6$ transition and 270 nm which is related to the absorption energy of the O^{2-} / Eu^{3+} charge transfer band (CTB).[11] PLEx was measured from 230 nm to 500 nm using the 614 nm emission peak. The excitation spectra contain a group of sharp peaks in the longer wavelength region, which can be ascribed to the f–f transitions within the $4f^6$ configuration of Eu^{3+} ions. Upon excitation at 393 nm, the emission spectrum is composed of a group of lines peaking at 579, 590, 614, 650 and 699 nm. They correspond to the $^5D_0$–^7F_J (J = 0, 1, 2, 3, 4) transition of the Eu^{3+} ions, respectively. The strongest peak is located at 614 nm, which is the characteristic peak of Eu^{3+} ions. The excitation intensity changes between 270 and 393 nm, whereby the

intensity of luminescence is far higher at 270 nm for lower dopant concentrations, with the emission at ex. 393 nm steadily increasing as the dopant concentration tends towards 3.4 mol % Eu^{3+}.

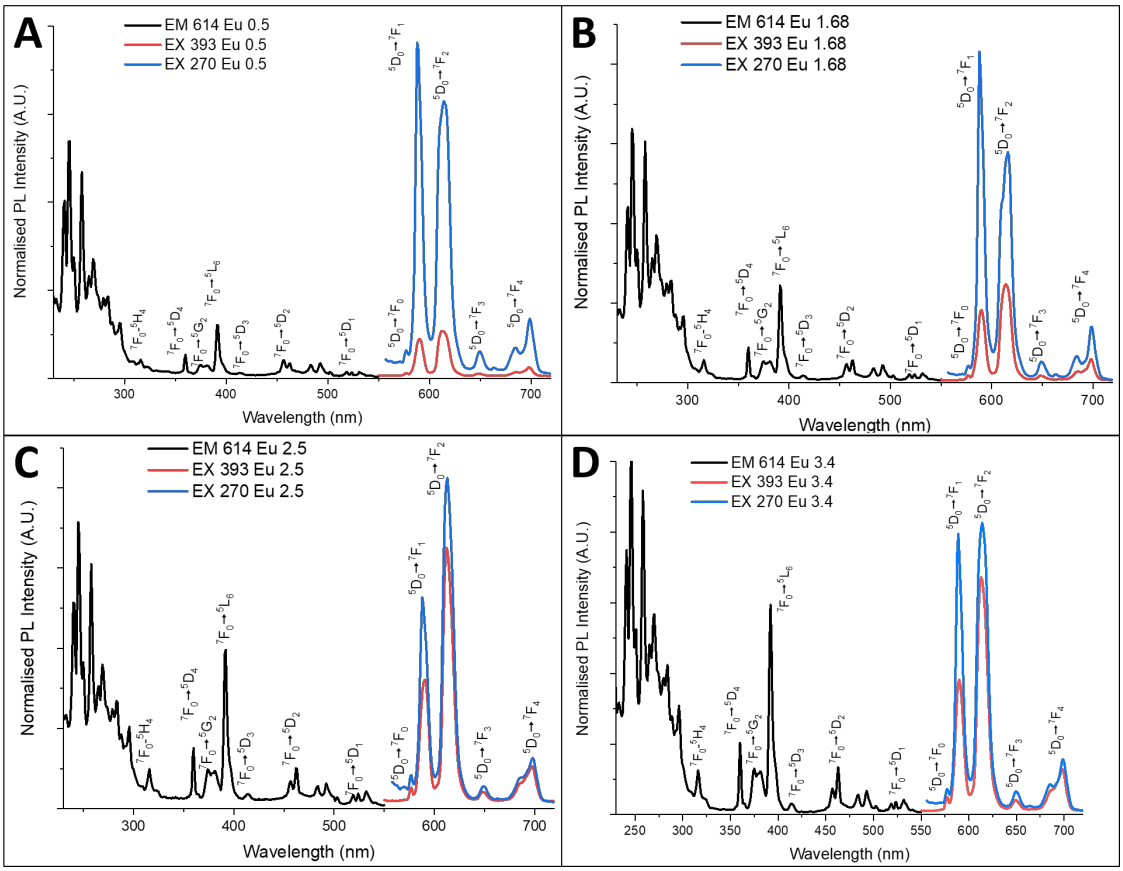

Figure 6.13: Emission and excitation photoluminescence spectra of the (A) 0.5 (B) 1.68 (C) 2.5 and (D) 3.4 mol% Eu^{3+} doped $CaCO_3$

In addition, it is interesting to note that the $^5D_0$–$^7F_2$ transition is an induced electric dipole type of transition,[12] the intensity of which depends strongly on the symmetry of the Eu^{3+} environment. However, $^5D_0$–$^7F_1$ is magnetic-dipole allowed and is independent of local symmetry.[13] Therefore the ratio between the $^5D_0$–$^7F_1$ and $^5D_0$–$^7F_2$ intensity peaks is termed the asymmetry ratio (R) and has been previously reported in literature[11] to correspond to the site asymmetry of the Eu^{3+} ion and can be evaluated for each doping level from the ratio of the areas of the peaks between

the $^5D_0$–$^7F_2$ electric dipole transition and the $^5D_0$–$^7F_1$ magnetic dipole transition using the equation shown in equation 6.1.[14]

$$R = I(^5D_0{-}^7F_{1)}/I(^5D_0{-}^7F_2) \tag{6.1}$$

This information is presented in tabular form in Table 6.2 and indicates that a minor increase in asymmetry occurs with increasing Eu^{3+} levels.

Mol % Eu	**Peak Intensity of $^5D_0$–$^7F_1$ (589 nm)**	**Peak integration of $^5D_0$–$^7F_1$ (589 nm)**	**Peak Intensity of $^5D_0$–$^7F_2$ (614 nm)**	**Peak integration of $^5D_0$–$^7F_2$ (614 nm)**	**Asymmetry factor of (r=I($^5D_0$–$^7F_1$/ I($^5D_0$–$^7F_2$)**
0.5	76210.5593	727534.275	80542.4089	1.54E+06	1.05684054
1.68	3220925	2.73E+07	3115651	4.50E+07	0.9673156
2.5	1969455	2.01E+07	3677405	5.18E+07	1.86721961
3.4	1702772	1.58E+07	2443170	3.51E+07	1.43481922

Table 6.2: Peak information and integration of Eu^{3+} doped $CaCO_3$ with 0.5, 1.68, 2.5, and 3.4 mol % Eu. This gives the asymmetry factor (R = I($^5D_0$–$^7F_{1)}$/I($^5D_0$–$^7F_2$)), for each doping level

A comparison of the emission intensities (ex. 270 nm) between different Eu^{3+} doping levels of the two most intense transitions ($^5D_0$–$^7F_1$, $^5D_0$–$^7F_2$) is shown in Figure 6.14. Two distinct trends are observed: a strong increase in emission intensity when comparing 0.5 to 1.68 mol % Eu^{3+}, and a decrease in emission intensity above 2.5 mol % Eu^{3+} (the percentage change relative to intensity is given in Table 6.3). Firstly, the dramatic increase in emission intensity is proposed to be strongly correlated with the new morphology which evolves as the Eu^{3+} doping level increases, forming the larger 'bow tie' structures. In this case, the surface area to volume ratio strongly de-

creases as a result of the large increase in crystallite size, therefore reducing surface quenching of the Eu^{3+} centres.[15] The decrease in Eu^{3+} emission found at doping levels above 2.5 mol % has previously been reported as concentration quenching[16,17] and has been explained by the occurrence of Ln-O-Ln interactions in the material in a range of host matrices[14,18] including distance-dependent resonance energy transfer and cross-relaxation transmission.[19] Secondly, it has been proposed that as Eu^{3+} is incorporated into the Ca based lattices, two Eu^{3+} replaces three Ca^{2+} in the lattice causing a charge disparity – hence as doping increases the lattice vacancies will increase too[14,18] These vacancies have been shown to cause quenching by providing an alternative de-excitation route from the excited Eu^{3+} ions.

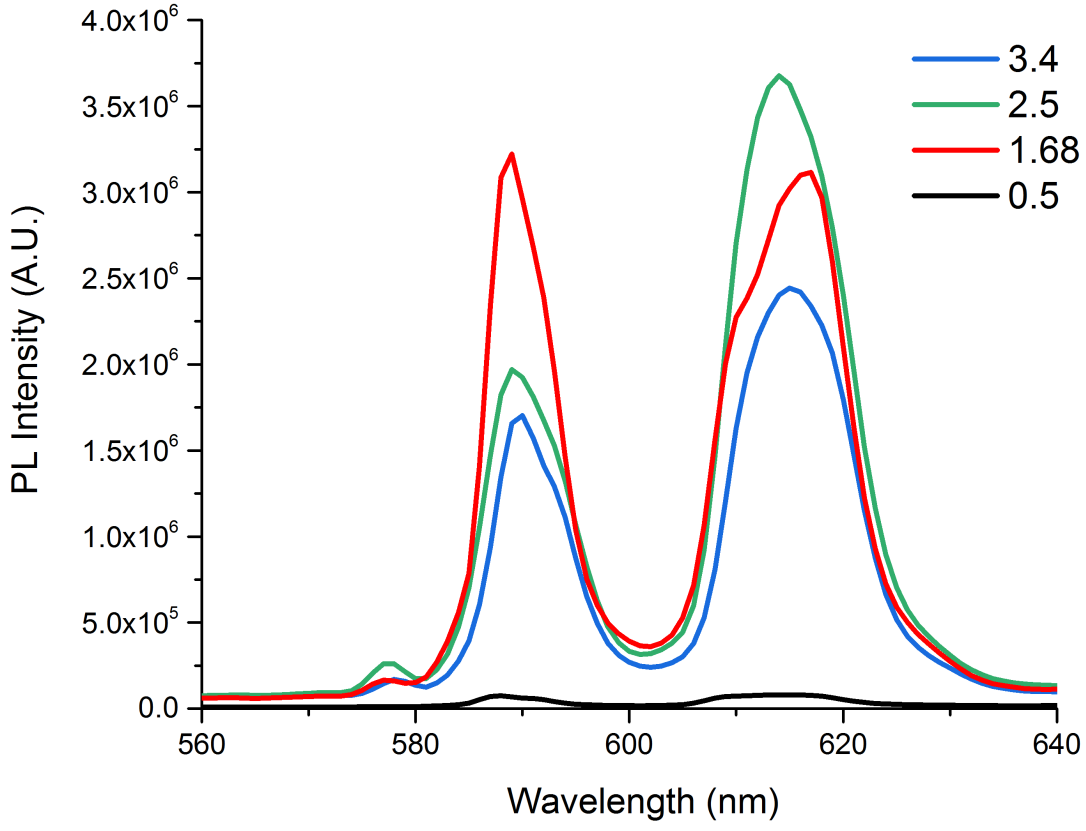

Figure 6.14: Comparative emission intensities of the two most intense transitions ($^5D_0$–$^7F_1$, $^5D_0$–$^7F_2$) for the various doping levels

Mol % Eu	**Intensity (589)**	**Integration**	**Intensity (614)**	**Integration**	**Ratio of peaks (RoP)**	**RoP integ-**	**Total integration**	**Ratio of integration**
0.5	76210.5593	727534.275	80542.4089	1.54E+06	1.05684054	2.12E+00	2.53E+06	3.37%
1.68	3220925	2.73E+07	3115651	4.50E+07	0.9673156	1.65E+00	7.48E+07	99.89%
2.5	1969455	2.01E+07	3677405	5.18E+07	1.86721961	2.58E+00	7.49E+07	100%
3.4	1702772	1.58E+07	2443170	3.51E+07	1.43481922	2.22E+00	5.31E+07	70.83%

Table 6.3: Integration and percentage change relative to intensity for Eu^{3+} doped $CaCO_3$

A further investigation of the resulting phosphorescent lifetimes was carried out with the resulting decay graphs illustrated in Figure 6.15 and in tabular form in Tables 6.4 and 6.5. Samples were measured from the 614 nm emission peak, while exciting at 393 nm. This data was fitted using a bi-exponential decay, giving an average time (avg) ranging from 0.4 - 1 ms (Table 6.4). The reason for bi-exponential decay is due to the Eu^{3+} dopant being found in the matrix in two distinct environments, which therefore gives rise to two exponential decay times – a shorter time in the range of 0.2 - 0.4 ms and a longer time of 1.0 - 1.5 ms. This corresponds well to reported bi-exponential fits of Eu^{3+} doped $CaCO_3$ samples in literature explained via the deduction that Eu^{3+} is occupying two different sites.[15,16,19] Firstly, the longer lifetimes (slow decay, τ_2) are assigned to Eu^{3+} occupying the centrosymmetric site of the lattice, replacing Ca^{2+} while the second is due to some Eu^{3+} ions being located at low-symmetry sites and/or at non-centrosymmetric sites, formed due to lattice defects such as distortion in grain boundary and/or surface/subsurface defects giving the second shorter lifetime (fast decay, τ_1).[15]

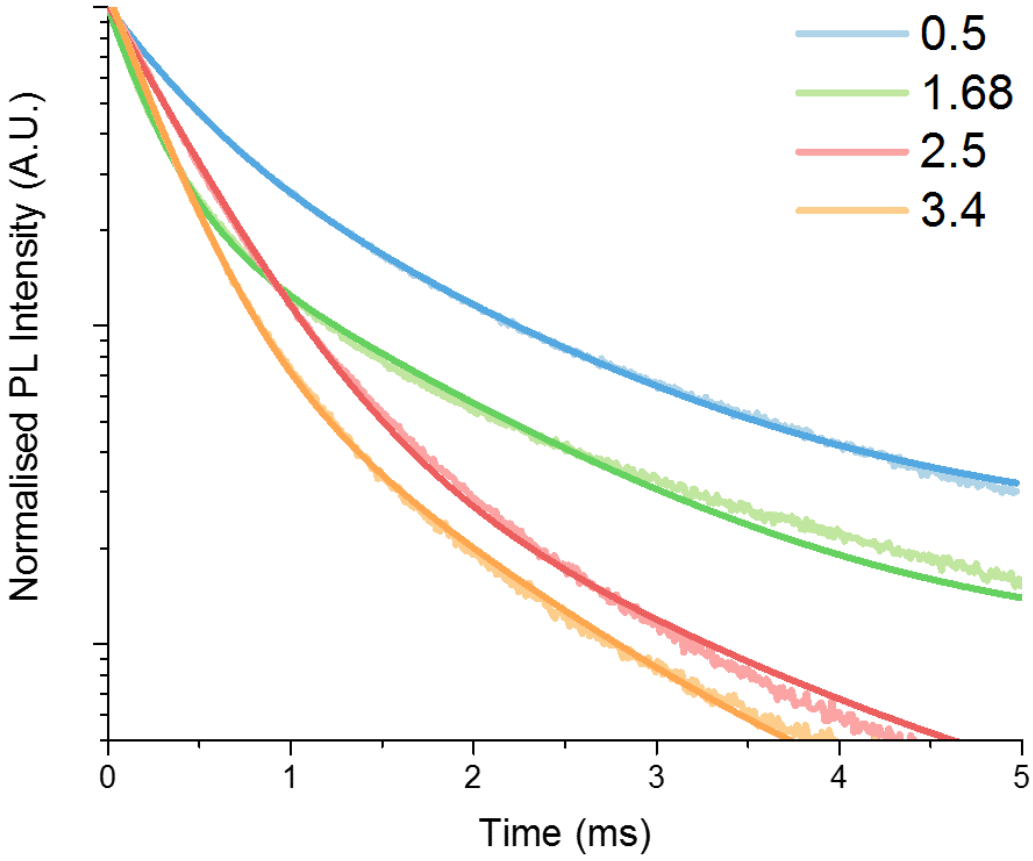

Figure 6.15: Photoluminescent decay of $CaCO_3$ doped with 0.5, 1.68, 2.5, and 3.4 mol % Eu^{3+} using a 393 nm excitation

Mol % Eu	τ_{avg} **(ms)**	τ_1 **(ms)**	A_1	τ_2 **(ms)**	A_2	**R-Square (COD)**
0.5	1.0316	0.38226	0.53924	1.27607	0.42925	0.99994
1.68	0.865731	0.21394	0.77453	1.2154	0.24429	0.99955
2.5	0.0635464	0.3975	0.9978	1.48793	0.07441	1
3.4	0.531158	0.26541	0.89213	1.03597	0.12032	1.09

Table 6.4: PL decay lifetimes of Eu^{3+} doped $CaCO_3$ with 0.5, 1.68, 2.5, and 3.4 mol % Eu^{3+} using a 393 nm excitation wavelength

Mol % Eu	τ_{avg} **(ms)**	τ_1 **(ms)**	A_1	τ_2 **(ms)**	A_2	**R-Square (COD)**
1.68	1.474	0.46002	0.51521	1.76683	0.46468	0.99988
2.5	1.1130	0.6621	0.78421	1.76522	0.20276	1

Table 6.5: PL decay lifetimes of Eu^{3+} doped $CaCO_3$ with 1.68 and 2.5 mol % Eu^{3+} using a 270 nm excitation wavelength

It is known that, even with low dopant concentration, a high local concentration of Eu^{3+} ions facilitates non-radiative decay pathways, due to Eu–Eu ion interactions, leading to a shortening in lifetimes.[15] A trend was also found of decreasing τ_{avg} with increasing Eu^{3+} emission, due to the increase in contribution of τ_1 relative to τ_2 with increasing Eu^{3+} concentrations, meaning the shorter decay lifetime makes a larger contribution to the overall decay. Again, this is to be expected if the shorter lifetime is due to Eu-Eu interactions, or due to an increase in crystal defect quenching sites due to Ca^{2+} vacancy production as discussed previously.

The luminescence of Tb^{3+} doped $CaCO_3$ 'bow ties' also showed the same distinctive spectra as reported in literature[20,21] as shown in Figure 6.16. PLEm was measured from 450 nm to 700 nm using an excitation of 226 nm while PLEx was measured from 200 to 475 nm using the 547 nm emission peak. The excitation spectra contain a group of sharp lines in the longer wavelength region, which can be ascribed to the f–f transitions within the $4f^8$ configuration of Tb^{3+} ions. Upon excitation at 226 nm, the emission spectrum is composed of a group of sharp lines presenting as split peaks at 486 and 495, 540 and 547, 582 and single peaks at 591, 620, 650, 672, and 684. These peaks correspond to the $^5D_4$–^7F_J (J = 0, 1, 2, 3, 4, 5, 6) transition of the Tb^{3+} ions, respectively.[20,22,23] The strongest peak is located at 540 and 547 nm, which is the characteristic peak of Tb^{3+} ions. A comparison of the PL intensity of

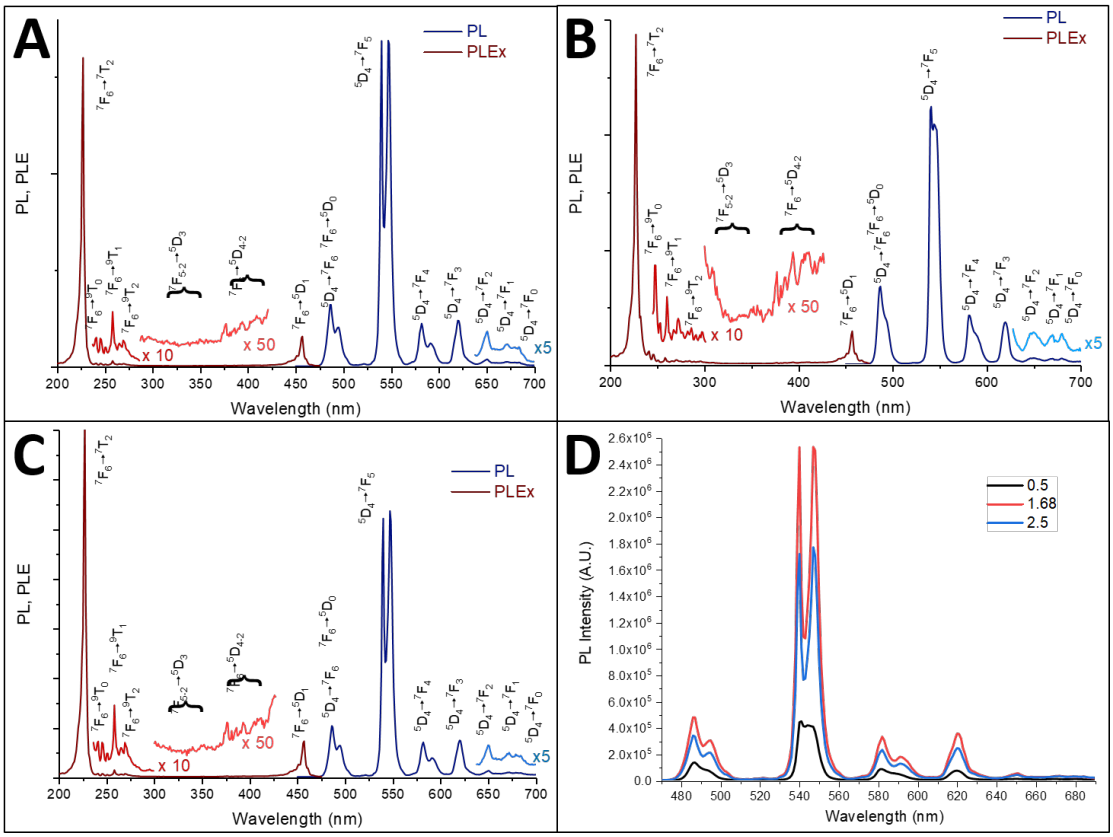

Figure 6.16: (A) 1.68 mol % (B) 2.5 mol % (C) 3.4 mol % Tb^{3+} doped $CaCO_3$ excitation and emission spectra and (D) comparative spectra of PL emission intensities for the three dopant concentrations

three Tb^{3+} doped samples produced (Figure 6.16 (D)) shows a large increase from 0.5 to 1.68 mol % Tb^{3+}, after which a decrease in intensity is observed, albeit to a level higher than 0.5 mol % Tb^{3+}. Therefore, the Tb^{3+} doped samples show a similar trend to the Eu^{3+} doped samples, in which an increase in PL occurs when transitioning from the nanoparticle structure to the much larger 'bow tie' microstructures, after which as the Tb^{3+} concentration increases, a decrease in PL is observed due to self-quenching effects of the lanthanides. In addition, the PL decay of the 1.68 mol % Tb doped sample (Figure 6.17 and Table 6.6) was measured showing an average lifetime of 10.31 $\pm$ 0.04 ms which is in line with reported results in literature.[24]

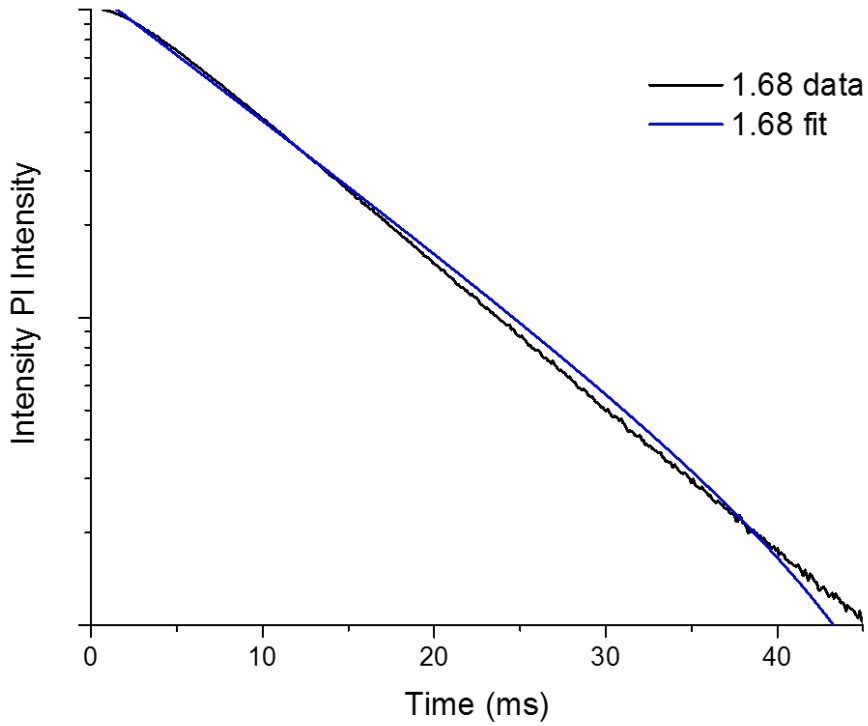

Figure 6.17: Photoluminescent decay graph of 1.68 mol % Tb^{3+} doped $CaCO_3$, showing original data and fitting emission

Sample	**Excitation wavelength**	$\tau_{\mathbf{avg}}$ **(ms)**
1.68	ex. 226	10.310833 ± 0.04

Table 6.6: PL decay lifetimes of 1.68 mol % Tb^{3+} doped $CaCO_3$ using a 226 nm excitation wavelength

6.4 Conclusions

In summary, for the first time we have successfully synthesised luminescent lanthanide doped calcium carbonate microstructures with a novel 'bow tie' morphology. The luminescent properties compare favourably with those previously reported for doped $CaCO_3$ based materials.

An in-depth study of the effect of various dopant concentrations has been carried out using XRD which correlates well with the luminescence results. Both studies show that at 0.5 mol % of Eu^{3+} or Tb^{3+} there is a minimal luminescence intensity corresponding with the lack of twinned structures. Above this point, twinning occurs, with an associated increase in luminescence until reaching a maximum at 2.5 mol % for Eu^{3+} and 1.68 mol % for Tb^{3+} doping, above which it is reduced. This trend in luminescence most likely arises from the order of magnitude increase in size of the 'bow tie' microstructures which prevents any concentration quenching until relatively high dopant concentrations.

The actual origin of twinning is determined to occur due to a combination of lanthanide dopants which possess a size and charge disparity with the Ca^{2+} that they are substituting in conjunction with the dry ice carbonation method, which increases the solubility of $CaCO_3$ and CO_2 thus allowing specific growth to occur. Experiments carried out using Ce^{3+} as a dopant (with a markedly similar ionic radius to Ca^{2+}) showed no onset of twinning, regardless of concentration. This, when considered alongside the observation that divalent dopants also fail to produce 'bow ties', illustrates that they likely result due to a combination of size and charge disparity. In addition, the importance of the dry ice carbonation method is evidenced by the absence of 'bow ties' when using gaseous CO_2 bubbling. The 'bow tie' morphology can also be conclusively linked to the presence of lanthanides and not, in fact, the counter ions due to the same 'bow tie' products of the control synthesis while using

$EuCl_3$ in place of $Eu(NO_3)_3$.

Overall, we believe that this work has particular importance in addressing the issue of retrograde solubility when synthesising novel $CaCO_3$ based materials, as well as the development of new materials with potential applications in a range of fields including rare earth chemistry, biological imaging and photonics.

References

(1) L. Z. Lakshtanov and S. L. S. Stipp, *Geochimica et cosmochimica acta*, 2004, **68**, 819–827.

(2) M. Voigt, V. Mavromatis and E. H. Oelkers, *Chemical Geology*, 2017, **462**, 30–43.

(3) N. L. Rosi and C. A. Mirkin, *Chemical Reviews*, 2005, **105**, 1547–1562.

(4) L. Wang, R. Yan, Z. Huo, L. Wang, J. Zeng, J. Bao, X. Wang, Q. Peng and Y. Li, *Angewandte Chemie International Edition*, 2005, **44**, 6054–6057.

(5) F. C. Donnelly, F Purcell-Milton, V Framont, O Cleary, P. W. Dunne and Y. K. Gun'ko, *Chemical Communications*, 2017, **53**, 6657–6660.

(6) R. D. Shannon, *Acta Crystallographica Section A*, 1976, **32**, 751–767.

(7) B. R. Heywood and S. Mann, *Langmuir*, 1992, **8**, 1492–1498.

(8) D. Rautaray, S. R. Sainkar, N. R. Pavaskar and M. Sastry, *CrystEngComm*, 2002, **4**, 626–630.

(9) A. F. Wallace, L. O. Hedges, A. Fernandez-Martinez, P. Raiteri, J. D. Gale, G. A. Waychunas, S. Whitelam, J. F. Banfield and J. J. De Yoreo, *Science*, 2013, **341**, 885.

(10) R Wiebe and V. L. Gaddy, *Journal of the American Chemical Society*, 1940, **62**, 815–817.

(11) V Blanco-Gutierrez, A Demourgues, V Jubera and M Gaudon, *J. Mater. Chem. C*, 2014, **2**, 9969–9977.

(12) P. A. Tanner, *Chemical Society Reviews*, 2013, **42**, 5090–5101.

(13) G. Gao, N. Da, S. Reibstein and L. Wondraczek, *Optics Express*, 2010, **18**, A575–A583.

(14) Y.-F. Wu, Y.-T. Nien, Y.-J. Wang and I.-G. Chen, *Journal of the American Ceramic Society*, 2012, **95**, 1360–1366.

(15) Y. Dai, H. Zou, H. Zhu, X. Zhou, Y. Song, Z. Shi and Y. Sheng, *CrystEngComm*, 2017, **19**, 2758–2767.

(16) Y. Gao, Y. Sun, H. Zou, Y. Sheng, X. Zhou, B. Zhang and B. Zhou, *Materials Science and Engineering: B*, 2016, **203**, 52–58.

(17) H. Li, Y. Sheng, H. Zhang, J. Xue, K. Zheng, Q. Huo and H. Zou, *Powder Technology*, 2011, **212**, 372–377.

(18) Y. Sun, H. Zou, B. Zhang, X. Zhou, Q. Huo and Y. Sheng, *Journal of Materials Chemistry C*, 2015, **3**, 5316–5321.

(19) M. Liu, M. Kang, K. Chen, Y. Mou and R. Sun, *Applied Physics A*, 2018, **124**, 249.

(20) Y. Onishi, T. Nakamura and S. Adachi, *Japanese Journal of Applied Physics*, 2016, **55**, 112401.

(21) M. Shang, G. Li, X. Kang, D. Yang, D. Geng and J. Lin, *ACS Applied Materials & Interfaces*, 2011, **3**, 2738–2746.

(22) J.-i. Nara and S. Adachi, *ECS Journal of Solid State Science and Technology*, 2013, **2**, R135–R141.

(23) K. Sawada, T. Nakamura and S. Adachi, *Journal of Alloys and Compounds*, 2016, **678**, 448–455.

(24) Q. Cheng, Y. Dong, M. Kang and P. Zhang, *Journal of Luminescence*, 2014, **156**, 91–96.

Chapter 7

Investigation of the Parameters Controlling Industrial Carbonation

7.1 Introduction

In terms of practical applications, $CaCO_3$ is one of the most commonly used filler materials in existence. Its industrial uses span a huge variety of industries from the paint and plastics industries where it is used as a white filler, to the pharmaceutical and agricultural industries where it finds uses as an acidity regulator as well as a filler for a variety of over-the-counter medication. The preferred method of industrial $CaCO_3$ formation typically involves a process whereby bulk limestone is calcined at typically 800-1000 °C to form CaO. The oxide is then hydrated with an excess of H_2O to form a $Ca(OH)_2$ slurry (if an excess of water is not used the process is referred to as dry hydration). CO_2 is then re-introduced to the slurry to form precipitated calcium carbonate (PCC). PCC is more useful than its bulk counterpart owing to its newly formed nano-morphology as well its increased purity and activity.

The industrial partners for this research, McGraths Cong Ltd., are a family owned company located in Cong, Co. Mayo. Their quarry produces some of the highest purity limestone commercially available at up to 99.2% purity. Their products play a key role in construction, road surfacing, agriculture, as well as in the production of glass, sugar, plastics, rubbers and paints. Importantly, their products' specific uses dependent on the size and morphology of the PCC formed.

Specifically, the industrial aspect of this work has focused on the investigation into the effect of various synthetic parameters on the morphology of $CaCO_3$ formed. Being the most stable polymorph, calcite was the preferred product for the industrial partners, McGraths Cong Ltd.

7.2 Aims

The main aim of this area of work is to investigate the carbonation process of CaO by CO_2 which is used for the industrial production of $CaCO_3$. A study of a variety of parameters and their effects on the morphology formed is planned. Specifically, a study is to be focused in determining the effect of the $Ca(OH)_2$ slurry concentration on the morphology formed. Using these results, an investigation into the effect of the CO_2 flow rate is planned. Subsequently, the effect of the reaction temperature is to be studied as $CaCO_3$ production is typically carried out at room temperature. It is particularly important that these parameters are studied, as the preferential synthesis of rhombohedral or scalenohedral calcite is of great importance to industrial $CaCO_3$ production where the morphology formed directly determines the industrial role of the $CaCO_3$ formed.

7.3 Results and Discussion

Initially, all experiments were carried out using a round-bottom flask and either a glass pipette or deflected point septum-penetrating needle. However, in an effort to more closely develop a system analogous to that used in industry, a 200 mL graduated cylinder was chosen as the reaction vessel, while a fritted glass filter was used as the method of CO_2 introduction. This fritted glass was used as it produces microbubbles which aid in the monodispersity and size reduction of the final product.

The general reaction scheme can be summarised in the following manner: Bulk limestone is calcined at around 800 - 1000 ^{o}C to form calcium oxide.

$$CaCO_3 \xrightarrow{\Delta} CaO + CO_{2(g)}$$

The oxide formed is then hydrated using an excess of water in an exothermic procedure known as 'lime slaking'.

$$CaO + H_2O \longrightarrow Ca(OH)_2 + \Delta$$

CO_2 is then bubbled through the hydroxide suspension leading to the formation of PCC.

$$Ca(OH)_2 + CO_{2(g)} \longrightarrow CaCO_3 + H_2O$$

7.3.1 Effect of Initial $Ca(OH)_2$ Concentration

The initial concentration of the $Ca(OH)_2$ slurry was varied between 0.05 mol L^{-1} and 1 mol L^{-1}. The reactions were carried out at ambient temperature, with a total volume of 50 mL and 30 min carbonation time to ensure accurate comparison. The investigation showed that at lower initial concentrations a rhombohedral morphology is favoured (see SEM images, Figures 7.1a and 7.1b). XRD was carried out on these samples to identified the polymorph formed which was determined to be calcite (Figure 7.2). The specific parameters used, as well as the morphologies formed, are detailed below in Table 7.1.

Volume (ml)	**CaO (g)**	**$Ca(OH)_2$ (M)**	**Stirring time (min)**	**Carbonation time (min)**	**Resulting morphology**
50	0.14	0.05	30	30	Rhombohedra
50	0.28	0.1	30	30	Rhombohedra
50	1.4	0.5	30	30	Scalenohedra
50	2.8	1	30	30	Scalenohedra

Table 7.1: Table illustrating the various parameters used in the examination of the effect of the initial $Ca(OH)_2$ concentration and the resulting morphologies formed

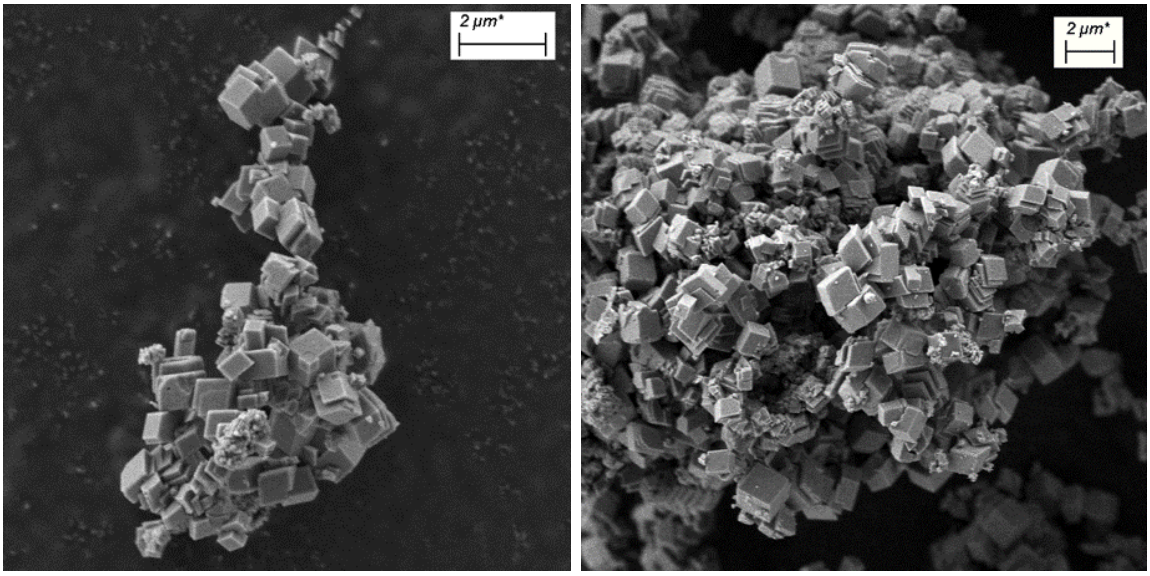

Figure 7.1: SEM images of rhombohedral calcite particles synthesised at (a) 0.05 and (b) 0.1 mol L^{-1} $Ca(OH)_2$

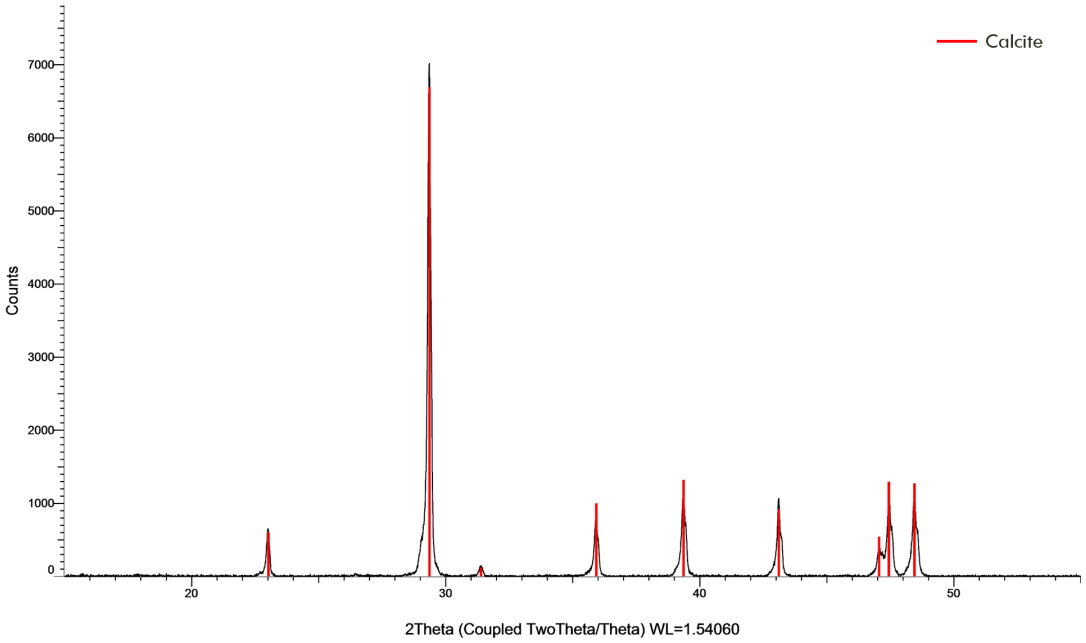

Figure 7.2: XRD Pattern of calcium carbonate synthesised at 0.1 mol L^{-1} showing characteristic calcite peaks

At and above a 0.5 mol L^{-1} concentration, there is a marked shift towards scalenohedral particles (Figures 7.3a and 7.3b) which, again, was identified as calcite using XRD (Figure 7.4).

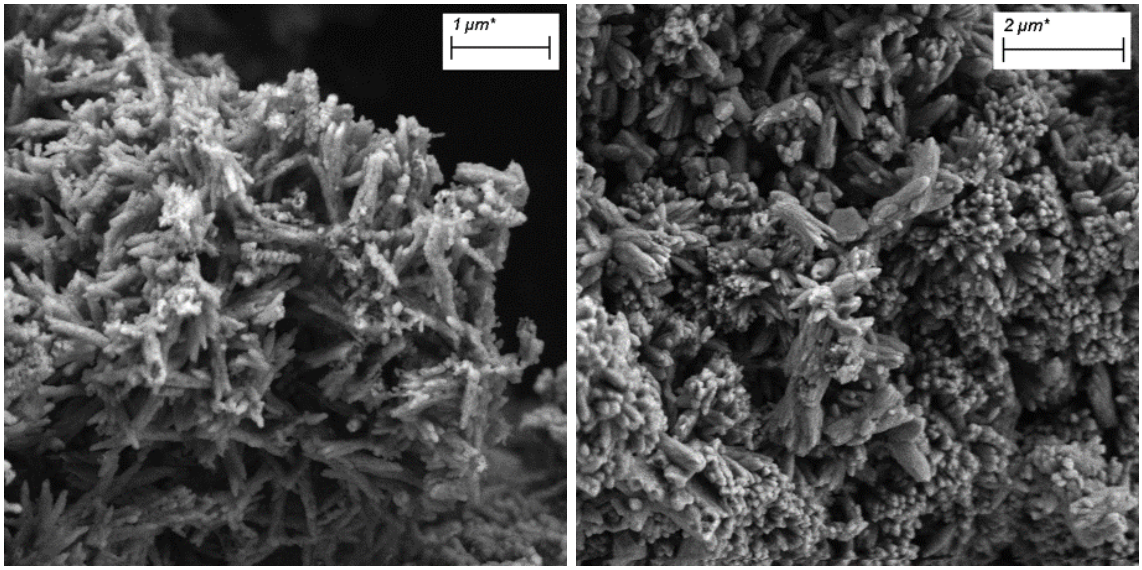

Figure 7.3: SEM images of rhombohedral calcite particles synthesised at (a) 0.5 and (b) 1 mol L^{-1} $Ca(OH)_2$

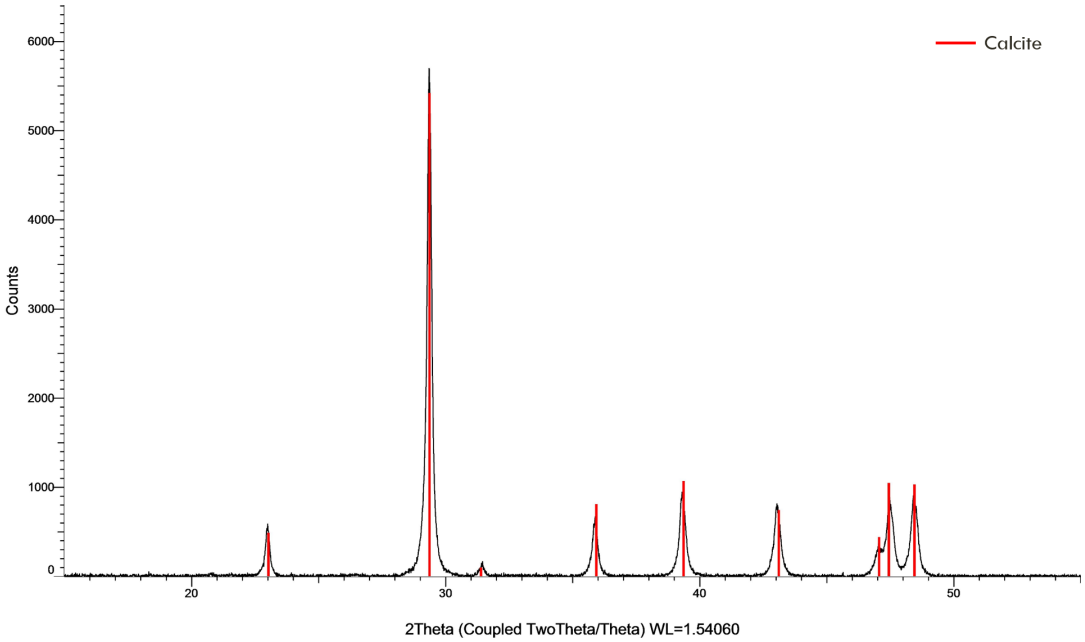

Figure 7.4: XRD Pattern of calcium carbonate synthesised at 0.5 mol L^{-1} $Ca(OH)_2$ showing characteristic calcite peaks

This observation can be explained by the fact that lower initial concentrations tend towards a rhombohedral morphology whereas an increase results in the formation of scalenohedral calcite. This arises due to the fact that Ca^{2+} ions adsorb more

strongly to the more polar {214} face of scalenohedral calcite than the respective rhombohedral {104} face.[1–4] Therefore, the higher concentration serves to stabilise the scalenohedral {214} calcite morphology.

7.3.2 Effect of CO_2 Flow Rate

Having determined that low $Ca(OH)_2$ concentrations tend towards rhombohedral calcite while higher concentrations stabilise scalenohedral calcite, the effect of the CO_2 flow rate used on the $CaCO_3$ particles formed was studied using a lower (0.1 mol L^{-1}) and higher (0.5 mol L^{-1}) concentration. A detailed description of the synthesis parameters, and morphology formed is detailed below in Table 7.2.

$Ca(OH)_2$ conc. (M)	**CaO added (g)**	**CO_2 flow rate (L min^{-1})**	**Total volume (ml)**	**Resulting morphology**
0.1	0.28	0.1	50	nano-rhombohedra
0.1	0.28	0.2	50	nano- and micro-rhombohedra
0.1	0.28	0.3	50	nano- and micro-rhombohedra
0.1	0.28	0.4	50	micro-rhombohedra
0.1	0.28	0.5	50	micro-rhombohedra
0.5	1.4	0.1	50	nano-scalenohedra
0.5	1.4	0.2	50	nano-scalenohedra
0.5	1.4	0.3	50	micro-scalenohedra
0.5	1.4	0.4	50	micro-scalenohedra
0.5	1.4	0.5	50	micro-scalenohedra

Table 7.2: Table illustrating the various parameters used in the examination of the effect of the CO_2 flow rate used and the resulting morphologies formed

Using a $Ca(OH)_2$ concentration of 0.1 mol L^{-1}, a flow rate of 0.1 L min^{-1} CO_2 resulted in rhombohedral nanoparticles as illustrated by Figures 7.5a and 7.5b. As before, these materials were analysed by XRD to confirm the presence of calcite (Figure 7.6).

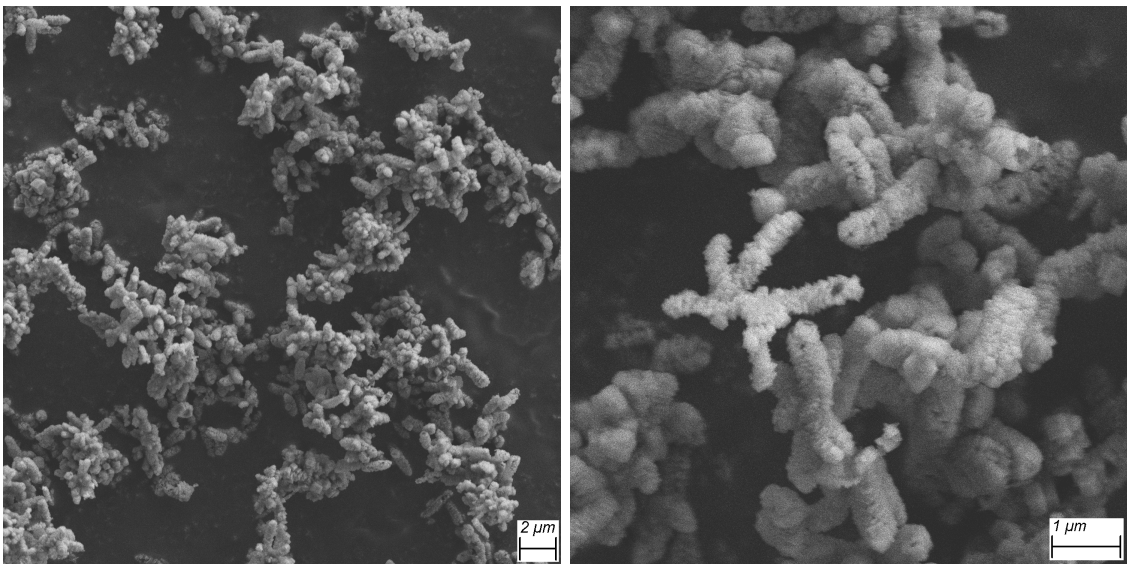

Figure 7.5: SEM images of calcite synthesised at 0.1 mol L^{-1} $Ca(OH)_2$ with 0.1 L min^{-1} CO_2 flow rate

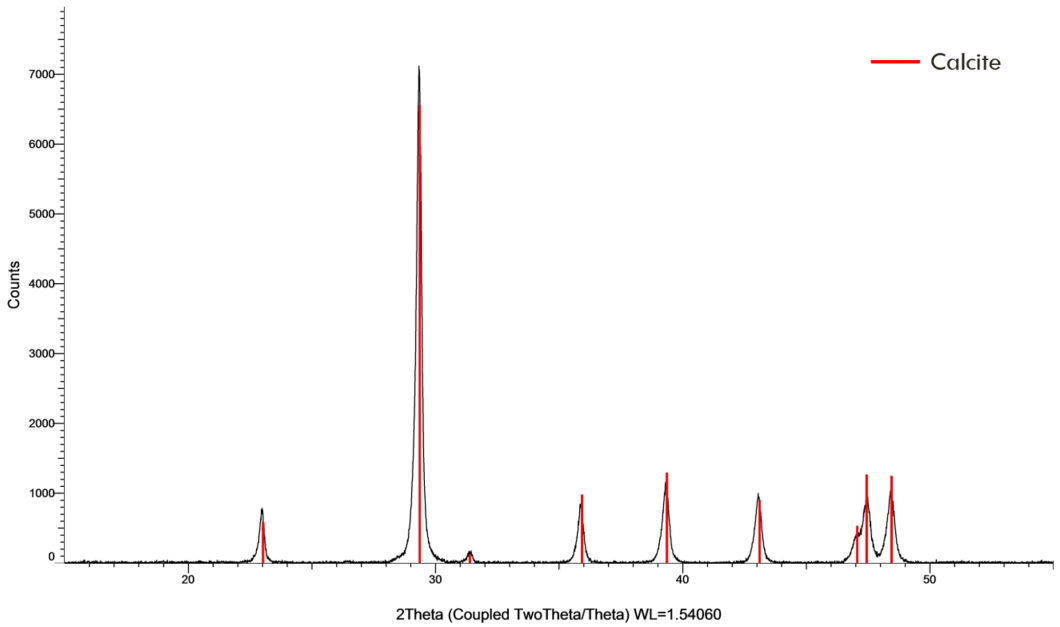

Figure 7.6: XRD Pattern of calcium carbonate synthesised at 0.1 mol L^{-1} $Ca(OH)_2$ with 0.1 L min^{-1} CO_2 flow rate

An increase in the flow rate to 0.2 (Figures 7.7a and 7.7b) and 0.3 L min^{-1} (Figures 7.7c and 7.7d), whilst maintaining a 0.1 mol L^{-1} concentration lead to two populations of particles, namely rhombohedral nano- and micro-particles. This would imply that at these CO_2 flow rates there are two competitive processes for the production of either nano- or micro- particles. Both samples were confirmed as calcite using XRD with the pattern of the 0.2 mol L^{-1} CO_2 sample shown in Figure 7.8.

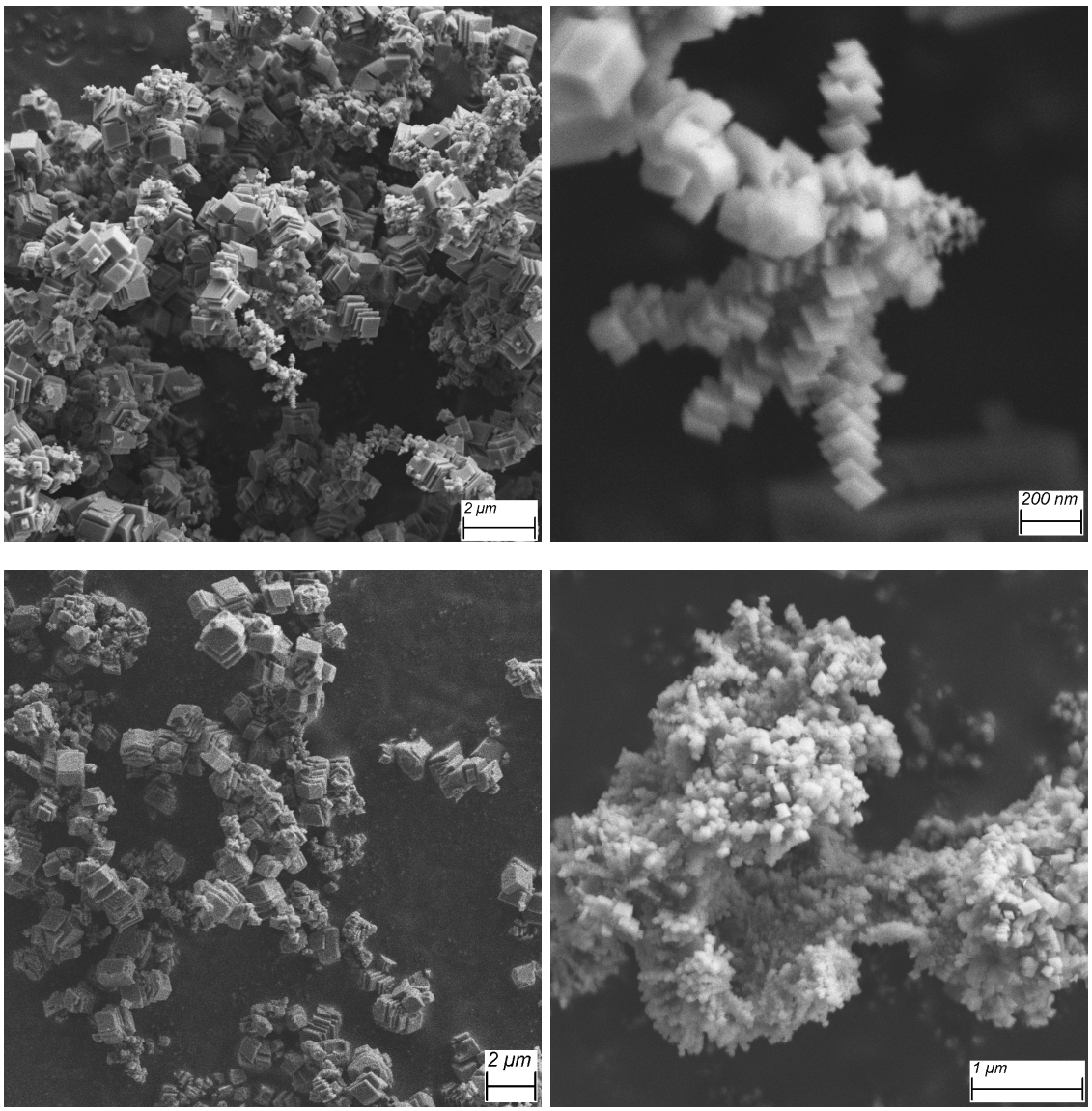

Figure 7.7: SEM images of calcite synthesised at 0.1 mol L^{-1} $Ca(OH)_2$ using a CO_2 flow rate of (a and b, above) 0.2 and (c and d, below) 0.3 L min^{-1}

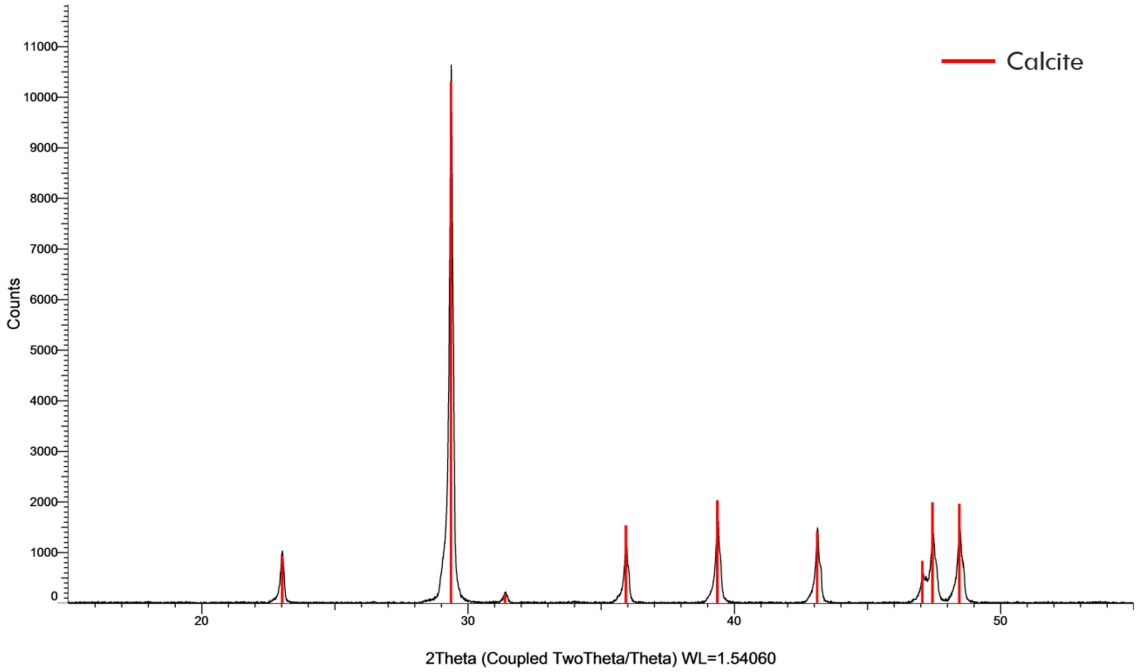

Figure 7.8: XRD Pattern of calcium carbonate synthesised at 0.1 mol L^{-1} $Ca(OH)_2$ with 0.2 L min^{-1} CO_2 flow rate

In order to preferentially form the larger rhombohedral microparticles, the CO_2 flow rate was further increased to 0.4 and 0.5 L min^{-1}. As expected, this resulted exclusively in rhombohedral microparticles (Figures 7.9a and 7.9b, respectively). Both products were once again confirmed to be predominantly calcite with only minor evidence of a vateritic phase (the pattern for the 0.4 mol L^{-1} CO_2 sample is shown in Figure 7.10).

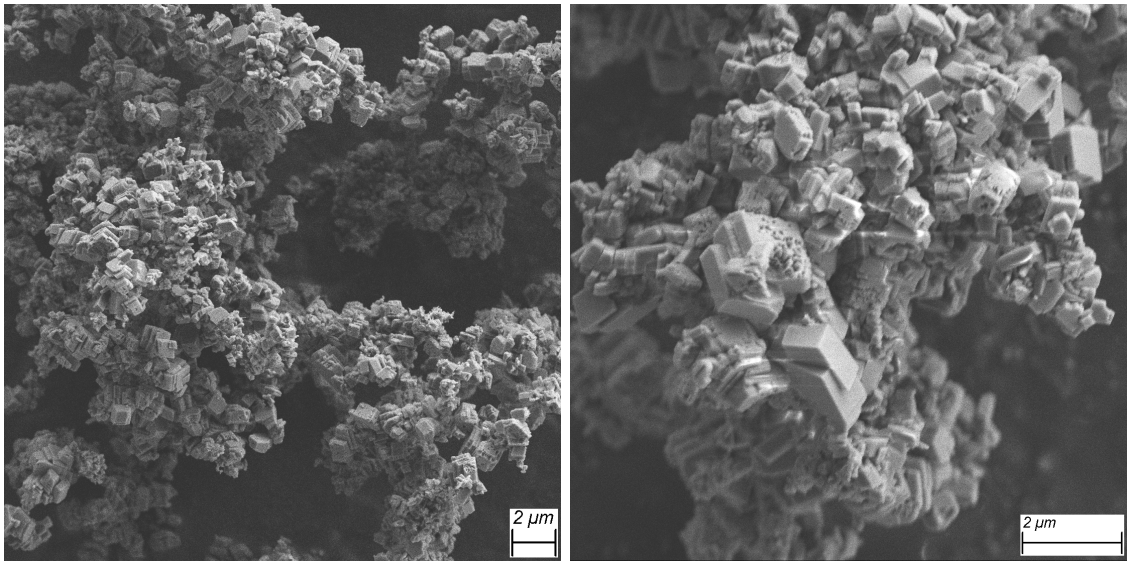

Figure 7.9: SEM images of calcite synthesised at 0.1 mol L^{-1} $Ca(OH)_2$ with (a) 0.4 and (b) 0.5 L min^{-1} CO_2 flow rate

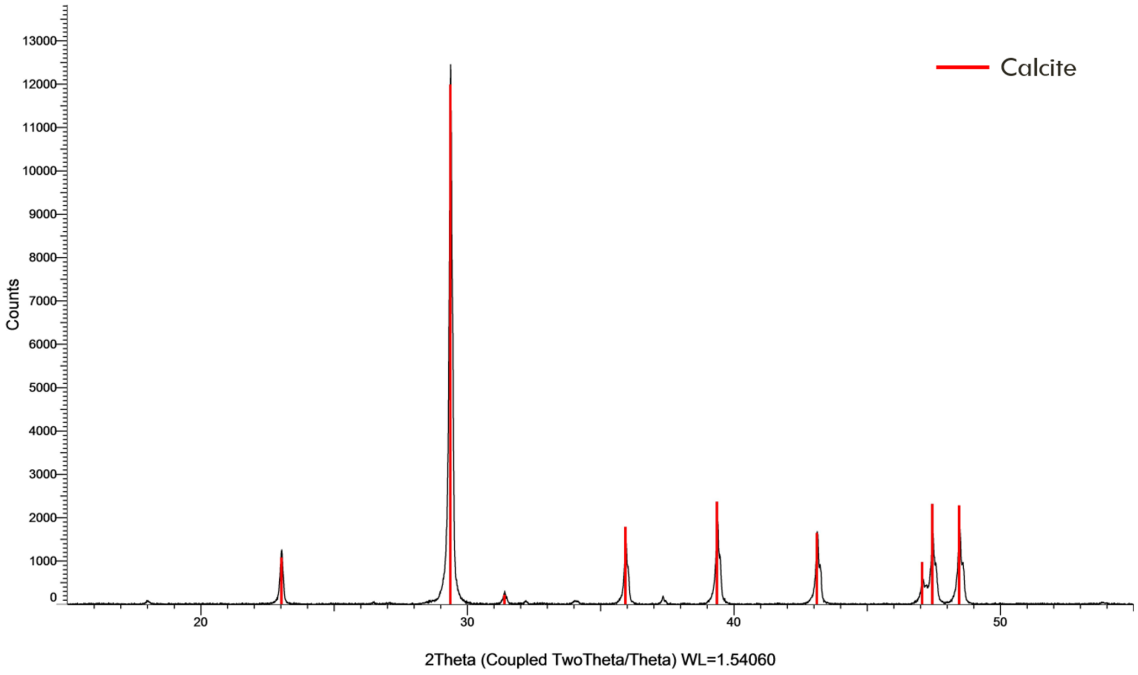

Figure 7.10: XRD Pattern of calcium carbonate synthesised at 0.1 mol L^{-1} $Ca(OH)_2$ with 0.4 L min^{-1} CO_2 flow rate

In an effort to study the effect of the CO_2 flow rate on the synthesis of scalenohedral calcite, a $Ca(OH)_2$ concentration of 0.5 mol L^{-1} was chosen once again. Similar to the trends observed for rhombohedral calcite, lower CO_2 flow rates, specifically 0.1 and 0.2 L min^{-1} resulted in nanosized particles, in this case scalenohedra (Figures 7.11a and 7.11b, respectively). XRD analysis again confirmed that all samples were composed of the calcite phase (Figure 7.12).

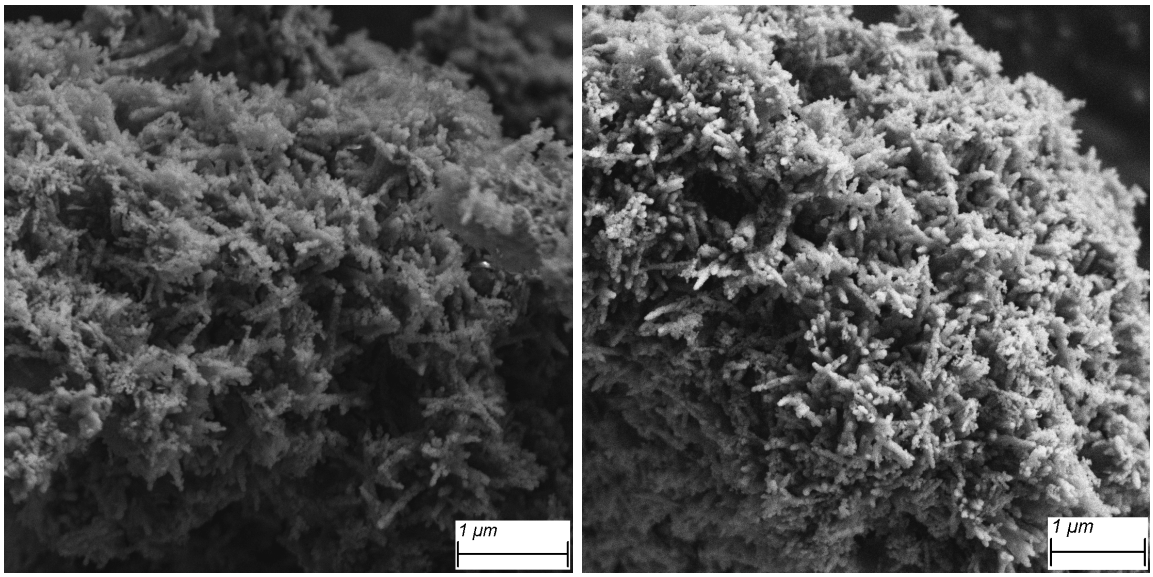

Figure 7.11: SEM images of calcite synthesised at 0.5 mol L^{-1} $Ca(OH)_2$ with CO_2 flow rates of (a) 0.1 and (b) 0.2 min^{-1}

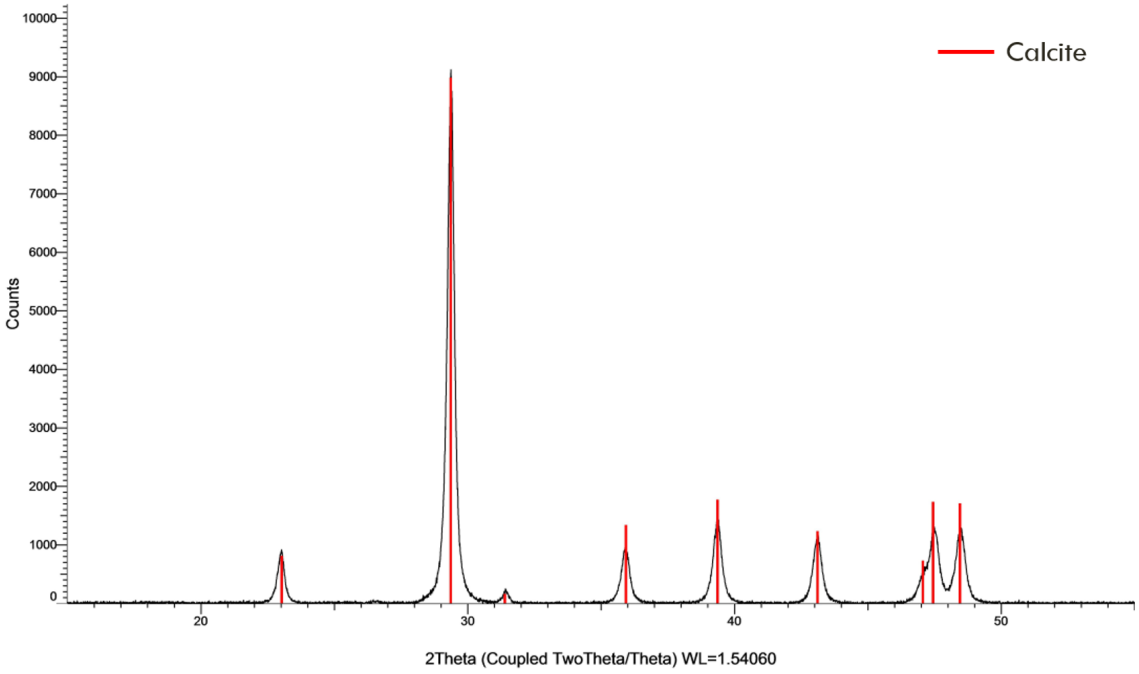

Figure 7.12: XRD Pattern of calcium carbonate synthesised at 0.5 mol L^{-1} $Ca(OH)_2$ with 0.1 L min^{-1} CO_2 flow rate

Continuing the trend previously observed, an increase in the CO_2 flow rate led to larger microparticles, in this case scalenohedra. Figure 7.13a, 7.13b and 7.13c illustrate the products of the syntheses using CO_2 flow rates of (a) 0.3 (b) 0.4 and (c) 0.5 min^{-1}, respectively.

While there has previously been some research correlating an increase in CO_2 flow rate with an increase in $CaCO_3$ particle size[2], a definitive reason has yet to be determined. One potential explanation is the inherent effect of increasing the flow rate on the size of the bubbles formed, whereby the bubble size increases in line with an increasing flow rate.[5] With larger bubbles, as has been previously shown[6], it is to be expected that some increase in particle size will occur.

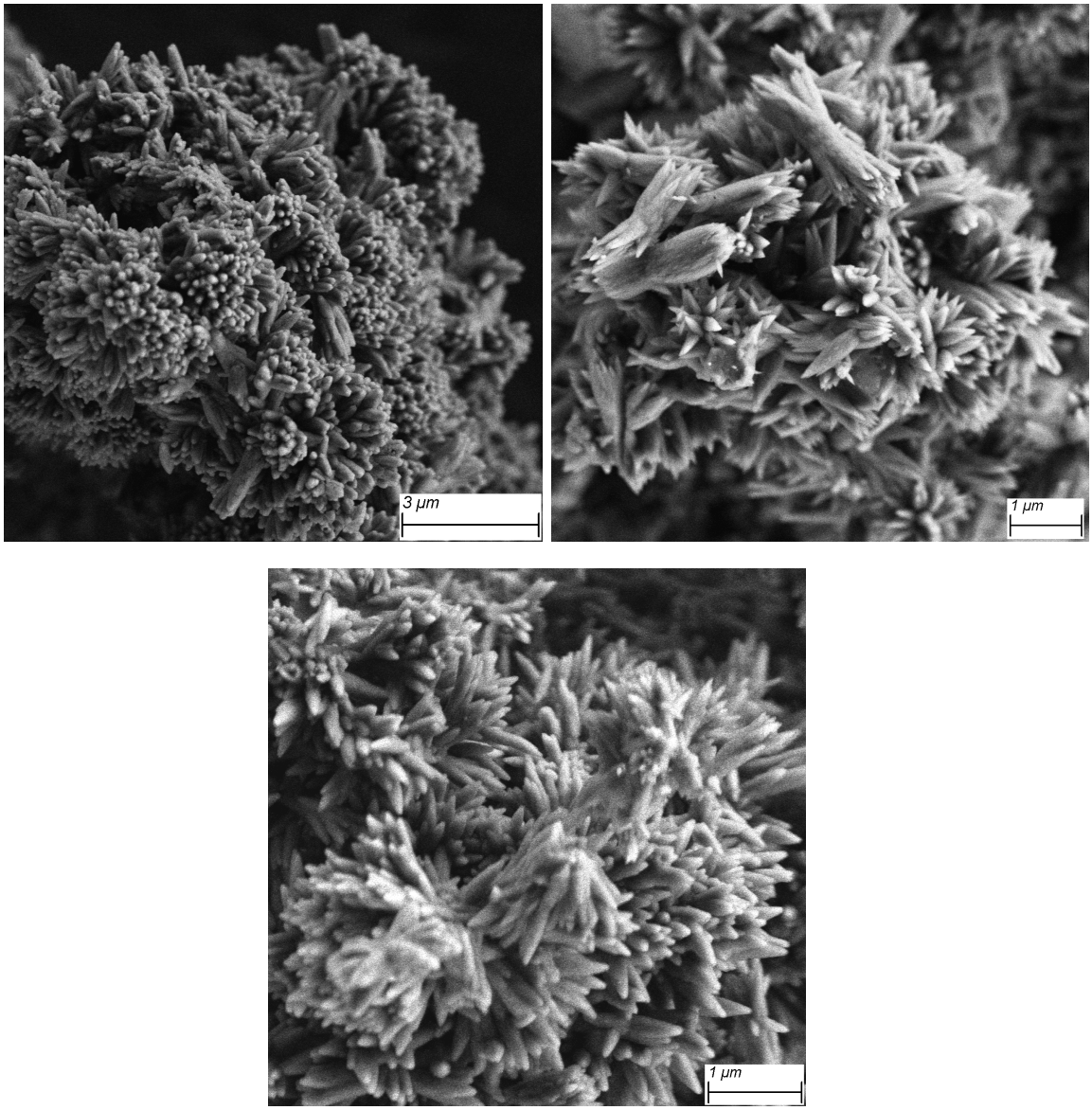

Figure 7.13: SEM images of calcite synthesised at 0.5 mol L^{-1} $Ca(OH)_2$ with CO_2 flow rates of (a) 0.3 (b) 0.4 and (c) 0.5 min^{-1}

7.3.3 Effect of Reaction Temperature

As with the study regarding CO_2 flow rate, the analysis of the effect of the reaction temperature was studied, again using both a lower (0.2 mol L^{-1}, in this case) and higher (0.5 mol L^{-1}) concentration. In order to do this, the carbonation was again completed in a 200 ml graduated cylinder with fritted glass to replicate the conditions experienced in an industrial environment, while the temperature was varied between 40 and 100 °C. Again, all products were characterised by XRD and SEM, and a detailed description of the synthesis parameters and products formed can be found below in Table 7.3.

$Ca(OH)_2$ conc. (M)	**CaO added (g)**	**Reaction temperature (°C)**	**Total volume (ml)**	**Resulting morphology**
0.2	0.56	40	50	rhombohedra & scalenohedra
0.2	0.56	60	50	rhombohedra & scalenohedra
0.2	0.56	100	50	rhombohedra & scalenohedra
0.5	1.4	40	50	scalenohedra
0.5	1.4	60	50	scalenohedra
0.5	1.4	100	50	scalenohedra

Table 7.3: Table illustrating the various parameters used in the examination of the effect of the reaction temperature and the resulting morphologies formed

At 0.2 mol L^{-1}, an increase from ambient temperature to 40 °C resulted in two populations of nanoparticles: nano-sized calcite rhombohedra (Figure 7.14a), and larger micro-sized scalenohedra (Figure 7.14b). This pattern was repeated as the temperature was increased to both 60 °C (Figures 7.15a and 7.15b) and 100 °C (Figures 7.16a and 7.16b), while XRD was used to confirm all samples as phase pure calcite (the pattern for the $CaCO_3$ produced with 0.2 mol L^{-1} $Ca(OH)_2$ at 60 °C,

is shown in Figure 7.17). This can be explained by the combination of the effect of the temperature on the overall solution saturation and the fact that the reaction is diffusion limited i.e. the rate of carbonation is different at the interface of the CO_2 bubbler than it is in the surrounding areas.

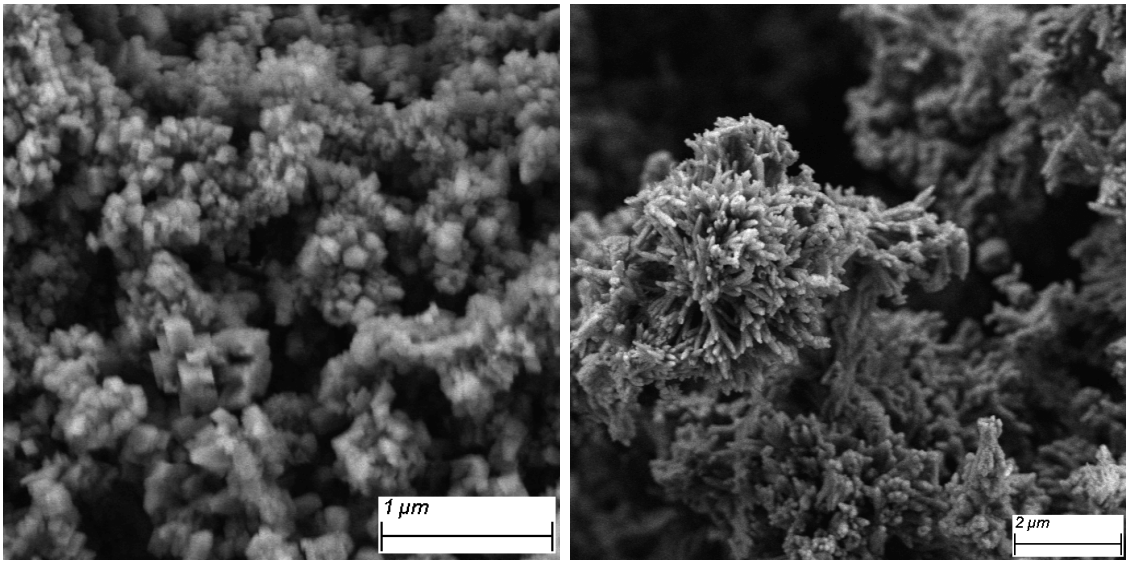

Figure 7.14: SEM images of (a) nano-sized rhombohedral and (b) micro-sized scalenohedral calcite produced from 0.2 mol L^{-1} $Ca(OH)_2$ @ 40 °C

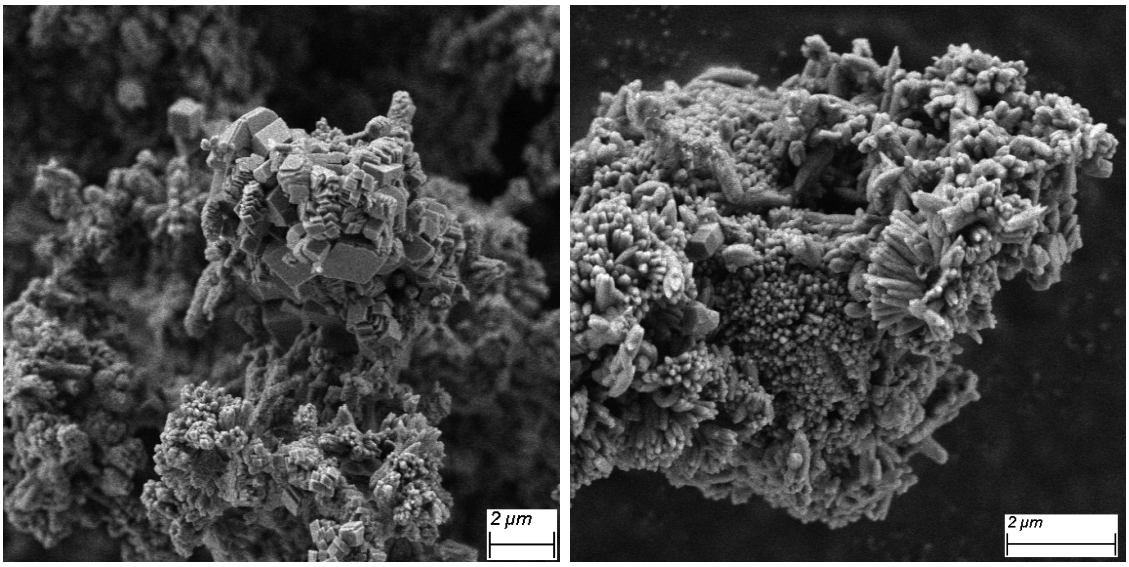

Figure 7.15: SEM images of (a) nano-sized rhombohedral and (b) micro-sized scalenohedral calcite produced from 0.2 mol L^{-1} $Ca(OH)_2$ @ 60 °C

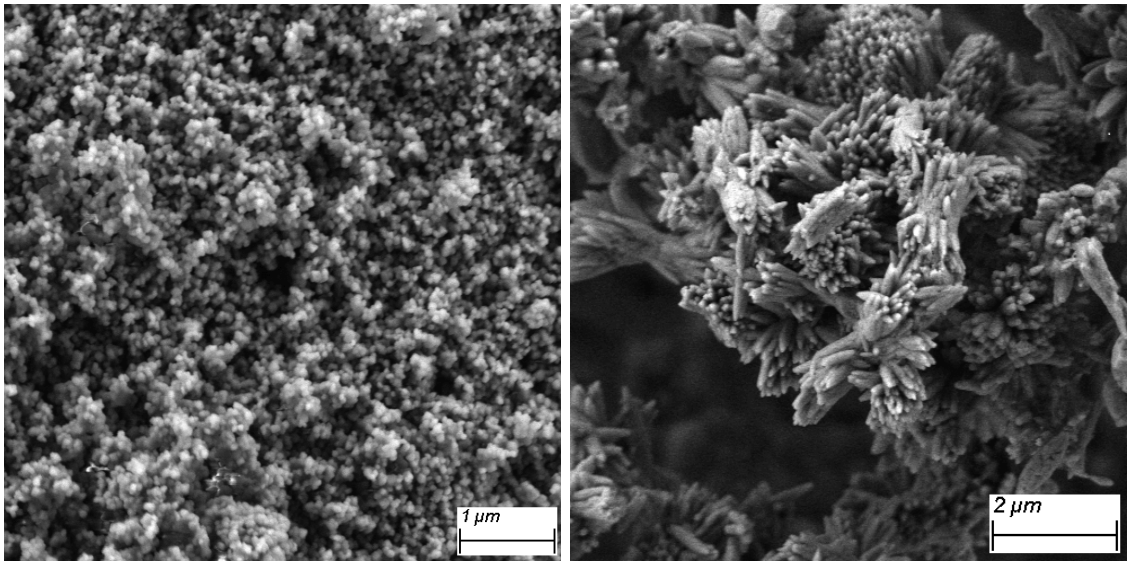

Figure 7.16: SEM images of (a) nano-sized rhombohedral and (b) micro-sized scalenohedral calcite produced from 0.2 mol L^{-1} $Ca(OH)_2$ @ 100 °C

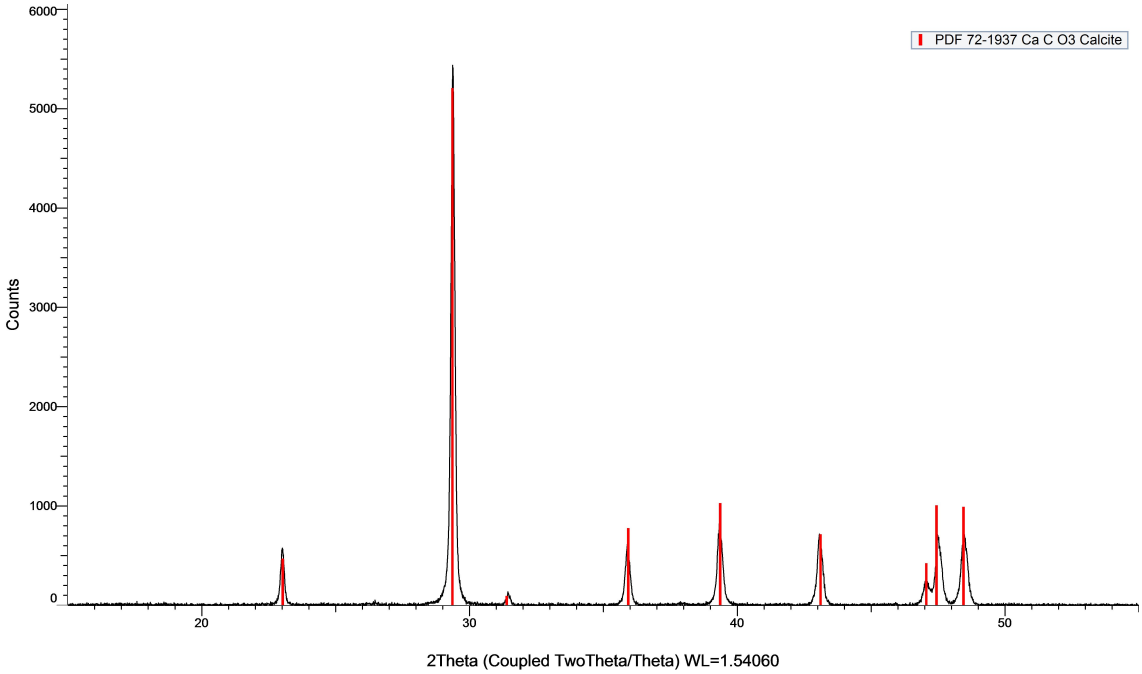

Figure 7.17: XRD Pattern of calcium carbonate produced from 0.2 mol L^{-1} $Ca(OH)_2$ @ 60 °C

The increase in temperature to 40, 60 and 100 °C did not have a noticeable effect when the concentration was set at 0.5 mol L^{-1} (See Figures 7.18a, 7.18b and 7.18c, respectively). However, as with the investigations on the effect of initial concentration, the significant result was the lack of rhombohedral particles.

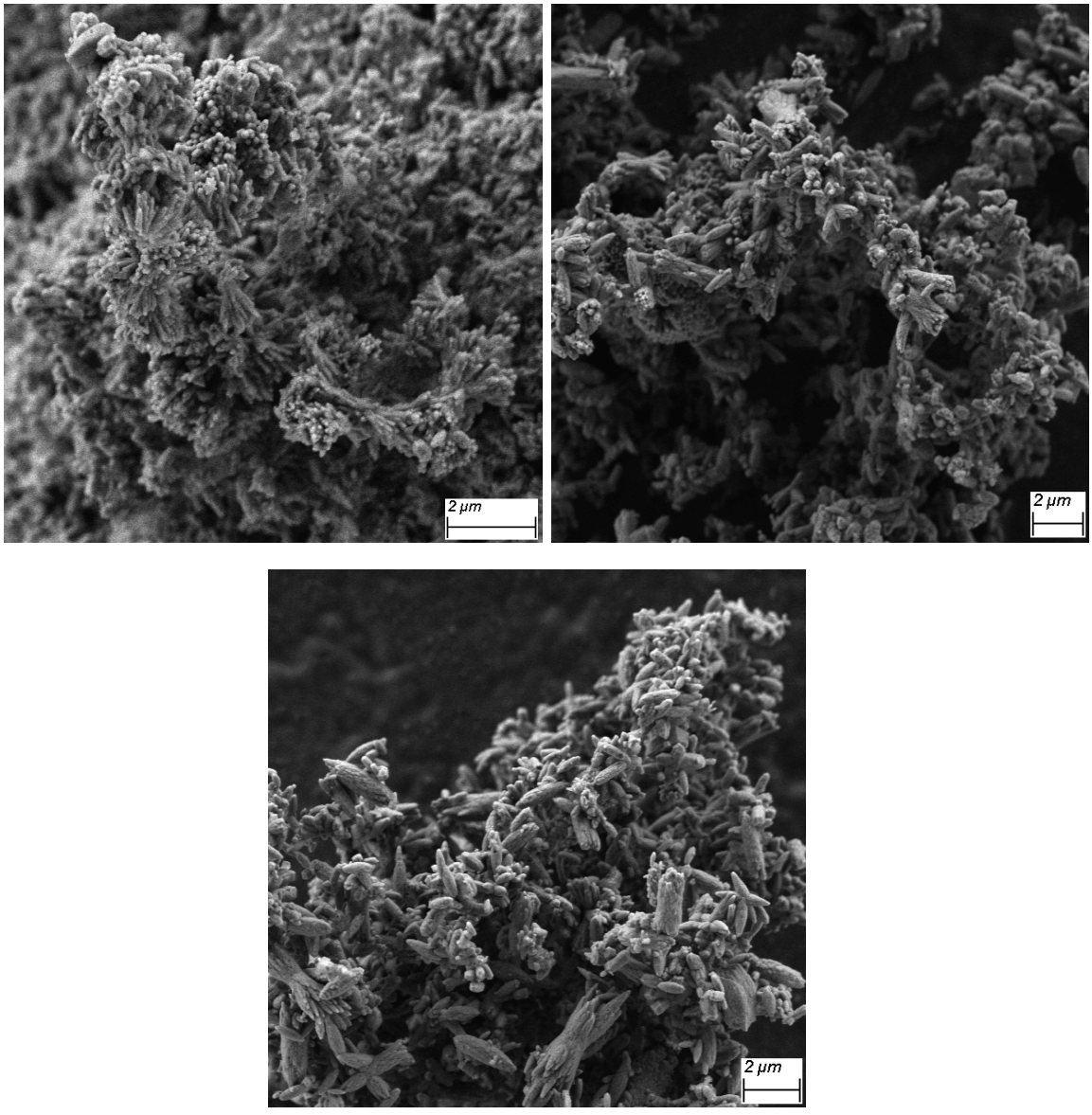

Figure 7.18: SEM images of 0.5 mol L^{-1} $Ca(OH)_2$ @ (a) 40 (b) 60 and (c) 100 °C

From this, and previous studies, it follows that the initial concentration is the dominant factor in the overall morphology obtained. While the temperature likely has a significant effect on both particle size and morphology, it seems that the initial concentration predetermines this, however it is obviously essential to take into account the overall effect that the temperature has on the level of solution saturation.

7.4 Conclusions

In conclusion, the preferential synthesis of either rhombohedral or scalenohedral calcite has successfully been achieved whilst investigating the effect of varying the initial $Ca(OH)_2$ slurry concentration, CO_2 flow rate as well as the reaction temperature.

Overall it is clearly evident that the initial $Ca(OH)_2$ concentration is the predetermining factor as, while changing the other two parameters has an effect, they are in keeping with the results of this study. This is, as mentioned, to be expected given the ability of the higher Ca^{2+} concentration to stabilise the {214} facet which is dominant in scalenohedral calcite. The observation that an increasing CO_2 flow rate serves to increase the particle size is a particularly useful one, as it allows the discrimination between not only rhombohedral and scalenohedral calcite, but also between their nano- and micro-sized forms. An increase in the reaction temperature results in a mixture of $CaCO_3$ particles of various shapes and sizes. This is a more complex problem to solve and would likely require a much more in-depth study based on a large variation of $Ca(OH)_2$ concentrations and temperatures, and this will be carried out in future work.

The results of these studies have also proven hugely useful to McGrath's Cong, for whom the preferential synthesis of rhombohedral and scalenohedral calcite is a highly important asset. Thus, we believe that these studies have contributed usefully to the further development of industrial carbonation techniques.

References

(1) M. Ukrainczyk, M. Gredičak, I. Jerić and D. Kralj, *Crystal Growth & Design*, 2014, **14**, 4335–4346.

(2) T. Thriveni, N. Um, S.-Y. Nam, Y. J. Ahn, C. Han and J. W. Ahn, *Journal of the Korean Ceramic Society*, 2014, **51**, 107–114.

(3) Ö. Cizer, C. Rodriguez-Navarro, E. Ruiz-Agudo, J. Elsen, D. Van Gemert and K. Van Balen, *Journal of Materials Science*, 2012, **47**, 6151–6165.

(4) D. Aquilano, F. Otálora, L. Pastero and J. M. García-Ruiz, *Progress in Crystal Growth and Characterization of Materials*, 2016, **62**, 227–251.

(5) A. A. T. Alkhalidi and R. S. Amano, *Water and Environment Journal*, 2015, **29**, 105–113.

(6) J.-H. Bang, K. Song, S. Park, C. Jeon, S.-W. Lee and W. Kim, *Energies*, 2015, **8**, 12304–12313.

Chapter 8

Conclusions and Future Work

8.1 Conclusions

This project has yielded a range of $CaCO_3$-based nano- and micro-structural materials which have been produced using a variety of synthetic techniques, both established and new. All materials have been fully characterised by a number of instrumental techniques that enabled us to establish the nature and properties of these materials.

Through chemical precipitation methods, a variety of interesting chiral $CaCO_3$ materials have been synthesised. Using amino acids, chiroptically active $CaCO_3$ hollow microspheres have been developed for the first time. These microspheres have the potential to be used as both new asymmetric catalysts and drug delivery vesicles. For catalysis, their large surface areas and definitive shape represent a promising catalytic support. The doping of these microspheres with catalytically active agents could result in a recyclable asymmetric heterogeneous catalyst, with significance at both the academic and industrial level. Their use as potential drug delivery agents, where their induced chirality might be used for biorecognition to achieve more specific delivery, is currently one of the focuses of our research. Furthermore, the work

on drug delivery has yielded potentially biocompatible drug delivery systems with a high level of bioavailability. Future work in this area will involve the tuning of the pores in the microspheres synthesised to allow efficient, and controllable drug release, and the associated drug release studies are ongoing. Using lanthanides such as europium, we aim to dope these microspheres to allow the synthesis of both chiral luminescent particles, and luminescent microspheres for targeted drug delivery. Such bimodal systems have not previously been reported for calcium carbonate as a supporting material.

A new unique method for the synthesis of $CaCO_3$ nanostructures using dry ice carbonation has been developed. This technique achieves high phase purity and particle size control, using appropriate solvent systems. Potentially this new carbonation approach can also be used in the large scale production of other important carbonate nanomaterials (e.g. Li_2CO_3, $SrCO_3$), opening new possibilities in this research area and a variety of relevant industrial applications. This dry ice approach gives an opportunity to perform the carbonation process at low temperatures, favouring the nucleation phase over growth and enabling the production of small metal carbonate nanoparticles of high monodispersity, which is not feasible to achieve in ambient or high temperature syntheses. The use of low temperatures can also enable the synthesis of unstable carbonate polymorphs such as vaterite and potentially other metal carbonate polymorphs with unusual morphologies. This approach is economical and intrinsically scalable and therefore potentially applicable at the industrial scale.

Building on this new method, the synthesis of lanthanide-doped $CaCO_3$ microstructures has also been achieved. These materials present a novel 'bow tie' morphology and have luminescent properties which are favourable when compared to previous doped $CaCO_3$ materials.

New carbonate-based nanomaterials produced by this novel approach show enormous potential for use in drug-delivery, paper manufacturing, catalysis and other applications in which size control and phase purity are essential. Therefore, future work will involve development of dry ice carbonation for the preparation of new nano- and micro-structured $CaCO_3$, Li_2CO_3, $SrCO_3$, $ZnCO_3$ and other metal carbonate based materials.

Regarding industrial carbonation, a definitive optimised method for the synthesis of rhombohedral or scalenohedral calcite has been developed for our industrial partners, while the effect of initial $Ca(OH)_2$ slurry concentration, CO_2 flow rate, and reaction temperature have been studied in depth.

8.2 Future work

This project has revealed a number of new research avenues which would be interesting to explore. Specifically, we plan to carry out the following research, which we believe will further develop the field of $CaCO_3$ based nano- and micro- structural materials:

1. Further optical characterisation of the as-synthesised multi-modal $CaCO_3$ microspheres will be carried out including, but not limited to, the solid state analysis of the Au NP loaded microspheres to confirm their encapsulation.

2. Subsequently, the application of the multi-modal microspheres in various fields of biomedicine e.g. cellular imaging and biosensing, will be investigated. Following on from this, we will explore the loading of these microspheres with various other materials e.g. magnetic nanoparticles as well as other luminescent species.

3. The use of the proline-functionalised $CaCO_3$ microspheres as heterogeneous catalysts for an asymmetric aldol is currently being studied and whilst they have been proven to be effective catalysts for the reaction, an enantiomerically pure product has not, as of yet, been obtained.

4. The continuation of the work into an effect NSAID-based drug delivery using $CaCO_3$ microspheres as a drug delivery vesicle in order to attain an effective and repeatable drug release profile.

5. A study on the effects of aging on the $CaCO_3$ helices will be carried out in an attempt to couple the coiling of the helix with the CD signal observed.

6. The synthesis of Eu^{3+} doped $CaCO_3$ helices with a view to investigating the possible existence of circularly polarised luminescence (CPL).

7. The expansion of the new dry ice carbonation to other metal carbonates e.g. Li_2CO_3, $ZnCO_3$, $MgCO_3$.

8. A thorough and sequential investigation into the effect of Lanthanide-doping on $CaCO_3$. This research has already yielded interesting results with the observation that 2 mol% Er and Yb doped $CaCO_3$ result in $CaCO_3$ nanoparticles which are smaller than has been previously reported (see Figure 8.1) as well as some interesting products.

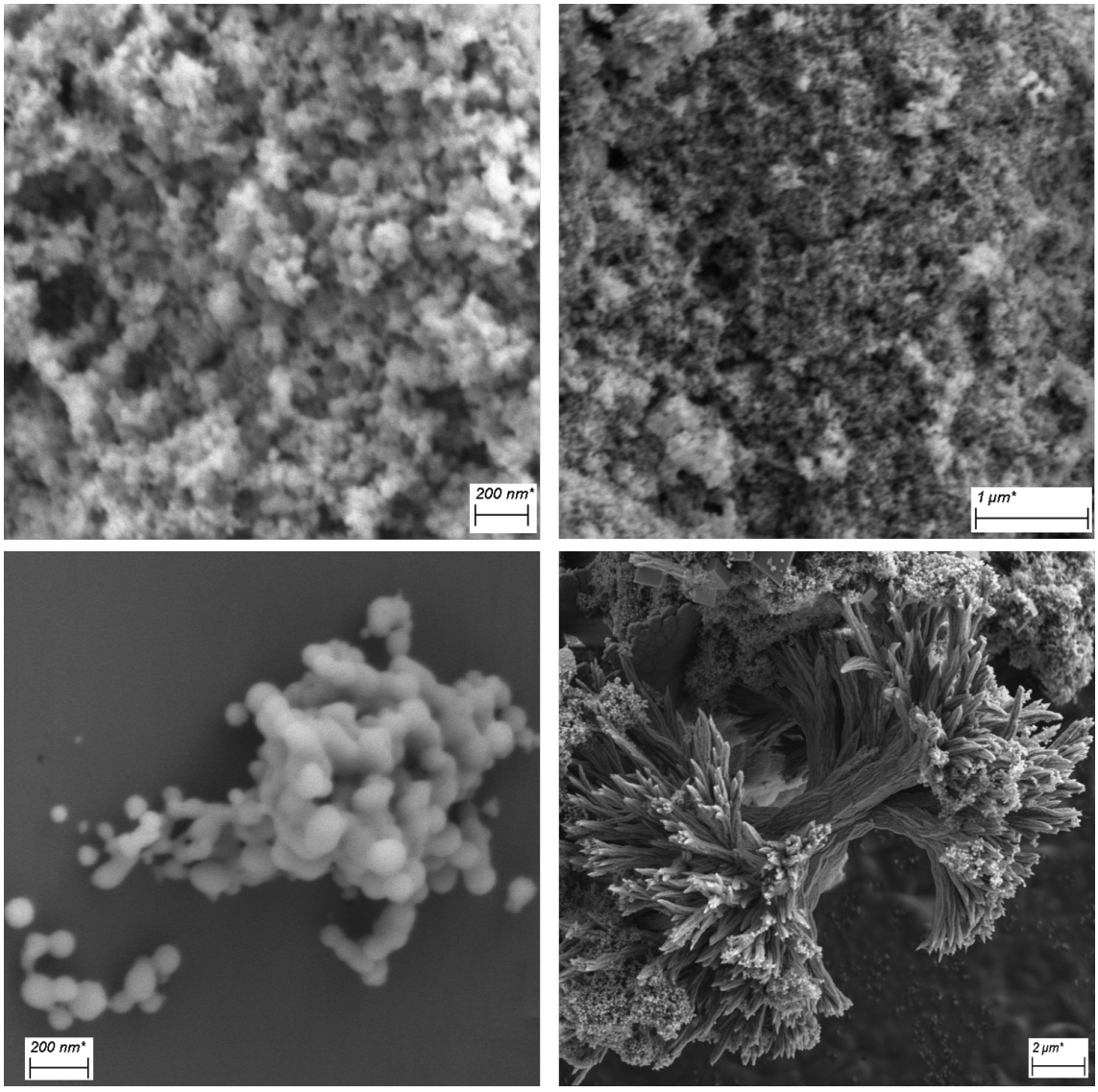

Figure 8.1: SEM images of some of the products obtained with 2 mol % Er and Yb doped $CaCO_3$

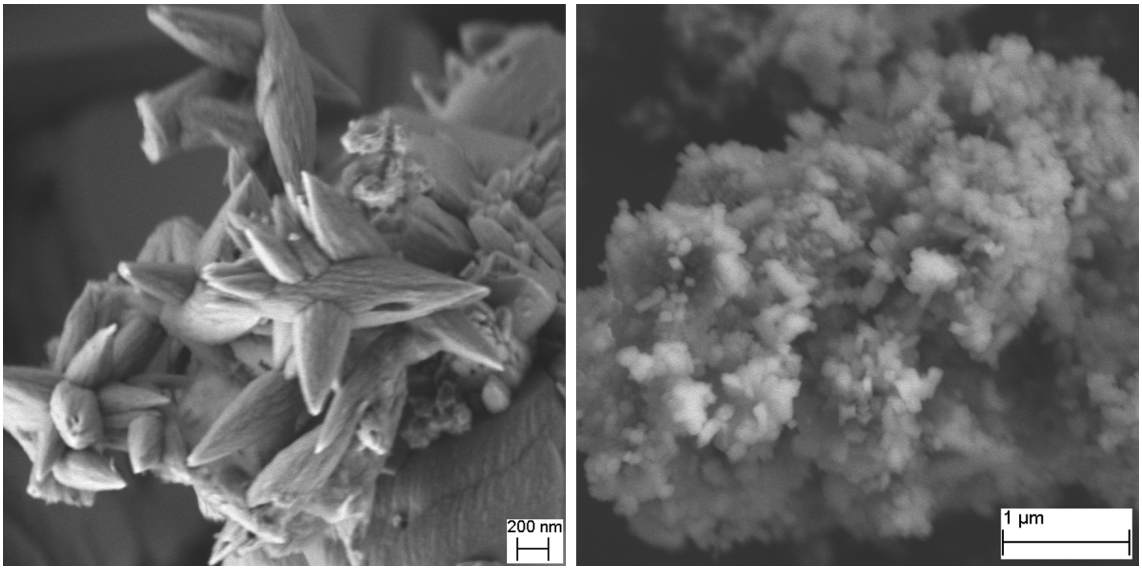

Figure 8.2: SEM images of $CaCO_3$ produced by CO_2 bubbling in the presence of (left) DTAB and (right) terpineol

9. The effect of various additives and surfactants on the products of industrial carbonation are currently being investigated and have resulted in some interesting products e.g. with the use of terpineol and citric acid (see Figure 8.2).

10. Finally, we have started our work on the use of porous $CaCO_3$ microspheres as a membrane for the chiral separation of various products e.g. mono- and disaccharides *D/L* lactic acid. These studies will be continued in the near future.

Publications and Conference Presentations

Publication list

F. C. Donnelly, F Purcell-Milton, V Framont, O Cleary, P. W. Dunne and Y. K. Gun'ko, Chemical Communications, 2017, **53**, 6657–6660.

F. C. Donnelly, F. Purcell-Milton, P. W. Dunne, A. Rulikowska, V. Alguacil and Y. K. Gun'ko, Materials Today Communications, 2019, **20**, DOI:10.1016/j.mtcomm.2019.100590.

I. V. Martynenko, D. Kusíc, F. Weigert, S. Stafford, **F. C. Donnelly**, R. Evstigneev, Y. Gromova, A. V. Baranov, B. Rühle, H.-J. Kunte, Y. K. Gun'ko, and U. Resch-Genger, Analytical Chemistry, 2019, **91**, 12661–12669.

Conference Presentations

2019 MRS Spring Meeting and Exhibit, *Synthesis and Characterisation of Calcium Carbonate-Based Nano- and Micro- Structural Materials*, April 25, 2019